AD-A250 801

(1)

NUMERICAL STUDY OF AXIAL TURBULENT FLOW OVER LONG CYLINDERS

By
João C. Neves, Parviz Moin and Robert D. Moser

DTIC
ELECTE
JUN 0 1 1992
S D
A

Prepared with the support of the
Office of Naval Research
under contract N00014-88-k-0145
and in cooperation with the
Naval Underwater Systems Center

Report No. TF-54

Thermosciences Division
Department of Mechanical Engineering
Stanford University
Stanford, California 94305

April 1992

92-11834

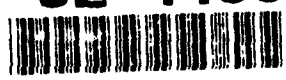

92 4 29 137

NUMERICAL STUDY OF AXIAL TURBULENT FLOW OVER LONG CYLINDERS

By

João C. Neves, Parviz Moin and Robert D. Moser

Prepared with the support of the
Office of Naval Research
under contract N00014-88-k-0145
and in cooperation with the
Naval Underwater Systems Center

Accesion For
NTIS CRA&I ☑
DTIC TAB ☐
Unannounced ☐
Justification
By
Distribution /
Availability Codes
Dist | Avail and / or Special
A-1

Report No. TF-54

Thermosciences Division
Department of Mechanical Engineering
Stanford University
Stanford, California 94305

April 1992

Statement A per telecon James Fein
ONR/Code 1221
Arlington, VA 22217-5000

NWW 5/29/92

AD-A250801 Words/Phrases(4 words max) that match Thesaurus Entries

TEXT	THESAURUS
BOUNDARY	Boundaries
BOUNDARY LAYER	Boundary Layer
CABLES	Cables
CHANNEL	Channels
CURVATURE	Curvature
ENERGY	Energy
EQUATION	Equations
FLOW	Flow
FLOW FIELDS	Flow Fields
FRICTION	Friction
KINETIC	Kinetics
KINETIC ENERGY	Kinetic Energy
LAYER	Layers
LAYERS	Layers
MEAN	Mean
MOMENTUM	Momentum
NUMBER	Numbers
PRESSURE	Pressure
QUADRANT	Quadrants
REGION	Regions
REGIONS	Regions
REYNOLDS NUMBER	Reynolds Number
SCALE	Scale
SIMULATION	Simulation
SIMULATIONS	Simulation
SKIN FRICTION	Skin Friction
SLOPE	Slope
SONAR	Sonar
SPEED	Velocity
STATISTICS	Statistics
THICKNESS	Thickness
TRANSVERSE	Transverse
TURBULENCE	Turbulence
TURBULENT FLOW	Turbulent Flow
TURBULENT FLOWS	Turbulent Flow
VELOCITY	Velocity
VORTICES	Vortices
WALL	Walls

@1@ AD-A250801 92-17
@20@ u
@23@ Boundaries, Boundary Layer, ~~Cables~~, Channels, Curvature, Energy, Equations, ~~Flow~~, Flow Fields, ~~Friction~~, Kinetic Energy, ~~Kinetics~~, Layers, Mean, Momentum, ~~Numbers~~, Pressure, Quadrants, Regions, Reynolds Number, Scale, ~~Simulation~~, Skin Friction, Slope, Sonar, Statistics, ~~Thickness~~, Transverse, Turbulence, ~~Turbulent~~ Flow, Velocity, Vortices, Walls.
@24@ u
@27@ Convex transverse curvature effects in wall bounded turbulent flows are significant if the boundary layer thickness is large compared to the

AD-A250801 (Cont'd)

radius of curvature. The curvature affects the inner part of the flow if a+, the cylinder radius in wall units, is small. This flow regime is common in sonar devices towed by long cables. Two direct numerical simulations of transversely curved flows were performed and statistical and structural data were extracted from the computed flow fields. The effects of the transverse curvature were identified by comparing the present results with those of the plane channel simulation, performed at a similar Reynolds number. As expected, the transversely curved turbulent flow exhibits many features common to the planar flows: near-wall low speed streaks, near-wall inclined shear layers, near-wall streamwise vortices, Reynolds shear stress dominated by second and fourth quadrant events, etc. As the curvature increases, the skin friction increases, the slope of the logarithmic region decreases and turbulence intensities are reduced. Several turbulence statistics are found to scale with a curvature dependent velocity scale derived from the mean momentum equation. Near the wall, the flow is more anisotropic than in the plane channel with a larger percentage of the turbulent kinetic energy resulting from the streamwise velocity fluctuations. Near-wall streamwise vortices are the strongest sources of pressure fluctuations. As the curvature increases, regions of strong normal vorticity develop near the wall.

@28@ u

Abstract

Convex transverse curvature effects in wall bounded turbulent flows are significant if the boundary layer thickness is large compared to the radius of curvature. The curvature affects the inner part of the flow if a^+, the cylinder radius in wall units, is small. This flow regime is common in sonar devices towed by long cables.

Two direct numerical simulations of transversely curved flows were performed and statistical and structural data were extracted from the computed flow fields. The effects of the transverse curvature were identified by comparing the present results with those of the plane channel simulation, performed at a similar Reynolds number. As expected, the transversely curved turbulent flow exhibits many features common to the planar flows: near-wall low speed streaks, near-wall inclined shear layers, near-wall streamwise vortices, Reynolds shear stress dominated by second and fourth quadrant events, etc. As the curvature increases, the skin friction increases, the slope of the logarithmic region decreases and turbulence intensities are reduced. Several turbulence statistics are found to scale with a curvature dependent velocity scale derived from the mean momentum equation. Near the wall, the flow is more anisotropic than in the plane channel with a larger percentage of the turbulent kinetic energy resulting from the streamwise velocity fluctuations. Near-wall streamwise vortices are the strongest sources of pressure fluctuations. As the curvature increases, regions of strong normal vorticity develop near the wall.

As the curvature increases the wall pressure fluctuations are dominated by smaller spanwise length scales. Fractional contributions from various layers in the flow to the wall r.m.s. pressure are marginally affected by the curvature. The ratio of the axial to azimuthal length scales of the wall pressure fluctuations increase with increasing curvature. Curvature dependent time and length scales are identified that collapse the high frequency range of the wall pressure temporal spectra and the high wave number range of the wall pressure streamwise spectra of flows with different curvatures. Taylor's hypothesis holds for the wall pressure fluctuations with a lower convection velocity than in the planar case.

Acknowledgments

This work was supported by the Office of Naval Research under Contract number N00014-88-k-0145, and in cooperation with the Naval Underwater Systems Center in New London, CT. Dr. Jack Hanson of ONR got us interested in this problem. Dr. James Fein of ONR was the Technical Monitor, and brought to our attention the issues of interest to the Navy. We appreciate several useful technical discussions with Dr. David Hurdis of NUSC and are grateful for his continued interest in this project. Computer time was provided by the NASA Ames Research Center and the NAS Office. Their support is greatfully acknowledged.

The authors are grateful to Mr. H. Choi for his help with the plane channel database. Thanks are also due to Professors S. K. Lele and P. Bradshaw for helpful comments on a draft of this report.

Table of Contents

Page

Abstract ii
Acknowledgements iii
Table of Contents iv
List of Tables vi
List of Figures vii
Nomenclature xviii

Chapter

1. Introduction 1
1.1 Transverse Curvature Effects 1
1.2 The Wall Pressure 5
1.3 Motivation and Objectives 6

2. Model Problem 9
2.1 Equations of Motion 9
2.1.1 Boundary Conditions 12
2.1.2 Radial Coordinate Stretching 13
2.2 Uncoupling of the Viscous Operator 13
2.3 Time Advancement 15
2.4 Continuity at the Boundaries 17
2.5 The Mean Flow 19
2.6 Code Verification 20
2.6.1 Numerical Resolution 22

3. The Velocity and Vorticity 27
3.1 Mean Velocity Statistics 27
3.1.1 The Mean Velocity Profile 31
3.2 Turbulence Statistics 33
3.2.1 Turbulence Intensities 35

3.2.2 Reynolds Shear Stress 37
3.2.3 Velocity Scaling 39
3.3 Quadrant Analysis 40
3.4 The Vorticity 48
3.5 Instantaneous Turbulent Flow Structures 55

4. Pressure Fluctuations 79
4.1 Pressure Source Terms 80
4.2 Computational Considerations 84
4.2.1 Spatial Spectra 85
4.2.2 Temporal Spectra 85
4.3 Spatial Spectra 88
4.4 Two-point Correlations 91
4.5 Green's Function Representation 96
4.6 Temporal Spectra 103
4.7 2-D Spectra and Correlations 105
4.8 Convection Velocity and Taylor's Hypothesis 105

5. Summary and Conclusions 115

Appendices 119

A. Reynolds Stress Budgets 119

B. The Green's Function for Pressure 133

C. Flow Databases 137
C.1 Velocity and Pressure Data 137
C.2 Wall Data 138

References 141

List of Tables

Tables		Page
2.1 *a*	Critical Reynolds number (Re_c) for 2-D Taylor vortices	21
2.1 *b*	Torque for 2-D Taylor vortices	21
2.1 *c*	Wave speed of 3-D Taylor vortices ($\lambda/d = 3.0$, $m = 6$)	22
2.2	Grid Resolution parameters	23
3.1	Mean flow parameters	28
3.2 *a*	Mean flow parameters (Willmarth *et al.* [1976])	29
3.2 *b*	Mean flow parameters (Luxton *et al.* [1984])	29
3.2 *c*	Mean flow parameters (Lueptow & Haritonidis [1987])	29
3.3	Streamwise vortex parameters	50
4.1	Temporal resolution parameters	84
4.2	Wall pressure parameters	88

List of Figures

Figures Page

1.1 Experimental data available for the axial turbulent flow along a circular cylinder: ▵ Luxton *et al.* (1984); + Lueptow *et al.* (1985) and Lueptow & Haritonidis (1987); × Willmarth & Yang (1970) and Willmarth *et al.* (1976); ◇ Rao & Keshavan (1972); ○ Afzal & Narasimha (1976); ▽ Richmond (1957); □ Yu (1959); • present calculations. 2

2.1 Computational domain illustrated by the grid at the surface of the cylinder ($r = a$) and at the outer edge of the layer ($r = a + 1$). The mean flow is parallel to the axis of the cylinder. 11

2.2 Azimuthal (spanwise, $\delta \Delta k_\theta = \delta / r$) spectra of the velocity fluctuations normalized by δ and u_τ for $\delta/a = 5$ (a) and for $\delta/a = 11$ (b): —— $E_{v_z v_z}$; – – – $E_{v_\theta v_\theta}$. 23

2.3 Axial (streamwise) spectra of the velocity fluctuations normalized by δ and u_τ for $\delta/a = 5$ (a and b) and for $\delta/a = 11$ (c and d): —— $E_{v_z v_z}$; - - - - $E_{v_r v_r}$; – – – $E_{v_\theta v_\theta}$. 24

2.4 Axial (streamwise) two-point correlations of the velocity fluctuations for $\delta/a = 5.0$ with $L_z/\delta = 4\pi$ (a and b) and for $\delta/a = 11.0$ with $L_z/\delta = 6\pi$ (c and d): —— $R_{v_z v_z}$, - - - - $R_{v_r v_r}$, – – – $R_{v_\theta v_\theta}$. 25

3.1 Mean-velocity profiles: – – – plane channel (Kim *et al.* [1987]); cylinders with —— $\delta/a = 5$ and - - - - $\delta/a = 11$; ····· planar law of the wall, $U^+ = y^+$, and log law, $U^+ = 2.5 \ln(y^+) + 5.5$. 30

3.2 Total stress normalized by u_τ: analytical for cylinders with —— $\delta/a = 5$ and - - - - $\delta/a = 11$; symbols for computed results with ○ for $\delta/a = 5$ and with ▵ for $\delta/a = 11$. 32

3.3 Root-mean-square velocity fluctuations normalized by u_τ: (a) Axial (streamwise) intensity, (b) Normal intensity, (c) Azimuthal (spanwise) intensity; – – – plane channel (Kim *et al.* [1987]); cylinders with —— $\delta/a = 5$ and - - - - $\delta/a = 11$. 34

3.4 The energy partition parameter $K^* = 2\overline{v_z^2}/(\overline{v_r^2} + \overline{v_\theta^2})$: – – – plane channel (Lee *et al.* [1990]); cylinders with —— $\delta/a = 5$ and - - - - $\delta/a = 11$. 35

3.5 Pressure strain term of the streamwise intensity ($\overline{v_z{}^2}$) budget equation normalized ν and u_τ: cylinders with —— $\delta/a = 5$ and ---- $\delta/a = 11$; —·— plane channel (Mansour *et al.* [1988]). 36

3.6 Reynolds shear stress normalized by u_τ: cylinders with —— $\delta/a = 5$ and ---- $\delta/a = 11$; —·— plane channel (Kim *et al.* [1987]). 37

3.7 Correlation coefficient: cylinders with —— $\delta/a = 5$ and ---- $\delta/a = 11$; —·— plane channel (Kim *et al.* [1987]). 38

3.8 Velocity scaling function $\mathcal{F}(y/\delta; \delta/a)$: —·— plane channel ($\delta/a = 0$); cylinders with —— $\delta/a = 5$ and ---- $\delta/a = 11$. 39

3.9 Root-mean-square velocity fluctuations normalized by $\underline{u}$: (*a*) Axial (streamwise) intensity, (*b*) Normal intensity, (*c*) Azimuthal (spanwise) intensity; —·— plane channel (Kim *et al.* [1987]); cylinders with —— $\delta/a = 5$ and ---- $\delta/a = 11$. 41

3.10 Reynolds shear stress (*a*), Production (*b*) and dissipation (*c*) of turbulent kinetic energy normalized by ν and $\underline{u}$: cylinders with —— $\delta/a = 5$ and ---- $\delta/a = 11$; —·— plane channel (Mansour *et al.* [1988]). 42

3.11 Reynolds shear stress for each quadrant normalized by the mean Reynolds shear stress: (*a*) $\delta/a = 5$, (*b*) $\delta/a = 11$: ····· first; ---- second; —·— third; —·— fourth quadrant. 43

3.12 Fractional contribution to $-\overline{v_z v_r}$ from each quadrant as a function of threshold for $\delta/a = 5$; ---- first; —— second; —·— third; ····· fourth quadrants: (*a*) $y^+ = 8$ (*b*) $y^+ = 13.1$ (*c*) $y^+ = 51.1$. 44

3.13 Fractional contribution to $-\overline{v_z v_r}$ from each quadrant as a function of threshold for $\delta/a = 11$:---- first; —— second; —·— third; ····· fourth quadrants: (*a*) $y^+ = 8.9$ (*b*) $y^+ = 13.2$ (*c*) $y^+ = 51.7$. 45

3.14 Skewness profiles of the velocity fluctuations: (*a*) $S(v_z)$, (*b*) $S(v_r)$, (*c*) $S(v_\theta)$; —·— plane channel (Kim *et al.* [1987]); cylinders with —— $\delta/a = 5$ and ---- $\delta/a = 11$. 46

3.15 Flatness profiles of the velocity fluctuations: (*a*) $F(v_z)$, (*b*) $F(v_r)$, (*c*) $F(v_\theta)$; —·— plane channel (Kim *et al.* [1987]); cylinders with —— $\delta/a = 5$ and ---- $\delta/a = 11$. 47

3.16 Root-mean-square vorticity fluctuations normalized by ν and u_τ: (a) Axial (streamwise) intensity, (b) Normal intensity, (c) Azimuthal (spanwise) intensity; ——— plane channel (Kim *et al.* [1987]); cylinders with —— $\delta/a = 5$ and ---- $\delta/a = 11$. 49

3.17 Root-mean-square vorticity fluctuations normalized by ν and u_τ in global coordinates for (a) $\delta/a = 5$ and (b) $\delta/a = 11$: ——- Axial intensity; ---- Azimuthal intensity; ——— Normal intensity. 52

3.18 *a* Distribution of the inclination of the angle, Θ_{rz}, of the projection of the vorticity vectors in (r, z)-planes for $\delta/a = 5.0$; data weighted with the magnitude of the projected vorticity. (a) $y^+ = 0.66$; (b) $y^+ = 4.10$; (c) $y^+ = 8.02$; (d) $y^+ = 16.31$; (e) $y^+ = 25.38$; (f) $y^+ = 38.76$; (g) $y^+ = 51.85$; (h) $y^+ = 69.66$; (i) $y^+ = 96.25$. 53

3.18 *b* Distribution of the inclination of the angle, Θ_{rz}, of the projection of the vorticity vectors in (r, z)-planes for $\delta/a = 11.0$; data weighted with the magnitude of the projected vorticity. (a) $y^+ = 0.72$; (b) $y^+ = 4.46$; (c) $y^+ = 8.74$; (d) $y^+ = 17.77$; (e) $y^+ = 27.56$; (f) $y^+ = 42.24$; (g) $y^+ = 56.52$; (h) $y^+ = 75.96$; (i) $y^+ = 104.90$. 54

3.19 Contours of axial velocity fluctuations (v_z), normalized by u_τ, on a plane (I_z) normal to the mean velocity: (a) $\delta/a = 5$ with contour levels from $-5.2\ u_\tau$ to $3.55\ u_\tau$; (b) $\delta/a = 11$ with contour levels from $-4.95\ u_\tau$ to $4.05\ u_\tau$. The contour increments of $0.25\ u_\tau$. The solid contours denote the low-speed fluctuations ($v_z < 0$) and the dotted contours denote the high-speed fluctuations ($v_z > 0$). 56

3.20 Contours of axial velocity fluctuations (v_z), normalized by u_τ, on a plane (II_z) normal to the mean velocity: (a) $\delta/a = 5$ with contour levels from $-5.2\ u_\tau$ to $3.3\ u_\tau$; (b) $\delta/a = 11$ with contour levels from $-4.2\ u_\tau$ to $3.3\ u_\tau$. The contour increment is $0.25\ u_\tau$. The solid contours denote the low-speed fluctuations ($v_z < 0$) and the dotted contours denote the high-speed fluctuations ($v_z > 0$). 57

3.21 Azimuthal two-point correlations of the velocity fluctuations for (a) $\delta/a = 5.0$ and for (b) $\delta/a = 11$: —— $R_{v_z v_z}$, ---- $R_{v_r v_r}$, ——— $R_{v_\theta v_\theta}$. 58

3.22 The mean spanwise streak spacing Λ^+ estimated from the two-point correlations of v_z: + plane channel (Kim *et al.* [1987]); cylinders: o, for $\delta/a = 5$ and $\triangle$, for $\delta/a = 11$. 59

3.23 Contours of radial (wall-normal) velocity fluctuations (v_r), normalized by u_τ, on a plane (I_z) normal to the mean velocity: (a) $\delta/a = 5$ with contour levels from $-1.8\ u_\tau$ to $1.3\ u_\tau$; (b) $\delta/a = 11$ with contour levels from $-0.95\ u_\tau$ to $1.05\ u_\tau$. The contour increment is $0.25\ u_\tau$. The solid contours denote the negative radial velocity ($v_r < 0$) and the dotted contours denote the positive radial velocity ($v_r > 0$). 60

3.24 Contours of radial (wall-normal) velocity fluctuations (v_r), normalized by u_τ, on a plane (II_z) normal to the mean velocity: (a) $\delta/a = 5$ with contour levels from $-1.05\ u_\tau$ to $1.3\ u_\tau$; (b) $\delta/a = 11$ with contour levels from $-0.95\ u_\tau$ to $1.29\ u_\tau$. The contour increment is $0.25\ u_\tau$. The solid contours denote the negative radial velocity ($v_r < 0$) and the dotted contours denote the positive radial velocity ($v_r > 0$). 61

3.25 The shear rate parameter $S^* = 2q^2(d\overline{V}_z/dy)/\epsilon$: ——— plane channel (Lee *et al.* [1990]); cylinders with —— $\delta/a = 5$ and ---- $\delta/a = 11$. 62

3.26 Contours of axial velocity fluctuations (v_z), normalized by u_τ and ν, on an unwrapped cylindrical surface at $y^+ \approx 5$: (a) $\delta/a = 5$ with contour levels from $-2.2\ u_\tau$ to $5.55\ u_\tau$; (b) $\delta/a = 11$ with contour levels from $-2.2\ u_\tau$ to $4.85\ u_\tau$. The axial length of the domain displayed is $3\pi\delta$ and the contour increment is $0.25\ u_\tau$. The solid contours denote the low-speed fluctuations ($v_z < 0$) and the dotted contours denote the high-speed fluctuations ($v_z > 0$). 63

3.27 The length scale parameter L^* based on v_z: ——— plane channel (Lee *et al.* [1990]); cylinders with —— $\delta/a = 5$ and ---- $\delta/a = 11$. 65

3.28 The length scale parameter: L^* based on ω_θ for cylinders with ——— $\delta/a = 5$ and ---- $\delta/a = 11$; L^* based on ω_z for cylinders with —·— $\delta/a = 5$ and ····· $\delta/a = 11$. 65

3.29 Contours of axial (streamwise) vorticity fluctuations (ω_z), normalized by u_τ and ν, on a plane (I_z) normal to the mean velocity: (a) $\delta/a = 5$ with contour levels from $-0.34\ u_\tau^2/\nu$ to $0.5\ u_\tau^2/\nu$; (b) $\delta/a = 11$ with contour levels from $-0.3\ u_\tau^2/\nu$ to $0.38\ u_\tau^2/\nu$. The contour increment is $0.04\ u_\tau^2/\nu$. The solid contours

denote the negative vorticity ($\omega_z < 0$) and the dotted contours denote the positive vorticity ($\omega_z > 0$). 66

3.30 Contours of axial (streamwise) vorticity fluctuations (ω_z), normalized by u_τ and ν, on a plane (II_z) normal to the mean velocity: (a) $\delta/a = 5$ with contour levels from $-0.34\ u_\tau^2/\nu$ to $0.5\ u_\tau^2/\nu$; (b) $\delta/a = 11$ with contour levels from $-0.26\ u_\tau^2/\nu$ to $0.22\ u_\tau^2/\nu$. The contour increment is $0.04\ u_\tau^2/\nu$. The solid contours denote the negative vorticity ($\omega_z < 0$) and the dotted contours denote the positive vorticity ($\omega_z > 0$). 67

3.31 Contours of azimuthal vorticity fluctuations (ω_θ), normalized by u_τ and ν, on an azimuthal plane (I_θ) through the axis of the cylinder. The axial length of the domain displayed is $3\pi\delta$: (a) $\delta/a = 5$ with contour levels from $-0.74\ u_\tau^2/\nu$ to $0.56\ u_\tau^2/\nu$; (b) $\delta/a = 11$ with contour levels from $-0.9\ u_\tau^2/\nu$ to $0.42\ u_\tau^2/\nu$. The contour increment is $0.04\ u_\tau^2/\nu$. The solid contours denote the negative vorticity ($\omega_\theta < 0$) (aligned with the mean vorticity) and the dotted contours denote the positive vorticity ($\omega_\theta > 0$). 68

3.32 Contours of azimuthal vorticity fluctuations (ω_θ), normalized by u_τ and ν, on an azimuthal plane (II_θ) through the axis of the cylinder. The axial length of the domain displayed is $3\pi\delta$: (a) $\delta/a = 5$ with contour levels from $-0.74\ u_\tau^2/\nu$ to $0.56\ u_\tau^2/\nu$; (b) $\delta/a = 11$ with contour levels from $-0.9\ u_\tau^2/\nu$ to $0.42\ u_\tau^2/\nu$. The contour increment is $0.04\ u_\tau^2/\nu$. The solid contours denote the negative vorticity ($\omega_\theta < 0$) (aligned with the mean vorticity) and the dotted contours denote the positive vorticity ($\omega_\theta > 0$). 69

3.33 Contours of azimuthal vorticity fluctuations (ω_θ), normalized by u_τ and ν, on a plane (I_z) normal to the mean velocity: (a) $\delta/a = 5$ with contour levels from $-0.58\ u_\tau^2/\nu$ to $0.54\ u_\tau^2/\nu$; (b) $\delta/a = 11$ with contour levels from $-0.66\ u_\tau^2/\nu$ to $0.5\ u_\tau^2/\nu$. The contour increment is $0.04\ u_\tau^2/\nu$. The solid contours denote the negative vorticity ($\omega_\theta < 0$) (aligned with the mean vorticity) and the dotted contours denote the positive vorticity ($\omega_\theta > 0$). 70

3.34 Contours of azimuthal vorticity fluctuations (ω_θ), normalized by u_τ and ν, on a plane (II_z) normal to the mean velocity: (a) $\delta/a = 5$ with contour levels from $-0.38\ u_\tau^2/\nu$ to $0.5\ u_\tau^2/\nu$; (b) $\delta/a = 11$ with contour levels from $-0.9\ u_\tau^2/\nu$ to $0.46\ u_\tau^2/\nu$. The contour increment is $0.04\ u_\tau^2/\nu$. The solid contours

denote the negative vorticity ($\omega_\theta < 0$) (aligned with the mean vorticity) and the dotted contours denote the positive vorticity ($\omega_\theta > 0$). 71

3.35 Contours of azimuthal vorticity fluctuations (ω_θ), normalized by u_τ and ν, on an unwrapped cylindrical surface at $y^+ \approx 15$. The axial length of the domain displayed is $3\pi\delta$: (a) $\delta/a = 5$ with contour levels from $-0.58\ u_\tau^2/\nu$ to $0.32\ u_\tau^2/\nu$; (b) $\delta/a = 11$ with contour levels from $-0.73\ u_\tau^2/\nu$ to $0.62\ u_\tau^2/\nu$. The contour increment is $0.05\ u_\tau^2/\nu$. The solid contours denote the negative vorticity ($\omega_\theta < 0$) (aligned with the mean vorticity) and the dotted contours denote the positive vorticity ($\omega_\theta > 0$). 72

3.36 Contours of radial (wall-normal) vorticity fluctuations (ω_r), normalized by u_τ and ν, on a plane (I_z) normal to the mean velocity: (a) $\delta/a = 5$ with contour levels from $-0.38\ u_\tau^2/\nu$ to $0.46\ u_\tau^2/\nu$; (b) $\delta/a = 11$ with contour levels from $-0.3\ u_\tau^2/\nu$ to $0.38\ u_\tau^2/\nu$. The contour increment is $0.04\ u_\tau^2/\nu$. The solid contours denote the negative vorticity ($\omega_r < 0$) and the dotted contours denote the positive vorticity ($\omega_r > 0$). 74

3.37 Contours of radial (wall-normal) vorticity fluctuations (ω_r), normalized by u_τ and ν, on a plane (II_z) normal to the mean velocity: (a) $\delta/a = 5$ with contour levels from $-0.46\ u_\tau^2/\nu$ to $0.5\ u_\tau^2/\nu$; (b) $\delta/a = 11$ with contour levels from $-0.26\ u_\tau^2/\nu$ to $0.22\ u_\tau^2/\nu$. The contour increment is $0.04\ u_\tau^2/\nu$. The solid contours denote the negative vorticity ($\omega_r < 0$) and the dotted contours denote the positive vorticity ($\omega_r > 0$). 75

3.38 Contours of the pressure fluctuations (p), normalized by ρ and u_τ, on a plane (I_z) normal to the mean velocity: (a) $\delta/a = 5$ with contour levels from $-4.1\ \rho u_\tau^2$ to $2.1\ \rho u_\tau^2$; (b) $\delta/a = 11$ with contour levels from $-2.5\ \rho u_\tau^2$ to $1.5\ \rho u_\tau^2$. The contour increment is $0.2\ \rho u_\tau^2$. The solid contours denote the negative pressure ($p < 0$) and the dotted contours denote the positive pressure ($p > 0$). . 76

3.39 Contours of the pressure fluctuations (p), normalized by ρ and u_τ, on a plane (II_z) normal to the mean velocity: (a) $\delta/a = 5$ with contour levels from $-2.5\ \rho u_\tau^2$ to $1.5\ \rho u_\tau^2$; (b) $\delta/a = 11$ with contour levels from $-1.7\ \rho u_\tau^2$ to $0.5\ \rho u_\tau^2$. The contour increment is $0.2\ \rho u_\tau^2$. The solid contours denote the negative pressure ($p < 0$) and the dotted contours denote the positive pressure ($p > 0$). . 77

3.40 Contours of radial vorticity fluctuations (ω_r), normalized by u_τ and ν, on an unwrapped cylindrical surface at $y^+ \approx 15$. The axial length of the domain

displayed is $3\pi\delta$: (a) $\delta/a = 5$ with contour levels from $-0.79\ u_\tau^2/\nu$ to $0.66\ u_\tau^2/\nu$; (b) $\delta/a = 11$ with contour levels from $-0.49\ u_\tau^2/\nu$ to $0.56\ u_\tau^2/\nu$. The contour increment is $0.05\ u_\tau^2/\nu$. The solid contours denote the negative vorticity ($\omega_r < 0$) and the dotted contours denote the positive vorticity ($\omega_r > 0$). 78

4.1 Root-mean-square pressure normalized by u_τ: —·— plane channel (Kim *et al.* [1987]); cylinders with —— $\delta/a = 5$ and ---- $\delta/a = 11$. 80

4.2 Profiles of the root-mean-squares of the pressure source terms normalized by ν and u_τ: (a) linear contribution: cylinders with —— $\delta/a = 5$ and ---- $\delta/a = 11$; (b) nonlinear contribution: cylinders with —— $\delta/a = 5$ and ---- $\delta/a = 11$; total source terms: cylinders with —·— $\delta/a = 5$ and —·— $\delta/a = 11$. 81

4.3 Profiles of the root-mean-square value of the nonlinear contributions to the source terms normalized by ν and u_τ: (a) $\delta/a = 5$, (b) $\delta/a = 11$; —— $(\partial v_r/\partial r)^2$, ····· $(2/r)(\partial v_r/\partial\theta - v_\theta)(\partial v_\theta/\partial r)$, —·— $(1/r^2)(\partial v_\theta/\partial\theta + v_r)^2$,—·—·— $(\partial v_z/\partial z)^2$, ---- $2(\partial v_z/\partial r)(\partial v_r/\partial z)$, —·— $(2/r)(\partial v_z/\partial\theta)(\partial v_\theta/\partial z)$. 83

4.4 Signal of the wall pressure fluctuations normalized by $\overline{p^2}_w^{1/2}$: (a) plane channel; cylinders with (b) $\delta/a = 5$; (c) $\delta/a = 11$. 87

4.5 Spectra of the wall pressure fluctuations normalized by δ and u_τ: (a) Azimuthal (spanwise) spectra, (b) Axial (streamwise) spectra; —·— plane channel (Choi & Moin [1990]); cylinders ($\delta\Delta k_\theta = \delta/a$) with —— $\delta/a = 5$ and ---- $\delta/a = 11$; ····· -1 slope; —·— -5 slope. 89

4.6 Axial (streamwise) spectra of the wall pressure fluctuations normalized by δ_f and u_τ: —·— plane channel (Choi & Moin [1990]) ($\delta/a = 0$, $\delta_f = \delta$); cylinders with —— $\delta/a = 5$ and ---- $\delta/a = 11$. 90

4.7 Spectra of the wall pressure fluctuations normalized by δ and $\overline{p^2}_w^{1/2}$: (a) Azimuthal (spanwise) spectra, (b) Axial (streamwise) spectra; —·— plane channel (Choi & Moin [1990]); cylinders ($\delta\Delta k_\theta = \delta/a$) with —— $\delta/a = 5$ and ---- $\delta/a = 11$. 92

4.8 Spectra of the wall pressure fluctuations normalized by u_τ and δ ($\delta\Delta k_\theta = \delta/a$): ($a$) $\delta/a = 5$, (b) $\delta/a = 11$ (the scale of the ordinate is twice that of the abscissa). The contour levels are logarithmically distributed from 10^{-6} to 10^{-3} with exponent increments of 0.3. 93

4.9 Azimuthal (spanwise) two-point correlations of the wall pressure fluctuations as a function of (a) θ and of (b) θa^+: —— $\delta/a = 5$ ($a^+ \approx 43$); ---- $\delta/a = 11$ ($a^+ \approx 21$). 94

4.10 Axial (streamwise) two-point correlations of the wall pressure fluctuations: —— $\delta/a = 5$ and ---- $\delta/a = 11$. 95

4.11 Contour plot of two-point correlations of the wall pressure fluctuations for plane channel (Choi & Moin [1990]) as a function of the streamwise (r_x^+) and spanwise (r_z^+) separations. The contour levels are from 0.1 to 0.9 with increments of 0.1. 96

4.12 Contour plot of two-point correlations of the wall pressure fluctuations as a function of the axial (r_z^+ - streamwise) and azimuthal ($a^+\theta$ - spanwise) separations. The contour levels are from 0.1 to 0.9 with increments of 0.1. 97

4.13 Fractional contributions to the root-mean-square wall pressure fluctuations from sources located at $y_o \in [0, y_s]$: —·— plane channel; cylinders with —— $\delta/a = 5$ and ---- $\delta/a = 11$ ($y_s = r_s - a$). The result is normalized by the total wall pressure intensity. 98

4.14 Contour plot of two-point correlations of the contributions to the wall pressure fluctuations in the plane channel from flow perturbations in the interval (a) $[0, y_s]$ and (b) $[y_s, 1]$ (1 denotes the channel centerline) as a function of the streamwise (r_x^+) and spanwise (r_z^+) separations. The contour levels are from 0.1 to 0.9 with increments of 0.1 and $y_s \approx 0.2$ ($y_s^+ \approx 36$). 99

4.15 Contour plot of two-point correlations of the contributions to the wall pressure fluctuations for $\delta/a = 5$ from flow perturbations in the interval (a) $[a, r_s]$ and (b) $[r_s, a+1]$ as a function of the axial (r_z^+ - streamwise) and azimuthal ($a^+\theta$ - spanwise) separations. The contour levels are from 0.1 to 0.9 with increments of 0.1 and $y_s \approx 0.2$ ($y_s^+ = r_s^+ - a^+ \approx 46$). 100

4.16 Contour plot of two-point correlations of the contributions to the wall pressure fluctuations for $\delta/a = 11$ from flow perturbations in the interval (a) $[a, r_s]$ and (b) $[r_s, a+1]$ as a function of the axial (r_z^+ - streamwise) and azimuthal ($a^+\theta$ - spanwise) separations. The contour levels are from 0.1 to 0.9 with increments of 0.1 and $y_s \approx 0.2$ ($y_s^+ = r_s^+ - a^+ \approx 49$). 101

4.17 Temporal spectra of the wall pressure fluctuations normalized by τ_w^2 and (a) δ/u_τ time scale; (a) δ/u_f time scale: —·— plane channel (Choi & Moin [1990]) ($\delta/a = 0$, $u_f = u_\tau$); cylinders with —— $\delta/a = 5$ and ---- $\delta/a = 11$; ····· -1 slope; —·— -5 slope. 104

4.18 Contour plot of the axial (streamwise) wave-number-frequency spectra of the wall pressure fluctuations normalized by u_τ and δ: (a) $\delta/a = 5$ and the contour levels are from 0.00035 to 0.0070; (b) $\delta/a = 11$ and the contour levels are from 0.00035 to 0.0035. The contour increments are 0.00035. . . 106

4.19 Contour plot of two-point correlations of the wall pressure fluctuations as a function of the axial (streamwise) spatial (r_z^+) and temporal (r_t^+) separations: (a) $\delta/a = 5$; (b) $\delta/a = 11$. The contours are from 0.1 to 0.9 with increments of 0.1. 107

4.20 Convection velocity normalized by U_∞ as a function of the (a) streamwise separation (r_z/δ^*) and of the (b) temporal separation (r_t^+): cylinders: o, for $\delta/a = 5$ and $\triangle$, for $\delta/a = 11$. 109

4.21 Convection velocity normalized by U_∞ as a function of the streamwise wave number: cylinders: o, for $\delta/a = 5$ and $\triangle$, for $\delta/a = 11$. 110

4.22 Convection velocity normalized by U_∞ as a function of frequency: cylinders: o, for $\delta/a = 5$ and $\triangle$, for $\delta/a = 11$. 110

4.23 Conversion of the Temporal spectrum to the axial (streamwise) wave-number spectrum using Taylor's hypothesis for (a) $\delta/a = 5$, and for (b) $\delta/a = 11$: —— $E_{pp}(k_z)$; ---- from $\phi_{pp}(\omega)$ using Taylor's hypothesis ($U_c \simeq 0.65U_\infty$). 111

4.24 Axial (streamwise) similarity function $F_z(k_z U_c(\omega)/\omega)$. The frequency range of $\omega\delta/u_\tau$ is: (a) from 31.13 to 311.3 with increments of 31.13 for $\delta/a = 5$ and (b) from 38.08 to 380.8 with increments of 38.08 for $\delta/a = 11$. . . . 113

4.25 Azimuthal (spanwise) similarity function $F_\theta(k_\theta U_c(\omega)/\omega)$. The frequency range of $\omega\delta/u_\tau$ is: (a) from 31.13 to 311.3 with increments of 31.13 for $\delta/a = 5$ and (b) from 38.08 to 380.8 with increments of 38.08 for $\delta/a = 11$. . 114

A.1 Transport equation balance of the axial turbulence intensity normalized by ν and u_τ for (a) $\delta/a = 5$ and (b) $\delta/a = 11$: —— production, ---- dissipation

rate, ····· velocity-pressure (pressure diffusion), —·— turbulent transport, —·— viscous diffusion. 124

A.2 Transport equation balance of the normal turbulence intensity normalized by ν and u_τ for (a) $\delta/a = 5$ and (b) $\delta/a = 11$: —— production, ---- dissipation rate, ····· velocity-pressure (pressure diffusion), —·— turbulent transport, —·— viscous diffusion. 125

A.3 Transport equation balance of the azimuthal turbulence intensity normalized by ν and u_τ for (a) $\delta/a = 5$ and (b) $\delta/a = 11$: —— production, ---- dissipation rate, ····· velocity-pressure (pressure diffusion), —·— turbulent transport, —·— viscous diffusion. 126

A.4 Transport equation balance of the Reynolds shear stress normalized by ν and u_τ for (a) $\delta/a = 5$ and (b) $\delta/a = 11$: —— production, ---- dissipation rate, ····· velocity-pressure (pressure diffusion), —·— turbulent transport, —·— viscous diffusion. 127

A.5 Transport equation balance of the turbulent kinetic energy normalized by ν and u_τ for (a) $\delta/a = 5$ and (b) $\delta/a = 11$: —— production, ---- dissipation rate, ····· velocity-pressure (pressure diffusion), —·— turbulent transport, —·— *viscous diffusion.* 128

A.6 Velocity pressure gradient term of the turbulent kinetic energy equation normalized by ν and u_τ: —·— plane channel (Mansour *et al.* [1988]); cylinders with —— $\delta/a = 5$ and ---- $\delta/a = 11$. 129

A.7 Dissipation of turbulent kinetic energy normalized by ν and u_τ: —·— plane channel (Mansour *et al.* [1988]); cylinders with —— $\delta/a = 5$ and ---- $\delta/a = 11$. 129

A.8 Production of turbulent kinetic energy normalized by ν and u_τ: —·— plane channel (Mansour *et al.* [1988]); cylinders with —— $\delta/a = 5$ and ---- $\delta/a = 11$. 130

A.9 Turbulent transport of turbulent kinetic energy normalized by ν and u_τ: —·— plane channel (Mansour *et al.* [1988]); cylinders with —— $\delta/a = 5$ and ---- $\delta/a = 11$. 130

A.10 Viscous diffusion in turbulent kinetic energy equation normalized by ν and u_τ: ——— plane channel (Mansour *et al.* [1988]); cylinders with —— $\delta/a = 5$ and ---- $\delta/a = 11$. 131

Nomenclature

Roman Symbols

a	Cylinder radius.
a^+	Cylinder radius in viscous units.
C_f	Skin friction coefficient, $2\tau_w/(\rho U_\infty^2)$.
$d = R_o - R_i$	Taylor-Couette flow cylinder gap.
$E_{pp}(k_z)$	Axial (streamwise) 1D energy spectrum of the pressure.
$E_{pp_c}(k_{zc})$	Streamwise 1D energy spectrum of the pressure transformed from the power spectrum through Taylor's hypothesis.
$E_{pp}(k_\theta)$	Azimuthal (spanwise) 1D energy spectrum of the pressure.
$E_{vv}(k_z)$	Axial (streamwise) 1D energy spectrum of the velocity component v.
$E_{vv}(k_\theta)$	Azimuthal (spanwise) 1D energy spectrum of the velocity component v.
f	Source terms of the pressure Poisson equation.
f_w	Window function.
$F(v_z, v_r, v_\theta)$	Flatness factor of the velocity.
F_z, F_θ	Axial and azimuthal wall pressure similarity functions.
$\mathcal{F}$	Curvature dependent velocity scaling function.
G	Inner cylinder torque in Taylor-Couette flow.
$\hat{\mathcal{G}}$	Green's function of the Laplacian operator.
H	Boundary layer shape factor.
$\vec{\mathbf{H}}$	Convective term vector.
H_z, H_r, H_θ	Components of the convective term vector.
$\tilde{H}_r, \tilde{H}_\tau$	Modified convective terms.
I_θ, II_θ	Surfaces through the axis of the cylinder.
I_z, II_z	Surfaces normal to the mean velocity.

k_θ	Azimuthal (spanwise) wave-number.
k_z	Axial (streamwise) wave-number.
k_{zc}	Convection axial (streamwise) wave-number.
K^*	Energy partition parameter.
$\mathcal{L}$	Strum-Liouville operator.
L_{θ_i}	Perimeter of the circumference of the cylinder.
L_{θ_o}	Perimeter of the outer circumference of the computational domain.
L_t	Temporal length of the wall pressure overlapping domains.
L_T	Temporal length of the wall pressure record.
L_z	Length of the computational domain in the axial direction.
L^*	Length scale anisotropy parameter.
$L^\theta_{v_z}$	Length scale based on the azimuthal (spanwise) two-point correlations of v_z.
$L^z_{v_z}$	Length scale based on the axial (streamwise) two-point correlations of v_z.
$\dot{M}$	Axial mass flux.
m, k	Wave-number index pair in the azimuthal and axial directions.
N_z, N_r, N_θ	Number of grid points in the axial, radial and azimuthal directions.
N_s	Number of wall data samples.
p	Pressure fluctuation.
$p_{r_s^-}$	Wall pressure fraction due to sources at $r_o \in [a, r_s]$.
$p_{r_s^+}$	Wall pressure fraction due to sources at $r_o \in [r_s, a+1]$.
P	Pressure.
$\overline{P}$	Mean pressure.
P_h, P_i	Homogeneous and inhomogeneous pressure.
p_w	Wall pressure fluctuations.
$\tilde{p}_w$	Filtered wall pressure fluctuations.

q^2	Turbulent kinetic energy.
r	Radial coordinate.
r_e	Radius of Rankine vortex.
r_o	Radial position of a source in axisymmteric coordinates.
r_s	Radial wall pressure source position cutoff.
r_t^+	Temporal separation in viscous units.
r_x^+	Streamwise separation in viscous units in the plane channel.
r_z^+	Axial separation in viscous units in the cylinders and spanwise separation in viscous units in the plane channel.
R_i, R_o	Inner and outer radius of the computational domain.
$R_{vv}(z)$	Axial (streamwise) two-point correlation function of the velocity component v.
$R_{vv}(\theta)$	Azimuthal (spanwise) two-point correlation function of the velocity component v.
$R_{pp}(z)$	Axial (streamwise) two-point correlation function of the pressure.
$R_{pp}(\theta)$	Azimuthal (spanwise) two-point correlation function of the pressure.
Re_a	Reynolds number based on U_∞ and a.
Re_c	Critical Reynolds number in Taylor-Couette flows.
Re_d	Gap Reynolds number in Taylor-Couette flows.
Re_δ	Reynolds number based on U_∞ and δ.
Re_Γ	Rankine vortex circulation Reynolds number.
Re_τ	Reynolds number based on u_τ and δ.
S	Mean shear rate parameter.
$S(v_z, v_r, v_\theta)$	Skewness factor of the velocity.
S_{cy}	Cylinder surface area.
S^*	Non-dimensional mean shear rate parameter.
t	Time.
T_l	Chebyshev polynomial of order l.

U_c	Convection velocity.
u_f	Curvature dependent global velocity scale.
U_∞	Mean velocity at the outer edge of the domain.
U^+	Mean velocity profile normalized by u_τ.
u_τ	Friction velocity.
$\underline{u}$	velocity scaling.
V_{cy}	Flow volume.
$\vec{\mathbf{V}}$	Velocity vector.
v_e	Rankine vortex edge velocity.
V_{rh}, V_{ri}	Inhomogeneous and homogeneous radial velocity.
V_z, V_r, V_θ	Axial, radial and azimuthal components of the velocity field.
$\overline{V}_z, \overline{V}_r, \overline{V}_\theta$	Axial, radial and azimuthal mean velocity components.
v_z, v_r, v_θ	Axial, radial and azimuthal components of the fluctuating velocity field.
y	Coordinate normal to the wall.
y^+_{max}	Mean position of the center of the near-wall Rankine vortex.
y^+_{min}	Mean position of the edge of the near-wall Rankine vortex.
y^+	Distance from the wall in viscous units.
y_o	Normal position of a source in cartesian coordinates.
y_s	Wall pressure source position cutoff.
z	Axial coordinate.

Greek Symbols

α_1, α_2	Constants in the enforcement of the pressure boundary conditions.
β	Radial coordinate stretching parameter.
δ	Boundary layer thickness.
δ_f	Curvature dependent global length scale.
$\delta(r - r_o)$	Dirac delta 'function' with source at $r = r_o$.

$\Delta k_\theta, \Delta k_z$	Wave-number resolution in the azimuthal and axial directions.
δ^*	Boundary layer displacement thickness.
Δt	Time step.
Δt_s	Sampling frequency.
$\Delta\theta_i{}^+, \Delta\theta_o{}^+$	Grid spacing in the azimuthal direction at $r = a$ and $r = a + 1$.
$\Delta\omega$	Frequency resolution.
ϵ	Viscous dissipation of turbulent kinetic energy.
γ	Strength of the near-wall Rankine vortex.
Γ	Circulation of the near-wall Rankine vortex.
λ	Spanwise wavelength of Taylor vortices.
Λ	Mean spanwise streak spacing.
μ	Molecular viscosity.
∇^2	Laplacian operator.
ν	Kinematic viscosity.
$\vec{\mathbf{\Omega}}$	Vorticity vector.
ω	Frequency.
$\omega_z, \omega_r, \omega_\theta$	Axial, radial and azimuthal components of the fluctuating vorticity field.
$\Omega_z, \Omega_r, \Omega_\theta$	Axial, radial and azimuthal components of the vorticity field.
Ω_i	Angular speed of inner cylinder.
ϕ_{pp}	Wall pressure temporal spectrum.
$\Phi_{pp}(k_z, \omega)$	Two-dimensional wall pressure frequency/streamwise wave number spectrum.
ρ	Density.
$\sigma_{r\theta}, \sigma_{\theta z}, \sigma_{zr}$	Components of the shear stress.
τ	Total stress.
τ_w	Wall shear stress.
θ	Azimuthal coordinate.

θ^*	Boundary layer momentum thickness.
Θ_{rz}	Angle of the projection of the vorticity in (r, z)-planes.
Υ	Velocity field dependent variable.
ξ	Chebyshev coordinate.

Tensor Notation

g^{ij}	Coordinate metric tensor.
v^i	Contravariant velocity fluctuations.
V^i	Contravariant velocity.
$\overline{V}^i$	Contravariant mean velocity.
(x_1, x_2, x_3)	Tensorial coordinates.
$_{,k}$	Contravariant derivative.

Other Symbols

$^+$	Indicates normalization in wall coordinates.
$\overline{}$	Indicates averaging in time and in the axial and azimuthal directions.
$< \quad >$	Indicates averaging in the axial and azimuthal directions.
$\tilde{}$	Indicates temporal filtering.
$\hat{}$	Indicates Fourier transform.

CHAPTER 1

Introduction

Turbulent flows that evolve over surfaces with convex curvature normal to the mean flow are common in engineering applications. However, it is only for strong curvatures that the curvature effects become noticeable. For this reason this flow has received less attention than its planar counterpart, and the body of experimental data available is limited. Transversely curved turbulent flows with large curvature effects occur over sonar devices towed by long cables. Of particular interest is the characteristics of the wall pressure fluctuations underneath the transversely curved boundary layers.

1.1 Transverse Curvature Effects

In turbulent flows with transverse curvature there is an additional length scale, the cylinder radius, a. The added complexity introduced by the new length scale is evident in the laminar flow regime. While in the planar case the absence of a length scale leads to the self-similar Blasius velocity profile, in the axisymmetric boundary layer there is no self-similar laminar solution (Seban & Bond [1951]).

The new length scale gives rise to several flow regimes that are characterized by the ratios of the cylinder radius to the flow length scales: the boundary layer thickness δ, and the viscous length scale ν/u_τ. The two resulting parameters, δ/a and a^+, define a two-dimensional parameter space in which three flow regimes can be identified. If δ/a is small the curved boundary layer is similar tc the planar boundary layer. In some applications the boundary layer may grow to be several times thicker than the radius (large δ/a), in which case the transverse curvature affects the flow differently depending on the magnitude of a^+. If δ/a is large, and a^+ is also large, then the curvature only affects the outer part of the flow. If δ/a

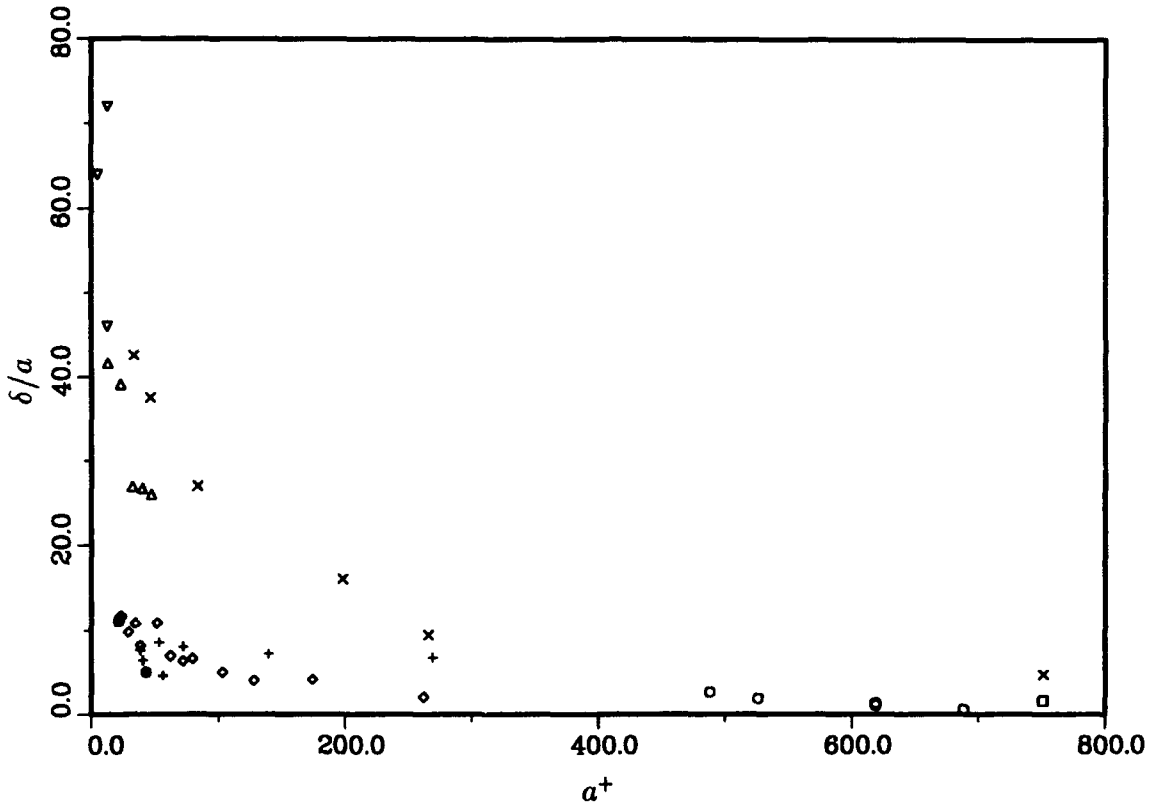

FIGURE 1.1 Experimental data available for the axial turbulent flow along a circular cylinder given as a function of the parameters δ/a and a^+ : $\triangle$ Luxton *et al.* (1984); + Lueptow *et al.* (1985) and Lueptow & Haritonidis (1987); × Willmarth & Yang (1970) and Willmarth *et al.* (1976); $\diamond$ Rao & Keshavan (1972); $\circ$ Afzal & Narasimha (1976); $\triangledown$ Richmond (1957); $\square$ Yu (1959); • present calculations.

is large and a^+ is small, the curvature affects both the inner and the outer parts of the flow.

Some of the flow parameters δ/a and a^+ that have been investigated experimentally are summarized in Figure 1.1. Lueptow (1988) provides a comprehensive review of the experimental investigations of this flow. With the exception of Afzal & Narasimha (1976), whose boundary layers have characteristics very similar to those of the flat plate, in most experiments the influence of curvature is predominantly on the outer part of the flow. Some of the experiments of Luxton *et al.* (1984) ($9 \leq a^+ \leq 47$ and $26 \leq \delta/a \leq 42$) and of Willmarth *et al.* (1976) ($2 \leq \delta/a \leq 42$ and $a^+ > 33$) are within the range where both the inner and outer parts of the flow are affected. In the experiments of Rao & Keshavan (1972) ($4 \leq \delta/a \leq 12$ and $a^+ > 23$)

and Lueptow *et al.* (1985) and Lueptow & Haritonidis (1987) ($4 \leq \delta/a \leq 8$ and $a^+ > 38$) the curvature primarily affects the outer layer.

One of the characteristics of flows with transverse curvature is larger skin friction coefficients (C_f) than in planar flows of similar Reynolds number (see for example Rao & Keshavan [1972] or Willmarth *et al.* [1976]). In the viscous sublayer of transversely curved flows the momentum equilibrium is expressed by $r\tau = a\tau_w$ (Glauert & Lighthill [1955]). Reid & Wilson (1963) and Rao (1967) proposed a curvature dependent law of the wall,

$$U^+ = a^+ \ln\left(1 + \frac{y^+}{a^+}\right), \tag{1.1.1}$$

which predicts curvature effects on the sublayer for sufficiently small a^+.

To achieve large δ/a, experiments are typically performed over long tubes or wires of very small diameter (Luxton *et al.* [1984] and Lueptow *et al.* [1985] and Lueptow & Haritonidis [1987]). In such experimental facilities, the structural isolation of the wires, the aeroelastic interaction between the flow and the wire, the alignment of the cylinder with the mean flow, and the cylinder sag are major concerns. In addition, if a^+ is small, the size of the measuring probe (*e.g.*, hot wire) relative to the cylinder diameter becomes an issue in near-wall measurements. Finally, some of the measurement techniques used are based on the assumption that close to the wall the mean velocity profile is the same as that of the flat plate (see for example Richmond [1957] and Lueptow *et al.* [1985]). Attempts to address some of these problems are described by Willmarth & Yang (1970) and Lueptow & Haritonidis (1987).

If δ/a is not large (Rao & Keshavan [1972] and Lueptow *et al.* [1985]), the logarithmic region of the mean velocity profile has the same slope as the planar case. This flow regime is described analytically by Afzal & Narasimha (1976) with the method of matched asymptotic expansions. They conclude that when $\delta/a = \mathrm{O}(1)$ and in the limit of $a^+ \to \infty$, the axisymmetric turbulent boundary layer must have logarithmic and velocity defect profiles of the same form as in the planar turbulent boundary layer. The two parameters in the logarithmic velocity profile are found to depend on δ/a (Afzal & Narasimha [1976]). As δ/a increases and a^+ decreases, the mean velocity profiles exhibit a logarithmic region with a

decreasing slope (Lueptow *et al.* [1985]), and for sufficiently large δ/a and small a^+, the logarithmic region deteriorates and becomes negatively curved (Willmarth *et al.* [1976] and Luxton *et al.* [1984]). Some effort has been devoted to identifying the curvature dependence of the logarithmic velocity profile, however, it is clear from Leuptow's (1988) review that no consensus exists on this issue. Nevertheless, the available data suggests that when δ/a is small and a^+ is large the slope of the logarithmic region tends to scale with δ/a (Lueptow *et al.* [1985]). As δ/a increases and a^+ decreases, the logarithmic profile depends on both parameters (Willmarth *et al.* [1976], Luxton *et al.* [1984]).

The Reynolds shear stress in the outer part of the transversely curved boundary layer is lower than its planar counterpart (Lueptow *et al.* [1985]). Reynolds shear stress quadrant contributions in the transversely curved turbulent boundary layers are similar to those in the planar geometry (Lueptow & Haritonidis [1987]). At $y^+ \approx 39$ Lueptow *et al.* [1987] measured higher fractional contributions from second and forth quadrant events than in the planar case for weak events. Intense events are found to have a lower contribution to the Reynolds shear stress.

The axial and normal turbulence intensities measured by Luxton *et al.* (1984) or Lueptow & Haritonidis (1987) are also lower than their flat plate counterparts in the outer part of the boundary layer. Close to the wall ($y^+ < 20$), the measured axial intensities have magnitudes similar to those of the planar case, with maxima ($\overline{v_z^2}^{1/2}/u_\tau \approx 3.2$) also located at $y^+ \simeq 12$.

In a visualization study of axial flow over a cylinder, Lueptow & Haritonidis (1987) observed large scale structures moving across the cylinder. It is not clear whether the observed transverse flow motions are the result of oscillations of the wire (Lueptow [1989]). Since these large structures were linked to the azimuthal velocity component (Lueptow & Haritonidis [1987]) they should significantly affect the intensity of the azimuthal velocity fluctuations, which unfortunately were not measured. Similar large scale structures were also observed by Luxton *et al.* (1984) for larger curvatures ($\delta/a \geq 20$) only. Luxton *et al.* (1984) suggested that these large scale structures are important for turbulence generation in this flow.

1.2 The Wall Pressure

Knowledge of the characteristics of the wall pressure fluctuations is important for understanding flow-induced sound generation and the structural interaction between the flow and the body. A comprehensive treatment of this subject is given by Blake (1986). Since transversely curved turbulent flows occur over sonar devices towed by long cables, it is important to understand the characteristics of the wall pressure fluctuations in the flow regime where δ/a is large and a^+ is small. Reviews of measured wall pressure fluctuations on a flat plate are given by Willmarth (1975) and Eckelmann (1989). The effects of transverse curvature on the space-time characteristics of the wall pressure were investigated experimentally by Willmarth & Yang (1970) for $\delta/a \approx 2$ and by Willmarth *et al.* (1976) for $\delta/a \approx 4$. Since in both studies $a^+ = O(10^3)$, the curvature effects were limited to the outer part of the flow.

Many of the difficulties in the measurement of the wall pressure fluctuations can be overcome by the use of direct numerical simulations (Handler *et al.* [1984] and Choi & Moin [1990]). However, simulations are limited to low Reynolds numbers. There is some evidence (Willmarth [1975]) that the root-mean-square (r.m.s.) pressure normalized by the mean wall shear decreases with decreasing Reynolds number. This was confirmed by Choi & Moin (1990), who also found that the spectrum of the wall pressure fluctuations decreases with decreasing Reynolds number for low frequencies when scaled with inner variables and for high frequencies when scaled with the outer variables. In the two transversely curved turbulent boundary layer studies of the wall pressure fluctuations no appreciable effect of curvature on the r.m.s. wall pressure was found (Willmarth & Yang [1970]).

As had been found in previous experiments (Willmarth & Wooldridge [1962], Wills [1964], Emmerling [1974]), the large scale pressure correlation contours of Choi & Moin (1990) were more elongated in the spanwise direction than in the streamwise direction. The curvature dependence of the wall pressure correlations has not been established. Willmarth & Yang (1970) ($\delta/a \approx 2$) suggest that for large separations the ratio of spanwise to streamwise length scales decreases. However, their later study for $\delta/a \approx 4$ (Willmarth *et al.* [1976]) shows the opposite trend. Nevertheless, the wall pressure (Willmarth *et al.* [1976]) is significantly correlated around the cylinder and the azimuthal extent of the correlation increases with

increasing curvature. Willmarth & Yang (1970) argued that the main effect of the transverse curvature is to reduce the spanwise length scale of the large eddies, located in the outer part of the boundary layer.

In the planar turbulent boundary layer (Willmarth & Wooldridge [1962]) as well as in the transversely curved turbulent boundary layer (Willmarth & Yang [1970] and Willmarth *et al.* [1976]), the space-time wall pressure correlations indicate that the eddies decay after traveling a distance of the order of their size. Convection velocities can be defined from the wall pressure space-time correlation contours (Wills [1964]). In the planar geometry, there is a consensus among the experimental (Willmarth & Wooldridge [1962], Panton & Linebarger [1974]) and numerical (Choi & Moin [1990]) values reported for the convection velocity, which is about $0.8U_\infty$. Using a definition of the convection velocity that is independent of temporal separation (Wills [1964]), Choi & Moin (1990) found a convection velocity of $0.72U_\infty$, for which Taylor's hypothesis was more accurate for large structures than for small ones. In the transversely curved turbulent flows of Willmarth & Yang (1970) and Willmarth *et al.* (1976), convection velocities identical to that of the planar case were reported.

1.3 Motivation and Objectives

Direct numerical simulation of turbulence is the ideal tool for the study of turbulent flows at low Reynolds numbers. This technique is also well suited for providing spatially and temporally resolved data to study the characteristics of the wall pressure fluctuations, as well as for identifying the structural features in the flow.

Since, as the curvature increases, the circumference of the cylinder decreases, there will be fewer structures around the cylinder. In this sense the transversely curved flow in the large δ/a and small a^+ regime is a better setting for the study of the mechanisms of wall bounded flows. This is similar to the minimal channel of Jimenez & Moin (91) with the added advantage that the periodic boundary condition in the transverse direction are the natural boundary conditions.

The study described in the following chapters had the following objectives:

i) to develop a pseudo-spectral method for the incompressible Navier-Stokes equations in cylindrical coordinates with a no-stress outer boundary;

ii) to generate a spatially resolved database for turbulent flow with transverse curvature to study curvature effects on the turbulence statistics as well as instantaneous flow structures;

iii) to identify scaling parameters that link the statistics of the transversely curved flows with those of the planar case;

iv) to study the effects of the transverse curvature on the pressure field; to generate a temporally and spatially resolved database of the wall pressure and wall shear stresses and to study the space-time characteristics of the wall pressure fluctuations.

CHAPTER 2

The Model Problem

This chapter describes the numerical approach used to solve the incompressible Navier-Stokes equations for the axial flow over a cylinder. The key features of the method are the truncation of the semi-infinite domain in the radial direction, the decoupling of the viscous operators of the radial and azimuthal momentum equations, the calculation of the pressure through a variant of the method of Kleiser & Schumann (1981) and the imposition of the far field boundary conditions. In addition, a new dependent variable is defined (Υ), and the velocity is obtained from the solution of two partial differential equations for V_r and Υ and algebraic equations for V_θ and V_z. The validation of the numerical approach is discussed at the end of the chapter with the calculation of the stability characteristics of several two- and three-dimensional Taylor-Couette flows.

Throughout the chapter the velocity scale is the friction velocity, $u_\tau = \sqrt{\tau_w/\rho}$, where τ_w is the mean wall shear stress. The thickness of the layer is δ, and the superscript $^+$ denotes the scaling with the viscous length, ν/u_τ. Total fields are indicated by upper case symbols and fluctuating fields are denoted by lower case symbols. For example, $\vec{\mathbf{V}}$ and $\vec{\mathbf{v}}$ are the total and fluctuating velocity vectors, respectively.

2.1 Equations of Motion

To solve the Navier-Stokes equations for axial flow along a cylinder we use cylindrical coordinates (r, θ, z), where r is the radial coordinate, θ is the azimuthal coordinate and z the axial coordinate. In cylindrical coordinates the incompressible Navier-Stokes equations are (see for example Batchelor [1967]):

$$\frac{\partial V_r}{\partial t} + H_r = -\frac{\partial P}{\partial r} + \frac{1}{Re_\tau}\left(\nabla^2 V_r - \frac{V_r}{r^2} - \frac{2}{r^2}\frac{\partial V_\theta}{\partial \theta}\right), \qquad (2.1.1\ a)$$

$$\frac{\partial V_\theta}{\partial t} + H_\theta = -\frac{1}{r}\frac{\partial P}{\partial \theta} + \frac{1}{Re_\tau}\left(\nabla^2 V_\theta - \frac{V_\theta}{r^2} + \frac{2}{r^2}\frac{\partial V_r}{\partial \theta}\right), \qquad (2.1.1\ b)$$

$$\frac{\partial V_z}{\partial t} + H_z = -\frac{\partial P}{\partial z} + \frac{1}{Re_\tau}\nabla^2 V_z, \qquad (2.1.1\ c)$$

where $\vec{\mathbf{H}} = (H_z, H_r, H_\theta)$ are the convective terms and the density is absorbed into the pressure. Note that, unlike their Cartesian counterparts, the viscous operators of the radial and azimuthal momentum equations are coupled. The continuity equation is given by

$$\frac{V_r}{r} + \frac{\partial V_r}{\partial r} + \frac{1}{r}\frac{\partial V_\theta}{\partial \theta} + \frac{\partial V_z}{\partial z} = 0. \qquad (2.1.1\ d)$$

The Laplacian operator is

$$\nabla^2 = \frac{\partial^2}{\partial r^2} + \frac{1}{r}\frac{\partial}{\partial r} + \frac{1}{r^2}\frac{\partial^2}{\partial \theta^2} + \frac{\partial^2}{\partial z^2}, \qquad (2.1.2)$$

and the convective terms (H_z, H_r, H_θ) are

$$\begin{aligned} H_r &= V_r\frac{\partial V_r}{\partial r} + \frac{V_\theta}{r}\frac{\partial V_r}{\partial \theta} + V_z\frac{\partial V_r}{\partial z} - \frac{V_\theta^2}{r}, \\ H_\theta &= V_r\frac{\partial V_\theta}{\partial r} + \frac{V_\theta}{r}\frac{\partial V_\theta}{\partial \theta} + V_z\frac{\partial V_\theta}{\partial z} + \frac{V_\theta V_r}{r}, \\ H_z &= V_r\frac{\partial V_z}{\partial r} + \frac{V_\theta}{r}\frac{\partial V_z}{\partial \theta} + V_z\frac{\partial V_z}{\partial z}. \end{aligned} \qquad (2.1.3)$$

From the divergence of the momentum equations one obtains the Poisson equation for the pressure

$$\nabla^2 P = -\nabla \cdot \vec{\mathbf{H}}. \qquad (2.1.4)$$

The flow under consideration is naturally homogeneous in the azimuthal direction and is assumed to be homogeneous in the axial direction. In the radial direction the semi-infinite domain is truncated to a finite one, where $r \in [a, a+1]$. At $r = a+1$, model boundary conditions are imposed. The flow is driven by a mild streamwise pressure gradient and reaches a statistically steady state. This model corresponds

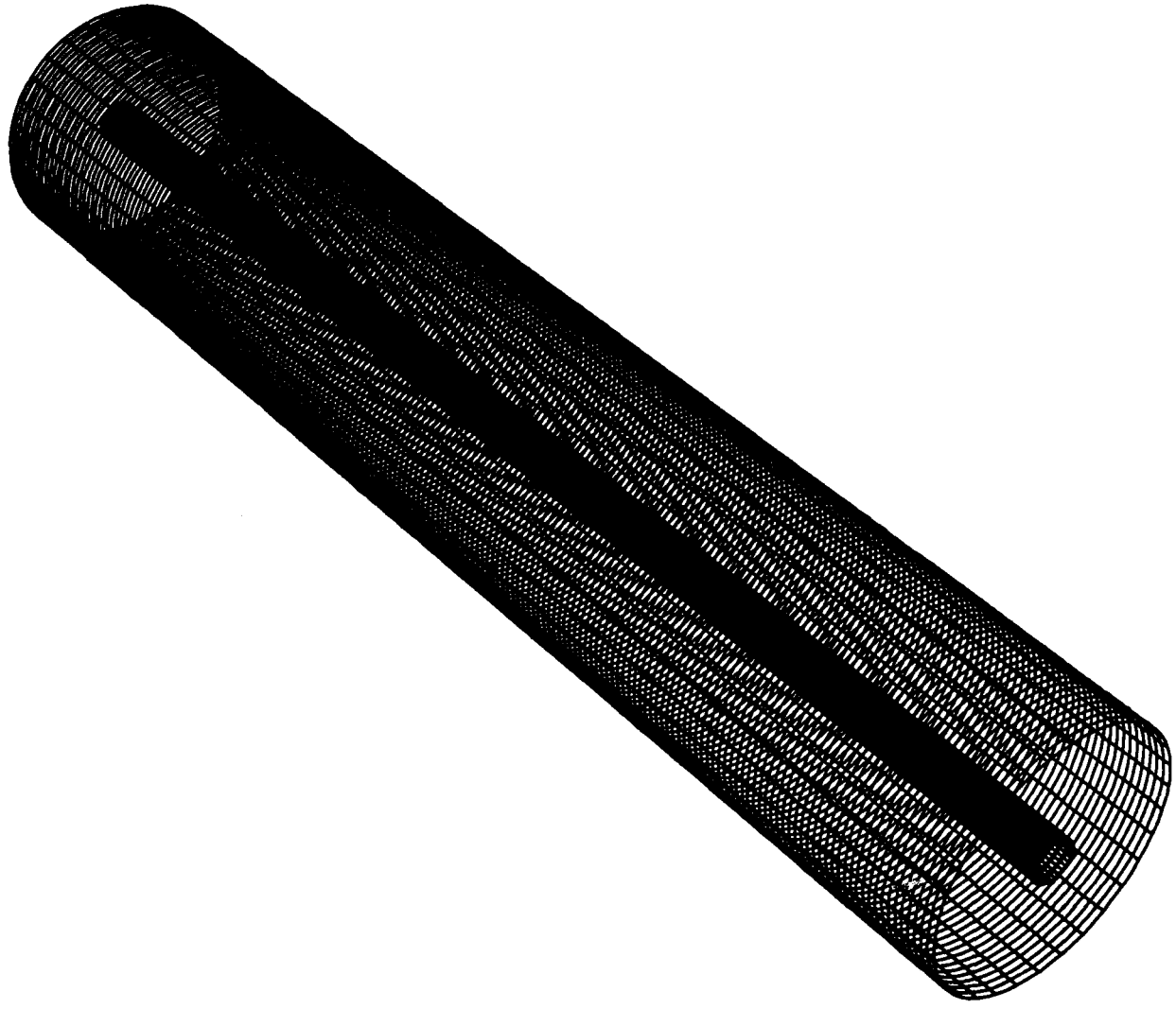

FIGURE 2.1 Computational domain illustrated by the grid at the surface of the cylinder ($r = a$) and at the outer edge of the layer ($r = a + 1$). The mean flow is parallel to the axis of the cylinder.

to a boundary layer with no spatial growth and is therefore an approximation to the physical case. Apart from the numerical advantages, the lack of spatial growth affords a better statistical sample for turbulence correlations.

Note that the domain truncation of this model prevents the occurrence of large scale viscous/inviscid interactions. Experiments (Luxton *et al.* [1984], Lueptow & Haritonidis [1987]) have reported that such structures periodically cross the cylinder. As discussed in Chapter 1 the origin of these structures may be due to vibrations of the cylinder and not purely a fluid dynamic phenomenon. In any case, our model is incapable of capturing such structures.

2.1.1 Boundary Conditions

On the surface of the cylinder ($r = a$) no-slip boundary conditions are imposed,

$$\vec{V}\Big|_{r=a} = 0. \qquad (2.1.5\ a)$$

In the axial direction, a finite domain of length L_z is chosen and periodic boundary conditions are imposed. In the azimuthal direction the flow is naturally periodic. In a semi-infinite domain the far field ($y \to \infty$) velocity boundary conditions for the axial flow along the cylinder are $V_z \to U_\infty$ and $(V_r, V_\theta) \to 0$. In the truncated domain in which the calculations are performed, we require that the radial component of the velocity be zero at $r = a + 1$. The boundary conditions for the axial and azimuthal velocity components are obtained by requiring that the surface shear stress be zero at the outer edge of the domain, that is, $\sigma_{r\theta}|_{r=a+1} = \sigma_{rz}|_{r=a+1} = 0$. Thus, we impose

$$V_r\Big|_{r=a+1} = 0, \qquad \frac{\partial}{\partial r}\left(\frac{V_\theta}{r}\right)\Big|_{r=a+1} = 0, \qquad \frac{\partial V_z}{\partial r}\Big|_{r=a+1} = 0. \qquad (2.1.5\ b)$$

The computational domain is illustrated in Figure 2.1.

2.1.2 Radial Coordinate Stretching

In the radial direction Chebyshev polynomial expansions (see for example Gottlieb & Orszag [1967]) are used. These expansions promote a high grid resolution at the edges of the domain ($r = a$ and $r = a + 1$). This is appropriate for the inner boundary where no-slip boundary conditions are imposed. However, at the outer edge of the domain fine resolution is not necessary because no sizable velocity gradients are expected there. To avoid this waste of resolution, the radial coordinate mapping

$$r = a - \frac{1}{2}(1 - \beta)\left(\frac{1 + \xi}{\beta - \xi}\right), \tag{2.1.6}$$

is used, which increases the resolution close to the cylinder surface at the expense of the resolution at the outer edge of the computational domain. In this expression, the Chebyshev variable $\xi \in [-1, 1] \Leftrightarrow r \in [a, a + 1]$ and the parameter $\beta = 6$ was used. Because the axial and azimuthal directions are periodic, we use Fourier expansions in these directions.

2.2 Uncoupling of the Viscous Operators

In the discussion that follows, the solution procedure is discussed without reference to the radial coordinate mapping (Equation 2.1.6) because its inclusion would only increase the algebraic complexity of the equations. Also in the remainder of the chapter the Fourier transformed (in θ and z) equations will be considered.

In the solution of the incompressible Navier-Stokes equations it is computationally convenient to eliminate the pressure. The fourth order formulation of (Kim *et al.* 1987) or the use of divergence-free expansion functions for the velocity field (Moser *et al.* 1983) are examples of how this can be achieved. In Cartesian coordinates, after eliminating the pressure, the momentum equations are only coupled through the nonlinear terms. In the cylindrical coordinate system the coupling is in both the convective terms and the viscous terms of the radial and azimuthal momentum equations. In order to decouple the radial and azimuthal momentum equations we define $\hat{\Upsilon}$ as ($\hat{}$ denotes the Fourier transform)

$$\hat{\Upsilon} = ik_z\hat{V}_\theta - im\hat{V}_z, \tag{2.2.1}$$

and recast the momentum equations in the following form:

$$\frac{\partial \hat{V}_r}{\partial t} + \hat{\tilde{H}}_r = -\frac{\partial \hat{P}}{\partial r} + \frac{1}{Re_\tau}\hat{\nabla}^2 \hat{V}_r, \qquad (2.2.2\ a)$$

$$\frac{\partial \hat{\Upsilon}}{\partial t} + \hat{\tilde{H}}_\Upsilon = k_z m(\frac{1}{r} - r)\hat{P} + \frac{1}{Re_\tau}\hat{\nabla}^2 \hat{\Upsilon} \qquad (2.2.2\ b)$$

where

$$\begin{aligned} \hat{\tilde{H}}_r &= \hat{H}_r + \frac{1}{Re_\tau}\left(\frac{\hat{V}_r}{r^2} + im\frac{2}{r^2}\hat{V}_\theta\right), \\ \hat{\tilde{H}}_\Upsilon &= ik_z\hat{H}_\theta - im\hat{H}_z - \frac{ik_z}{Re_\tau}\left(-\frac{\hat{V}_\theta}{r^2} + im\frac{2}{r^2}\hat{V}_r\right), \end{aligned} \qquad (2.2.3)$$

and

$$\hat{\nabla}^2 = \frac{1}{r}\frac{\partial}{\partial r}\left(r\frac{\partial}{\partial r}\right) - \frac{m^2}{r^2} - k_z^2, \qquad (2.2.4)$$

is the Fourier transformed Laplacian operator. The axial wave-number is

$$k_z = \frac{2\pi}{L_z}k, \qquad (2.2.5)$$

and the azimuthal wave-number is m.

In the numerical approach adopted, we solve first for $\hat{V}_r$, so it is convenient to express the boundary conditions for $\hat{\Upsilon}$ as a function of $\hat{V}_r$. At the surface of the cylinder we have $\hat{\Upsilon}(r = a) = 0$. At the outer edge of the domain the boundary conditions on the velocity (Equation 2.1.5 b) and continuity give

$$\left[(m^2 + rk_z^2)\frac{\partial \hat{\Upsilon}}{\partial r} - k_z^2\hat{\Upsilon}\right]_{r=a+1} = -k_z m\left(\frac{\partial \hat{V}_r}{\partial r}\right)_{r=a+1}. \qquad (2.2.6)$$

The computational advantage of this approach is that in Fourier space the continuity equation (Equation 2.1.1 *d*) and the definition of $\hat{\Upsilon}$ (Equation 2.2.1) determine an algebraic system of equations for $\hat{V}_z$ and $\hat{V}_\theta$ as a function of $\hat{V}_r$ and $\hat{\Upsilon}$. The solution of the system is

$$\begin{aligned}\hat{V}_\theta &= \frac{i}{m^2 + rk_z^2}\left[m\left(\hat{V}_r + r\frac{\partial \hat{V}_r}{\partial r}\right) - k_z r\hat{\Upsilon}\right], \\ \hat{V}_z &= \frac{i}{m^2 + rk_z^2}\left[k_z\left(\hat{V}_r + r\frac{\partial \hat{V}_r}{\partial r}\right) + m\hat{\Upsilon}\right],\end{aligned} \tag{2.2.7}$$

which is easier to solve than the partial differential equations that they replace.

2.3 Time Advancement

An implicit second order Crank-Nicholson scheme is used to time advance the viscous terms in these equations. The convective-like terms, $\hat{\tilde{H}}_r$ and $\hat{\tilde{H}}_\Upsilon$, are advanced explicitly with a second order Adams-Bashforth scheme. Note that the viscous contributions to $\hat{\tilde{H}}_r$ and $\hat{\tilde{H}}_\Upsilon$ do not involve radial derivatives, which could lead to numerical stability problems. A von Neumann stability analysis of the cross-terms in the viscous operators shows that they do not produce a severe stability limitation and can be treated explicitly.

The time discretized equations for $\hat{V}_r$ (Equation 2.2.2 *a*) and $\hat{\Upsilon}$ (Equation 2.2.2 *b*) at time step $n+1$ are:

$$\begin{aligned}(1 - \frac{\Delta t}{2Re_\tau}\hat{\nabla}^2)\hat{V}_r^{n+1} &= -\Delta t\frac{\partial \hat{P}^n}{\partial r} \\ &\quad -\frac{\Delta t}{2}\left(3\hat{H}_r^n - \hat{H}_r^{n-1}\right) + (1 + \frac{\Delta t}{2Re_\tau}\hat{\nabla}^2)\hat{V}_r^n, \qquad (2.3.1\ a) \\ \hat{V}_r^{n+1}\Big|_{r=a} &= 0, \qquad \hat{V}_r^{n+1}\Big|_{r=a+1} = 0,\end{aligned}$$

$$(1-\frac{\Delta t}{2Re_\tau}\hat{\nabla}^2)\hat{\Upsilon}^{n+1} = k_z m\Delta t(\frac{1}{r}-r)\hat{P}^n$$

$$-\frac{\Delta t}{2}\left(3\hat{H}_\Upsilon^n - \hat{H}_\Upsilon^{n-1}\right) + (1+\frac{\Delta t}{2Re_\tau}\hat{\nabla}^2)\hat{\Upsilon}^n,$$

$$\hat{\Upsilon}^{n+1}\Big|_{r=a} = 0, \qquad (2.3.1\ b)$$

$$\left[(m^2+rk_z^2)\frac{\partial\hat{\Upsilon}}{\partial r}^{n+1} - k_z^2\hat{\Upsilon}^{n+1}\right]_{r=a+1} = -mk_z\frac{\partial\hat{V}_r}{\partial r}^{n+1}\Big|_{r=a+1},$$

$$\hat{\nabla}^2\hat{P}^n = -\hat{\nabla}\cdot\left(\frac{3}{2}\hat{\vec{\mathbf{H}}}^n - \frac{1}{2}\hat{\vec{\mathbf{H}}}^{n-1}\right), \qquad (2.3.1\ c)$$

where the boundary conditions for the pressure (Equation 2.3.1 c) enforce the continuity equation at the boundaries (see Section **2.4**).

In this formulation, two elliptic operators, $(1-\Delta t\hat{\nabla}^2/(2Re_\tau))$ and $\hat{\nabla}^2$, need to be inverted for each wave number pair (m,k) at each time step.

The flow variables are represented by the following expansions

$$\begin{pmatrix}\vec{V}\\ P\end{pmatrix}(\xi,\theta,z,t) = \sum_{l=0}^{N_r} T_l(\xi) \sum_{m=-N_\theta/2}^{N_\theta/2-1} e^{im\theta} \sum_{k=-N_z/2}^{N_z/2-1} e^{i\frac{2\pi}{L_z}kz}\begin{pmatrix}\hat{\vec{\mathbf{V}}}\\ \hat{P}\end{pmatrix}_{lmk}(t), \qquad (2.3.2)$$

where $T_l(\xi)$ are the Chebyshev polynomials and $\hat{\vec{\mathbf{V}}}_{lmk}(t)$ and $\hat{P}_{lmk}(t)$ are the complex spectral coefficients for the velocity and pressure, respectively. (N_r, N_θ, N_z) denote the number of modes in the radial, azimuthal and axial directions respectively.

With the radial coordinate stretching, each elliptic operator results in a matrix with 12 diagonals above the main diagonal and 8 below. In addition, the boundary conditions fill the two bottom rows of each matrix. The high computational cost of the inversion of matrices with this band structure was one of the reasons for the adoption of a constant time step. Substantial savings in computer time are achieved by the precalculation and storage of the LU decompositions of the matrices corresponding to the operators $(1-\Delta t\hat{\nabla}^2/(2Re_\tau))$ and $\hat{\nabla}^2$.

The constant time step was chosen in accordance with numerical stability constraints. The CFL number

$$CFL = \pi \Delta t \left(\frac{|V_r|}{\Delta r} + \frac{|V_\theta|}{r\Delta\theta} + \frac{|V_z|}{\Delta z} \right) \Big|_{max} \tag{2.3.3}$$

was required to be less than 0.6 throughout the calculations.

2.4 Continuity at the Boundaries

The role of the pressure is to ensure a divergence free velocity field; thus the appropriate boundary conditions for the pressure at $r = a$ and $r = a + 1$ must be chosen such that continuity is satisfied everywhere including at the boundaries. Kleiser & Schumann's (1981) algorithm for the enforcement of continuity is used here.

We start by writing $\hat{P}$ and $\hat{V}_r$ as

$$\begin{aligned} \hat{P}^{n+1} &= \hat{P}_i^{n+1} + \alpha_1^{n+1}\hat{P}_{h_1} + \alpha_2^{n+1}\hat{P}_{h_2}, \\ \hat{V}_r^{n+1} &= \hat{V}_{ri}^{n+1} + \alpha_1^{n+1}\hat{V}_{rh_1} + \alpha_2^{n+1}\hat{V}_{rh_2}, \end{aligned} \tag{2.4.1}$$

where α_1^{n+1} and α_2^{n+1} are constants to be determined at each time step. $\hat{P}_i$ and $\hat{V}_{ri}^{n+1}$ are the particular solutions and satisfy

$$\hat{\nabla}^2 \hat{P}_i^n = -\hat{\nabla} \cdot \hat{\mathbf{H}}^n, \qquad P_i^n \Big|_{r=a,a+1} = 0, \tag{2.4.2}$$

and

$$\begin{aligned} (1 - \frac{\Delta t}{2Re_\tau}\hat{\nabla}^2)\hat{V}_{r_i}^{n+1} &= -\Delta t \frac{\partial \hat{P}_i^n}{\partial r} \\ &\quad -\frac{\Delta t}{2}\left(3\hat{H}_r^n - \hat{H}_r^{n-1}\right) + (1 + \frac{\Delta t}{2Re_\tau}\hat{\nabla}^2)\hat{V}_r^n, \\ \hat{V}_{ri}^{n+1}\Big|_{r=a} &= 0, \qquad \hat{V}_{ri}^{n+1}\Big|_{r=a+1} = 0, \end{aligned} \tag{2.4.3}$$

respectively.

$\hat{P}_{h_1}$ and $\hat{P}_{h_2}$ are obtained from:

$$\begin{aligned} &\hat{\nabla}^2 \hat{P}_{h_1} = 0, \qquad \hat{P}_{h_1}\Big|_{r=a} = 1, \qquad \hat{P}_{h_1}\Big|_{r=a+1} = 0, \\ &\hat{\nabla}^2 \hat{P}_{h_2} = 0, \qquad \hat{P}_{h_2}\Big|_{r=a} = 0, \qquad \hat{P}_{h_2}\Big|_{r=a+1} = 1. \end{aligned} \tag{2.4.4}$$

In order to satisfy Equations 2.3.1 *a* and 2.4.3, $\hat{V}_{rh_1}$ and $\hat{V}_{rh_2}$ are the solutions of

$$\begin{aligned} &(1 - \frac{\Delta t}{2Re_\tau}\hat{\nabla}^2)\hat{V}_{rh_1} = -\Delta t \frac{\partial \hat{P}_{h_1}}{\partial r}, \\ &\qquad \hat{V}_{rh_1}\Big|_{r=a} = 0, \qquad \hat{V}_{rh_1}\Big|_{r=a+1} = 0, \\ &(1 - \frac{\Delta t}{2Re_\tau}\hat{\nabla}^2)\hat{V}_{rh_2} = -\Delta t \frac{\partial \hat{P}_{h_2}}{\partial r}, \\ &\qquad \hat{V}_{rh_2}\Big|_{r=a} = 0, \qquad \hat{V}_{rh_2}\Big|_{r=a+1} = 0. \end{aligned} \tag{2.4.5}$$

With a constant time step Δt (used in the present calculations), P_{h_1}, P_{h_2}, V_{rh_1} and V_{rh_2} need to be calculated once, stored and used throughout the calculations.

The constants α_1^{n+1} and α_2^{n+1} are obtained at each time step from the the constraint imposed by the continuity equation at the boundaries. The radial derivative of the continuity equation and the velocity boundary conditions, given by Equations 2.1.5 *a* and 2.1.5 *b*, lead to the following compatibility conditions at the boundaries of the computational domain:

$$\frac{\partial \hat{V}_r^{n+1}}{\partial r}\Big|_{r=a} = 0, \qquad \frac{\partial}{\partial r}\left(r\frac{\partial \hat{V}_r^{n+1}}{\partial r}\right)\Big|_{r=a+1} = 0. \tag{2.4.6}$$

The expansion of $\hat{V}_r$ according to Equation 2.4.1 and the above compatibility conditions lead to the following system:

$$\begin{pmatrix} \left.\frac{\partial \hat{V}_{r_i}^{n+1}}{\partial r}\right|_{r=a} \\ \left.\frac{\partial}{\partial r}\left(r\frac{\partial \hat{V}_{r_i}^{n+1}}{\partial r}\right)\right|_{r=a+1} \end{pmatrix} =$$

$$- \begin{pmatrix} \left.\frac{\partial \hat{V}_{r_{h_1}}}{\partial r}\right|_{r=a} & \left.\frac{\partial \hat{V}_{r_{h_2}}}{\partial r}\right|_{r=a} \\ \left.\frac{\partial}{\partial r}\left(r\frac{\partial \hat{V}_{r_{h_2}}}{\partial r}\right)\right|_{r=a+1} & \left.\frac{\partial}{\partial r}\left(r\frac{\partial \hat{V}_{r_{h_1}}}{\partial r}\right)\right|_{r=a+1} \end{pmatrix} \begin{pmatrix} \alpha_1^{n+1} \\ \alpha_2^{n+1} \end{pmatrix} \quad , \tag{2.4.7}$$

which determines α_1^{n+1} and α_2^{n+1}. With these constants, the pressure and radial velocity fields that satisfy the continuity equation are uniquely determined.

2.5 The Mean Flow

The mean flow (corresponding to $m = 0$ and $k = 0$) in the axial direction is governed by the axial mean momentum equation

$$\begin{aligned} \frac{\partial \overline{V}_z}{\partial t} + \overline{H}_z &= -\frac{\partial \overline{P}}{\partial z} + \frac{1}{Re_\tau}\left[\frac{1}{r}\frac{\partial}{\partial r}\left(r\frac{\partial \overline{V}_z}{\partial r}\right)\right] \\ \overline{V}_z\Big|_{r=a} &= 0, \qquad \left.\frac{\partial \overline{V}_z}{\partial r}\right|_{r=a+1} = 0, \end{aligned} \tag{2.5.1}$$

where the overbar denotes average over θ and z planes.

The flow is driven by a mild axial pressure gradient so that it can reach a statistical steady state. In the cylindrical geometry the mass flux in the axial direction is given by

$$\dot{M} = 2\pi \int_a^{a+1} \overline{V}_z r dr. \tag{2.5.2}$$

Integration of the mean axial momentum equation in the radial direction gives

$$\frac{d\overline{P}}{dz} = -\frac{2}{1+2a}\int_{a}^{a+1} \overline{H}_z r dr - \frac{2a}{Re_\tau(1+2a)}\frac{\partial \overline{V}_z}{\partial r}\bigg|_{r=a}, \tag{2.5.3}$$

which determines the mean axial pressure gradient necessary to maintain a constant mass flux.

The only solution for $\overline{V}_r$ that satisfies the mean continuity equation and the boundary conditions is

$$\overline{V}_r = 0. \tag{2.5.4}$$

Finally, the mean flow in the azimuthal direction ($\overline{V}_\theta$) satisfies

$$\begin{aligned} &\frac{\partial \overline{V}_\theta}{\partial t} + \overline{H}_\theta = \frac{1}{Re_\tau}\left[\frac{\partial}{\partial r}\left(r\frac{\partial \overline{V}_\theta}{\partial r}\right) - \frac{\overline{V}_\theta}{r^2}\right], \\ &\overline{V}_\theta\Big|_{r=a} = 0, \qquad \frac{\partial}{\partial r}\left(\frac{\overline{V}_\theta}{r}\right)_{r=a+1} = 0. \end{aligned} \tag{2.5.5}$$

2.6 Code Verification

The method described above was extensively tested. The eigenvalues of the Stokes operator with homogeneous boundary conditions were computed. As expected, the eigenvalues are real and negative. Furthermore, they were verified to be in close agreement with the eigenvalues computed by Moser (1988) using a different numerical method.

In addition several Taylor Couette flow cases were computed. The extensive experimental and computational data available on Taylor Couette flow makes it an ideal test case for the code. First, the critical Reynolds number (Re_c) for the onset of Taylor vortices was computed and compared with the existing data. Comparisons with analytical (DiPrima & Eagles [1977]) and computational (Moser *et al.* [1983]) results for two gap widths are shown in Table 2.1 *a*. In this table and the remainder of the chapter R_i and R_o are the radii of the inner and outer cylinder, $d = R_o - R_i$ is

the gap width and λ is the axial wave-number of the vortices. The two-dimensional Taylor Couette flow is also characterized by the torque

$$G = 2\pi Re_d \left(r^2 \frac{d\overline{V}_\theta}{dr} - r\overline{V}_\theta \right) \Big|_{r=r_i}, \tag{2.6.1}$$

that must be applied to the inner cylinder to drive the flow. Calculated torque values for gap widths and Reynolds numbers for which there are both experiments (Donnelly & Simon [1960]) and computations (Moser *et al.* [1983]) are reported in Table 2.1 *b*. In all cases the two-dimensional calculations of the present code are in excellent agreement with both the experiments and previous calculations.

	$r_i/r_o = 0.5$ $\lambda/d = 3.976$	$r_i/r_o = 0.95$ $\lambda/d = 4.018$
DiPrima & Eagles (1977) †	184.99	68.19
Moser *et al.* (1983) *	185.99	68.2
present	184	68.2

Table 2.1 *a* Critical Reynolds number (Re_c) for 2-D Taylor vortices

	$r_i/r_o = 0.5$, $Re_d = 78.8$ $\lambda/d = 3.976$	$r_i/r_o = 0.95$, $Re_d = 195$ $\lambda/d = 4.018$
Donnelly & Simon (1960) ‡	1.479×10^3	5.26×10^5
Moser *et al.* (1983) *	1.487×10^3	5.42×10^5
present	1.486×10^3	5.43×10^5

Table 2.1 *b* Torque for 2-D Taylor vortices

* Computations; † Stability analysis; ‡ Experiments.

	$r_i/r_o = 0.868$	$r_i/r_o = 0.875$
	$Re_d = 458.1$	$Re_d = 243.5$
King *et al.* (1984)	$0.3344\Omega_i$ ‡ , $0.3347\Omega_i$ *	$0.3757\Omega_i$ *
present	$0.3343\Omega_i$	$0.3759\Omega_i$

Table 2.1 c Wave speed of 3-D Taylor vortices ($\lambda/d = 3.0$, $m = 6$)

To test the full three-dimensional code, the wave speeds of wavy Taylor vortices (Coles [1965]) were calculated for several gap Reynolds numbers (Re_d), axial wave lengths (λ/d) and wave numbers (m). The results of the present code are compared in Table 2.1 c to the data of King *et al.* (1984), which includes experiments and computations.

2.6.1 Numerical Resolution

The spatial resolution parameters describing the two turbulent flow simulations reported here are shown in Table 2.2.

Note that the effective azimuthal resolution, $\Delta\theta = 2\pi r/N_\theta$, depends on the radial location, with the coarsest resolution at the outer edge of the domain ($r = a + 1$). Because of this, the simulations are very well resolved in the azimuthal direction, near the wall. At the outer edge, the resolution appears to be adequate as shown by the velocity spectra in Figure 2.2. In Figure 2.3, the axial spectra of the velocity fluctuations at two distances from the wall are shown. In both simulations the axial resolution appears to be adequate with no energy accumulation at the high wave-numbers.

The length of the computational domain is set to be sufficiently large to ensure that the velocity is decorrelated for separations larger than half of the computational box, so that the imposed periodic boundary conditions will have minimal effects on the turbulence. Axial two-point correlations (Figure 2.4) show that this is roughly the case.

* Computations; † Stability analysis; ‡ Experiments.

δ/a	5	11
L_z	4π	6π
${L_z}^+$	2676	4656
${L_{\theta_i}}^+ = 2\pi a^+$	268	141
${L_{\theta_o}}^+ = 2\pi(a^+ + \delta^+)$	1608	1692
$\Delta_z^+ = {L_z}^+/N_z$	14	14
$\Delta_{\theta_i}^+ = {L_{\theta_i}}^+/N_\theta$	4	1
$\Delta_{\theta_o}^+ = {L_{\theta_o}}^+/N_\theta$	25	13
(N_z, N_r, N_θ)	(192,96,65)	(320,96,129)

Table 2.2 Grid resolution parameters

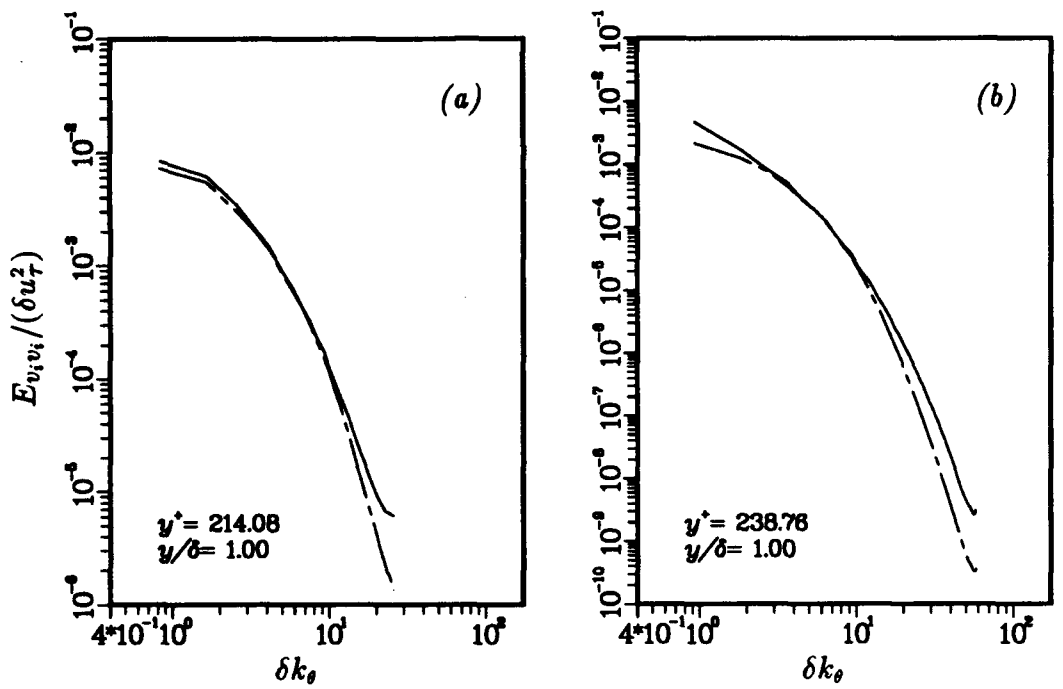

FIGURE 2.2 Azimuthal (spanwise, $\delta\Delta k_\theta = \delta/r$) spectra of the velocity fluctuations normalized by δ and u_τ for $\delta/a = 5$ (a) and for $\delta/a = 11$ (b): —— $E_{v_zv_z}$; ---- $E_{v_\theta v_\theta}$.

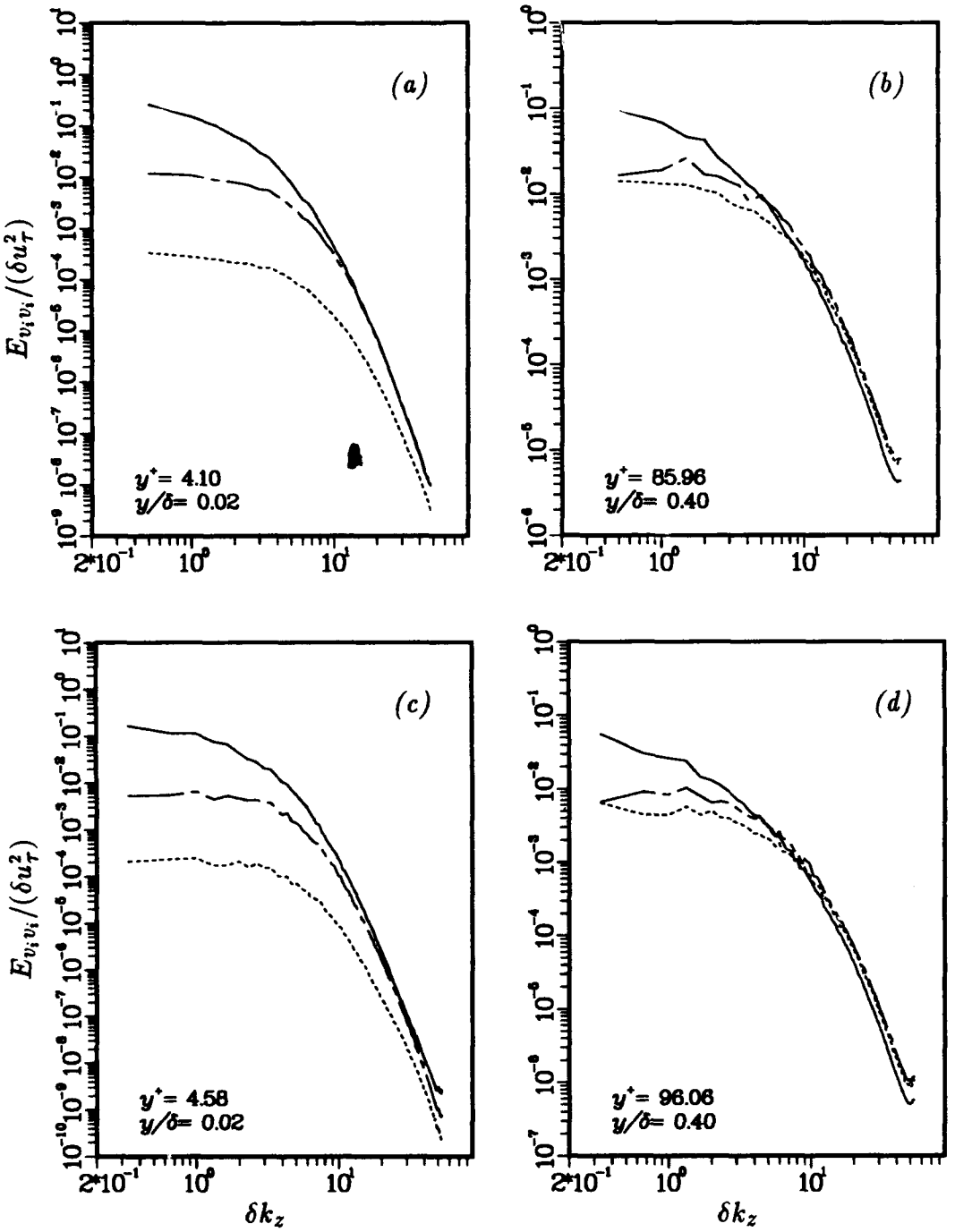

FIGURE 2.3 Axial spectra of the velocity fluctuations normalized by δ and u_τ for $\delta/a = 5$ (a and b) and for $\delta/a = 11$ (c and d): —— $E_{v_zv_z}$; ---- $E_{v_rv_r}$;—— $E_{v_\theta v_\theta}$.

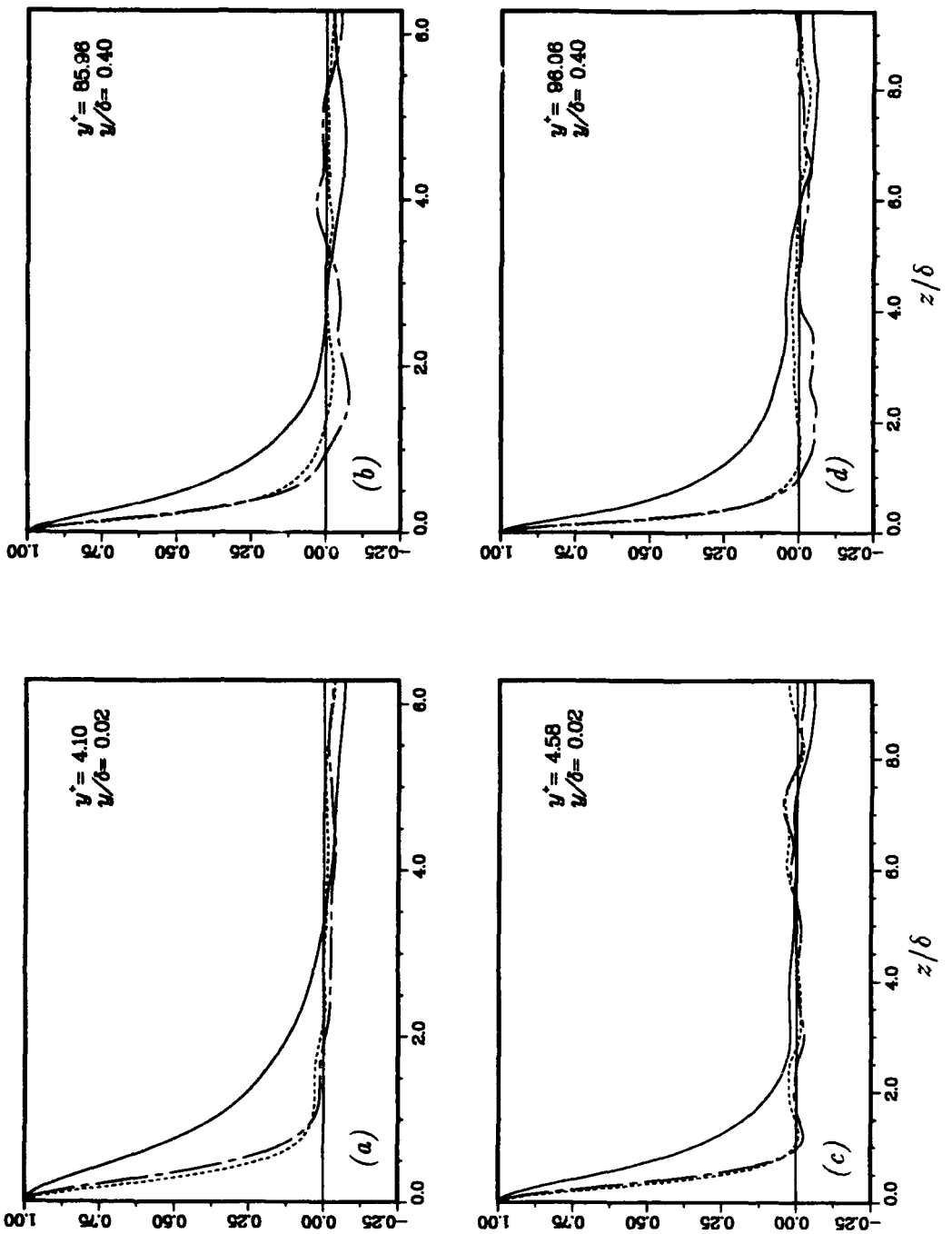

FIGURE 2.4 Axial two-point correlations of the velocity fluctuations for $\delta/a = 5.0$ with $L_z/\delta = 4\pi$ (a and b) and for $\delta/a = 11.0$ with $L_z/\delta = 6\pi$ (c and d): —— $R_{v_z v_z}$, ---- $R_{v_r v_r}$, ---- $R_{v_\theta v_\theta}$.

CHAPTER 3

The Velocity and Vorticity

This chapter describes the major statistical characteristics and time dependent structure of the velocity field. All the statistics presented are obtained from a sample collected after the calculations had reached the statistically steady state, and are calculated using spatial averaging over the domain in the θ and z directions and temporal averaging that covers 2.5 δ/u_τ time units in the $\delta/a = 5$ case and 2.1 δ/u_τ time units in the $\delta/a = 11$ case. Throughout the chapter the results are compared to those of the plane channel of Kim *et al.* (1987).

In Section **3.1** the properties of the mean flow are studied and compared with the available experimental data. In Section **3.2** turbulence intensities and the Reynolds shear stress are shown to decrease with increasing curvature. In addition, a curvature dependent local velocity scale, which collapses several flow statistics, is derived from the momentum equations. The structure of the Reynolds shear stress is discussed in Section **3.3**. Vorticity statistics are presented in Section **3.4**. Finally, the instantaneous structural characteristics of the flow are presented via contour plots in Section **3.5**.

3.1 Mean Velocity Statistics

Mean flow parameters for the present transversely curved flow simulations as well as for the plane channel ($\delta/a = 0$) are reported in Table 3.1. Because the Reynolds numbers of the three simulations are similar, the differences in Table 3.1 are due to the transverse curvature. For comparison, Tables 3.2 *a*, 3.2 *b* and 3.2 *c* contain the mean flow parameters of the experiments of Willmarth *et al.* (1976), Luxton *et al.* (1984) and Leuptow & Haritonidis (1987). In agreement with experimental observations, the skin friction coefficient,

$$C_f = 2\left(\frac{u_\tau}{U_\infty}\right)^2, \tag{3.1.1}$$

δ/a	0	5	11
a^+	–	43	21
C_f	6.04×10^{-3}	8.07×10^{-3}	9.87×10^{-3}
Re_δ	3300	3368	3418
Re_τ	180	214	239
Re_a	–	674	311
δ^*/δ	0.141	0.154	0.152
θ^*/δ	0.087	0.123	0.131
H	1.62	1.25	1.15

Table 3.1 Mean flow parameters

increases with increasing curvature (by as much as 63% for $\delta/a = 11$) when compared with the plane channel flow with comparable Reynolds number. However, in the simulations the magnitude of this increase is larger than has been observed experimentally, probably because of the much higher experimental Reynolds numbers ($Re_\delta = O(10^4)$). In Table 3.1 the boundary layer displacement and momentum thicknesses reported for the present transversely curved flow simulations are defined by (Luxton *et al.* [1984])

$$(a/\delta + \delta^*/\delta)^2 - (a/\delta)^2 = 2 \int_{a/\delta}^{a/\delta+1} \left(1 - \frac{\overline{V}_z}{U_\infty}\right) r dr, \qquad (3.1.2\ a)$$

and

$$(a/\delta + \theta^*/\delta)^2 - (a/\delta)^2 = 2 \int_{a/\delta}^{a/\delta+1} \left(\frac{\overline{V}_z}{U_\infty}\right)\left(1 - \frac{\overline{V}_z}{U_\infty}\right) r dr, \qquad (3.1.2\ b)$$

δ/a	4.7	16	37.5
a^+	751	198	46
C_f	3.04×10^{-3}	4.18×10^{-3}	7.84×10^{-3}
Re_δ	90380	69280	27600
Re_a	19230	4330	736

Table 3.2 *a* Experimental mean flow parameters (Willmarth *et al.* [1976]).

δ/a	26	26.9	41.6
a^+	47.4	32.1	13
C_f	7.3×10^{-3}	0.01	0.017
Re_δ	20386	12252	5962
Re_a	785	455	140
δ^*/δ	0.184	0.185	0.187
θ^*/δ	0.181	0.182	0.182
H	1.014	1.02	1.03

Table 3.2 *b* Experimental mean flow parameters (Luxton *et al.* [1984]).

δ/a	6.74	7.16	8.0
a^+	288	144	72
C_f	3.5×10^{-3}	3.8×10^{-3}	4.1×10^{-3}
Re_δ	46330	23700	12800
Re_a	6419	3209	1605

Table 3.2 *c* Experimental mean flow parameters (Lueptow & Haritonidis [1987]).

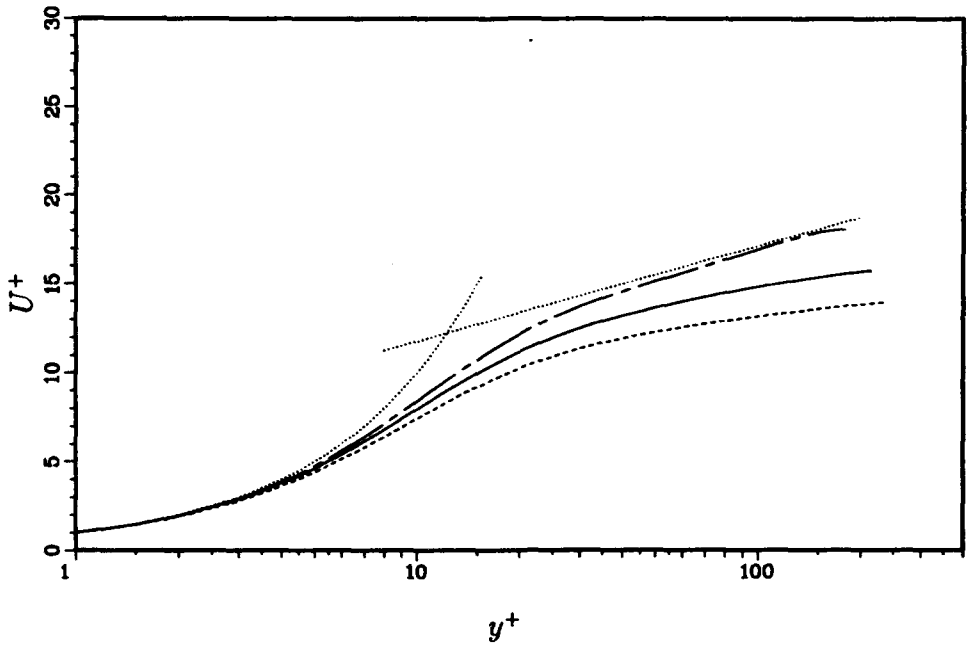

FIGURE 3.1 Mean-velocity profiles: —·— plane channel (Kim *et al.* [1987]); cylinders with —— $\delta/a = 5$ and ---- $\delta/a = 11$; ····· planar law of the wall, $U^+ = y^+$, and log law, $U^+ = 2.5\ln(y^+) + 5.5$.

respectively. Even though several different definitions for the displacement and momentum thicknesses in transversely curved flows have been proposed in the literature, there are several reasons to adopt the above definitions. The expression for the displacement thickness (Equation 3.1.2 *a*) is consistent with the usual mass flux displacement argument, and the momentum thickness defined by Equation 3.1.2 *b* arises in the axisymmetric integral momentum equation. In this sense, the two definitions have the same physical meaning as their planar counterparts, and in the flat plate limit ($\delta/a \to 0$), Equations 3.1.2 reduce to their planar counterparts (multiplying by δ/a before taking the limit $\delta/a \to 0$). Luxton *et al.* (1984) measured δ^*/δ and θ^*/δ according to the above expressions and find higher values than in the simulations. This is probably a result of the larger δ/a in the experiments. The shape factors ($H = \delta^*/\theta^*$) measured by Luxton *et al.* (1984) are around unity, whereas the shape factor in the simulations is larger than one and decreases with increasing δ/a due to an increase in the momentum thickness.

3.1.1 The Mean Velocity Profile

The mean velocity profile of the two transversely curved flows ($\delta/a = 5$ and 11) are compared to that in the plane channel flow in Figure 3.1. Because of the small values of a^+, the viscous sublayer mean velocity profiles are slightly affected by the curvature of the wall. In contrast most experiments (Rao & Keshavan [1972], Willmarth *et al.* [1976], Lueptow *et al.* [1985]), find no effect of curvature in the mean velocity profile for $y^+ < 20$. Clearly, in many of these experiments a^+ is too large for there to be a perceptible inner layer effect (for example $a^+ \approx 140$ and $\delta/a \approx 7$ in Lueptow & Haritonidis [1987]). However, even in experiments in which the values of a^+ are close to or below those of the simulations (for example Luxton *et al.* [1984] and Willmarth *et al.* [1976]), the measured mean velocity profiles agree with the planar velocity profile for $y^+ < 20$. This disagreement between the experiments and the simulations may be due to measurement difficulties close to the wall of the cylinder. In addition, it should be noted that, in many of the mean velocity measurements, the estimation of the friction velocity is estimated by assuming that the mean velocity profile of the transversely curved flow is not affected by the curvature near the wall. The mean velocity profiles of the present numerical experiments suggest that this assumption is not correct, at least in the flow regime of interest here, that of large δ/a and small a^+.

In the planar boundary layer, the assumption that the total stress is dominated by the viscous stress in the viscous sublayer leads to the planar law of the wall, $U^+ = y^+$. For the axisymmetric boundary layer in the absence of a pressure gradient, the mean momentum equilibrium in the viscous sublayer is expressed by

$$\frac{\tau}{\tau_w} = \frac{a}{r}, \tag{3.1.3}$$

as first noted by Glauert & Lighthill (1955). Assuming that the Reynolds shear stress is negligible in comparison to the viscous stress leads to the law of the wall for axisymmetric flows (Reid & Wilson [1963], Rao [1967]),

$$U^+ = a^+ \ln\left(1 + \frac{y^+}{a^+}\right). \tag{3.1.4}$$

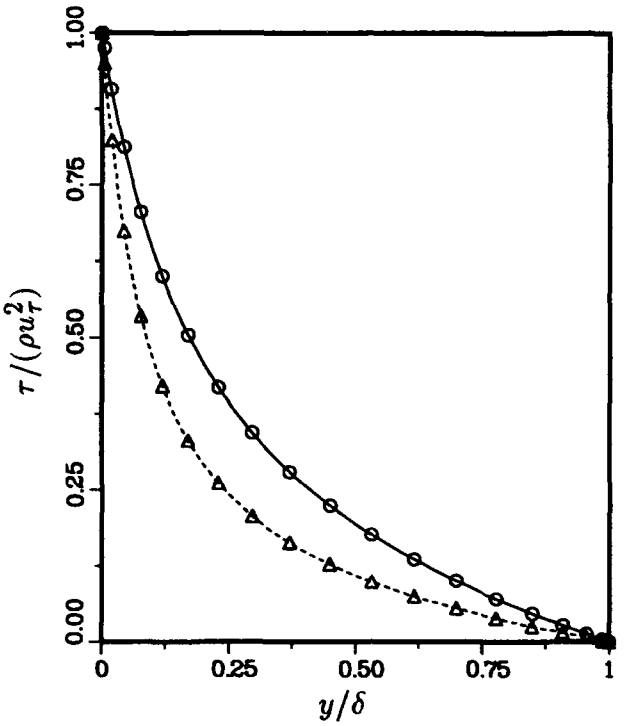

FIGURE 3.2 Total stress normalized by u_τ: analytical for cylinders with —— $\delta/a = 5$ and ---- $\delta/a = 11$; symbols for computed results with o for $\delta/a = 5$ and with $\triangle$ for $\delta/a = 11$.

Note that to second order in y^+, Equation 3.1.4 is given by

$$U^+ = y^+ \left(1 - \frac{y^+}{2a^+}\right). \tag{3.1.5}$$

Thus, the law of the wall for the viscous subalyer in transversely curved flows is equal to the planar viscous sublayer law of the wall, $U^+ = y^+$, plus a curvature dependent correction. Clearly, if a^+ is large the mean velocity profile near the wall does not deviate appreciably from the planar case. The mean velocity profiles given by Equation 3.1.4 are better approximations to the computed near-wall velocity profiles than the planar law of the wall.

As observed in several experiments (Lueptow *et al.* [1985], Luxton *et al.* [1984] and Willmarth *et al.* [1976]), the slope of the mean velocity profile in the logarithmic region decreases with increasing curvature and the profiles become negatively

curved. However, the dependence of the slope of the logarithmic region on the curvature is larger in the simulations than in experiments (Willmarth *et al.* [1976]). The difference seems to be associated with the flow regimes that were investigated by the various authors. Lueptow *et al.* (1985), for example, show that the slope of the logarithmic region does not change for small δ/a. This is not surprising because for small δ/a the curvature effects are limited to the outer part of the boundary layer in high Reynolds number flows. Based on the same measurements, Lueptow *et al.* (1985) also argued that the slope of the logarithmic region is not a function of a^+. The latter conclusion, however, is questionable because in those experiments a^+ is consistently large. These observations are in general agreement with the asymptotic analysis of the axisymmetric momentum equations in the limit of $\delta/a = O(1)$ and $a^+ \to \infty$ (Afzal & Narahsima [1976]). To lowest order in this limit, the axisymmetric boundary layer has both a logarithmic region and a outer velocity defect law. For smaller a^+ the parameters of the velocity profile in the two regions depends on both δ/a and a^+. The measurements of Luxton *et al.* (1984) for flows with larger δ/a than in the present simulations but with similar a^+ show logarithmic region slopes comparable to those reported here. The lack of consensus on this issue is summarized in the review of Lueptow (1988). A parametric study is necessary before a conclusion can be reached, but it seems that the slope of the logarithmic region is a function of both a^+ and δ/a when both the inner and outer layers are affected.

3.2 Turbulence Statistics

The statistical steady state is characterized by an equilibrium between the mean total stress and the applied streamwise pressure gradient. For the flows considered here this is expressed by

$$-\overline{uv} + \frac{1}{Re}\frac{d\overline{V}_z}{dr} = \rho u_\tau^2 \frac{a}{r}\frac{(a+\delta)^2 - r^2}{(a+\delta)^2 - a^2}. \tag{3.2.1}$$

Figure 3.2, shows the total stress (computed and analytical) for the present simulations. Note that the computed and analytical curves coincide in both simulations, indicating that the statistical steady state has been achieved.

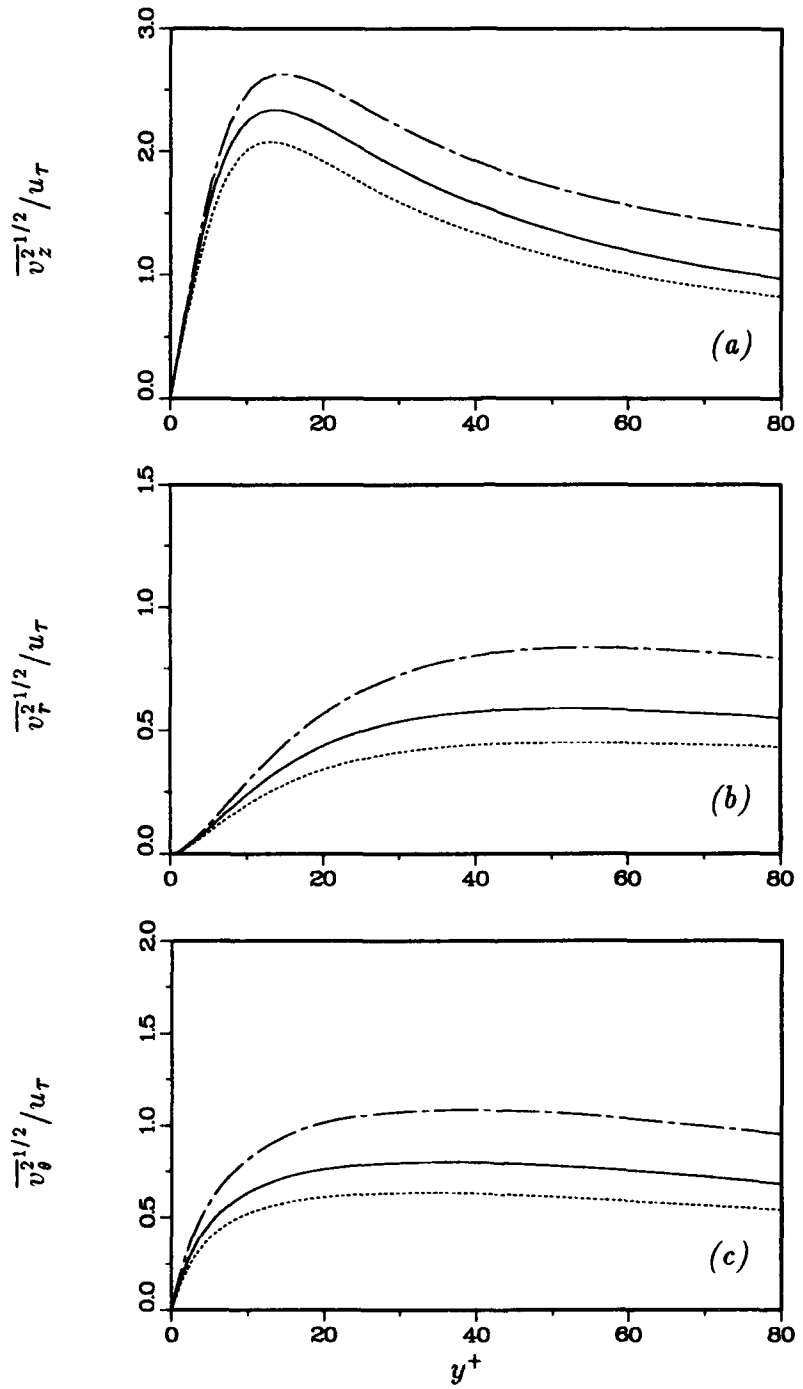

FIGURE 3.3 Root-mean-square velocity fluctuations normalized by u_τ: (a) Axial intensity, (b) Normal intensity, (c) Azimuthal intensity; ——— plane channel (Kim *et al.* [1987]); cylinders with —— $\delta/a = 5$ and ---- $\delta/a = 11$.

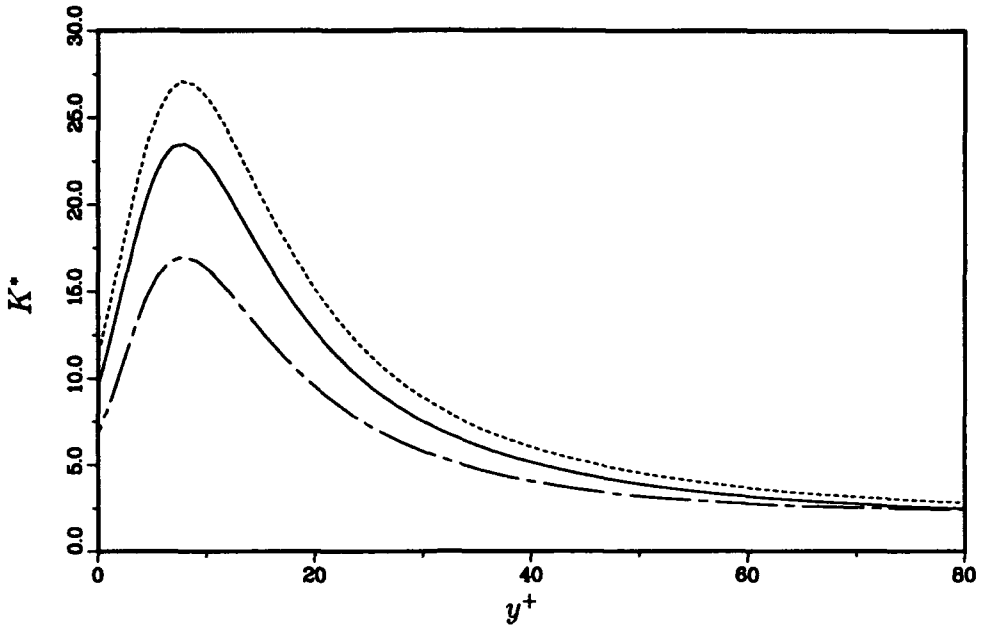

FIGURE 3.4 The energy partition parameter $K^* = 2\overline{v_z^2}/(\overline{v_r^2} + \overline{v_\theta^2})$: ——— plane channel (Lee *et al.* [1990]); cylinders with —— $\delta/a = 5$ and ---- $\delta/a = 11$.

3.2.1 Turbulence Intensities

The turbulence intensities normalized with the friction velocity decrease throughout the layer as the curvature increases (Figure 3.3). The streamwise component is the most energetic and the location of its maximum moves slightly towards the wall as the curvature increases. The smaller turbulent kinetic energy in the transversely curved flows can be attributed in part to the smaller surface area over which vorticity fluctuations can be generated relative to the volume of turbulent supported. The cylinder surface is apparently not less efficient as a source of turbulent kinetic energy; rather it has to supply a larger volume. This geometric difference is one of the reasons for the reduced intensity levels in the transversely curved flows. As the curvature increases the turbulence intensities in the outer part of the flow decrease in agreement with several experiments (Lueptow *et al.* [1985], Lueptow & Haritonidis [1987] and Luxton *et al.* [1984]). For experiments with comparable a^+, Luxton *et al.* [1984] report a maximum value of the streamwise intensity, $\overline{v_z^2}^{1/2}/U_\infty \approx 0.16$, similar to the simulation result of 0.15. However, for the larger a^+ experiments of Lueptow & Haritonidis (1987), the maximum value of $\overline{v_z^2}^{1/2}/u_\tau$ of 3.3 is higher than

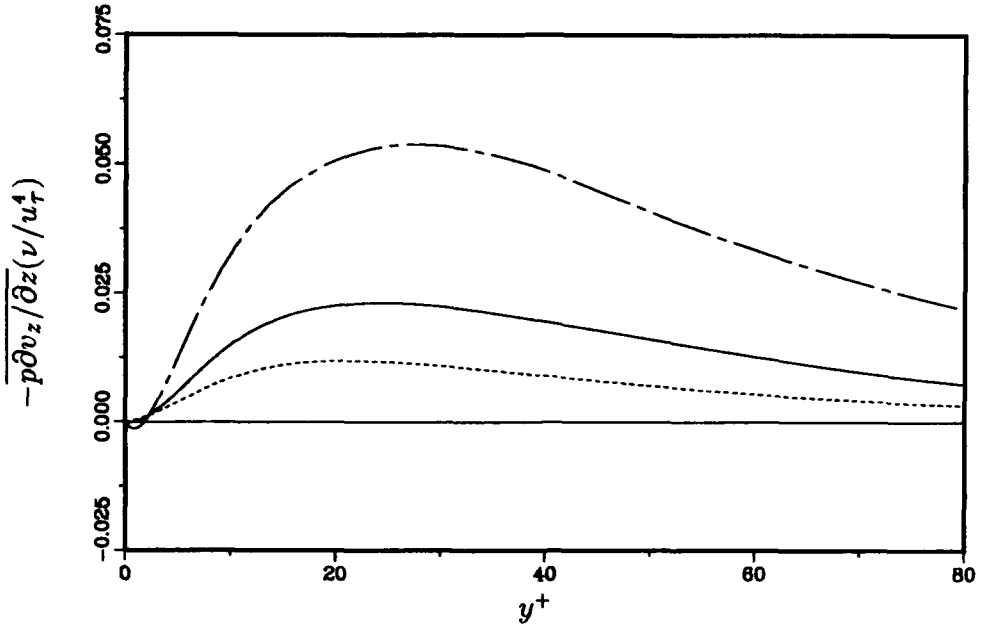

FIGURE 3.5 Pressure strain term of the streamwise intensity ($\overline{v_z{}^2}$) budget equation normalized ν and u_τ: cylinders with —— $\delta/a = 5$ and ---- $\delta/a = 11$; —·— plane channel (Mansour *et al.* [1988]).

in the flat plate, contrary to the simulation results. This may be due to the fact that in their flows a^+ is too large for there to be an inner layer curvature effect.

Similarly, the normal ($\overline{v_r^2}^{1/2}$) and azimuthal ($\overline{v_\theta^2}^{1/2}$) intensities are lower than in the planar case. However, the reductions in the normal and azimuthal intensities are greater than that of the axial intensity. The energy partition parameter (Lee *et al.* [1990]),

$$K^* = \frac{2\overline{v_z^2}}{\overline{v_r^2} + \overline{v_\theta^2}}, \tag{3.2.2}$$

shown in Figure 3.4, is a measure of the relative contributions to the turbulent kinetic energy of the streamwise turbulence intensity and the intensities normal to the mean flow. The attenuation of the normal and azimuthal velocity fluctuations is strongest for $y^+ < 30$ and increases with curvature.

Figure 3.4 suggests that the transfer of energy from the streamwise velocity component to the other two velocity components is strongly damped as the curvature increases. In the budget equations of the intensities (see Appendix **A**) it is the

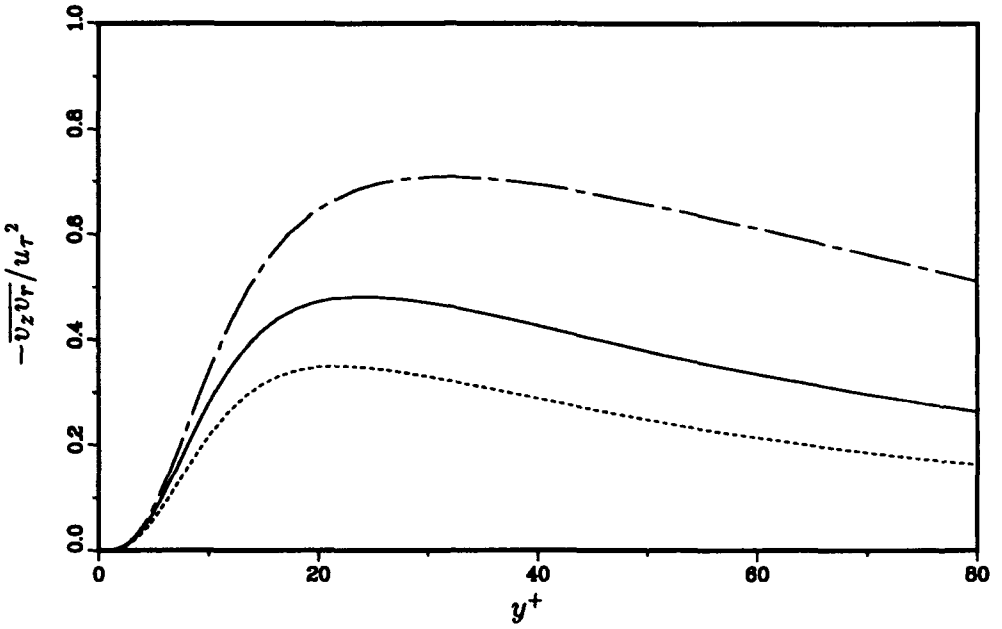

FIGURE 3.6 Reynolds shear stress normalized by u_τ: cylinders with —— $\delta/a = 5$ and ---- $\delta/a = 11$; —·— plane channel (Kim *et al.* [1987]).

pressure strain terms that are responsible for the intercomponent energy transfer. As shown in Figure 3.5, as the curvature increases, the pressure strain term of the budget equation for the streamwise intensity decreases significantly throughout the layer.

3.2.2 Reynolds Shear Stress

The Reynolds shear stress (Figure 3.6) is also reduced by curvature. The location of the maximum of the Reynolds shear stress profile is a function of δ/a and moves towards the wall with increasing curvature. However, this does not affect the position of the maximum in the production ($-\overline{v_z v_r} d\overline{V_z}/dy$) of turbulent kinetic energy ($y^+ \simeq 12$, see Figure 3.10 *b*). In the outer part of the layer the measurements of Lueptow *et al.* (1985) show that the Reynolds shear stress decreases with increasing curvature in agreement with the simulation results. In the inner layer, the measurements of the Reynolds shear stress reported by Lueptow *et al.* (1985) for the transversely curved flows do not differ appreciably from those of the planar case. In contrast with the present simulations the near-wall maximum of the

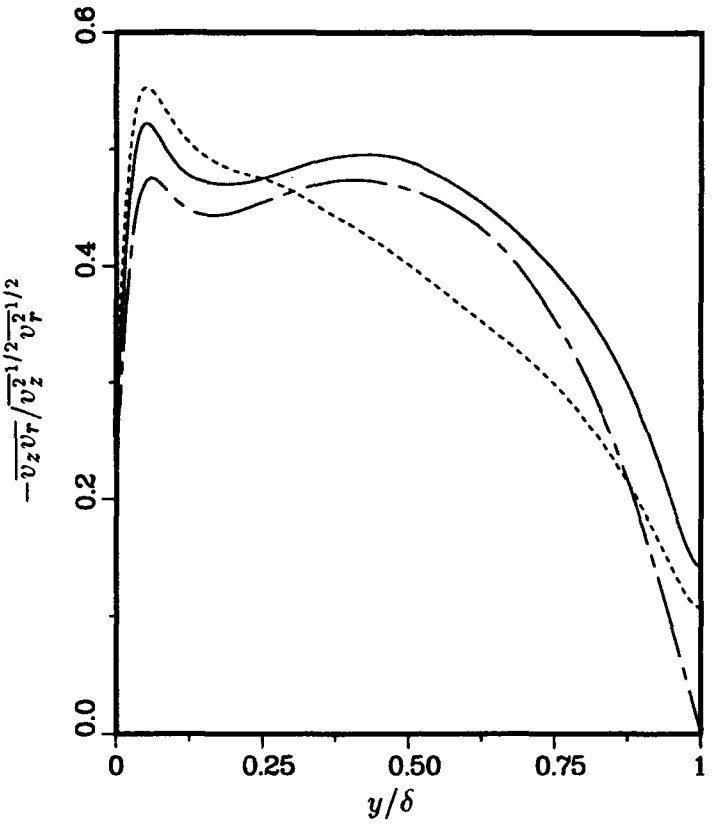

FIGURE 3.7 Correlation coefficient: cylinders with —— $\delta/a = 5$ and ---- $\delta/a = 11$; —·— plane channel (Kim *et al.* [1987]).

Reynolds shear stress ($-\overline{v_z v_r}/u_\tau^2$) reported by Leuptow *et al.* (1985) is about 0.8, similar to the plane channel result of Kim *et al.* (1987) (Figure 3.6).

The velocity correlation coefficient, shown in Figure 3.7, suggests that there are important differences both between the two transversely curved flows as well as between them and the plane channel. Close to the wall ($y/\delta < 0.2$), the streamwise and normal velocity fluctuations are increasingly better correlated as the curvature increases. Away from the wall, the large curvature case ($\delta/a = 11$) shows a significant reduction in the correlation coefficient. This may be an indication of flow stabilization, although for $\delta/a = 11$ the flow is a self sustaining turbulent flow and reaches statistically steady state.

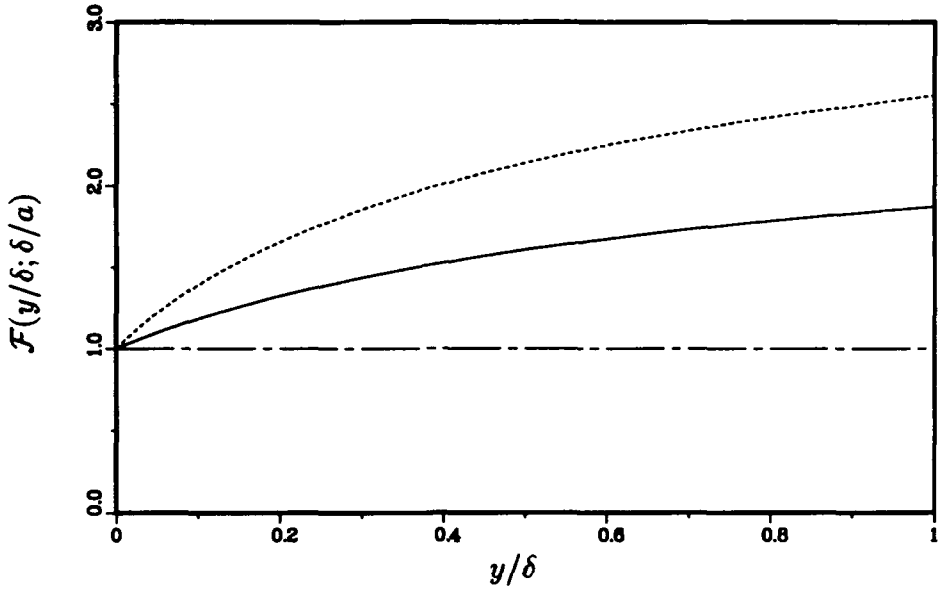

FIGURE 3.8 Velocity scaling function $\mathcal{F}(y/\delta;\delta/a)$: —·— plane channel ($\delta/a = 0$); cylinders with —— $\delta/a = 5$ and ---- $\delta/a = 11$.

3.2.3 Velocity Scaling

As a function of the distance to the wall the total stress (Equation 3.2.1) can be rewritten as

$$\tau = \rho u_\tau^2 \frac{a/\delta}{a/\delta + y/\delta}\left(1 + \frac{y/\delta}{1 + 2a/\delta}\right)(1 - y/\delta)\,. \tag{3.2.3}$$

In this form it can be easily compared with its planar counterpart

$$\tau = \rho u_\tau^2 (1 - y/\delta)\,, \tag{3.2.4}$$

which is a linear function of y/δ. These two expressions suggest the definition of a new velocity scale for the transversely curved flows

$$\underline{u} = u_\tau / \mathcal{F}(y/\delta;\delta/a), \tag{3.2.5}$$

where

$$\mathcal{F}(y/\delta;\delta/a) = \sqrt{\frac{a/\delta + y/\delta}{a/\delta}\left(1 + \frac{y/\delta}{1 + 2a/\delta}\right)^{-1}}\,. \tag{3.2.6}$$

Note that in the planar limit ($\delta/a \rightarrow 0$), $\mathcal{F}(y/\delta; \delta/a) \rightarrow 1$ and the planar velocity scale, $\underline{u} = u_\tau$, is recovered. Also, for small curvature ($\delta/a < 1$), $\mathcal{F} \approx 1$ throughout the layer, (Figure 3.8).

When scaled with $\underline{u}$, the turbulence intensities and Reynolds shear stress profiles of the two curved flows collapse (Figure 3.9 and Figure 3.10 *a*). The collapse with the plane channel stresses is also satisfactory except for the transverse turbulence intensity. Turbulence production and viscous dissipation apparently do not scale with $\underline{u}$ near the wall (Figure 3.10 *b* and 3.10 *c*).

3.3 Quadrant Analysis

The correlation coefficient profiles (Figure 3.6) suggest that the Reynolds shear stress producing events are strongly affected by curvature. In the transversely curved flows, the partition of the Reynolds shear stress among the four quadrants is very similar to that of the plane channel, as shown in Figure 3.11. It is a characteristic of wall bounded flows that the Reynolds shear stress is dominated by the second quadrant events ($v_z < 0$ and $v_r > 0$) in the outer layer, and by the fourth quadrant events ($v_z > 0$ and $v_r < 0$) in the inner layer. The crossover point between the domains of second and fourth quadrant events occurs at the same distance from the wall ($y^+ \simeq 12$) as in the plane channel.

The fractional contributions to each of the quadrants of the Reynolds shear stress are shown in Figures 3.12 and 3.13 for $\delta/a = 5$ and $\delta/a = 11$, respectively. At a given distance from the wall, the fractional contributions of each of the quadrants to the Reynolds shear stress in the transversely curved flows are similar to the corresponding fractional Reynolds shear stress contributions in the plane channel (Kim *et al.* [1987]). This invariance of the fractional contributions with curvature means that Reynolds shear stress events of any intensity contribute the same fraction of the total Reynolds shear stress in the transversely curved flows as in the plane channel. This is contrary to the measurements of Lueptow & Haritonidis (1987), who found that, in transversely curved flows, low intensity Reynolds shear stress events accounted for a larger percentage of the total Reynolds shear stress than in the planar case.

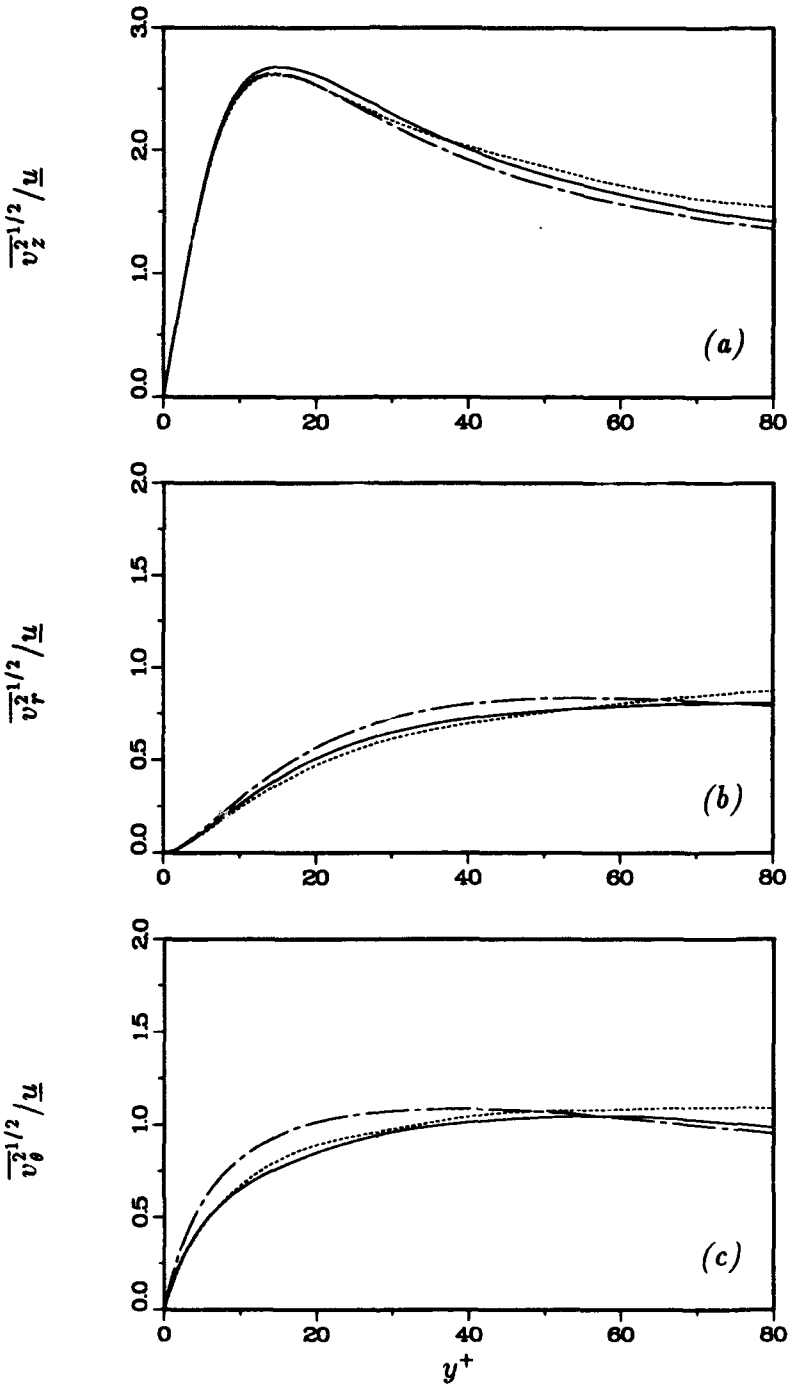

FIGURE 3.9 Root-mean-square velocity fluctuations normalized by $\underline{u}$: (a) Axial intensity, (b) Normal intensity, (c) Azimuthal intensity; —·— plane channel (Kim *et al.* [1987]); cylinders with —— $\delta/a = 5$ and ---- $\delta/a = 11$.

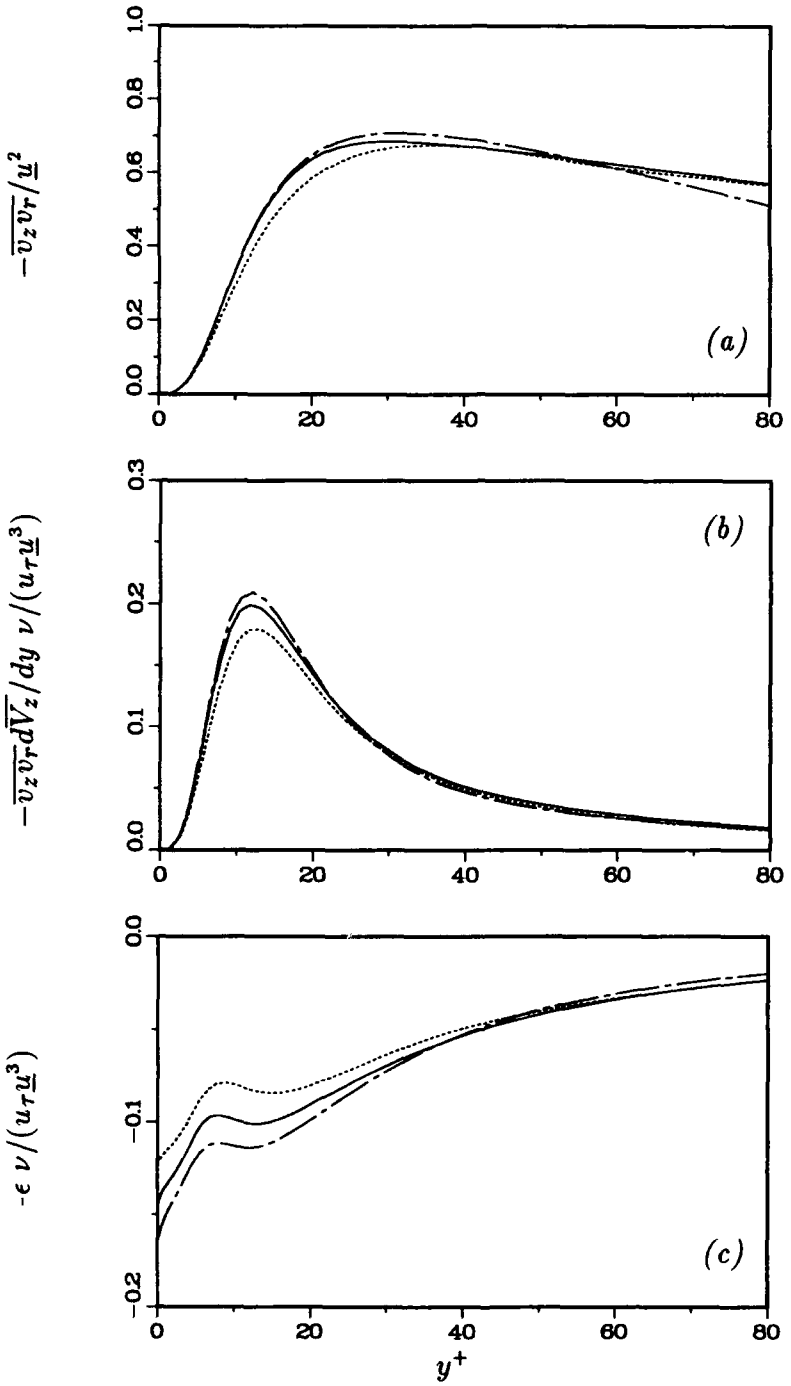

FIGURE 3.10 Reynolds shear stress (a), Production (b) and dissipation (c) of turbulent kinetic energy normalized by ν and $\underline{u}$: cylinders with —— $\delta/a = 5$ and ---- $\delta/a = 11$; —·— plane channel (Mansour *et al.* [1988]).

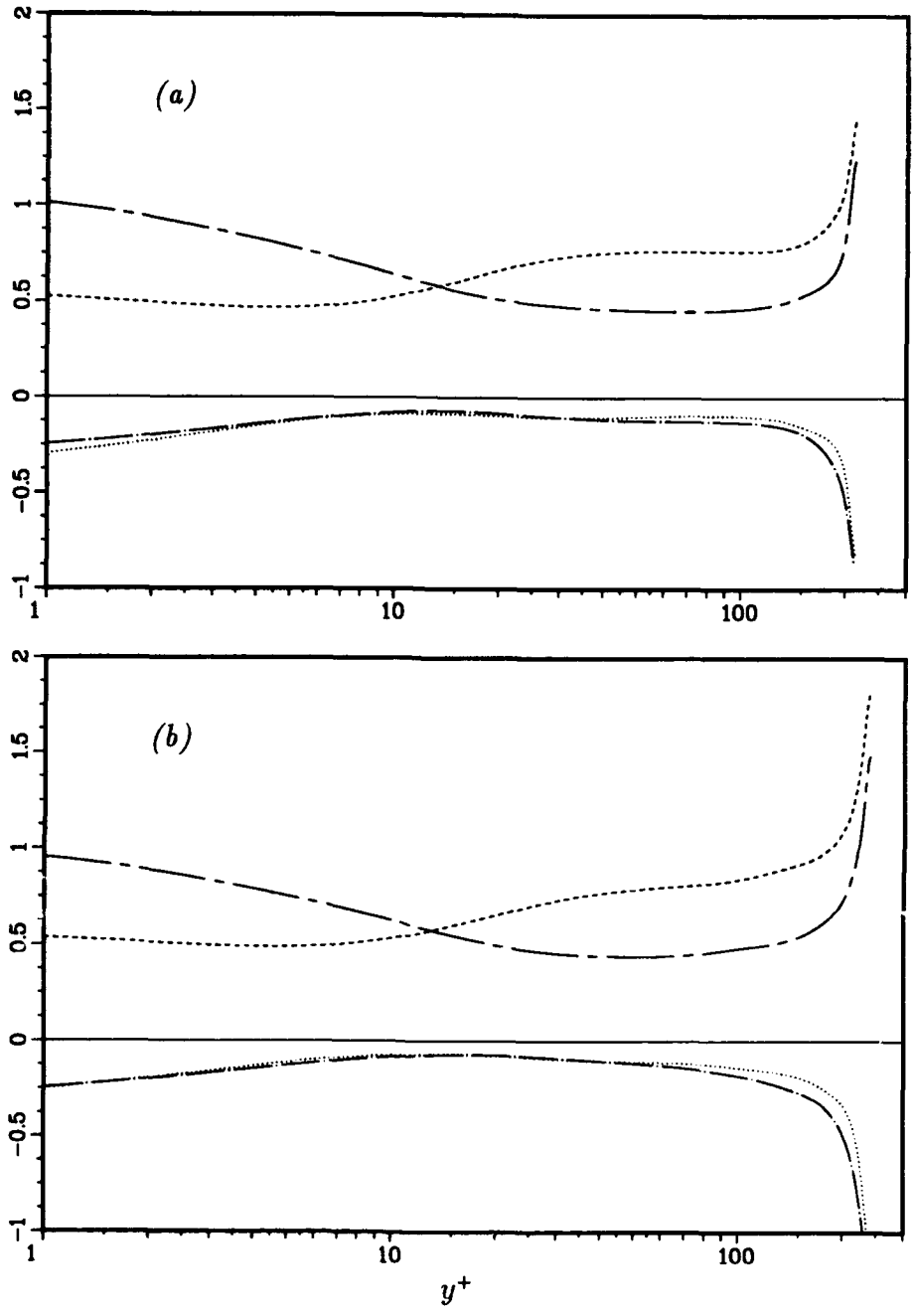

FIGURE 3.11 Reynolds shear stress for each quadrant normalized by the mean Reynolds shear stress: (*a*) $\delta/a = 5$, (*b*) $\delta/a = 11$: ····· first; ---- second; —·— third; —·— fourth quadrant.

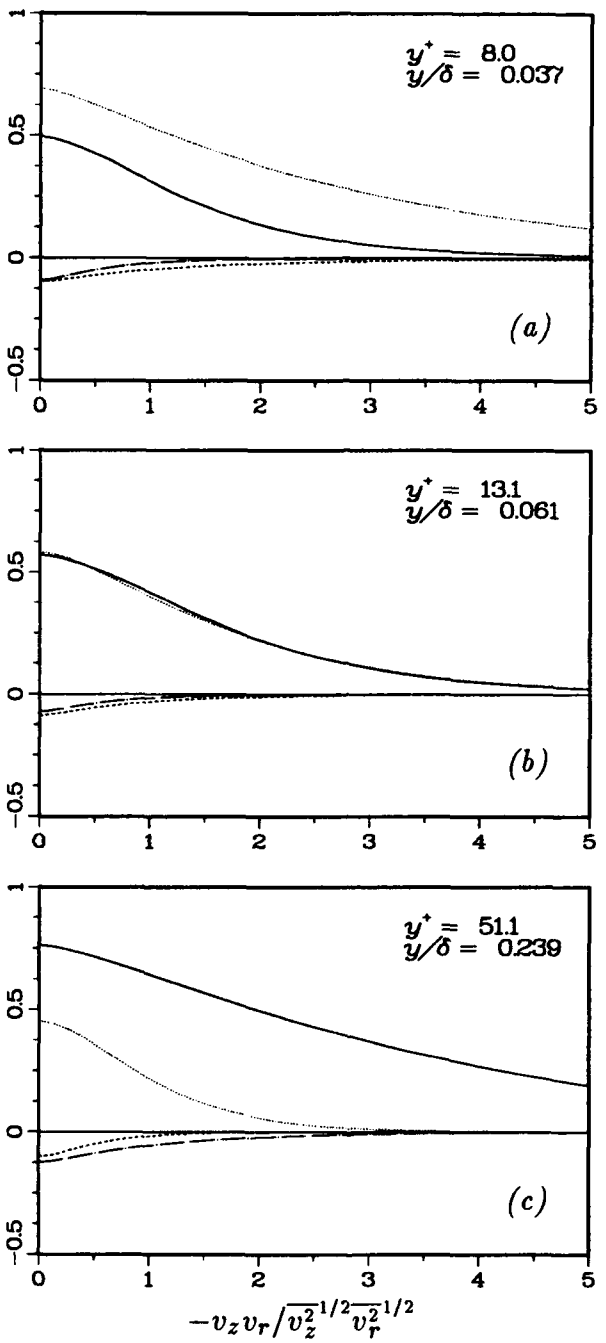

FIGURE 3.12 Fractional contribution to $-\overline{v_z v_r}$ from each quadrant as a function of threshold for $\delta/a = 5$; ---- first; —— second; —·— third; ····· fourth quadrants: (*a*) $y^+ = 8$ (*b*) $y^+ = 13.1$ (*c*) $y^+ = 51.1$.

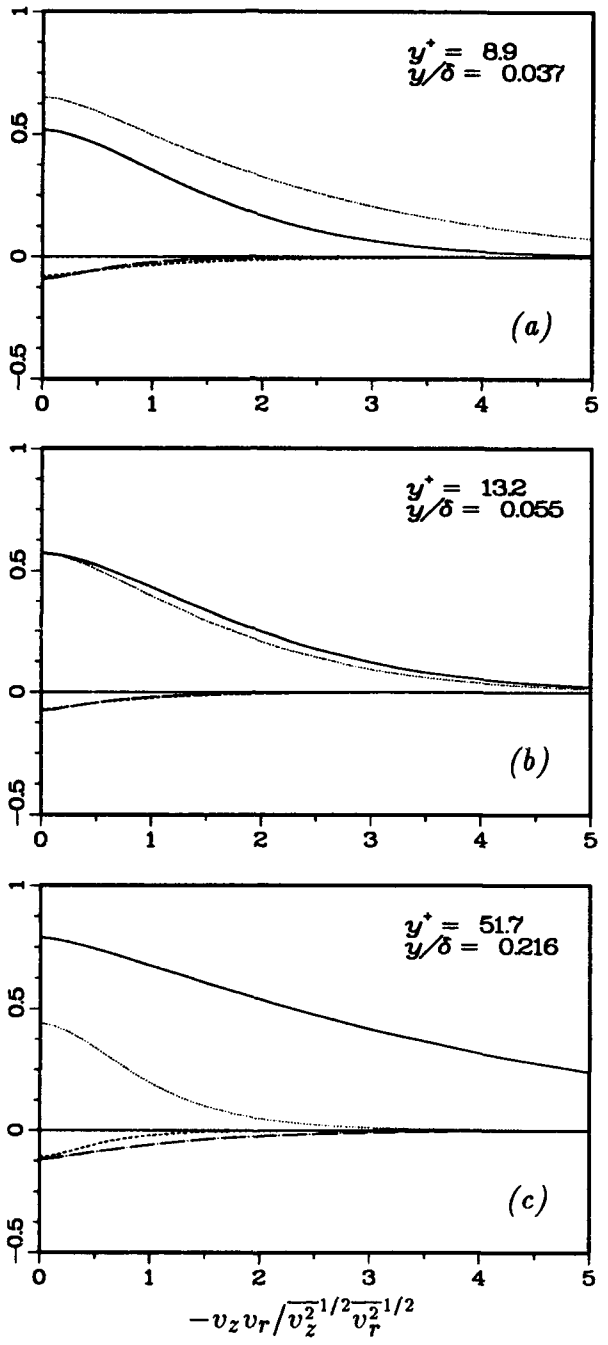

FIGURE 3.13 Fractional contribution to $-\overline{v_z v_r}$ from each quadrant as a function of threshold for $\delta/a = 11$:---- first; —— second; —·— third; ····· fourth quadrants: (*a*) $y^+ = 8.9$ (*b*) $y^+ = 13.2$ (*c*) $y^+ = 51.7$.

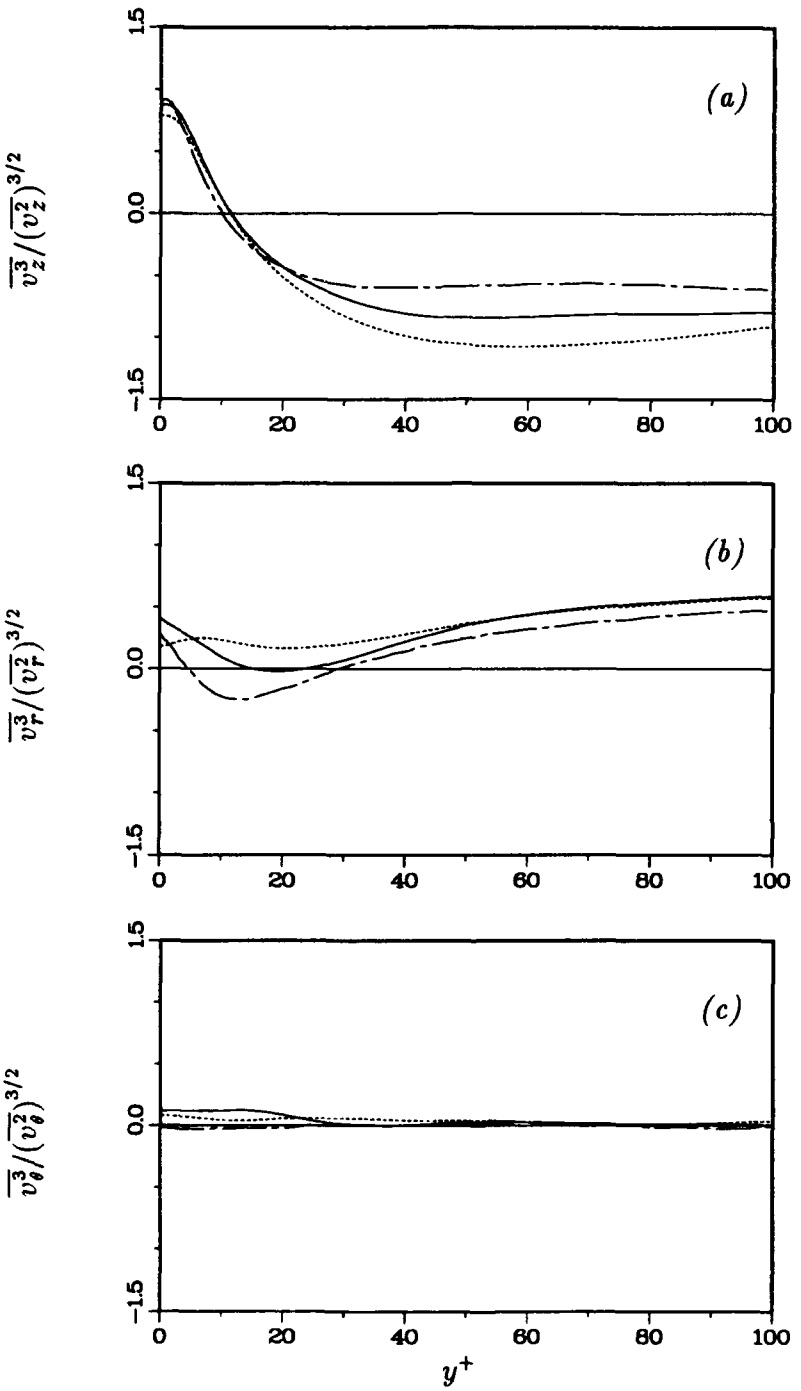

FIGURE 3.14 Skewness profiles of the velocity fluctuations: (*a*) $S(v_z)$, (*b*) $S(v_r)$, (*c*) $S(v_\theta)$; —·— plane channel (Kim *et al.* [1987]); cylinders with —— $\delta/a = 5$ and ---- $\delta/a = 11$.

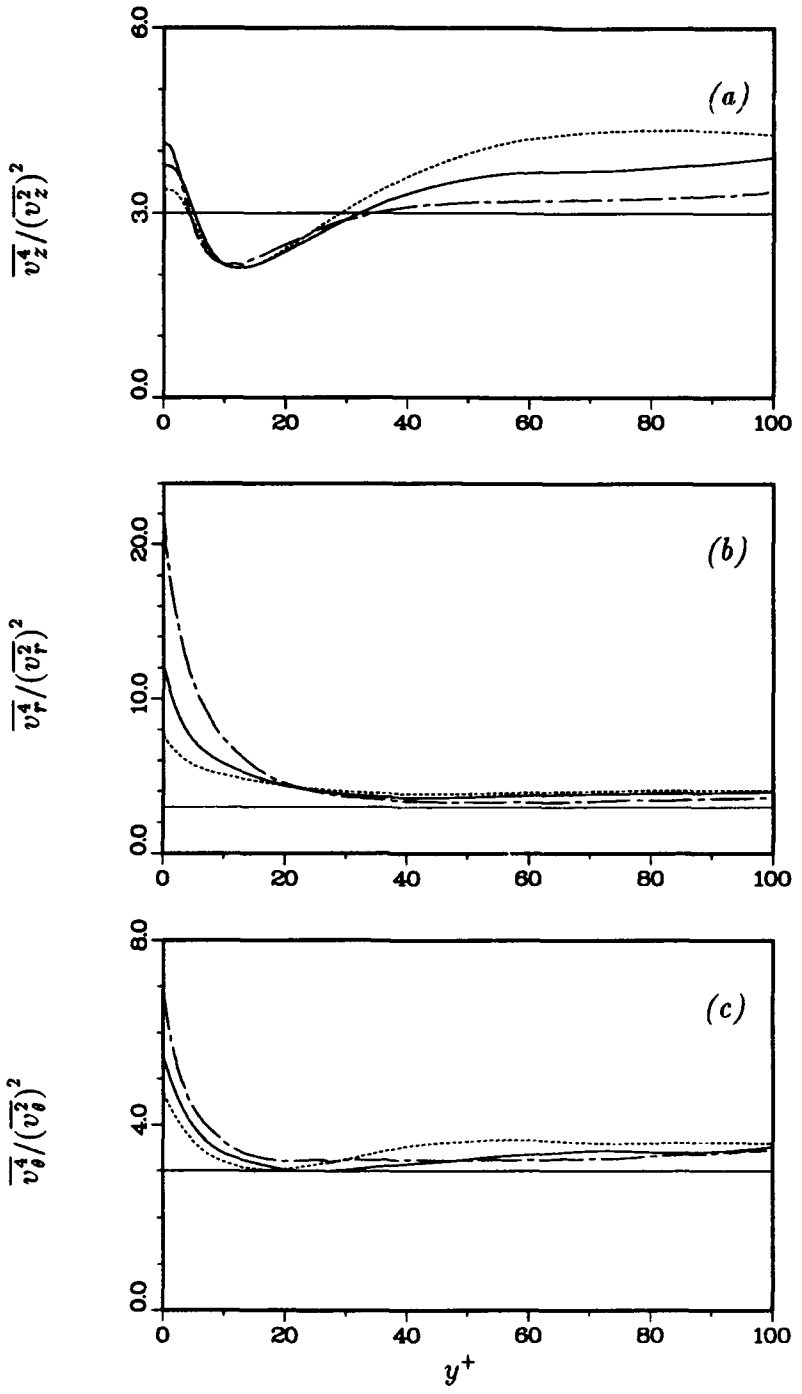

FIGURE 3.15 Flatness profiles of the velocity fluctuations: (*a*) $F(v_z)$, (*b*) $F(v_r)$, (*c*) $F(v_\theta)$; ——— plane channel (Kim *et al.* [1987]); cylinders with —— $\delta/a = 5$ and ---- $\delta/a = 11$.

The skewness factors of the velocity fluctuations, shown in Figure 3.14, indicate that there is a strong effect of the curvature on the streamwise and normal velocity fluctuations. As expected from the reflective symmetry of the Navier-Stokes equations, the skewness of v_θ is nearly zero everywhere. Deviations from zero are attributed to an inadequate statistical sample.

Away from the wall ($y^+ > 40$), the skewness of v_r is positive and increases slightly with increasing curvature, as was also observed by Luxton *et al.* (1984). In this region there are also strong negative streamwise velocity fluctuations, as denoted by the negative skewness of v_z, which decreases with increasing curvature.

Increasing the curvature does not significantly affect the skewness of the axial fluctuations (v_z) close to the wall ($y^+ < 20$). On the other hand, for $y^+ < 30$, there are significant differences in the skewness of the normal velocity fluctuations (v_r) between the three flows. While in the plane channel for $5 < y^+ < 30$ the skewness of v_r is negative, in the transversely curved flows the region of negative skewness diminishes and, for $\delta/a = 11$, the skewness of v_r is positive throughout the layer. For $y^+ < 12$, where fourth quadrant events dominate the Reynolds stress, the skewness of v_z is positive.

The flatness profiles of the velocity fluctuations are shown in Figure 3.15. Near the wall ($y^+ < 20$), the flatness of v_r and v_θ decrease sharply with increasing curvature. The flatness of v_z also decreases in the near-wall region ($y^+ < 5$). For $5 < y^+ < 30$ the flatness of v_z is not affected by the curvature and away from the wall ($y^+ > 30$) it increases with increasing curvature.

3.4 The Vorticity

In cylindrical coordinates the vorticity components are given by (see for example Batchelor [1967])

$$\begin{aligned}
\Omega_z &= \frac{1}{r}\left(\frac{\partial(rV_\theta)}{\partial r} - \frac{\partial V_r}{\partial \theta}\right), \\
\Omega_r &= \frac{1}{r}\frac{\partial V_z}{\partial \theta} - \frac{\partial V_\theta}{\partial z}, \\
\Omega_\theta &= \frac{\partial V_r}{\partial z} - \frac{\partial V_z}{\partial r}.
\end{aligned} \tag{3.4.1}$$

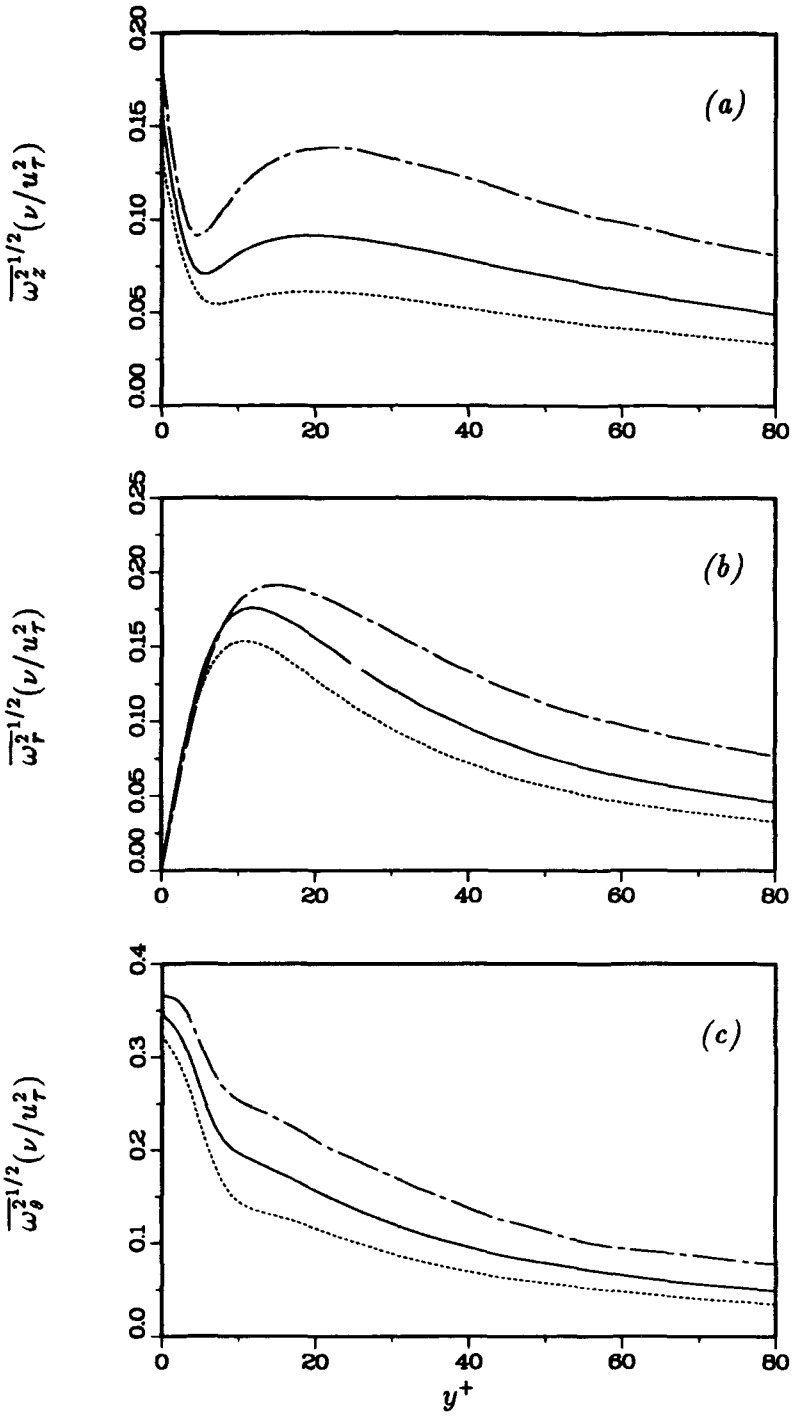

FIGURE 3.16 Root-mean-square vorticity fluctuations normalized by ν and u_τ: (a) Axial intensity, (b) Normal intensity, (c) Azimuthal intensity; ——— plane channel (Kim *et al.* [1987]); cylinders with —— $\delta/a = 5$ and ---- $\delta/a = 11$.

δ/a	0	5	11
r_e^+	16.7	13.8	13.5
y_{max}^+	21.0	19.7	20.1
v_e^+	2.31	1.26	0.83
γ^+	0.139	0.092	0.061
Re_Γ	242.6	110.0	70.2

Table 3.3 Streamwise vortex parameters

The vorticity intensities normalized by the mean wall shear stress, shown in Figure 3.16, decrease with increasing curvature. Unlike the velocity intensities, the vorticity intensities do not collapse in the outer part of the layer when scaled with the velocity scale $\underline{u}$. As in the plane channel, the axial vorticity intensity exhibits a near-wall local minimum and local maximum. Kim *et al.* (1987) linked the locations and intensity of these extrema to the average position and strength of the near-wall streamwise vortices. In their Rankine vortex model, the mean radius is estimated from the difference in the positions of the two extrema (y_{max}^+, y_{min}^+)

$$r_e^+ = y_{max}^+ - y_{min}^+. \qquad (3.4.2\ a)$$

The maximum value of the streamwise vorticity intensity is an estimate of the strength (γ) of the Rankine vortex, and the tangential velocity at the edge of the vortex is given by

$$v_e^+ = \gamma^+ r_e^+. \qquad (3.4.2\ b)$$

The location of the maximum of the streamwise intensity (y_{max}^+) is an estimate of the mean position of the center of the vortex core. From the circulation of the near-wall Rankine vortex

$$\Gamma = \int_0^{2\pi} v_e r_e d\theta, \qquad (3.4.2\ c)$$

a vortex circulation Reynolds number can be defined by

$$Re_\Gamma = \frac{\Gamma}{\nu} = 2\pi v_e^+ r_e^+. \qquad (3.4.2\ d)$$

These parameters of the near-wall streamwise vortices are listed in Table 3.3 for the two transversely curved flows as well as the plane channel flow of Kim *et al.* (1987). It is noteworthy that neither the core radius nor the position of the center of these vortices changes appreciably with curvature, even though the strength of the Rankine vortex is greatly reduced.

There are other important curvature effects on the vorticity intensities. Near the wall ($y^+ < 7$), the normal vorticity intensity ($\overline{\omega_r^2}^{1/2}$) is virtually unaffected by the curvature, while the other vorticity components decrease. In the outer part of the flow $\overline{\omega_r^2}^{1/2} \approx \overline{\omega_z^2}^{1/2}$ as shown in Figure 3.17.

The inclination of the projection of the vorticity vector in (r, z)-planes is given by

$$\Theta_{rz} = tan^{-1}\left(\frac{\omega_r}{\omega_z}\right). \qquad (3.4.3)$$

The probability density functions (p.d.f.s) of Θ_{rz}, weighted by the magnitude of the the projected vorticity vector (Moin & Kim [1985]), $(\omega_r^2 + \omega_z^2)/< \omega_r^2 + \omega_z^2 >$, are shown in Figures 3.18 *a* and 3.18 *b*. In the expression above, $<>$ indicates the mean of the quantity inside the brackets taken on the corresponding (z, θ) cylindrical surface. The following discussion refers to the weighted p.d.f.s, even though all the features described below are also evident in the unweighted p.d.f.s. The advantage of the weighting is that it enhances the contributions of the strong vorticity fluctuations.

Throughout the discussion of the orientation of the vorticity vector, the reader should bear in mind that the plane channel flow fields to which these results are compared were from the large eddy simulation of Moin & Kim (1985), which was performed for a Reynolds number of 13800 (based on the centerline velocity and δ). At the closest point to the wall ($y^+ \approx 4$) investigated by Moin & Kim (1985), the distribution of Θ_{rz} is centered around 0^o and $\pm 180^o$ since the normal vorticity must go to zero at the wall due to no-slip. In the transversely curved flows, this effect is not discernable in the histograms of Θ_{rz} for $y^+ > 2$. At $y^+ \approx 4$, both

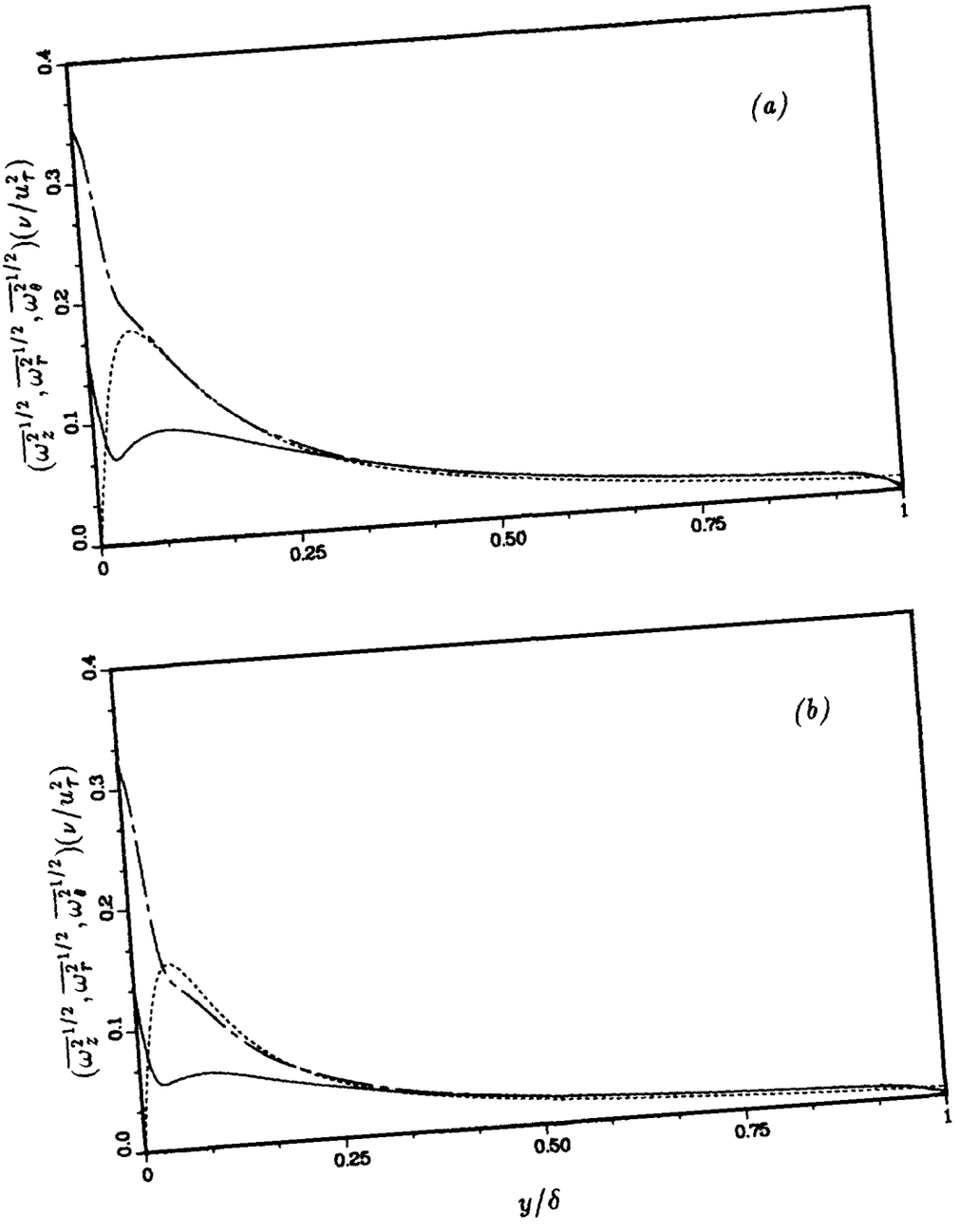

FIGURE 3.17 Root-mean-square vorticity fluctuations normalized by ν and u_τ in global coordinates for (*a*) $\delta/a = 5$ and (*b*) $\delta/a = 11$: —— Axial intensity; ---- Azimuthal intensity; –·–· Normal intensity.

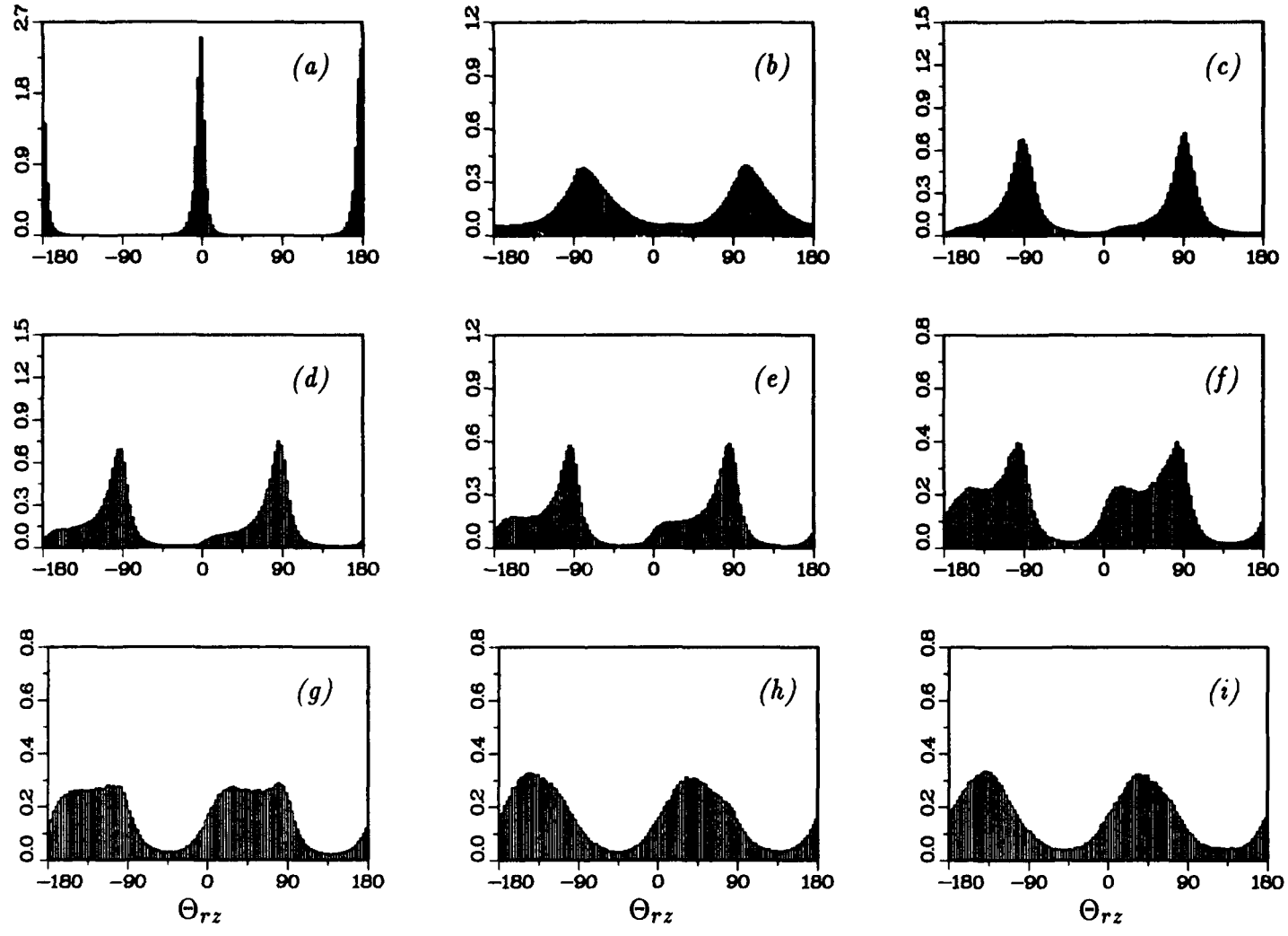

FIGURE 3.18 *a* Distribution of the inclination of the angle, Θ_{rz}, of the projection of the vorticity vectors in (r, z)-planes for $\delta/a = 5.0$; data weighted with the magnitude of the projected vorticity. (*a*) $y^+ = 0.66$; (*b*) $y^+ = 4.10$; (*c*) $y^+ = 8.02$; (*d*) $y^+ = 16.31$; (*e*) $y^+ = 25.38$; (*f*) $y^+ = 38.76$; (*g*) $y^+ = 51.85$; (*h*) $y^+ = 69.66$; (*i*) $y^+ = 96.25$.

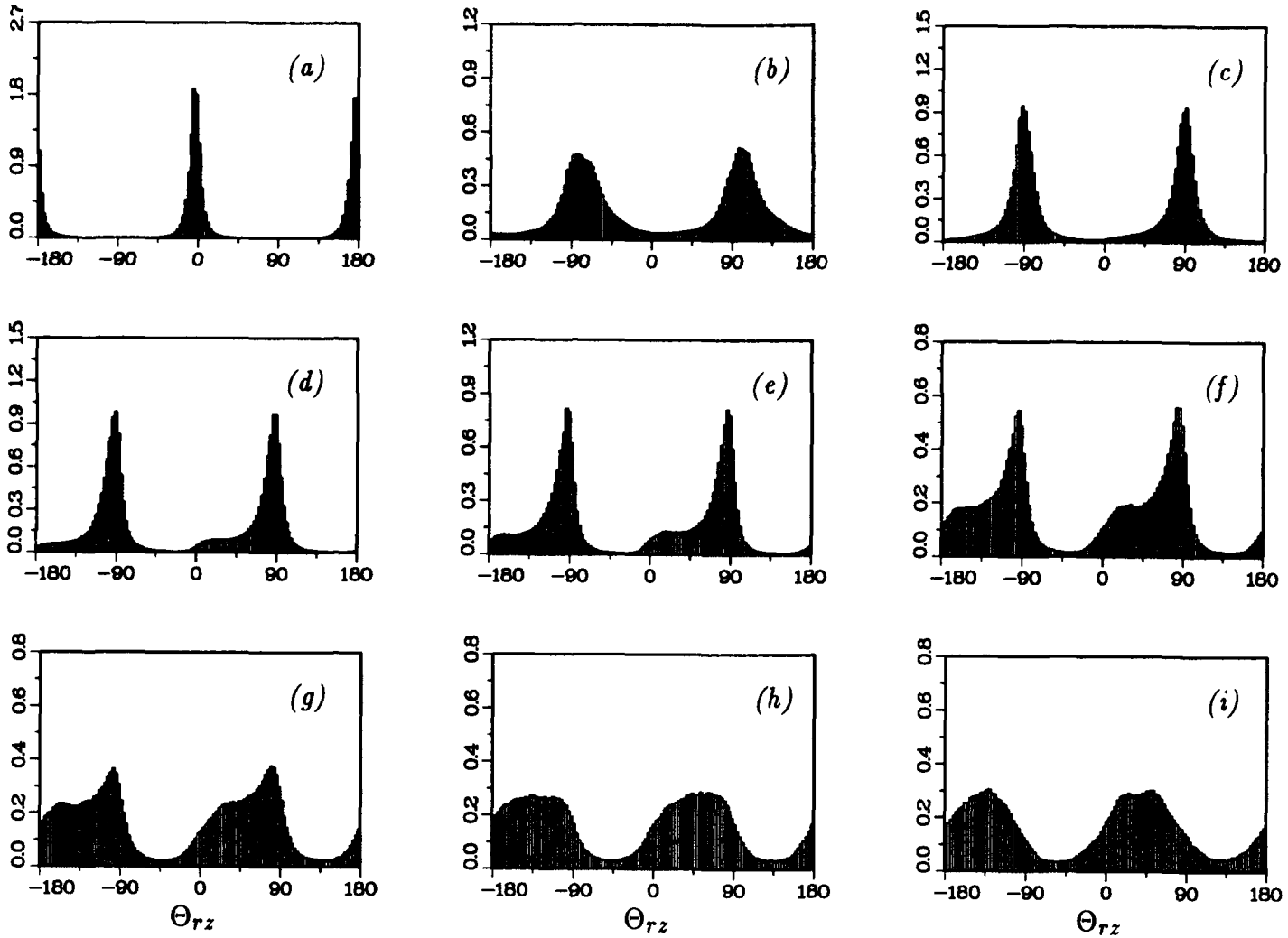

FIGURE 3.18 *b* Distribution of the inclination of the angle, Θ_{rz}, of the projection of the vorticity vectors in (r, z)-planes for $\delta/a = 11.0$; data weighted with the magnitude of the projected vorticity. (*a*) $y^+ = 0.72$; (*b*) $y^+ = 4.46$; (*c*) $y^+ = 8.74$; (*d*) $y^+ = 17.77$; (*e*) $y^+ = 27.66$; (*f*) $y^+ = 42.24$; (*g*) $y^+ = 56.52$; (*h*) $y^+ = 75.96$; (*i*) $y^+ = 104.90$.

curved flows have distributions of Θ_{rz} that peak around $\pm 90^o$. This distribution of Θ_{rz} persists up to $y^+ \approx 25$ in the $\delta/a = 5$ flow and up to $y^+ \approx 40$ in the $\delta/a = 11$ flow. Father from the wall, the the distributions gradually broaden, and by $y^+ \approx 52$ in the $\delta/a = 5$ flow and $y^+ \approx 75$ in the $\delta/a = 11$ the peak shifts to -135^o and 45^o as was observed by Moin & Kim (1985). It is only beyond these points, which is most of the domain, that the concentration of the distributions of Θ_{rz} shift to the -135^o and 45^o orientations.

In Moin & Kim (1985) the main mechanism of vorticity stretching in the plane channel was attributed to stretching by the mean shear, which has its principal axis at 45^o with the direction of the mean flow. They also pointed out that, according to Deissler (1969), when the normal and streamwise vorticity intensities are equal, the direction of the maximum vorticity in a shear flow is at 45^o to the mean flow. In the transversely curved flows there is an increasingly thicker layer around the cylinder, in which the vorticity has the $\pm 90^o$ orientation. This suggests that, as the curvature increases, vortical structures inclined at 45^o to the mean flow are probably more difficult to observe.

3.5 Instantaneous Turbulent Flow Structures

Contours of the streamwise velocity fluctuations (v_z) on two (r, θ) planes (normal to the mean flow) are shown in Figures 3.19 (plane I_z) and 3.20 (plane II_z). In the smaller curvature case ($\delta/a = 5$, see Figures 3.19 *a* and 3.20 *a*), the perimeter of the cylinder is about 270 wall units and in the snap shots shown only three to four low-speed streaks are observed around the cylinder. In the strongly curved case ($\delta/a = 11$, see Figures 3.19 *b* and 3.20 *b*), the perimeter of about 140 wall units apparently can only support two low-speed streaks. A better measure of the mean spacing between the low-speed streaks is given by the velocity correlations in the azimuthal direction at $y^+ \approx 12$, shown in Figure 3.21. The mean streak spacing is about 100 wall units in both flows at this radial location. Note however that the mean streak spacing has a nearly linear dependence on the distance from the wall (y^+) with a slope that increases with curvature (Figure 3.22).

Figures 3.23 and 3.24 show contours of the radial (wall-normal) velocity fluctuations in the same planes as Figures 3.19 and 3.20 respectively. The constraint imposed by the outer boundary conditions (Equation 2.1.5 *b*) on the radial motion

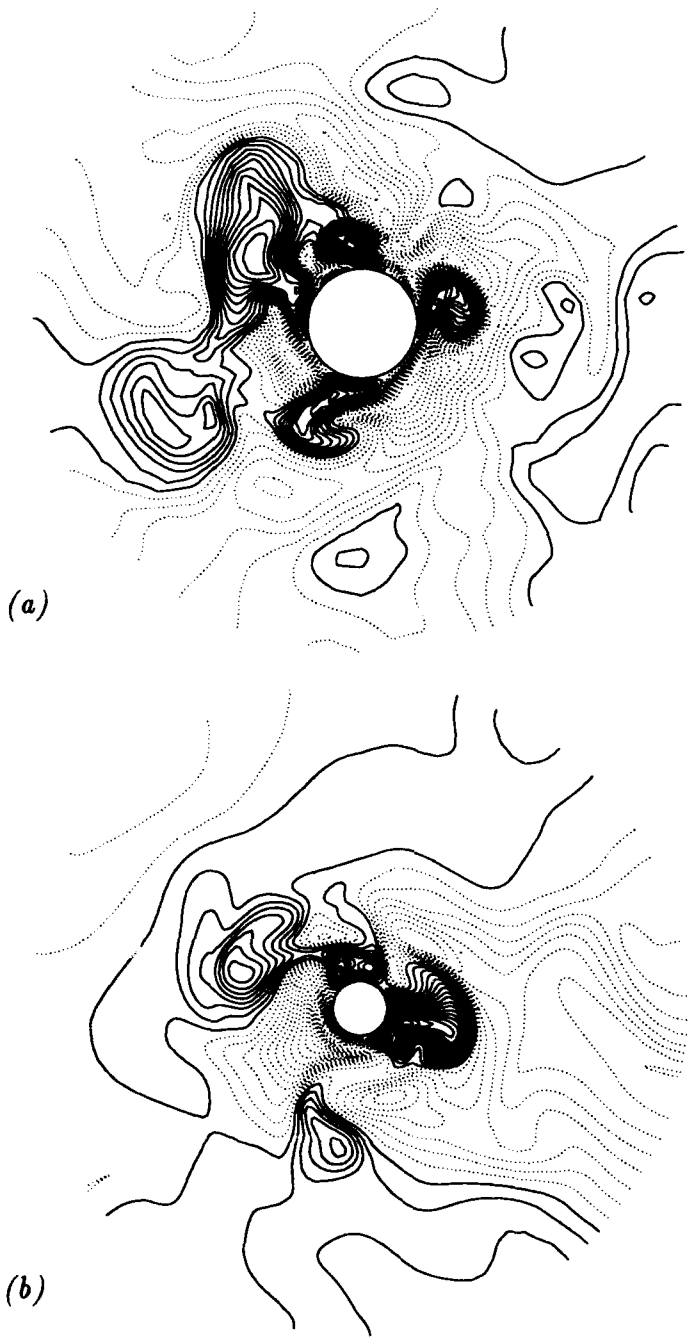

FIGURE 3.19 Contours of axial velocity fluctuations (v_z), normalized by u_τ, on a plane (I_z) normal to the mean velocity: (a) $\delta/a = 5$ with contour levels from -5.2 u_τ to 3.55 u_τ; (b) $\delta/a = 11$ with contour levels from -4.95 u_τ to 4.05 u_τ. The contour increments of 0.25 u_τ. The solid contours denote the low-speed fluctuations ($v_z < 0$) and the dotted contours denote the high-speed fluctuations ($v_z > 0$).

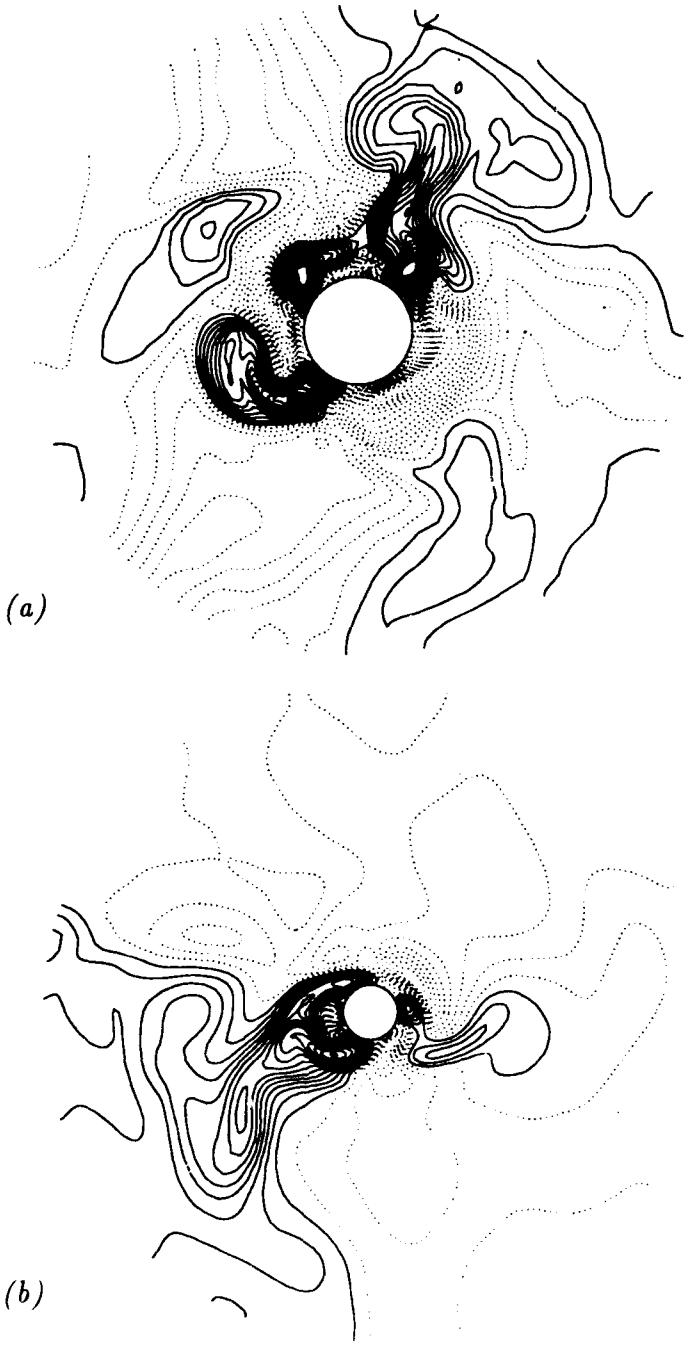

FIGURE 3.20 Contours of axial velocity fluctuations (v_z), normalized by u_τ, on a plane (II_z) normal to the mean velocity: (a) $\delta/a = 5$ with contour levels from -5.2 u_τ to 3.3 u_τ; (b) $\delta/a = 11$ with contour levels from -4.2 u_τ to 3.3 u_τ. The contour increment is 0.25 u_τ. The solid contours denote the low-speed fluctuations ($v_z < 0$) and the dotted contours denote the high-speed fluctuations ($v_z > 0$).

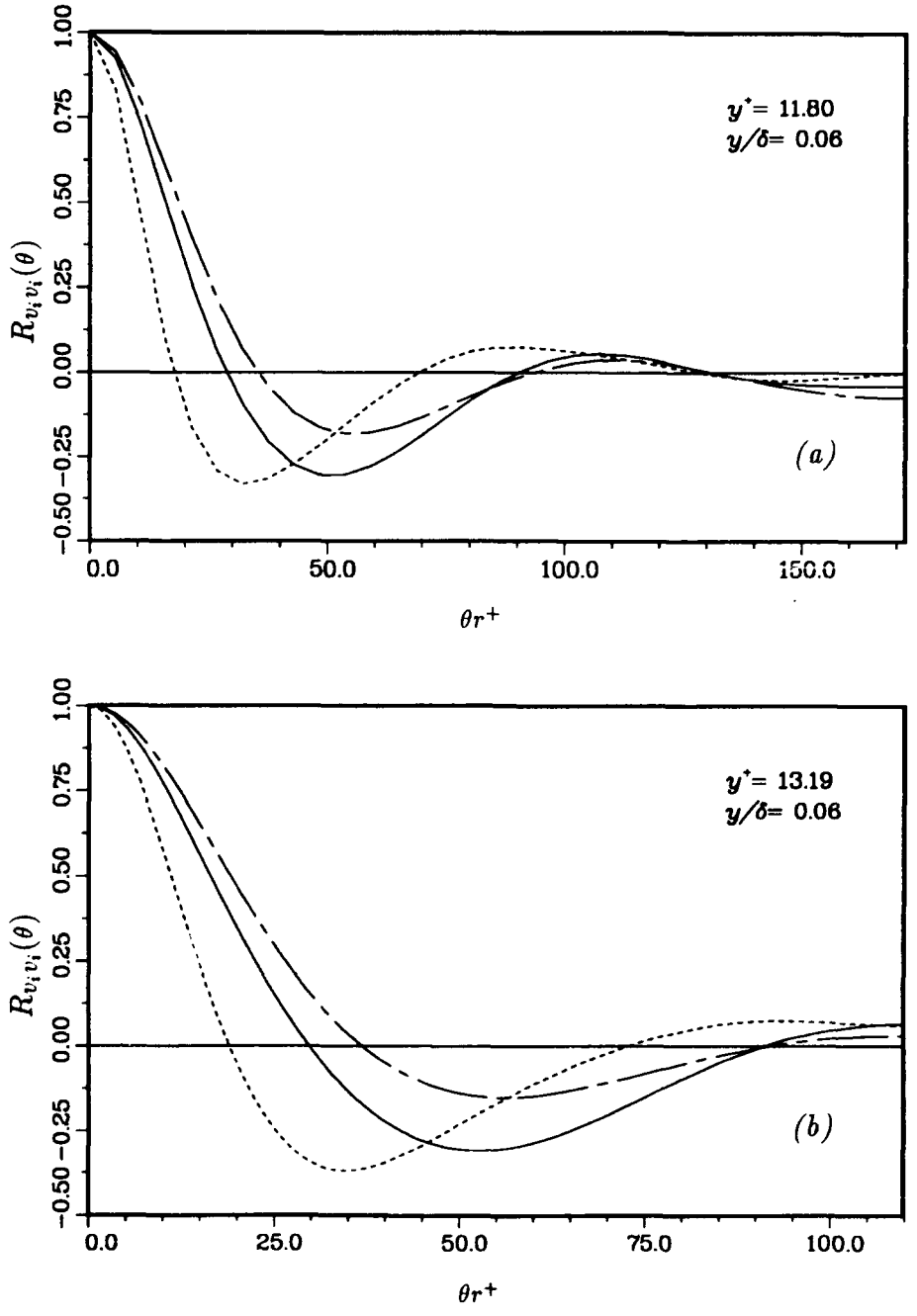

FIGURE 3.21 Azimuthal two-point correlations of the velocity fluctuations for (a) $\delta/a = 5.0$ and for (b) $\delta/a = 11$: —— $R_{v_z v_z}$, ---- $R_{v_r v_r}$, —·— $R_{v_\theta v_\theta}$.

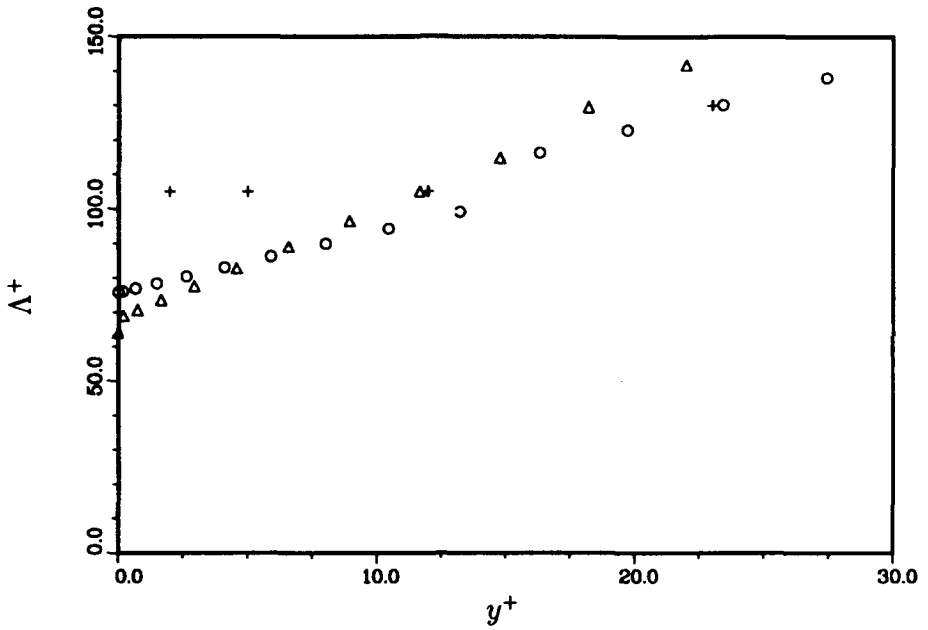

FIGURE 3.22 The mean spanwise streak spacing Λ^+ estimated from the two-point correlations of v_z: + plane channel (Kim *et al.* [1987]); cylinders: o, for $\delta/a = 5$ and Δ , for $\delta/a = 11$.

of structures in the outer part of the layer is evident particularly in the $\delta/a = 5$ flow (Figures 3.23 *a* and 3.24 *a*). From the contour plots of v_z and v_r, regions of sweep and ejection of fluid to and away from the cylinder surface can be easily identified.

In simulations of homogeneous turbulence with a small shear rate, Rogers & Moin (1987) showed that, even though the contours of the streamwsie velocity fluctuations tend to be elongated in the streamwise direction, no streaky structures were observed. In studies of homogeneous turbulence at a high shear rate, Lee *et al.* (1990) observed long streaks in the absence of a no-slip wall, and concluded that it is the magnitude of the mean shear rate that determines whether streaks are observed. These two studies suggest that the streamwise extent of the streaks is controlled by the mean shear. A measure of the strength of the mean shear is the shear rate parameter (Lee *et al.* [1990])

$$S^* = \frac{2Sq^2}{\epsilon}, \tag{3.5.1}$$

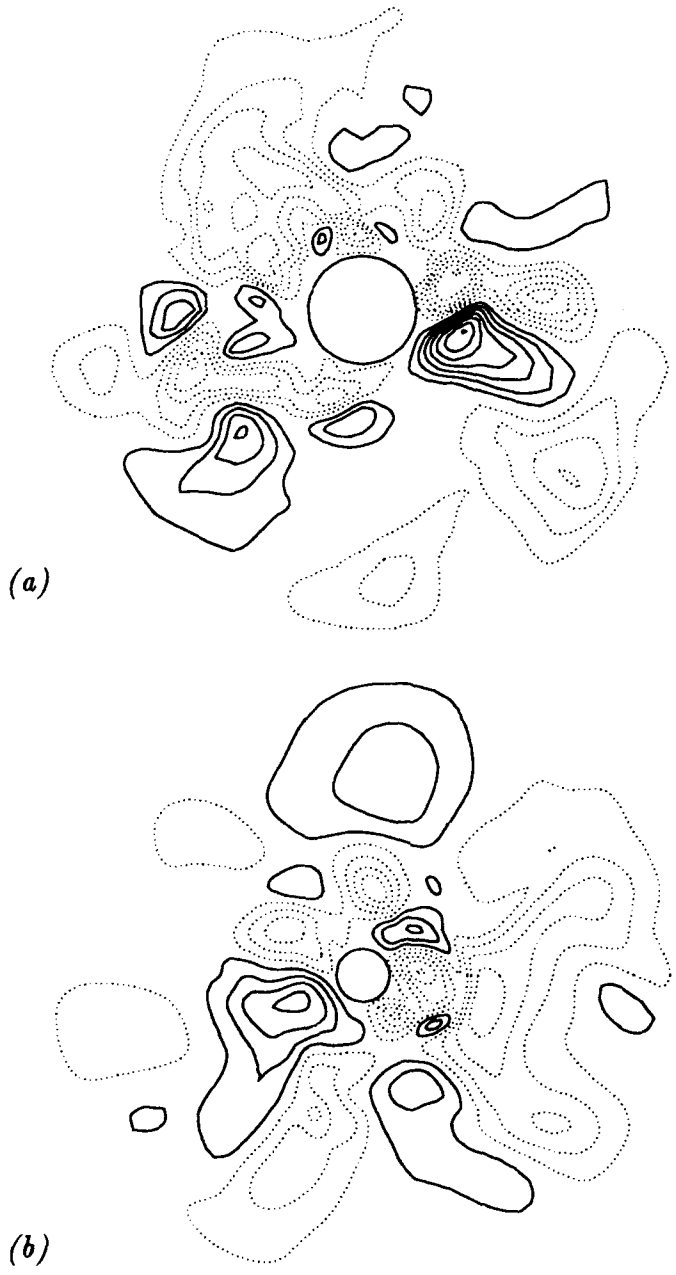

FIGURE 3.23 Contours of radial (wall-normal) velocity fluctuations (v_r), normalized by u_τ, on a plane (I_z) normal to the mean velocity: (a) $\delta/a = 5$ with contour levels from $-1.8\ u_\tau$ to $1.3\ u_\tau$; (b) $\delta/a = 11$ with contour levels from $-0.95\ u_\tau$ to $1.05\ u_\tau$. The contour increment is $0.25\ u_\tau$. The solid contours denote the negative radial velocity ($v_r < 0$) and the dotted contours denote the positive radial velocity ($v_r > 0$).

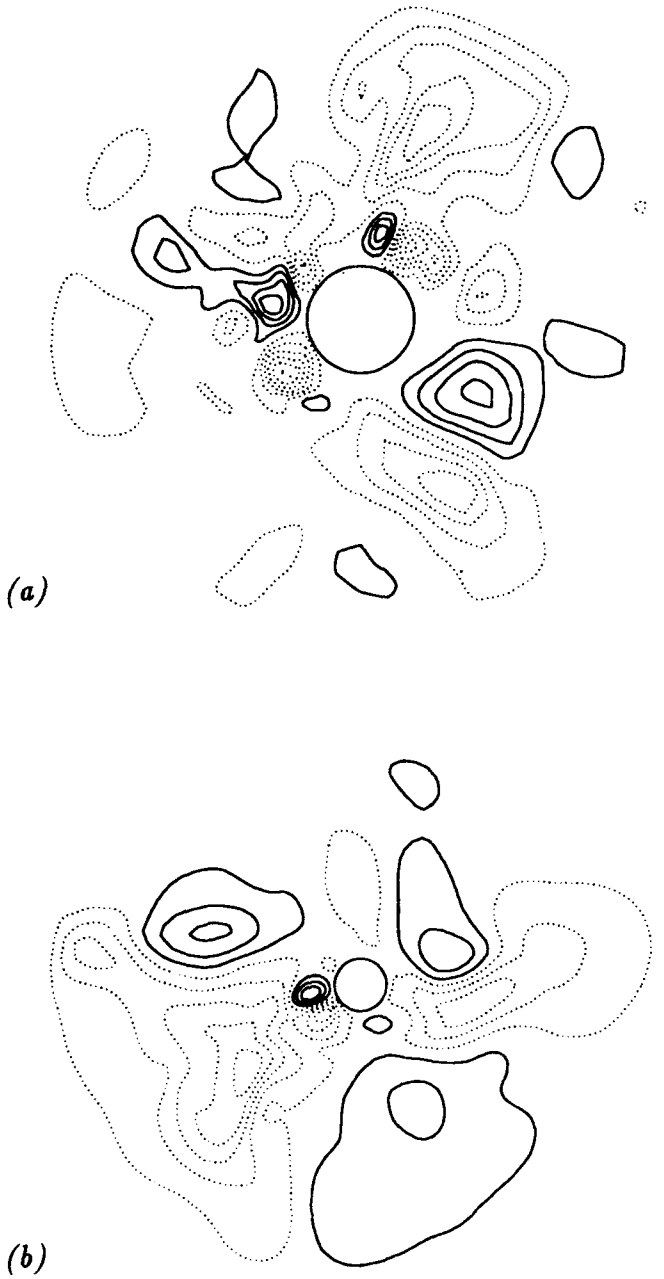

FIGURE 3.24 Contours of radial (wall-normal) velocity fluctuations (v_r), normalized by u_τ, on a plane (II_z) normal to the mean velocity: (a) $\delta/a = 5$ with contour levels from $-1.05\ u_\tau$ to $1.3\ u_\tau$; (b) $\delta/a = 11$ with contour levels from $-0.95\ u_\tau$ to $1.29\ u_\tau$. The contour increment is $0.25\ u_\tau$. The solid contours denote the negative radial velocity ($v_r < 0$) and the dotted contours denote the positive radial velocity ($v_r > 0$).

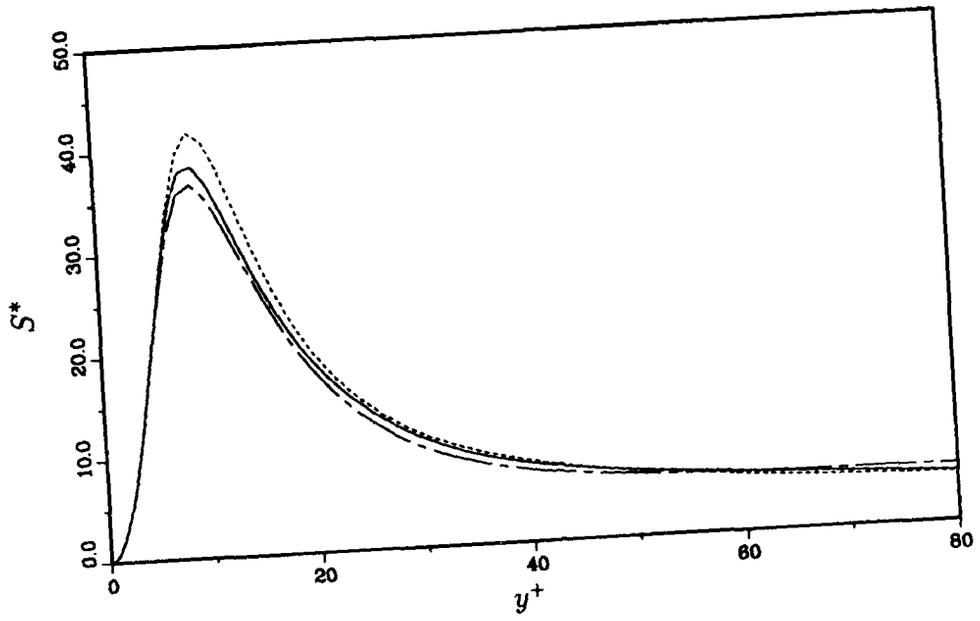

FIGURE 3.25 The shear rate parameter $S^* = 2q^2(d\overline{V}_z/dy)/\epsilon$: ——— plane channel (Lee *et al.* [1990]); cylinders with —— $\delta/a = 5$ and ---- $\delta/a = 11$.

where $S = d\overline{V}_z/dy|_w$ is the mean wall shear rate, q^2 is the turbulent kinetic energy and ϵ is the viscous dissipation. As the curvature increases Figure 3.25 shows that S^* increases near the point of maximum production of turbulent kinetic energy ($y^+ \approx 12$), suggesting that the axial length scale of the low speed streaks may increase as the curvature increases.

The low speed streaks can be seen in the contour plots of v_z on (z, θ) surfaces parallel to the cylinder at $y^+ \approx 5$, as shown in Figure 3.26. Note that the negative contours seem to be more elongated in the streamwise direction for the $\delta/a = 11$ flow.

A measure of the anisotropy of the flow structures is the ratio of the streamwise to the spanwise length scales (Lee *et al.* [1990]),

$$L^* = \frac{L^{(z)}}{2L^{(\theta)}}, \tag{3.5.2}$$

(a)

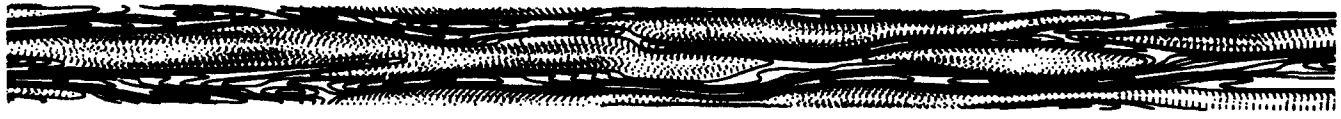

(b)

FIGURE 3.26 Contours of axial velocity fluctuations (v_z), normalized by u_τ and ν, on an unwrapped cylindrical surface at $y^+ \approx 5$: (*a*) $\delta/a = 5$ with contour levels from $-2.2\ u_\tau$ to $5.55\ u_\tau$; (*b*) $\delta/a = 11$ with contour levels from $-2.2\ u_\tau$ to $4.85\ u_\tau$. The axial length of the domain displayed is $3\pi\delta$ and the contour increment is $0.25\ u_\tau$. The solid contours denote the low-speed fluctuations ($v_z < 0$) and the dotted contours denote the high-speed fluctuations ($v_z > 0$).

where $L^{(z)}$ and $L^{(\theta)}$ are the axial and azimuthal integral scales of the quantity of interest. For example, when based on v_z, $L^{(z)}$ and $L^{(\theta)}$ are given by

$$L^{(z)}_{v_z}(y) = \int_0^{L_z/2} R_{v_z v_z}(y,z)dz,$$
$$L^{(\theta)}_{v_z}(y) = (a+y)\int_0^{\pi} R_{v_z v_z}(y,\theta)d\theta, \tag{3.5.3}$$

respectively. L^* based on the streamwise velocity fluctuations, which characterize the low speed streaks, was computed by Lee *et al.* (1990) for the plane channel; their results are compared to the present simulations in Figure 3.27. Close to the wall ($y^+ < 10$), L^* is significantly increased with increasing curvature. Since the spanwise length scale of the low-speed streaks in wall units is not greatly affected by curvature, their streamwise length scale must increase with δ/a. Away from the wall ($y^+ > 20$), L^* for the $\delta/a = 5$ cylinder has essentially the same value as in the plane channel. In the larger curvature case ($\delta/a = 11$) L^* away from the wall ($y^+ > 20$) is twice as large as its counterparts for the $\delta/a = 5$ cylinder and the plane channel.

In addition to the low speed streaks, near-wall flows are also characterized by near-wall vortical structures and internal shear layers. The near-wall streamwise vortices and internal shear layers are characterized by the streamwise and the spanwise vorticity fluctuations, ω_z and ω_θ, respectively. The length scale ratios defined in Equation 3.5.2, computed for both ω_z and ω_θ, are shown in Figure 3.28. For $y^+ > 10$, the length scale ratios for the two vorticity components are close to their isotropic value of unity. Near the wall ($y^+ < 10$), where the mean shear is largest (Figure 3.7), the length scale ratios of ω_θ and ω_z increase with increasing curvature. In particular, the higher near-wall L^* based on ω_z suggests that the near-wall streamwise vortices become longer as the curvature increases. Note also that both vorticity length scale ratios are only affected by curvature near the wall ($y^+ < 10$).

The near-wall shear layers that develop at the interface of the low and high speed flow regions are common in the two transversely curved flows as shown in Figures

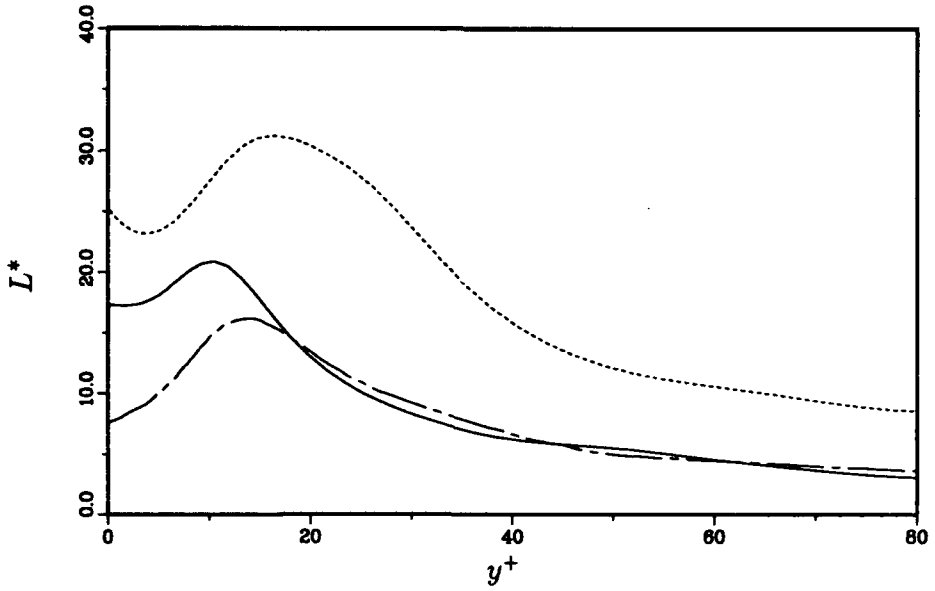

FIGURE 3.27 The length scale parameter L^* based on v_z: ——— plane channel (Lee *et al.* [1990]); cylinders with —— $\delta/a = 5$ and ---- $\delta/a = 11$.

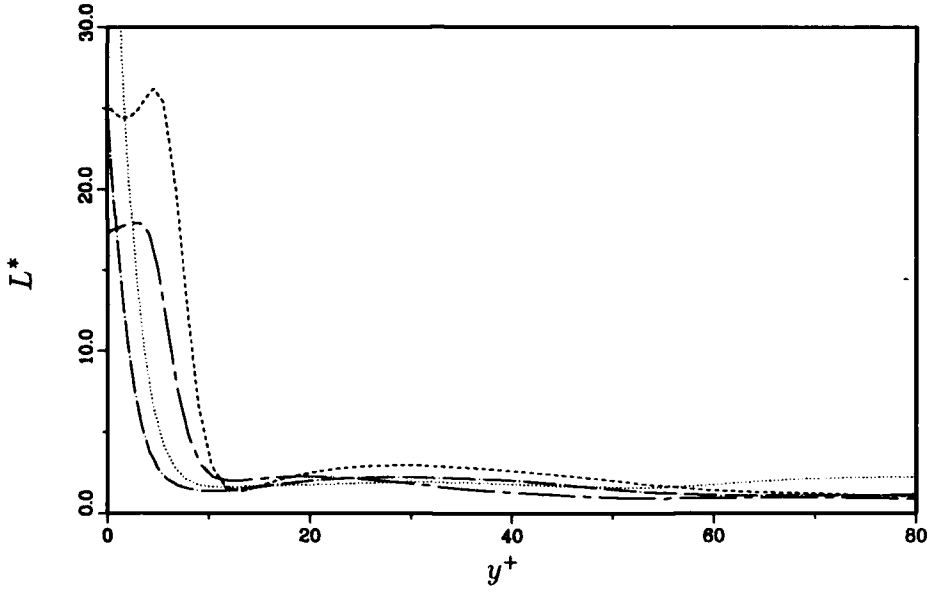

FIGURE 3.28 The length scale parameter: L^* based on ω_θ for cylinders with ——— $\delta/a = 5$ and ---- $\delta/a = 11$; L^* based on ω_z for cylinders with —·— $\delta/a = 5$ and ····· $\delta/a = 11$.

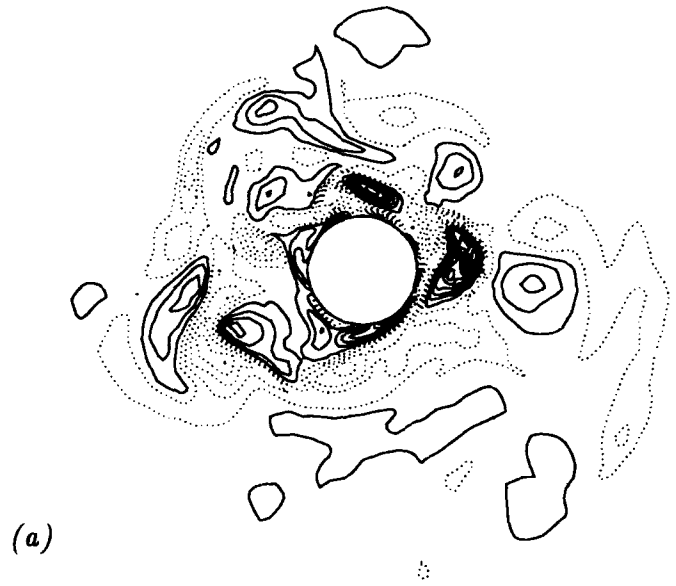

(a)

(b)

FIGURE 3.29 Contours of axial (streamwise) vorticity fluctuations (ω_z), normalized by u_τ and ν, on a plane (I_z) normal to the mean velocity: (a) $\delta/a = 5$ with contour levels from $-0.34\ u_\tau^2/\nu$ to $0.5\ u_\tau^2/\nu$; (b) $\delta/a = 11$ with contour levels from $-0.3\ u_\tau^2/\nu$ to $0.38\ u_\tau^2/\nu$. The contour increment is $0.04\ u_\tau^2/\nu$. The solid contours denote the negative vorticity ($\omega_z < 0$) and the dotted contours denote the positive vorticity ($\omega_z > 0$).

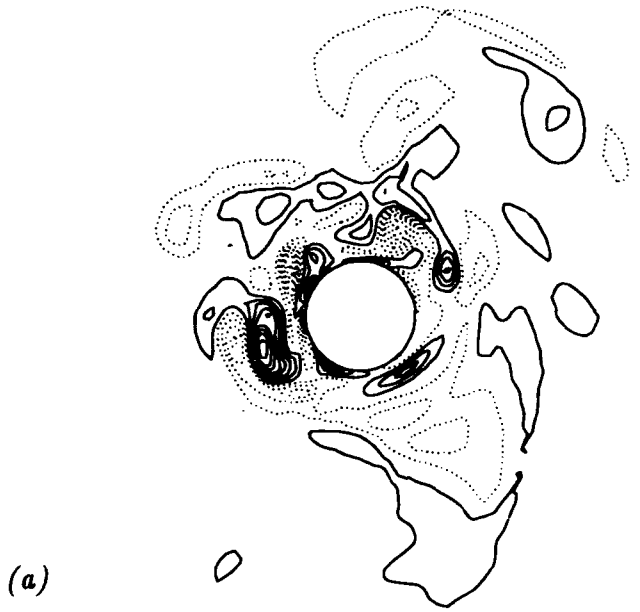

(a)

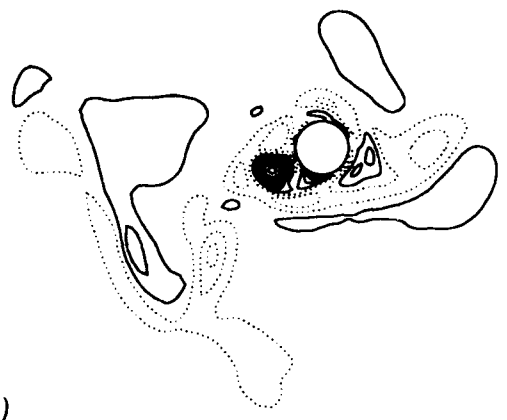

(b)

FIGURE 3.30 Contours of axial (streamwise) vorticity fluctuations (ω_z), normalized by u_τ and ν, on a plane (II_z) normal to the mean velocity: (a) $\delta/a = 5$ with contour levels from $-0.34\ u_\tau^2/\nu$ to $0.5\ u_\tau^2/\nu$; (b) $\delta/a = 11$ with contour levels from $-0.26\ u_\tau^2/\nu$ to $0.22\ u_\tau^2/\nu$. The contour increment is $0.04\ u_\tau^2/\nu$. The solid contours denote the negative vorticity ($\omega_z < 0$) and the dotted contours denote the positive vorticity ($\omega_z > 0$).

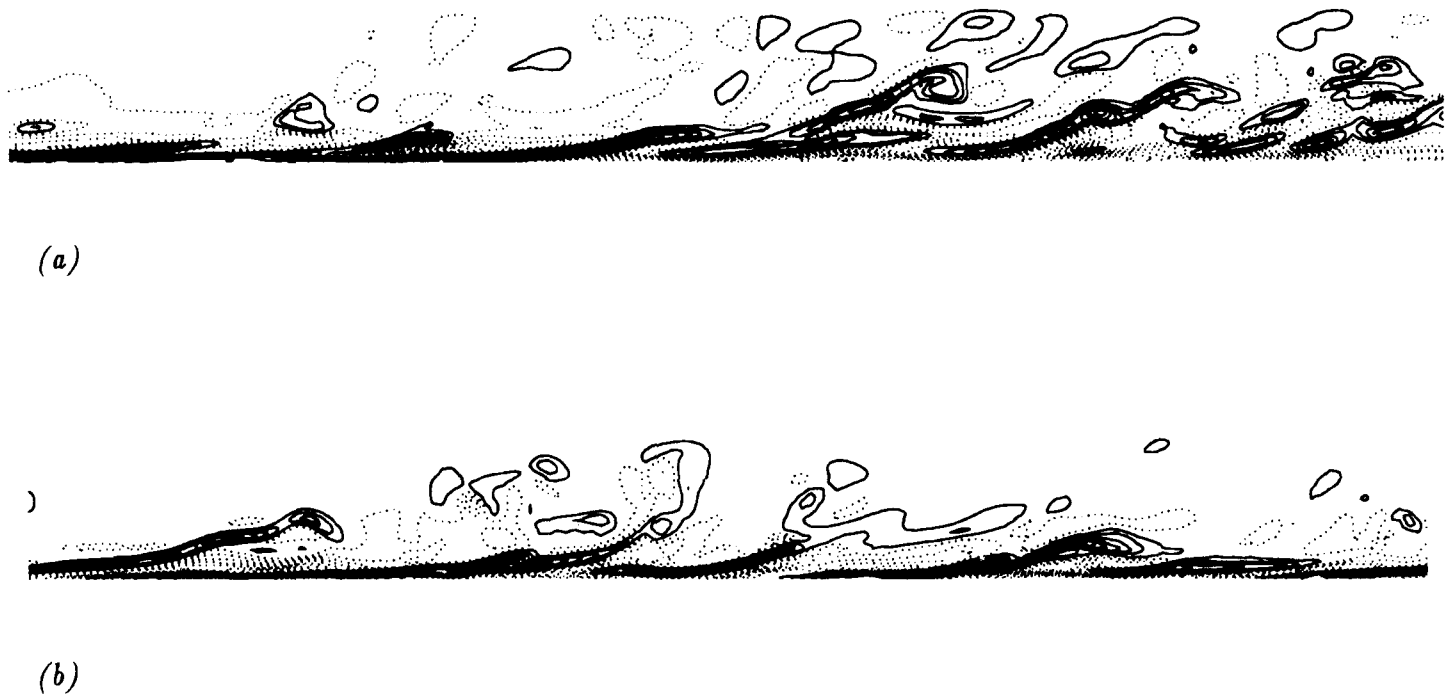

FIGURE 3.31 Contours of azimuthal vorticity fluctuations (ω_θ), normalized by u_τ and ν, on an azimuthal plane (I_θ) through the axis of the cylinder. The axial length of the domain displayed is $3\pi\delta$: (*a*) $\delta/a = 5$ with contour levels from $-0.74\ u_\tau^2/\nu$ to $0.56\ u_\tau^2/\nu$; (*b*) $\delta/a = 11$ with contour levels from $-0.9\ u_\tau^2/\nu$ to $0.42\ u_\tau^2/\nu$. The contour increment is $0.04\ u_\tau^2/\nu$. The solid contours denote the negative vorticity ($\omega_\theta < 0$) (aligned with the mean vorticity) and the dotted contours denote the positive vorticity ($\omega_\theta > 0$).

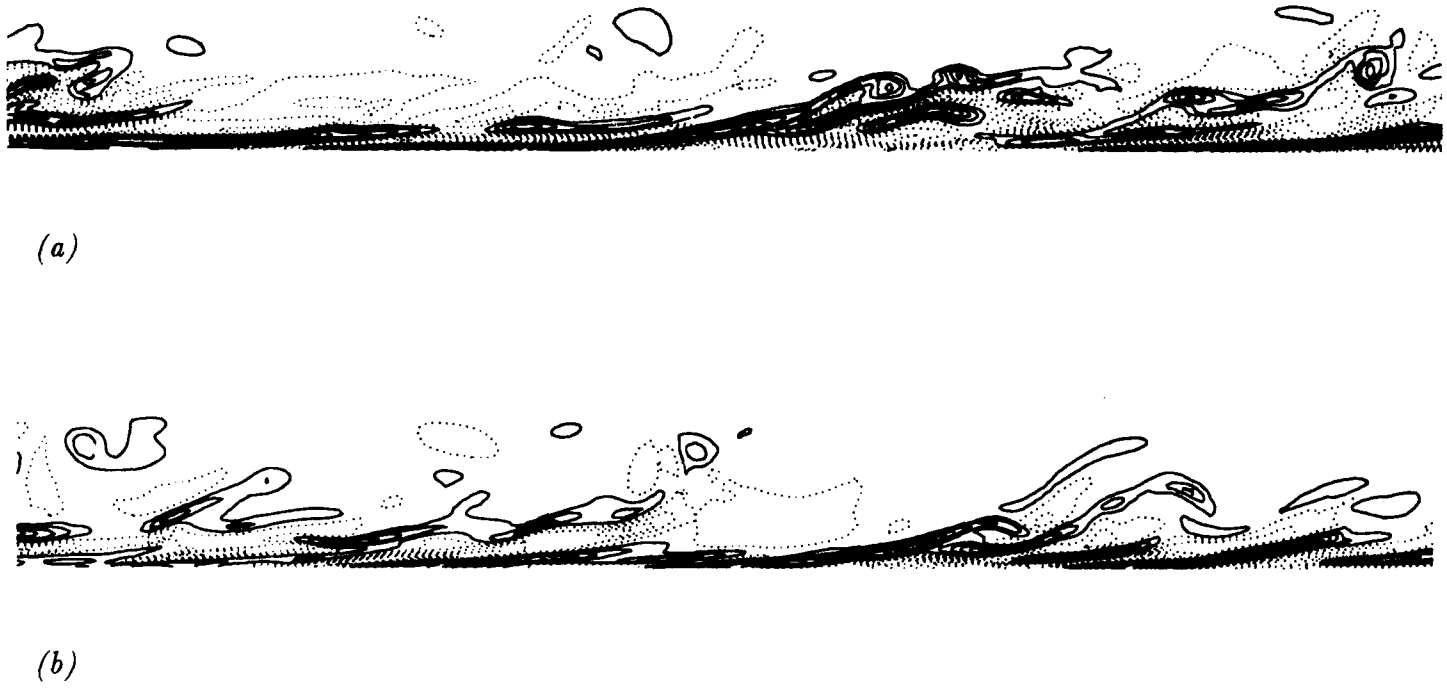

FIGURE 3.32 Contours of azimuthal vorticity fluctuations (ω_θ), normalized by u_τ and ν, on an azimuthal plane (II_θ) through the axis of the cylinder. The axial length of the domain displayed is $3\pi\delta$: (*a*) $\delta/a = 5$ with contour levels from $-0.74\ u_\tau^2/\nu$ to $0.56\ u_\tau^2/\nu$; (*b*) $\delta/a = 11$ with contour levels from $-0.9\ u_\tau^2/\nu$ to $0.42\ u_\tau^2/\nu$. The contour increment is $0.04\ u_\tau^2/\nu$. The solid contours denote the negative vorticity ($\omega_\theta < 0$) (aligned with the mean vorticity) and the dotted contours denote the positive vorticity ($\omega_\theta > 0$).

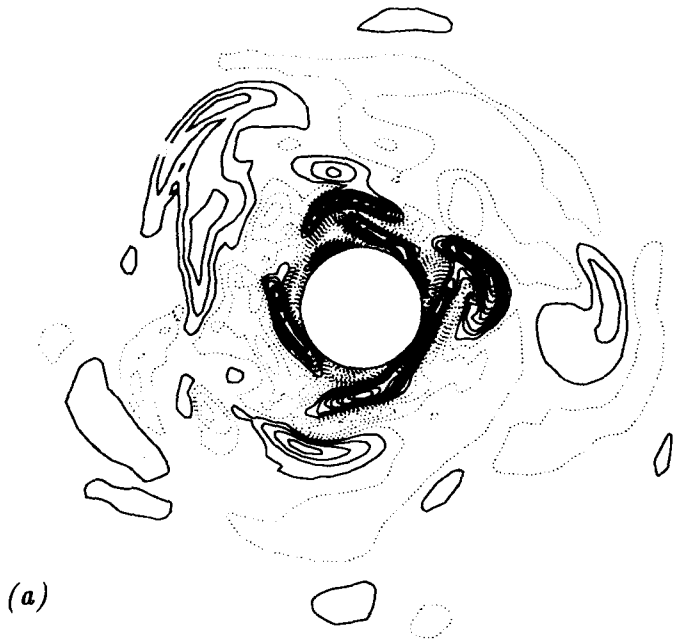

(a)

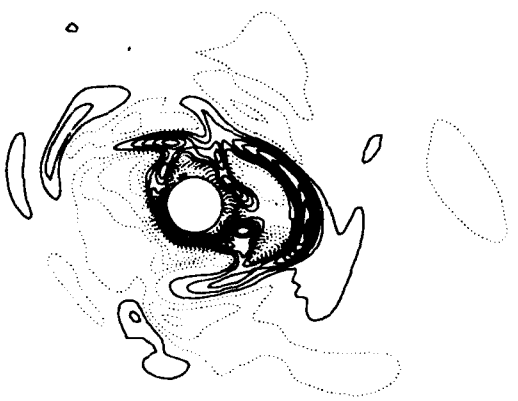

(b)

FIGURE 3.33 Contours of azimuthal vorticity fluctuations (ω_θ), normalized by u_τ and ν, on a plane (I_z) normal to the mean velocity: (*a*) $\delta/a = 5$ with contour levels from $-0.58\ u_\tau^2/\nu$ to $0.54\ u_\tau^2/\nu$; (*b*) $\delta/a = 11$ with contour levels from $-0.66\ u_\tau^2/\nu$ to $0.5\ u_\tau^2/\nu$. The contour increment is $0.04\ u_\tau^2/\nu$. The solid contours denote the negative vorticity ($\omega_\theta < 0$) (aligned with the mean vorticity) and the dotted contours denote the positive vorticity ($\omega_\theta > 0$).

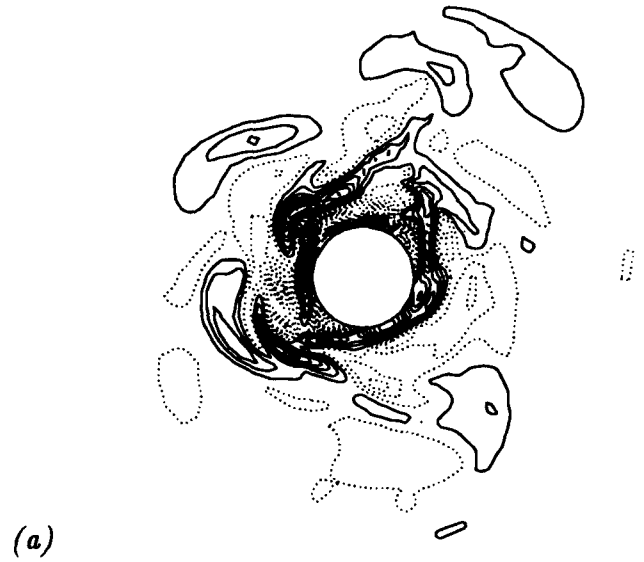

(a)

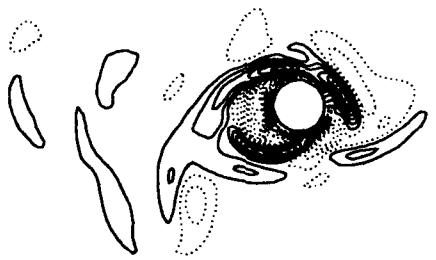

(b)

FIGURE 3.34 Contours of azimuthal vorticity fluctuations (ω_θ), normalized by u_τ and ν, on a plane (II_z) normal to the mean velocity: (*a*) $\delta/a = 5$ with contour levels from $-0.38\ u_\tau^2/\nu$ to $0.5\ u_\tau^2/\nu$; (*b*) $\delta/a = 11$ with contour levels from $-0.9\ u_\tau^2/\nu$ to $0.46\ u_\tau^2/\nu$. The contour increment is $0.04\ u_\tau^2/\nu$. The solid contours denote the negative vorticity ($\omega_\theta < 0$) (aligned with the mean vorticity) and the dotted contours denote the positive vorticity ($\omega_\theta > 0$).

(a)

(b)

FIGURE 3.35 Contours of azimuthal vorticity fluctuations (ω_θ), normalized by u_τ and ν, on an unwrapped cylindrical surface at $y^+ \approx 15$. The axial length of the domain displayed is $3\pi\delta$: (*a*) $\delta/a = 5$ with contour levels from $-0.58\ u_\tau^2/\nu$ to $0.32\ u_\tau^2/\nu$; (*b*) $\delta/a = 11$ with contour levels from $-0.73\ u_\tau^2/\nu$ to $0.62\ u_\tau^2/\nu$. The contour increment is $0.05\ u_\tau^2/\nu$. The solid contours denote the negative vorticity ($\omega_\theta < 0$) (aligned with the mean vorticity) and the dotted contours denote the positive vorticity ($\omega_\theta > 0$).

3.31 (plane I_z) and 3.32 (plane II_z) and have features similar to those of the plane channel. These two figures suggest that the higher curvature ($\delta/a = 11$) flow is more quiescent in the outer region in agreement with the lower velocity correlation coefficient (Figure 3.6). In Figures 3.33 and 3.34, cross sections of the internal shear layers by (r, θ) planes show that the shear layers have large azimuthal (spanwise) length scales relative to the cylinder radius. As the curvature increases the ratio of the spanwise length scale of the shear layers to the cylinder radius increases. These contour plots also suggest that the shear layers have a milder transverse curvature than the cylinder. Cuts of these shear layers by (z, θ) surfaces parallel to the cylinder (Figure 3.35) at $y^+ \approx 15$ show a characteristic arrow shape that is more noticeable in the higher curvature ($\delta/a = 11$) flow. Such arrow shapes are geometrically consistent with nearly planar inclined shear layers intersected by a cylindrical surface.

Kim (1989) demonstrated that the near-wall streamwise vortices contribute significantly to the source term of the pressure Poisson equation. As the curvature increases, there is an additional important source of pressure fluctuations (see Section **4.1**, Figure 4.3) associated with the strong near-wall radial (wall-normal) vorticity fluctuations (Figures 3.18 *a* and 3.18 *b*). Contours of the radial vorticity fluctuations in the same (r, θ) planes are shown in Figures 3.36 and 3.37. As in the plane channel, near the wall the regions where the radial vorticity fluctuations change sign are well correlated with the locations of the low-speed streaks but not necessarily with the streamwise vortices. Contours of the pressure in the same (r, θ) planes (Figures 3.38 and 3.39) show low pressure regions well correlated with the locations of the near-wall streamwise vortices. Apparently the normal vorticity fluctuations become a more prominent feature simply because, as the curvature increases, more of the turbulent kinetic energy is in the streamwise velocity fluctuations (Figure 3.4). Contours of the normal vorticity are shown in Figure 3.40 on (z, θ) surfaces parallel to the cylinder at $y^+ \approx 15$. In the $\delta/a = 11$ flow (Figure 3.40 *b*), the strong positive and negative contours of ω_r are well correlated with the intersections of the cylindrical surface at $y^+ \approx 15$ with the wall shear layers (Figure 3.35 *b*).

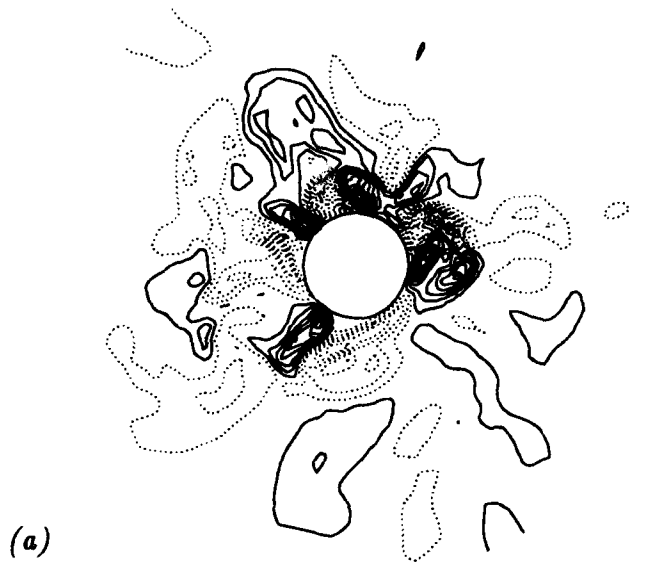

(a)

(b)

FIGURE 3.36 Contours of radial (wall-normal) vorticity fluctuations (ω_r), normalized by u_τ and ν, on a plane (I_z) normal to the mean velocity: (*a*) $\delta/a = 5$ with contour levels from $-0.38\ u_\tau^2/\nu$ to $0.46\ u_\tau^2/\nu$; (*b*) $\delta/a = 11$ with contour levels from $-0.3\ u_\tau^2/\nu$ to $0.38\ u_\tau^2/\nu$. The contour increment is $0.04\ u_\tau^2/\nu$. The solid contours denote the negative vorticity ($\omega_r < 0$) and the dotted contours denote the positive vorticity ($\omega_r > 0$).

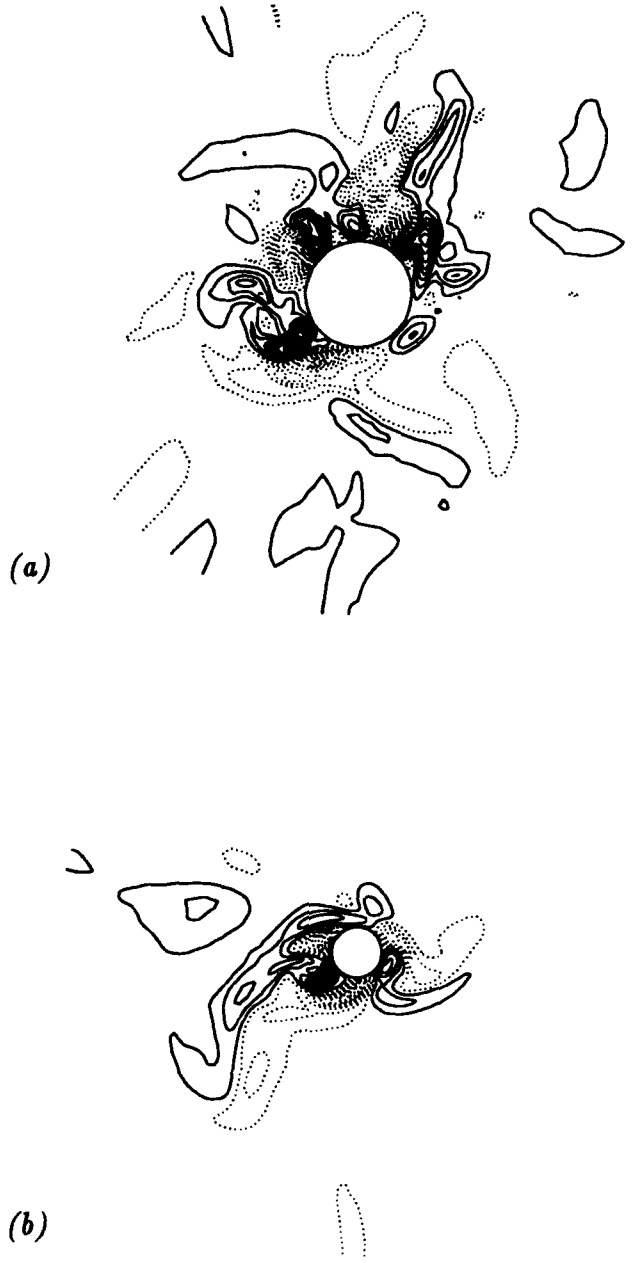

FIGURE 3.37 Contours of radial (wall-normal) vorticity fluctuations (ω_r), normalized by u_τ and ν, on a plane (II_z) normal to the mean velocity: (a) $\delta/a = 5$ with contour levels from $-0.46\ u_\tau^2/\nu$ to $0.5\ u_\tau^2/\nu$; (b) $\delta/a = 11$ with contour levels from $-0.26\ u_\tau^2/\nu$ to $0.22\ u_\tau^2/\nu$. The contour increment is $0.04\ u_\tau^2/\nu$. The solid contours denote the negative vorticity ($\omega_r < 0$) and the dotted contours denote the positive vorticity ($\omega_r > 0$).

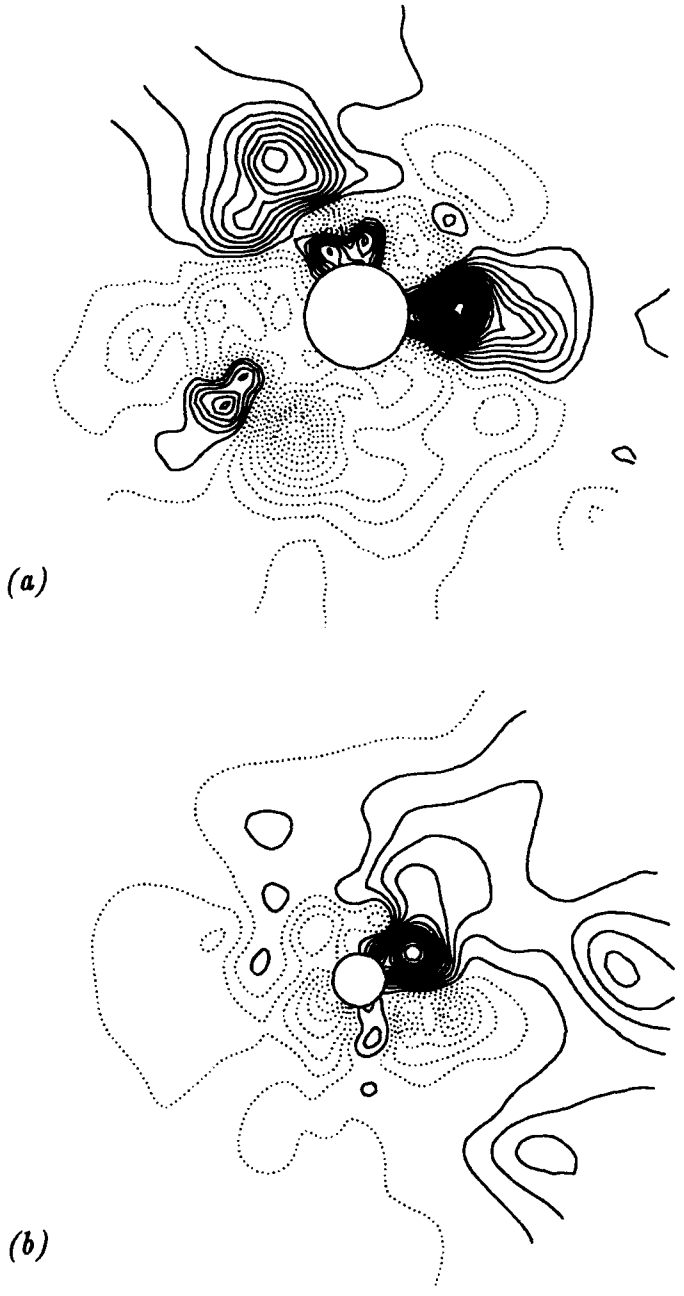

FIGURE 3.38 Contours of the pressure fluctuations (p), normalized by ρ and u_τ, on a plane (I_z) normal to the mean velocity: (a) $\delta/a = 5$ with contour levels from $-4.1\ \rho u_\tau^2$ to $2.1\ \rho u_\tau^2$; (b) $\delta/a = 11$ with contour levels from $-2.5\ \rho u_\tau^2$ to $1.5\ \rho u_\tau^2$. The contour increment is $0.2\ \rho u_\tau^2$. The solid contours denote the negative pressure ($p < 0$) and the dotted contours denote the positive pressure ($p > 0$).

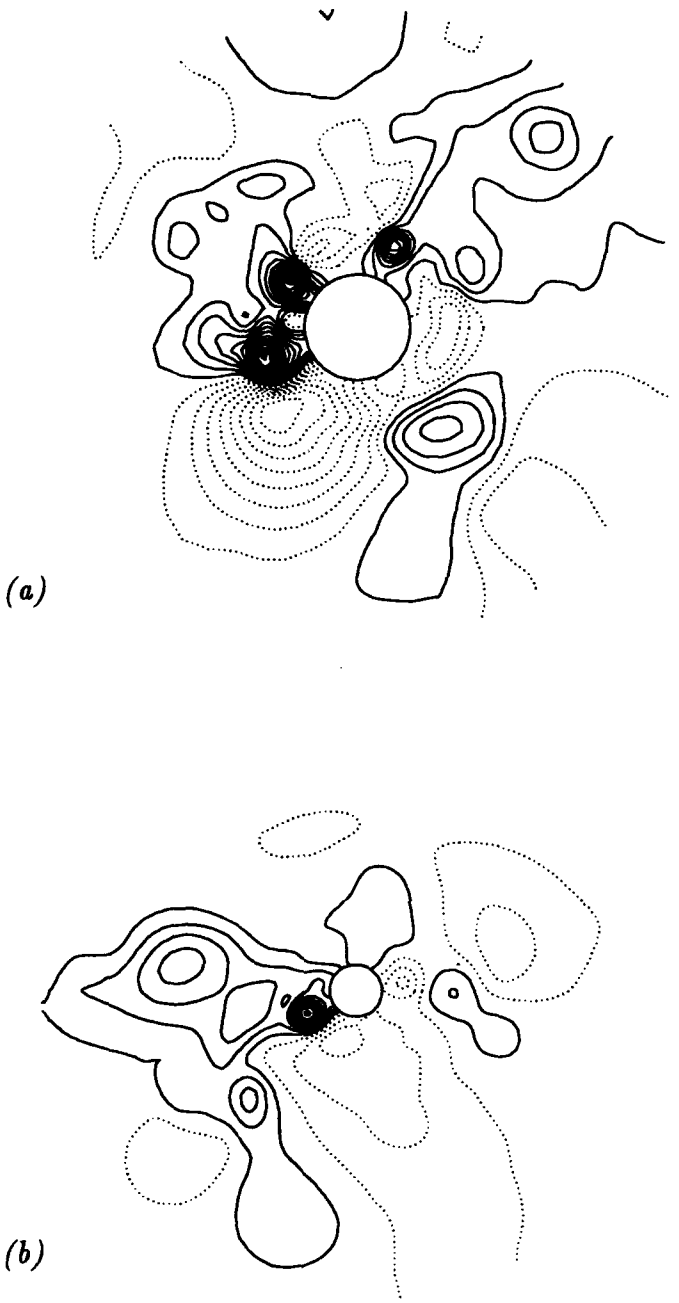

FIGURE 3.39 Contours of the pressure fluctuations (p), normalized by ρ and u_τ, on a plane (II_z) normal to the mean velocity: (a) $\delta/a = 5$ with contour levels from $-2.5\ \rho u_\tau^2$ to $1.5\ \rho u_\tau^2$; (b) $\delta/a = 11$ with contour levels from $-1.7\ \rho u_\tau^2$ to $0.5\ \rho u_\tau^2$. The contour increment is $0.2\ \rho u_\tau^2$. The solid contours denote the negative pressure ($p < 0$) and the dotted contours denote the positive pressure ($p > 0$).

(a)

(b)

FIGURE 3.40 Contours of radial vorticity fluctuations (ω_r), normalized by u_τ and ν, on an unwrapped cylindrical surface at $y^+ \approx 15$. The axial length of the domain displayed is $3\pi\delta$: (*a*) $\delta/a = 5$ with contour levels from -0.79 u_τ^2/ν to 0.66 u_τ^2/ν; (*b*) $\delta/a = 11$ with contour levels from -0.49 u_τ^2/ν to 0.56 u_τ^2/ν. The contour increment is 0.05 u_τ^2/ν. The solid contours denote the negative vorticity ($\omega_r < 0$) and the dotted contours denote the positive vorticity ($\omega_r > 0$).

CHAPTER 4

Pressure Fluctuations

Wall pressure fluctuations affect the acoustic characteristics (both radiation and detection) of underwater vehicles. In addition, in transversely curved turbulent flows over sonar devices, it is important to identify the pressure signals generated by the turbulent flow field. The aim of this chapter is to describe the effects of transverse curvature on the wall pressure fluctuations when both the outer and inner parts of the flow are affected by the curvature of the wall. For this flow regime (large δ/a and small a^+), there is only limited experimental data available on the statistical properties of the wall pressure fluctuations.

For comparison, the spatial and temporal spectra of the plane channel wall pressure fluctuations were also calculated from a database generated by Kim *et al.* (1987) and Choi & Moin (1990). As noted earlier, the Reynolds number of the plane channel flow and those of the present flows are similar, and thus differences in the statistical characteristics can be ascribed to the transverse curvature alone.

The wall pressure database on which the results of this chapter are based was generated after the flow had reached statistical steady state (Section **3.2**). Additional integration of the governing equations for wall pressure statistics were carried out for a period of 12.8 δ/u_τ time units in the $\delta/a = 5$ flow and for 8.6 time units in the $\delta/a = 11$ flow.

The effects of transverse curvature on the sources of pressure fluctuations are discussed in Section **4.1**. The computational method used to obtain the space-time characteristics of the wall pressure data is described in Section **4.2**. Section **4.3** contains the spatial spectra of the wall pressure fluctuations and in Section **4.4** the two-point correlations are presented. The fractional contributions of various flow regions to the wall pressure are studied in Section **4.5**. The temporal spectra are presented in Section **4.6**. Two-dimensional spectra and correlations are discussed in Section **4.7**. Finally, Section **4.8** treats the convection velocity of the wall pressure fluctuations.

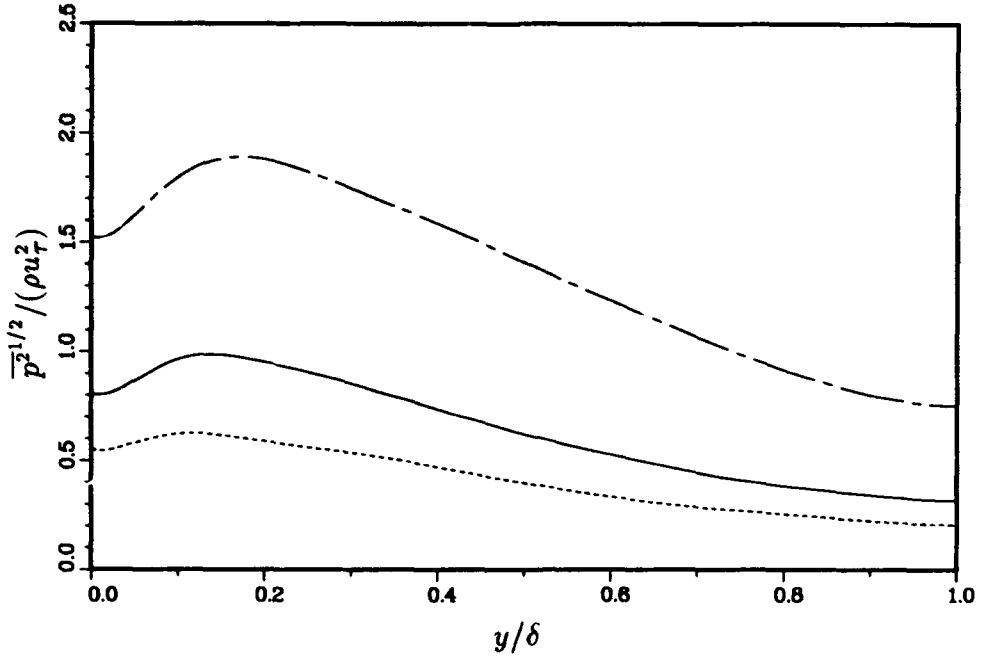

FIGURE 4.1 Root-mean-square pressure normalized by u_τ in global coordinates: ——— plane channel (Kim [1989]); cylinders with —— $\delta/a = 5$ and ---- $\delta/a = 11$.

4.1 Pressure Source Terms

The Poisson equation for the pressure field is obtained from the divergence of the Navier-Stokes equations (Equation 2.1.1),

$$\nabla^2 p = -2\frac{\partial \overline{V}_z}{\partial r}\frac{\partial v_r}{\partial z} - \left(\frac{\partial v_r}{\partial r}\right)^2 - \frac{2}{r}\frac{\partial v_\theta}{\partial r}\left(\frac{\partial v_r}{\partial \theta} - v_\theta\right)$$
$$- 2\frac{\partial v_z}{\partial r}\frac{\partial v_r}{\partial z} - \frac{1}{r^2}\left(\frac{\partial v_\theta}{\partial \theta} + v_r\right)^2 - \frac{2}{r}\frac{\partial v_z}{\partial \theta}\frac{\partial v_\theta}{\partial z} - \left(\frac{\partial v_z}{\partial z}\right)^2. \qquad (4.1.1\ a)$$

Boundary conditions for the pressure are obtained by evaluating the radial momentum equation at both edges of the domain,

$$\left.\frac{\partial p}{\partial r}\right|_{r=a} = \left.\frac{1}{Re_\tau}\frac{\partial^2 v_r}{\partial r^2}\right|_{r=a}, \qquad \left.\frac{\partial p}{\partial r}\right|_{r=a+1} = \left[-\frac{1}{Re_\tau}\frac{2}{r^2}\frac{\partial v_\theta}{\partial \theta} + \frac{{v_\theta}^2}{r}\right]_{r=a+1}. \qquad (4.1.1\ b)$$

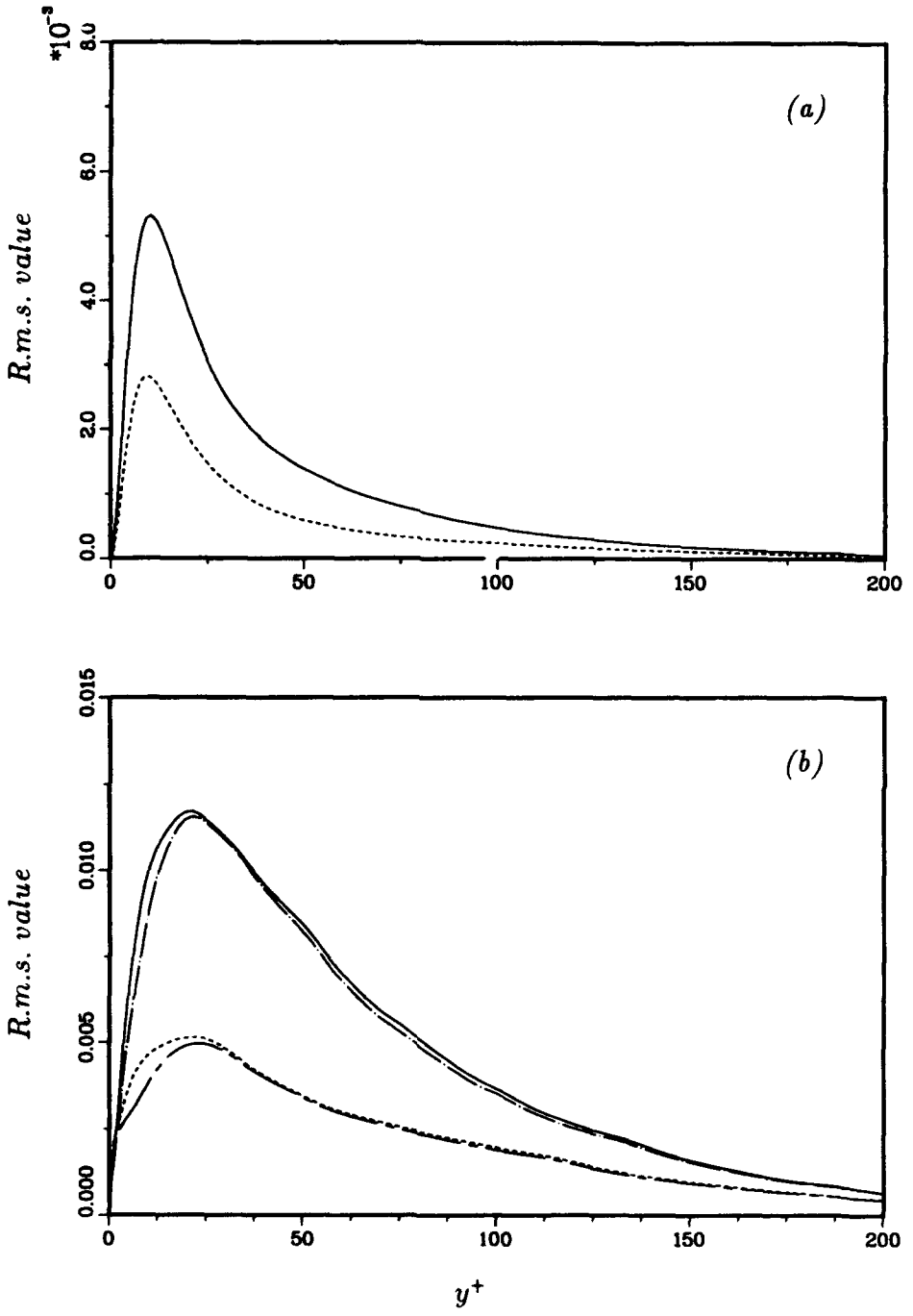

FIGURE 4.2 Profiles of the root-mean-square value of the pressure source terms normalized by ν and u_τ: (a) linear contribution: cylinders with —— $\delta/a = 5$ and ---- $\delta/a = 11$; (b) nonlinear contribution: cylinders with —— $\delta/a = 5$ and ---- $\delta/a = 11$; total source terms: cylinders with —·— $\delta/a = 5$ and —··— $\delta/a = 11$.

The first term on the right hand side of Equation 4.1.1 *a* represents the pressure source that results from the linear interaction of the mean shear with the turbulence. The next six terms are the pressure source terms that result from the nonlinear interactions within the turbulent flow field.

The pressure intensity normalized by the mean shear, shown in Figure 4.1, decreases across the layer with increasing curvature. In particular, the near-wall maximum of the pressure intensity is reduced by increasing the curvature. This suggests that the structures that are responsible for the maximum in the pressure intensity are weakened.

Contrary to what was generally accepted, Kim (1989) found that in turbulent channel flow the turbulence field interactions constitute the strongest sources of pressure fluctuations. In fact, the magnitude of the mean-square of the linear source term was about five times lower than the magnitude of the mean-square of the nonlinear source term. In the transversely curved turbulent flows reported here, the ratio of the magnitude of the mean-square of the nonlinear to the linear pressure source terms is large (Figure 4.2), even though, as the curvature increases, both sources of pressure fluctuations (linear and nonlinear) decrease.

In the plane channel the maximum of the mean square of the nonlinear terms occurs at about $y^+ \approx 20$, which is the same as the mean position of the near-wall vortices as well as the position of the maximum of the pressure intensity (Kim [1989]). In the transversely curved flows, the maximum of the pressure intensity is weakened as the curvature increases and at about the same position as in the plane channel flow ($y^+ \approx 20$, Figure 4.1). As the curvature increases, the average strength of the near-wall vortices is weakened while the average position of the vortex cores remains the same ($y^+ \approx 20$) (see Section **3.4**).

In order to associate the pressure intensity with the sources of pressure fluctuations in the flow, the various contributions to the nonlinear source terms of the pressure are examined (Figure 4.3). As in the plane channel the most important nonlinear source term is

$$\frac{2}{r}\left(\frac{\partial v_r}{\partial \theta} - v_\theta\right)\frac{\partial v_\theta}{\partial r}, \tag{4.1.2}$$

which contains significant contributions from the near-wall streamwise vortices. Note also that in both flows this source term develops near-wall ($y^+ \approx 5$) local

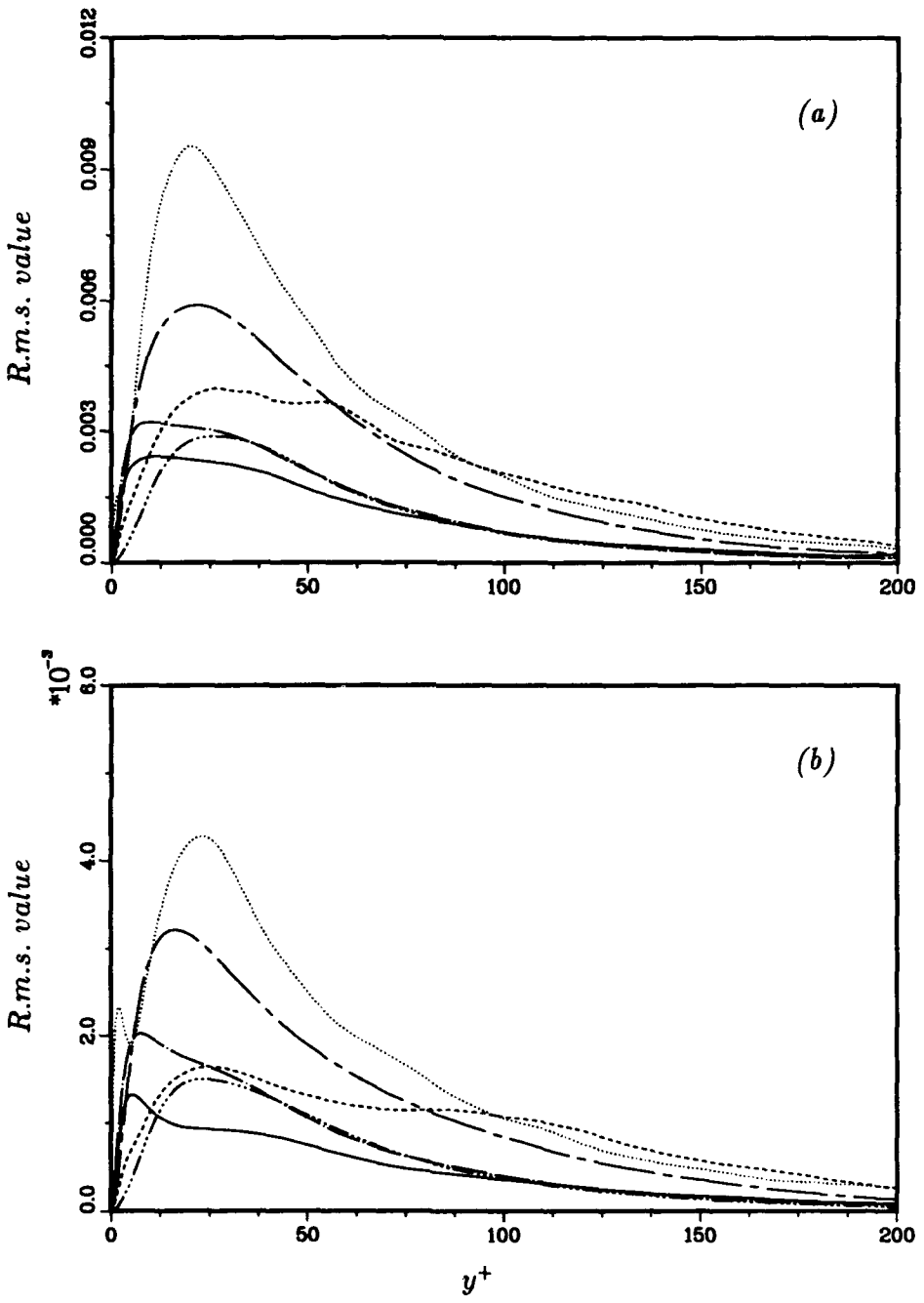

FIGURE 4.3 Profiles of the root-mean-square value of the nonlinear contributions to the source terms normalized by ν and u_τ: (a) $\delta/a = 5$, (b) $\delta/a = 11$; —— $(\partial v_r/\partial r)^2$, ····· $(2/r)(\partial v_r/\partial\theta - v_\theta)(\partial v_\theta/\partial r)$, —·— $(1/r^2)(\partial v_\theta/\partial\theta + v_r)^2$, —···— $(\partial v_z/\partial z)^2$, ---- $2(\partial v_z/\partial r)(\partial v_r/\partial z)$, —·— $(2/r)(\partial v_z/\partial\theta)(\partial v_\theta/\partial z)$.

δ/a	0	5	11
$L_T(u_\tau/\delta)$	9.36	12.9	8.6
$L_t(u_\tau/\delta)$	1.20	0.806	0.659
$\Delta t_s(u_\tau/\delta)$	3.75×10^{-3}	2.52×10^{-3}	2.06×10^{-3}
$\Delta t_s(u_\tau^2/\nu)$	0.675	0.539	0.494
$\Delta\omega(\delta/u_\tau)$	5.2	7.8	9.5
N_s	2560	5120	4160

Table 4.1 Temporal resolution parameters

extrema. Near the wall vorticity of opposite sign to the primary vortices may be responsible for this behavior.

Figure 4.3 also shows that, as the curvature increases, another nonlinear term,

$$\frac{2}{r}\frac{\partial v_z}{\partial \theta}\frac{\partial v_\theta}{\partial z}, \tag{4.1.3}$$

plays an increasingly important role in the pressure fluctuations. Note that the factors in this product are the two velocity gradients that define the radial component of the vorticity (Equation 3.4.1). As the curvature increases, strong normal vorticity fluctuations (with respect to the local streamwise vorticity fluctuations) become increasingly more common farther away from the wall (when measured in wall units).

4.2 Computational Considerations

The wall pressure was sampled at intervals Δt_s for a total period L_T, resulting in N_s time samples. In the temporal analysis a window of length L_t is used. These parameters are given in Table 4.1 for the three simulations under consideration. For the sake of simplicity only the one-dimensional spectra are discussed. The computation of the two-dimensional spectra is identical.

4.2.1 Spatial Spectra

The spatial spectra of the wall pressure fluctuations are obtained by averaging over all N_s samples. Thus the spectra in the axial and azimuthal directions are given by

$$E_{pp}(k_z) = \frac{2}{\Delta k_z N_s} \sum_{j=1}^{N_s} \left[\sum_{m=-N_\theta/2}^{N_\theta/2} \hat{p}_w(k_z, m\delta/a, t_j) \hat{p}_w^*(k_z, m\delta/a, t_j) \right],$$

$$E_{pp}(k_\theta) = \frac{2}{\Delta k_\theta N_s} \sum_{j=1}^{N_s} \left[\sum_{k=0}^{N_z/2} \hat{p}_w(2\pi k/L_z, k_\theta, t_j) \hat{p}_w^*(2\pi k/L_z, k_\theta, t_j) \right], \tag{4.2.1}$$

respectively. The Fourier transform of $p_w(z,\theta,t_j)$ is $\hat{p}_w(k_z, k_\theta, t_j)$ and $\hat{p}_w^*(k_z, k_\theta, t_j)$ is its complex conjugate. Note that the mean-square wall pressure is given by

$$\overline{p^2}_w = \Delta k_z \sum_{k=0}^{N_z/2} E_{pp}(2\pi k/L_z) = \Delta k_\theta \sum_{m=0}^{N_\theta/2} E_{pp}(m\delta/a). \tag{4.2.2}$$

4.2.2 Temporal Spectra

In the calculation of the temporal characteristics of the wall pressure the same techniques were used as in Choi & Moin (1990). The total length of the temporal domain for each of the flows (L_T), is divided into m overlapping intervals (with 50% overlap) of equal length (L_t). The length of each interval is thus given by

$$L_t = \frac{2L_T}{m+1}. \tag{4.2.3}$$

The choice of $m = 31$ and $m = 25$ was made for the $\delta/a = 5$ and $\delta/a = 11$ flows respectively, resulting in 320 samples in each interval. Since the wall pressure is

not temporally periodic in any of the intervals, the data is tapered at the edges of each interval by a window function $f_w(t)$, according to

$$\tilde{p}_w(t) = f_w(t)p_w(t), \qquad 0 \leq t \leq L_t, \tag{4.2.4}$$

where $p_w(t)$ denotes the wall pressure at a given time instant. For the sake of simplicity, in this section, the spatial dependence of the wall pressure fluctuations is omitted. In the analysis of the wall pressure for the plane channel Choi & Moin (1990) experimented with several window functions and reported no significant difference in the resulting temporal spectra. In the present calculations the Hanning window function

$$f_w(t) = \frac{1}{2} - \frac{1}{2}\cos\left(\frac{2\pi t}{L_t}\right), \tag{4.2.5}$$

is used. The properties of $f_w(t)$ as a window function are discussed by Harris (1978).

The temporal spectrum is estimated from

$$\phi_{pp}(\omega_j) = \frac{1}{\Delta\omega m}\sum_{i=1}^{m}\hat{\tilde{p}}_w(\omega_j)\hat{\tilde{p}}_w^*(\omega_j), \tag{4.2.6}$$

where $\hat{\tilde{p}}_w$ is the Fourier transform of $\tilde{p}_w$ in the i^{th} interval. The discrete frequencies, ω_j, are given by

$$\omega_j = \frac{2\pi}{L_t}j, \qquad j = 0, 1, 2, ..., M/2, \tag{4.2.7}$$

where $M = 2N_s/(m+1)$ is the number of samples in the interval. In general, because of the windowing, the variance of $\tilde{p}_w$ will not be equal to the variance of p_w. To preserve the root-mean-square (r.m.s.) value of p_w the spectrum ϕ_{pp} is rescaled so that

$$\overline{p_w^2} = \Delta\omega \sum_{j=-M/2}^{M/2}\phi_{pp}(\omega_j). \tag{4.2.8}$$

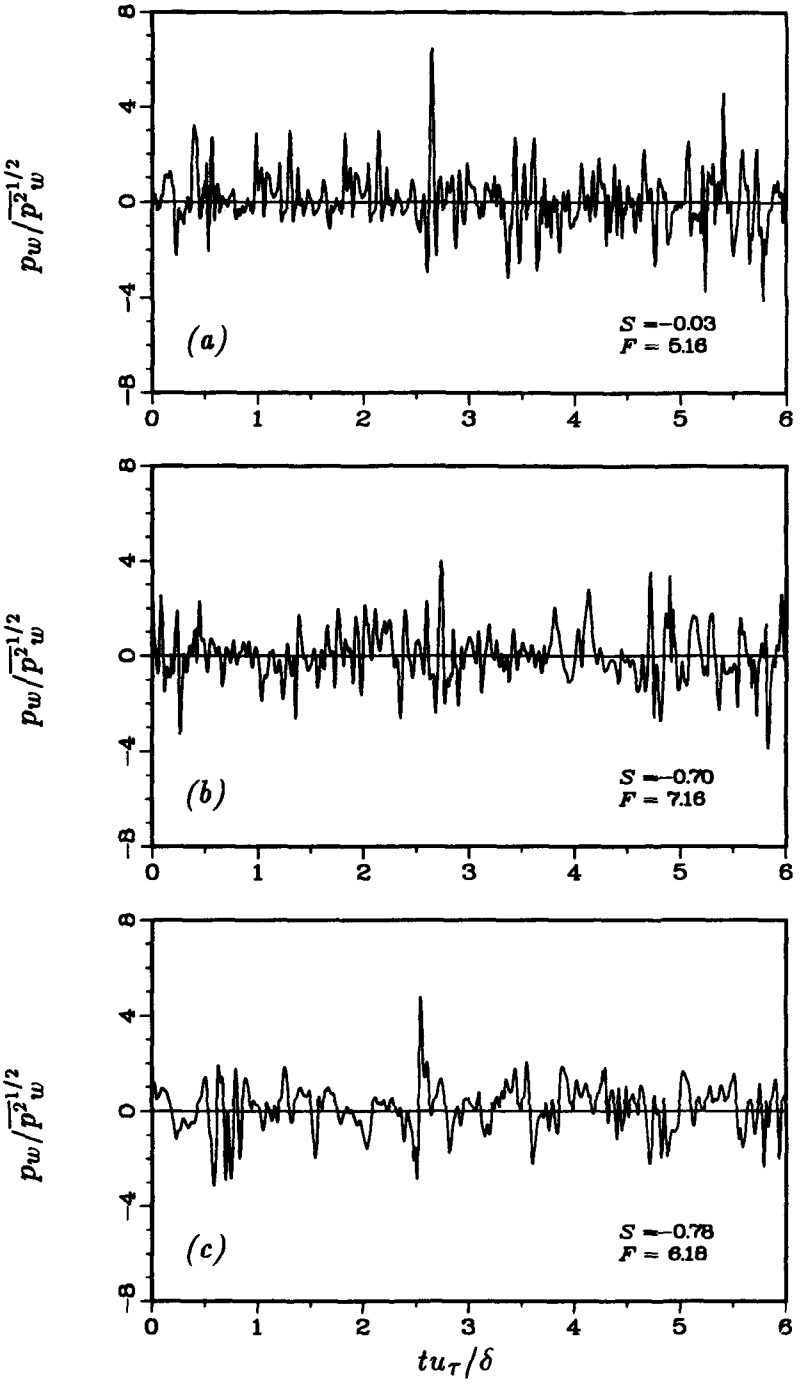

FIGURE 4.4 Signal of the wall pressure fluctuations normalized by $\overline{p^2}_w^{1/2}$: (*a*) plane channel; cylinders with (*b*) $\delta/a = 5$; (*c*) $\delta/a = 11$.

δ/a	0	5	11
$\overline{p_w^2}^{1/2}/(\rho u_\tau^2)$	1.54	0.84	0.58
$S(p_w)$	−0.03	−0.70	−0.78
$F(p_w)$	5.16	7.16	6.18

Table 4.2 Wall pressure parameters.

4.3 Spatial Spectra

Figure 4.4 shows a sample of the time traces of the wall pressure fluctuations normalized by their r.m.s. values. Note that, as the curvature increases, the high frequency content of the fluctuations is weakened. Apparently the different appearances of the wall pressure fluctuations in the two transversely curved flows, does not noticeably affect the flatness and skewness values (Table 4.2).

The strong dependence of the wall pressure intensity on the Reynolds number, documented by Choi & Moin (1990), is not a factor in the comparison of Table 4.1 because the Reynolds numbers of the three simulations are similar. In measurements of the wall pressure intensity in a boundary layer Willmarth & Yang (1970) concluded that the transverse curvature did not have a significant effect. However, this result is for a mild transverse curvature ($\delta/a \simeq 2$, $a^+ \simeq 4500$), in which only the outer part of the boundary layer was affected by the curvature. In addition, any small curvature dependence that was present in their study was probably overshadowed by the strong Reynolds number dependence of the wall pressure intensity. In subsequent wall pressure measurements on a cylinder (Willmarth *et al.* [1976]), for which $\delta/a \simeq 4$, the value of the wall r.m.s. pressure was not reported.

The one-dimensional wall pressure spectra as a function of the azimuthal (spanwise) and axial (streamwise) wave-numbers are shown in Figure 4.5, along with their planar counterparts (Choi & Moin [1990]). Note that the spanwise spectra (Figure 4.5 *a*) is not affected by the transverse curvature in the high wavenumber range. In the low wavenumber range the energy of the spanwise spectrum decreases

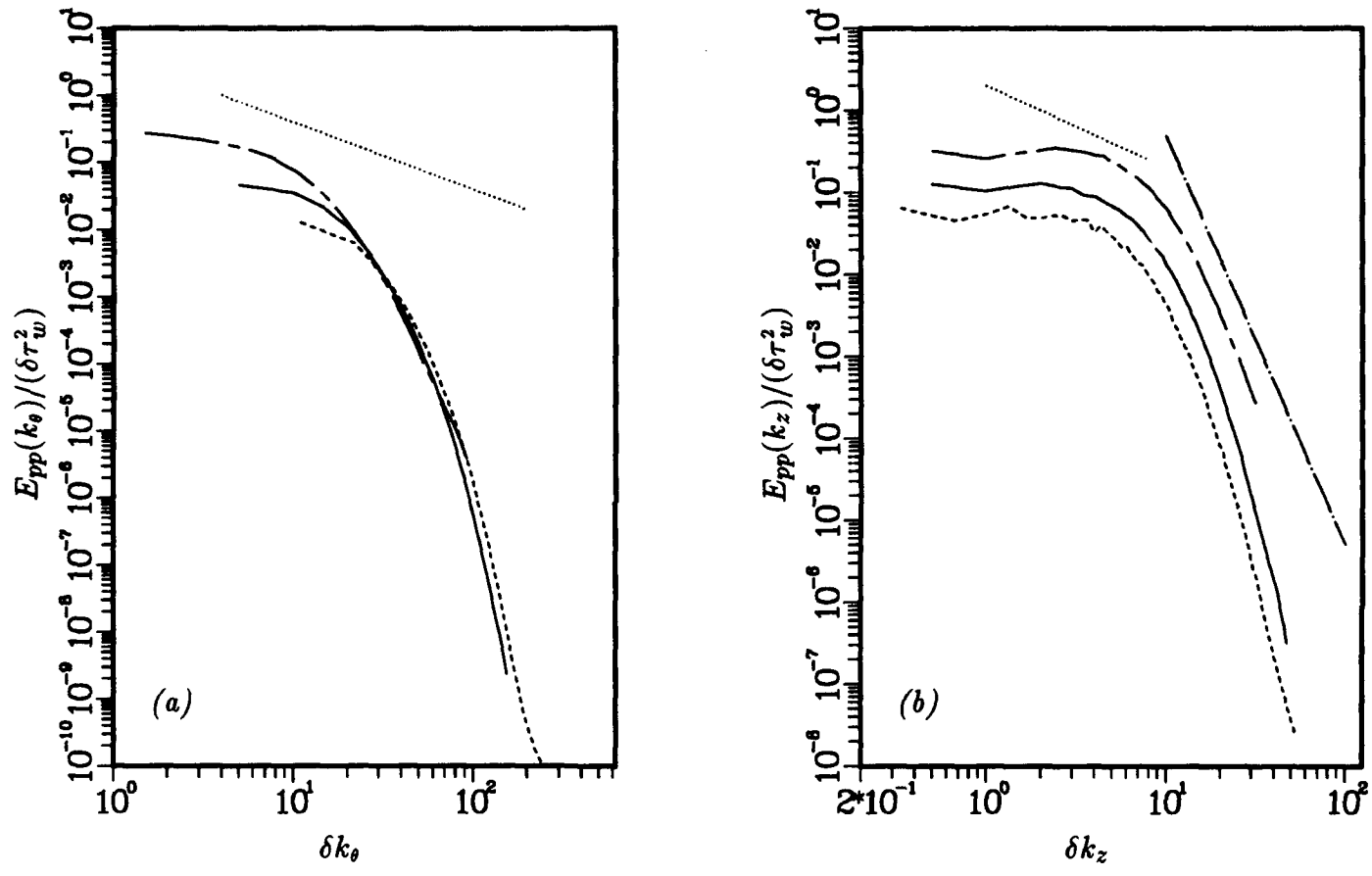

FIGURE 4.5 Spectra of the wall pressure fluctuations normalized by δ and u_τ: (a) Azimuthal (spanwise) spectra, (b) Axial (streamwise) spectra; —·— plane channel (Choi & Moin [1990]); cylinders ($\delta\Delta k_\theta = \delta/a$) with —— $\delta/a = 5$ and ---- $\delta/a = 11$; ····· -1 slope; —·— -5 slope.

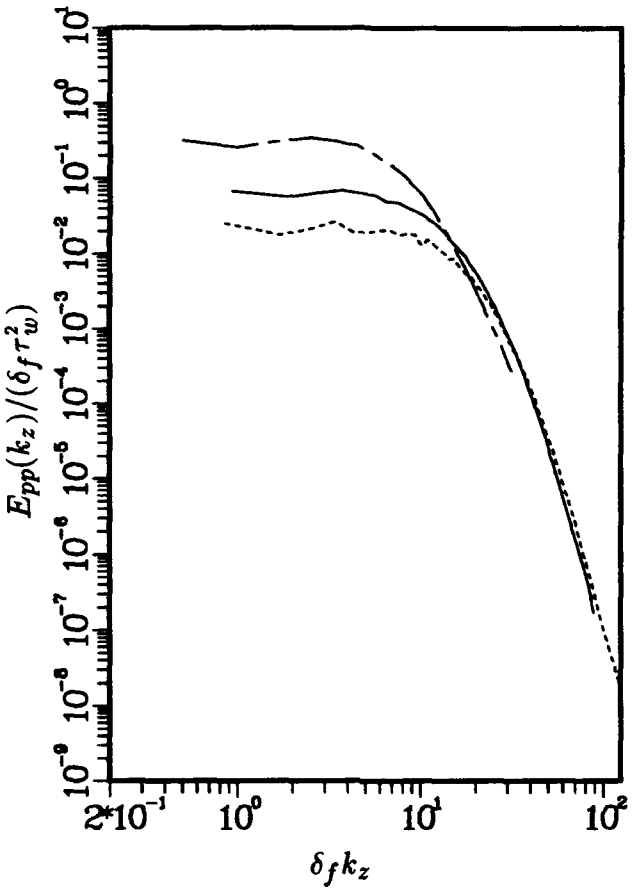

FIGURE 4.6 Axial (streamwise) spectra of the wall pressure fluctuations normalized by δ_f and u_τ: ——— plane channel (Choi & Moin [1990]) ($\delta/a = 0$, $\delta_f = \delta$); cylinders with —— $\delta/a = 5$ and ---- $\delta/a = 11$.

with increasing curvature. This suggests that the curvature mostly affects structures with large spanwise length scales (small δk_θ) than those with small spanwise length scales (large δk_θ). The streamwise spectral density of the wall pressure fluctuations decreases significantly with curvature for all scales (Figure 4.5 *b*). As expected, the three flows display a negligible wave-number range with the -1 slope in the streamwise spectrum. This feature is probably a result of the low Reynolds numbers of the three flows. The high wave-number range of the streamwise spectrum is associated with small structures and has a -5 slope in the planar case. In the transversely curved flows the axial spectra exhibit steeper slopes in the high wave-number range, indicating a weakening of structures in the buffer layer (Blake [1986]) that contribute to the wall pressure fluctuations.

In a transversely curved boundary layer, the volume of turbulent flow that must be supported per unit wall surface area is larger than in the plane channel case by a factor of $1 + \delta/(2a)$. This is a natural curvature parameter. It was found that when scaled with the curvature dependent length scale given by

$$\delta_f = \delta\sqrt{\left(1 + \frac{\delta}{2a}\right)}, \tag{4.3.1}$$

the axial (streamwise) spectrum of the wall pressure fluctuations of the plane channel flow and of the transversely curved flows collapse in the high wave number range, as shown in Figure 4.6. This length scale is related to the velocity scale defined in Section **3.2.3** (Equation 3.2.5, see Section **4.6**). Spectra normalized with $\overline{p^2}_w^{1/2}$ are shown in Figure 4.7.

The two-dimensional spatial wall pressure spectra are shown in Figure 4.8. As in the planar case (see Fig. 12 of Choi & Moin [1990]) the transversely curved spectra are elongated in the the spanwise direction. However, as the curvature increases the azimuthal (spanwise) elongation of the spectrum increases. In addition the energy of the large structures (small δk_z or δk_θ) decreases with increasing curvature.

4.4 Two-point correlations

In the two previous studies of the wall pressure fluctuations in boundary layers with transverse curvature (Willmarth & Yang [1970] and Willmarth *et al.* [1976]) it was shown that, as the curvature increases, the wall pressure becomes better correlated around the cylinder. This trend is also evident in the present flows as shown in Figure 4.9 *a*. Note, however, that in viscous units the azimuthal (spanwise) correlation length decreases with increasing curvature (Figure 4.9 *b*). In the axial two-point correlations (Figure 4.10), the zero-crossing point, $R_{pp}(z/\delta^*) = 0$, is reached at $z/\delta^* = 3.9$ in the $\delta/a = 5$ flow and at $z/\delta^* = 4.6$ in the $\delta/a = 11$ flow. Both values are higher than the value of 2 reported by Willmarth & Yang (1970) and Wilmarth *et al.* (1976), however, when compared with the value of 3.4 reported by Choi & Moin (1990) for the plane channel, a trend towards larger axial length scales with increasing curvature is discernible.

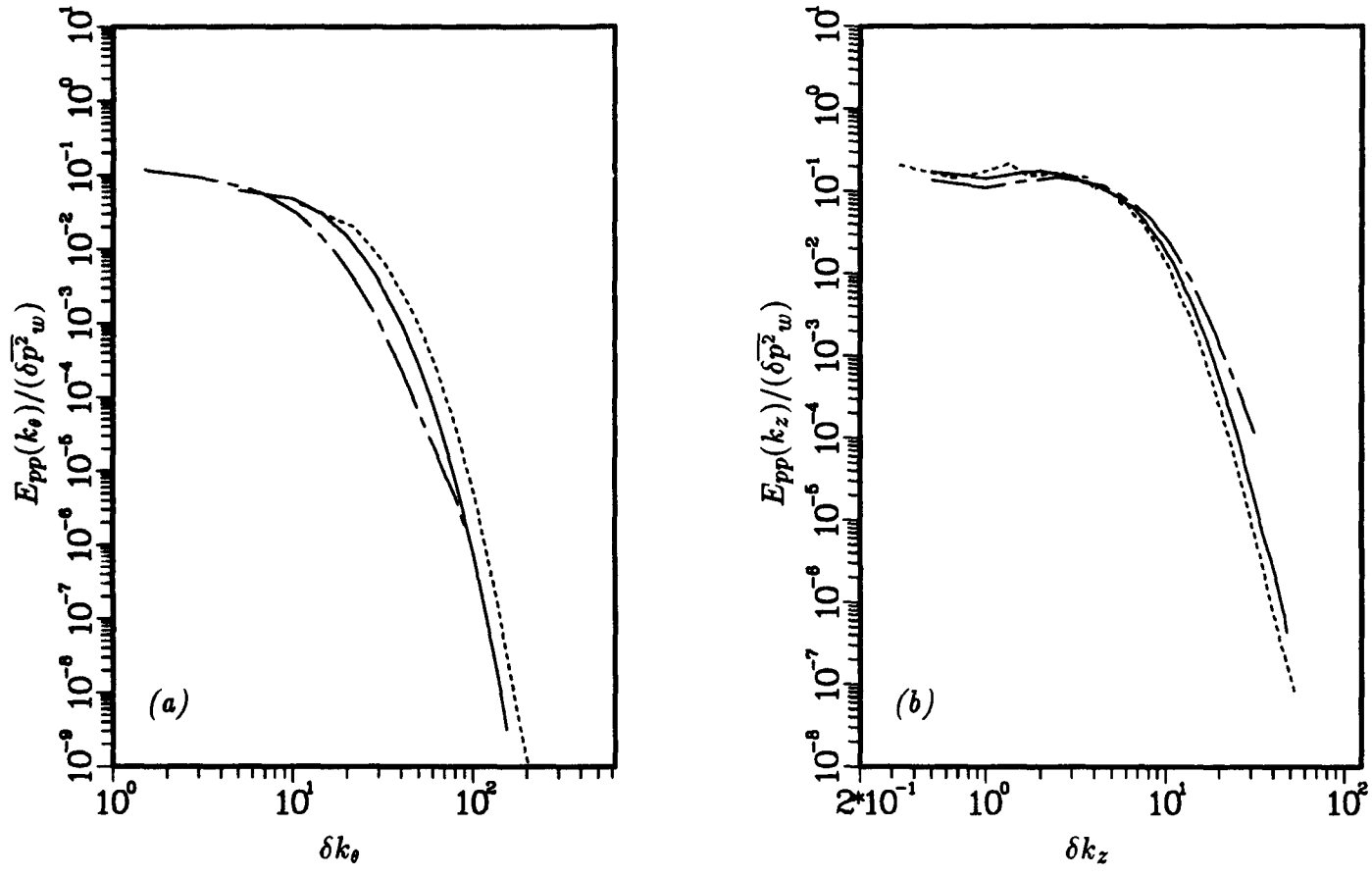

FIGURE 4.7 Spectra of the wall pressure fluctuations normalized by δ and $\overline{p^2}_w^{1/2}$: (a) Azimuthal (spanwise) spectra, (b) Axial (streamwise) spectra; —·— plane channel (Choi & Moin [1990]); cylinders ($\delta\Delta k_\theta = \delta/a$) with —— $\delta/a = 5$ and ---- $\delta/a = 11$.

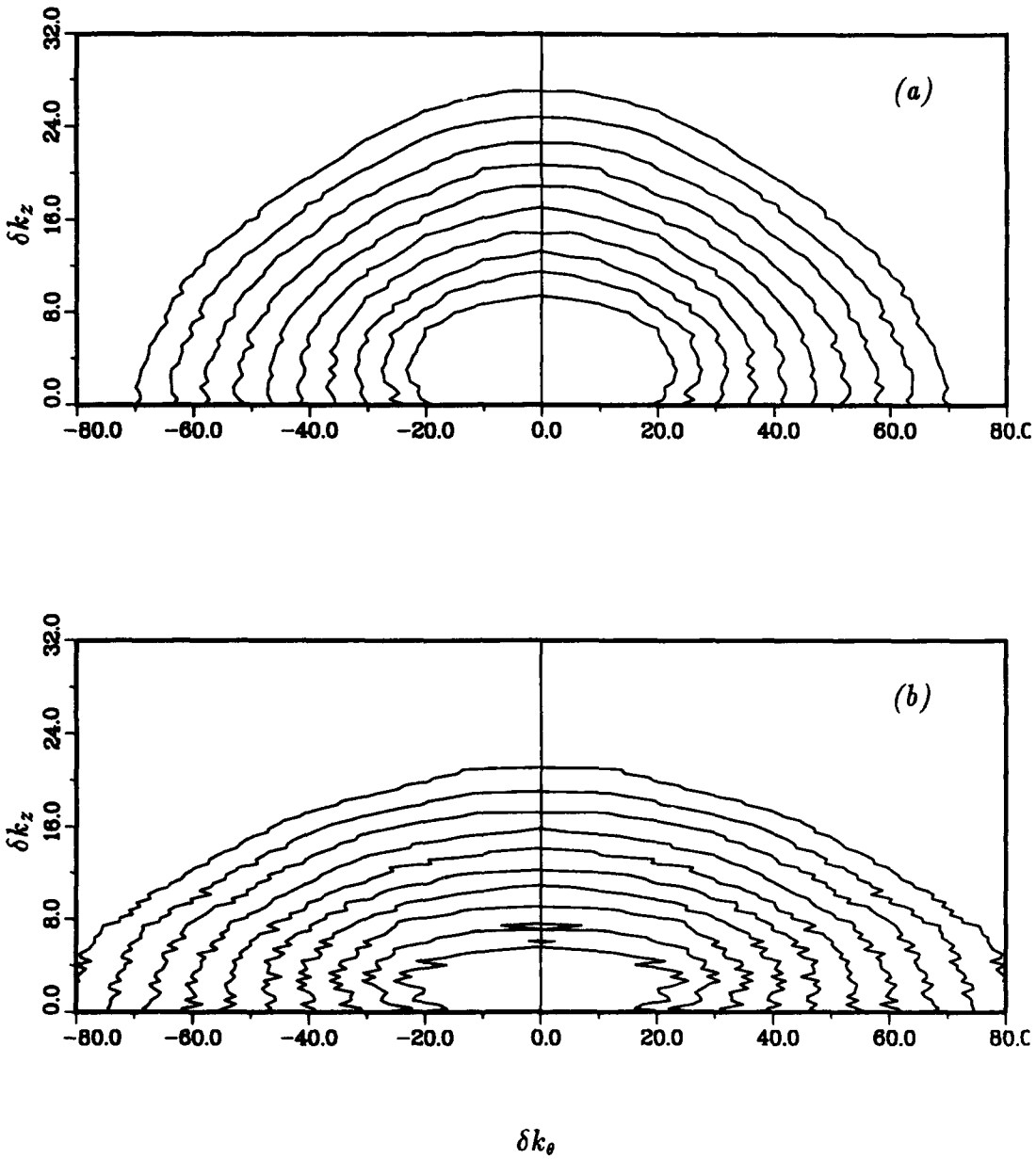

FIGURE 4.8 Spectra of the wall pressure fluctuations normalized by u_τ and δ ($\delta\Delta k_\theta = \delta/a$, and the scale of the ordinate is twice that of the abscissa): (a) $\delta/a = 5$, (b) $\delta/a = 11$. The contour levels are logarithmically distributed from 10^{-6} to 10^{-3} with exponent increments of 0.3.

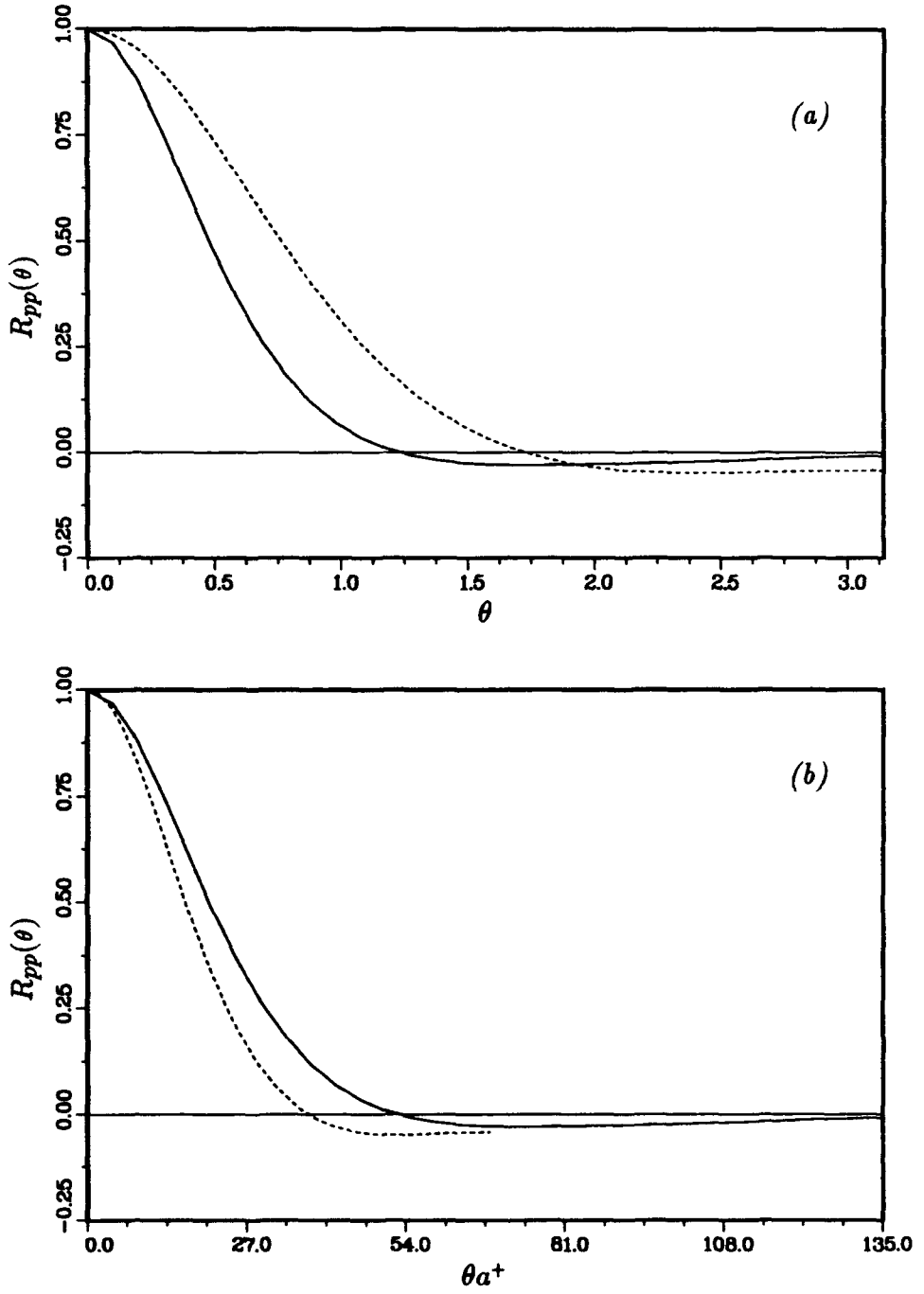

FIGURE 4.9 Azimuthal (spanwise) two-point correlations of the wall pressure fluctuations as a function of (*a*) θ and of (*b*) θa^+: —— $\delta/a = 5$ ($a^+ \approx 43$); ---- $\delta/a = 11$ ($a^+ \approx 21$).

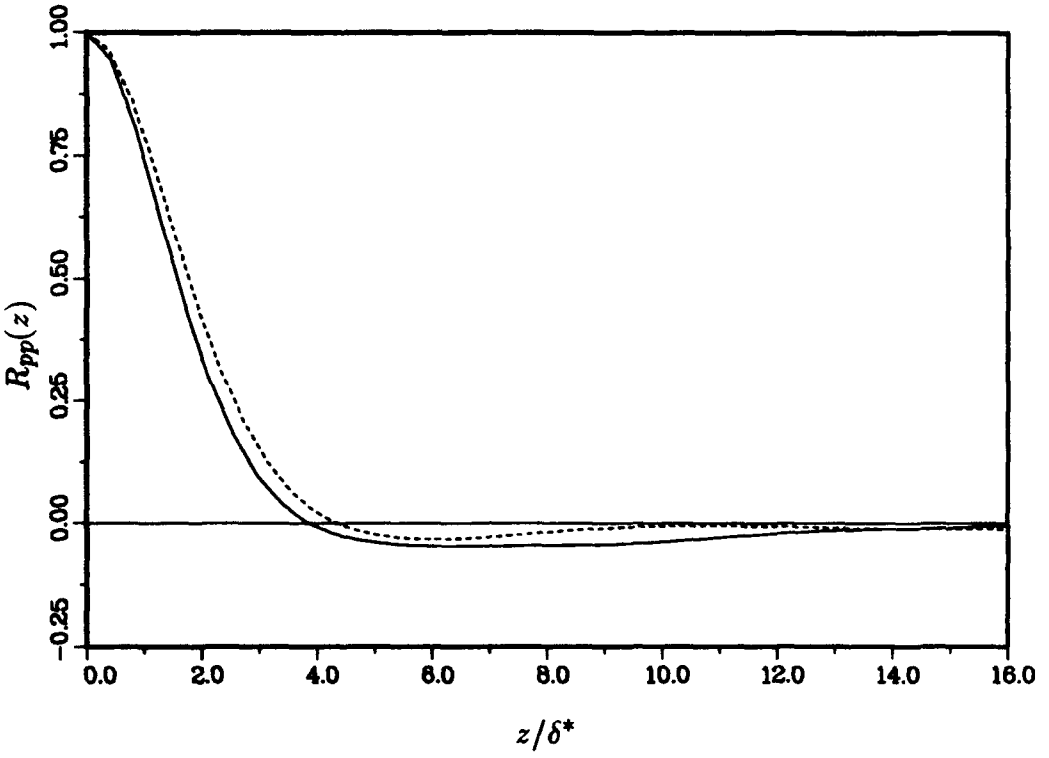

FIGURE 4.10 Axial (streamwise) two-point correlations of the wall pressure fluctuations: —— $\delta/a = 5$ and ---- $\delta/a = 11$.

For small separations, the wall pressure correlation contours in the planar case (Willmarth *et al.* [1962], Choi & Moin [1990]) are nearly circular and, as the separation increases, the ratio of the spanwise to the streamwise length scales increases. In contrast with the planar wall pressure correlation contours, in a transversely curved flow Willmarth & Yang (1970) ($\delta/a = 2$ and $a^+ \approx 4500$) report wall pressure correlation contours which, for large separations, are compressed in the spanwise direction. However, the $\delta/a = 4$ measurements of Willmarth *et al.* (1976) seem to be inconsistent with this apparent trend. Figure 4.11 shows the correlation contours of the wall pressure fluctuations for the plane channel flow. For large separation the correlation contours are elongated in the spanwise direction. In contrast, Figure 4.12 shows that, as the curvature increases, there is a significant increase in the ratio of the axial to azimuthal length scales for all separations.

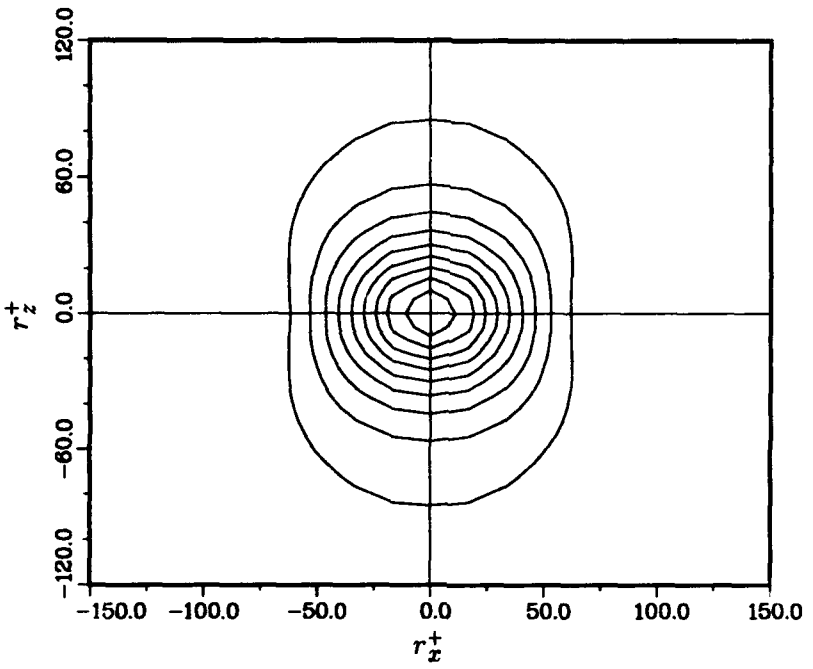

FIGURE 4.11 Contour plot of two-point correlations of the wall pressure fluctuations for plane channel (Choi & Moin [1990]) as a function of the streamwise (r_x^+) and spanwise (r_z^+) separations. The contour levels are from 0.1 to 0.9 with increments of 0.1.

4.5 Green's Function Representation

Further insight into the spatial structure of the the wall pressure fluctuations can be obtained by representing the pressure field in terms of the Green's function of the Poisson operator.

From the analysis presented in Appendix **B**, in transversely curved flows the Fourier coefficient of the wall pressure fluctuations are given by

$$\hat{p}(r) = \int_a^{a+1} \hat{\mathcal{G}}(r, r_o)\hat{f}(r_o) r_o dr_o + \\ a\hat{\mathcal{G}}(r, a)\frac{d\hat{p}}{dr}\bigg|_{r=a} - (a+1)\hat{\mathcal{G}}(r, a+1)\frac{d\hat{p}}{dr}\bigg|_{r=a+1}, \tag{4.5.1}$$

where r_o is the radial position of the source, $\hat{f}$ denotes the Fourier transform of the source of the pressure Poisson equation (Equation 4.1.1 *a*) and $\hat{\mathcal{G}}$ is the Green's

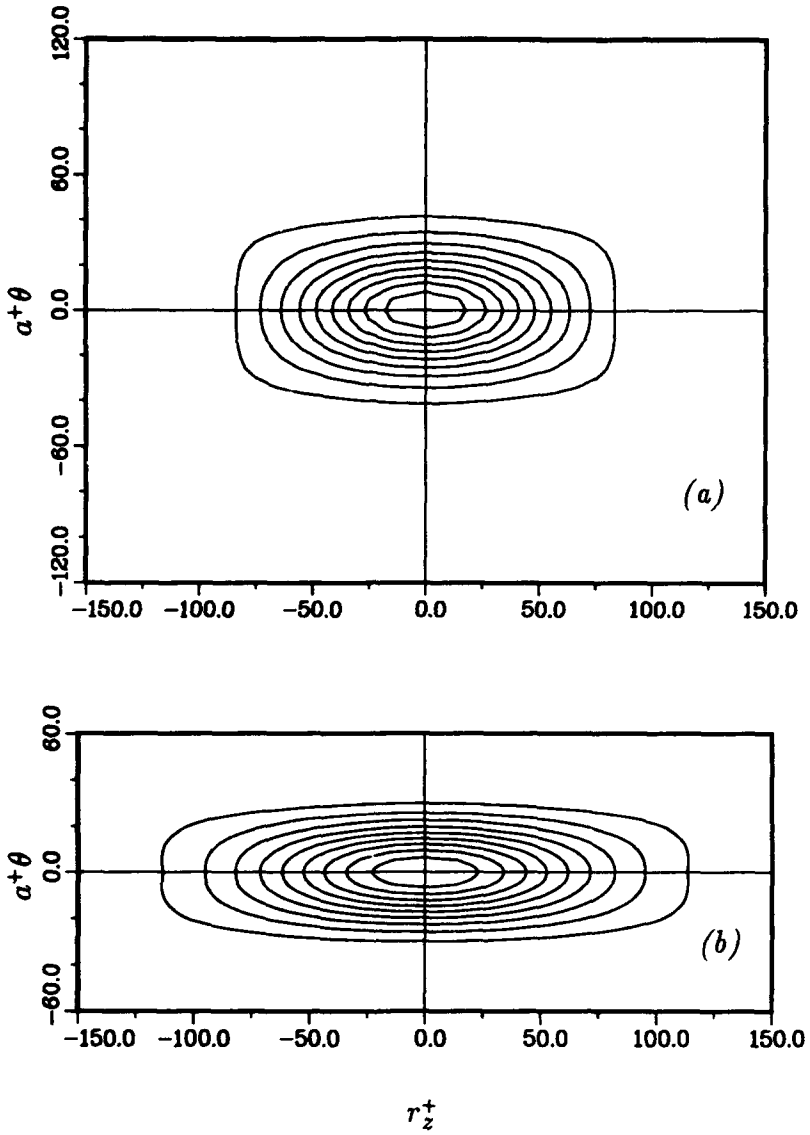

FIGURE 4.12 Contour plot of two-point correlations of the wall pressure fluctuations for (*a*) $\delta/a = 5$ and for (*b*) $\delta/a = 11$ as a function of the axial (r_z^+ - streamwise) and azimuthal ($a^+\theta$ - spanwise) separations. The contour levels are from 0.1 to 0.9 with increments of 0.1.

function of the Laplacian operator in cylindrical coordinates with derivative boundary conditions. The global nature of the pressure field is clear in Equation 4.5.1 due to the volume integral of $\hat{\mathcal{G}}(r, r_o)\hat{f}(r_o)$ over the whole flowfield. From Equation 4.5.1 the contributions to the wall pressure fluctuations ($\hat{p}_{r_s^-}$) from sources located in the volume close to the cylinder surface at $a \leq r_o \leq r_s$ are given by

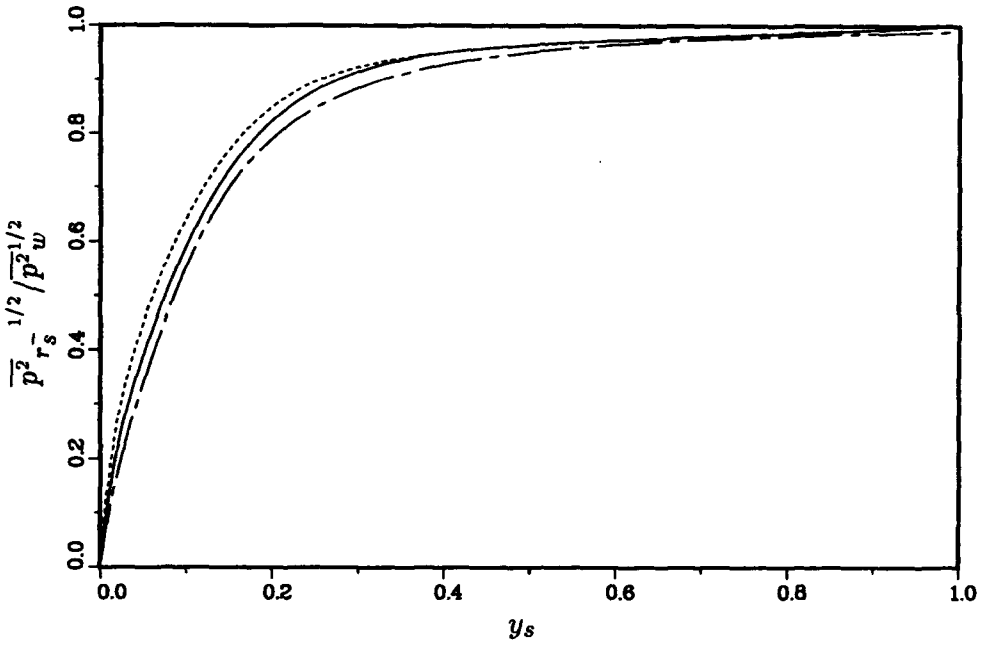

FIGURE 4.13 Fractional contributions to the root-mean-square wall pressure fluctuations from sources located at $y_o \in [0, y_s]$: ——— plane channel; cylinders with —— $\delta/a = 5$ and ---- $\delta/a = 11$ ($y_s = r_s - a$). The result is normalized by the total wall pressure intensity.

$$\hat{p}_{r_s^-} = \int_a^{r_s} \hat{\mathcal{G}}(a, r_o)\hat{f}(r_o) r_o dr_o + a\hat{\mathcal{G}}(a,a)\frac{d\hat{p}}{dr}\bigg|_{r=a} - r_s\hat{\mathcal{G}}(a,r_s)\frac{d\hat{p}}{dr}\bigg|_{r=r_s}. \tag{4.5.2}$$

Likewise, the contributions of the outer part of the volume of the flow ($r_s \leq r_o \leq a+1$) to the wall pressure fluctuations ($\hat{p}_{r_s^+}$) are given by

$$\hat{p}_{r_s^+} = \int_{r_s}^{a+1} \hat{\mathcal{G}}(a, r_o)\hat{f}(r_o) r_o dr_o + r_s\hat{\mathcal{G}}(a,r_s)\frac{d\hat{p}}{dr}\bigg|_{r=r_s} - (a+1)\hat{\mathcal{G}}(a,a+1)\frac{d\hat{p}}{dr}\bigg|_{r=a+1}. \tag{4.5.3}$$

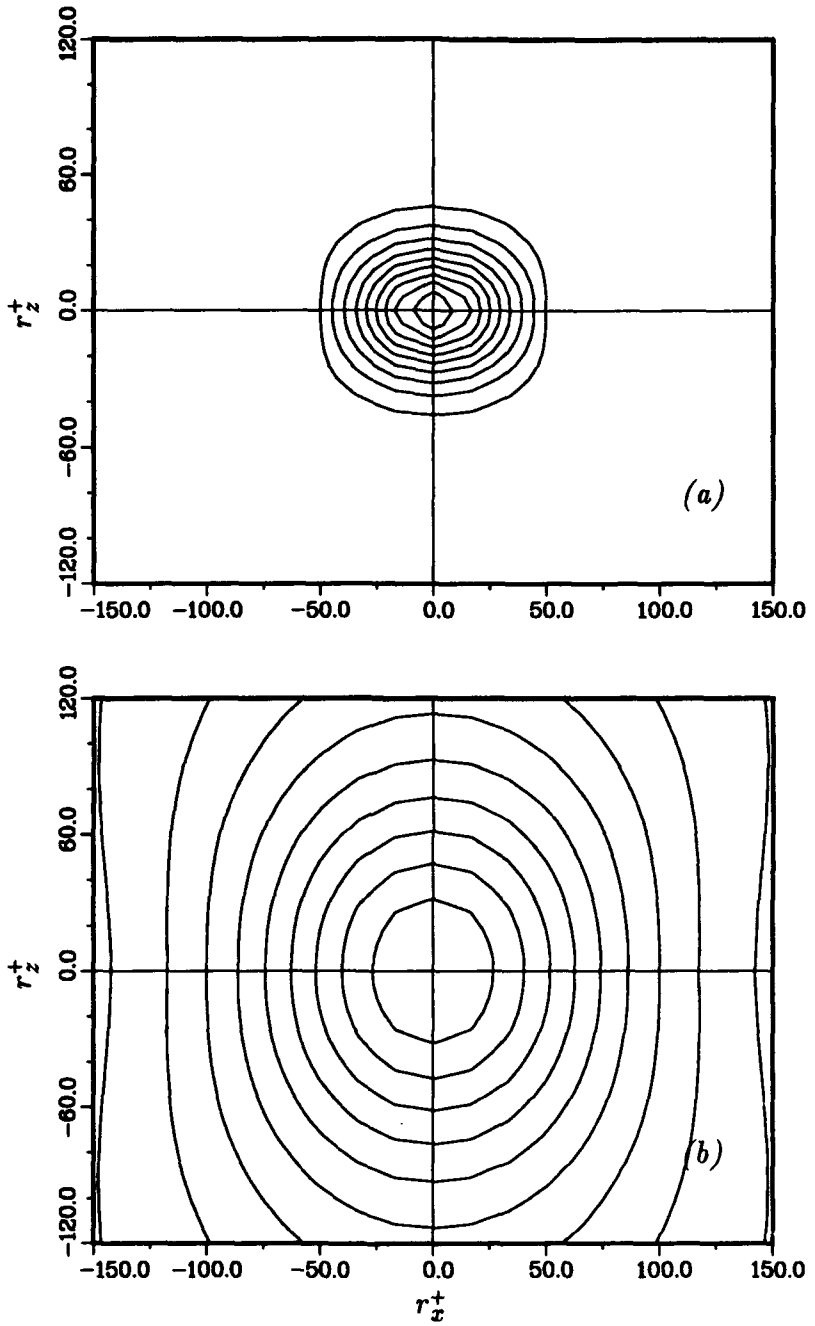

FIGURE 4.14 Contour plot of two-point correlations of the contributions to the wall pressure fluctuations in the plane channel from flow perturbations in the interval (*a*) $[0, y_s]$ and (*b*) $[y_s, 1]$ (1 denotes the channel centerline) as a function of the streamwise (r_x^+) and spanwise (r_z^+) separations. The contour levels are from 0.1 to 0.9 with increments of 0.1 and $y_s \approx 0.2$ ($y_s^+ \approx 36$).

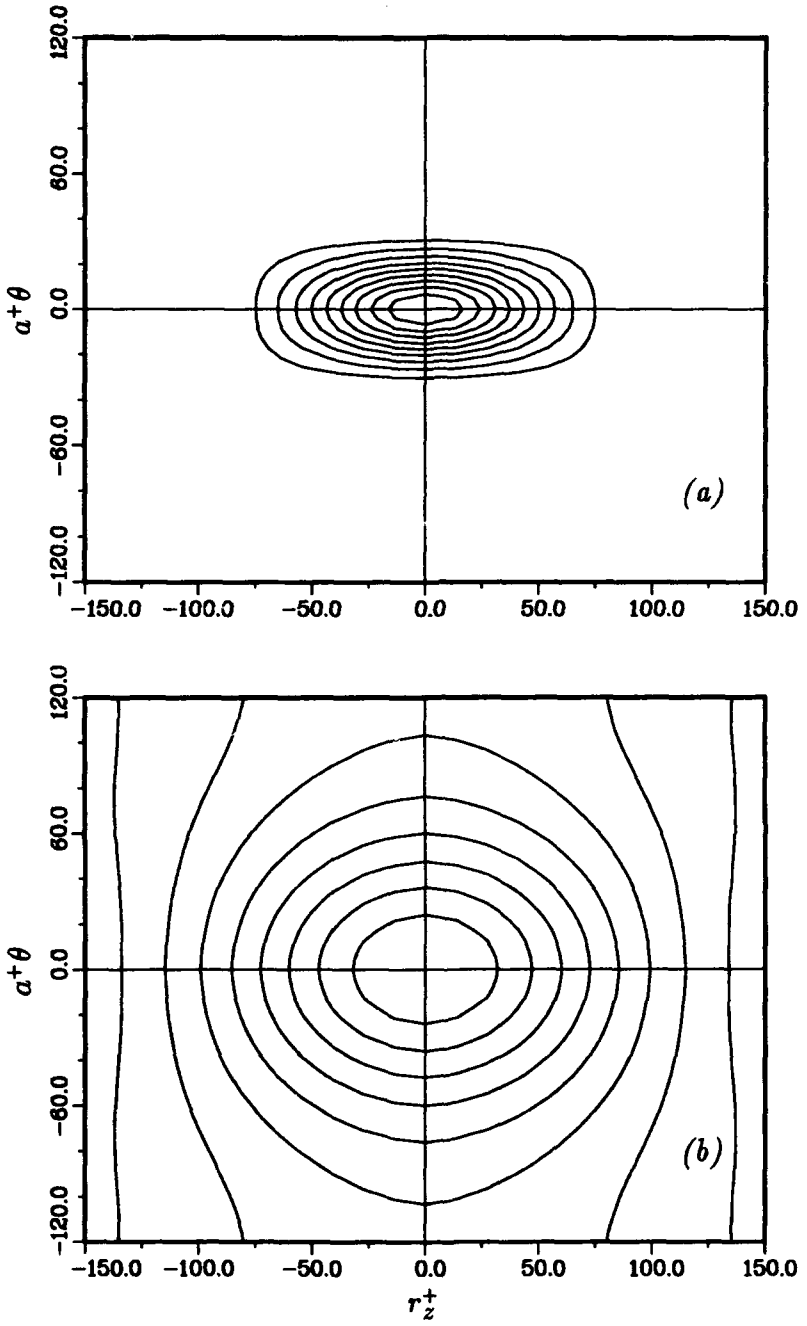

FIGURE 4.15 Contour plot of two-point correlations of the contributions to the wall pressure fluctuations for $\delta/a = 5$ from flow perturbations in the interval (a) $[a, r_s]$ and (b) $[r_s, a+1]$ as a function of the axial (r_z^+ - streamwise) and azimuthal ($a^+\theta$ - spanwise) separations. The contour levels are from 0.1 to 0.9 with increments of 0.1 and $y_s \approx 0.2$ ($y_s^+ = r_s^+ - a^+ \approx 46$).

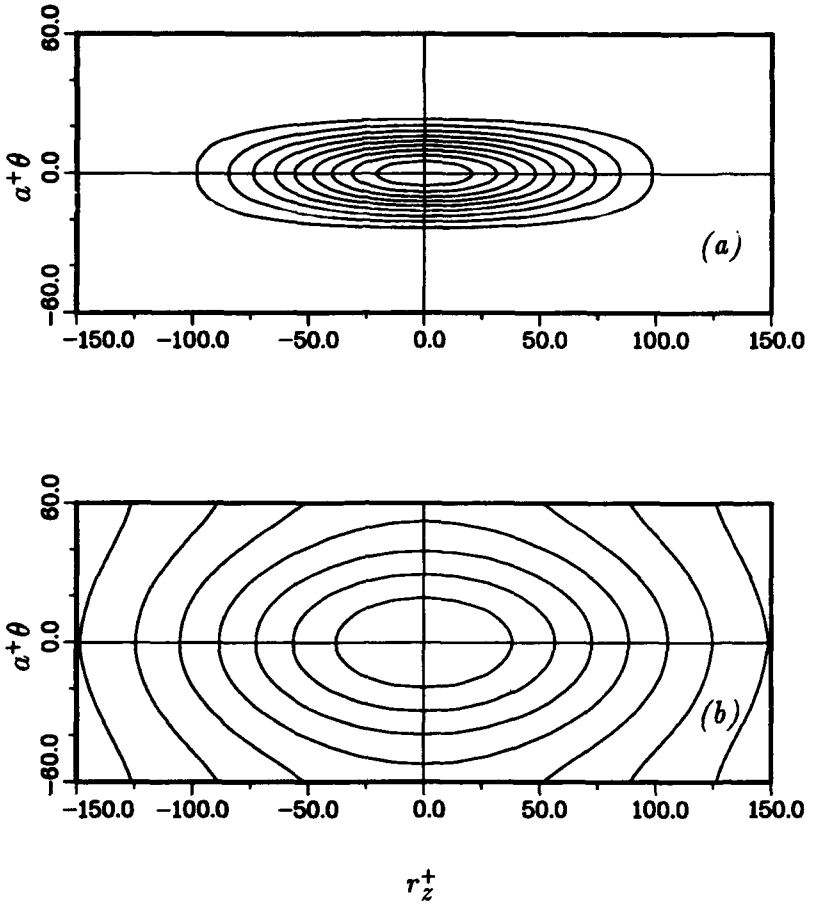

FIGURE 4.16 Contour plot of two-point correlations of the contributions to the wall pressure fluctuations for $\delta/a = 11$ from flow perturbations in the interval (a) $[a, r_s]$ and (b) $[r_s, a+1]$ as a function of the axial (r_z^+ - streamwise) and azimuthal ($a^+\theta$ - spanwise) separations. The contour levels are from 0.1 to 0.9 with increments of 0.1 and $y_s \approx 0.2$ ($y_s^+ = r_s^+ - a^+ \approx 49$).

Similar expressions can be obtained for the plane channel. The root-mean-square of the contributions to the wall pressure fluctuations normalized by the total wall r.m.s. pressure is shown in Figure 4.13 as a function of the cutoff r_s. For the two transversely curved flows as well as the plane channel more than 80% of the wall r.m.s. pressure fluctuations are produced by the inner part of the domain ($0 \leq r_o \leq y_s = r_s - a \approx 0.2$). Note that, as the curvature increases, there is a slight increase in the wall pressure fractional contributions from the near-wall ($y_s < 0.2$) part of the flow.

Small separation correlation contours result from small scale pressure fluctuations typically associated with the inner part of the boundary layer, while the large separation correlation contours have significant contributions from large scale motions in the outer part of the boundary layer. This is emphasized in Figure 4.14 which shows the plane channel two-point correlations of $\hat{p}_{y_s^-}$ and $\hat{p}_{y_s^+}$ for $y_s \approx 0.2$. It is clear that the spanwise elongation of the planar wall pressure correlation contours is due to disturbances in the outer part of the layer (Figure 4.14 *b*). Note also that for this cutoff ($y_s \approx 0.2$) the shape of the planar wall pressure correlation contours due to the inner part of the flow are slightly elongated in the streamwise direction (Figure 4.14 *a*).

The two-point correlations of $\hat{p}_{r_s^-}$ and $\hat{p}_{r_s^+}$ for $y_s = r_s - a \approx 0.2$ are shown in Figures 4.15 and 4.16 for $\delta/a = 5$ and for $\delta/a = 11$, respectively. In both cases the two point correlations of the wall pressure fluctuations due to contributions from the volume close to the cylinder have a streamwise aspect ratio similar to that shown in Figure 4.12 for the contributions of the whole flow. On the other hand, in the $\delta/a = 5$ flow, the shape of the correlation contours of the wall pressure fluctuations due to the outer part of the flow ($y_o \in [y_s \approx 0.2, 1.0]$, see Figure 4.15 *b*) have nearly circular shapes for small separations and a spanwise orientation for large separations. The same trend is also evident in the $\delta/a = 11$ flow, although, a streamwise orientation is discernible in the wall pressure correlation contours due to sources in the outer part of the flow (Figure 4.16 *b*). Wall pressure correlation contours due to the outer part of the flow, obtained for larger values of the cutoff ($y_s > 0.2$, not shown), become increasingly oriented in the spanwise direction in both transversely curved flows ($\delta/a = 5$ and $\delta/a = 11$), however, the spanwise stretching effect of the outer part of the flow on the wall pressure correlations decreases as the curvature increases.

The fact that, in the three flows, the wall pressure correlations due to the near-wall part of the flow are elongated in the streamwise direction implies that the near-wall structures are responsible for this shape. The curvature trend shown in Figures 4.14 through 4.16 is consistent with the length scale parameter L^* based on v_z (see Section **3.5**, Figure 3.25) which suggests that relative to the plane channel, as the curvature increases, the ratio of the streamwise to spanwise length scales increases near the wall for both flows and away from the wall in only the $\delta/a = 11$ case. Thus, it is conjectured that, as the curvature increases, the inner part of the

flow plays an increasingly important role in determining the length scales of the wall pressure fluctuations.

4.6 Temporal Spectra

The temporal spectra of the wall pressure fluctuations of the two transversely curved turbulent flows is compared to their planar counterpart in Figure 4.17 *a*. As expected from the streamwise one-dimensional spectrum, the temporal spectrum decreases at all frequencies with increasing curvature.

In the wall pressure temporal spectra measurements of Willmarth & Yang (1970) and Willmarth *et al.* (1976), a reduction in the intensity of the high frequency range was also observed. However, the effect of curvature on the inner part of the boundary layer in their flow regime (high a^+), and therefore on the high frequency range of their wall pressure temporal spectra should have been negligible. This apparent inconsistency in the experimental data may be related to probe spatial resolution problems, which were not corrected for.

Using the curvature dependent length scale defined in Section **4.3** (Equation 4.3.1), a curvature dependent time scale (δ_f/u_τ) can be defined:

$$\frac{\delta_f}{u_\tau} = \frac{\delta}{u_\tau}\sqrt{\left(1+\frac{\delta}{2a}\right)}. \tag{4.6.1}$$

When scaled with this curvature dependent time scale the temporal spectrum of the wall pressure fluctuations of the two transversely curved flows collapse with their planar counterpart in the high frequency range (Figure 4.17 *b*). Also note that this time scale is related to the velocity scale $\underline{u}$ defined in Section **3.2.3** (Equation 3.2.5) by

$$\frac{\delta_f}{u_\tau} = \frac{\delta}{\underline{u}(y/\delta=1)}. \tag{4.6.2}$$

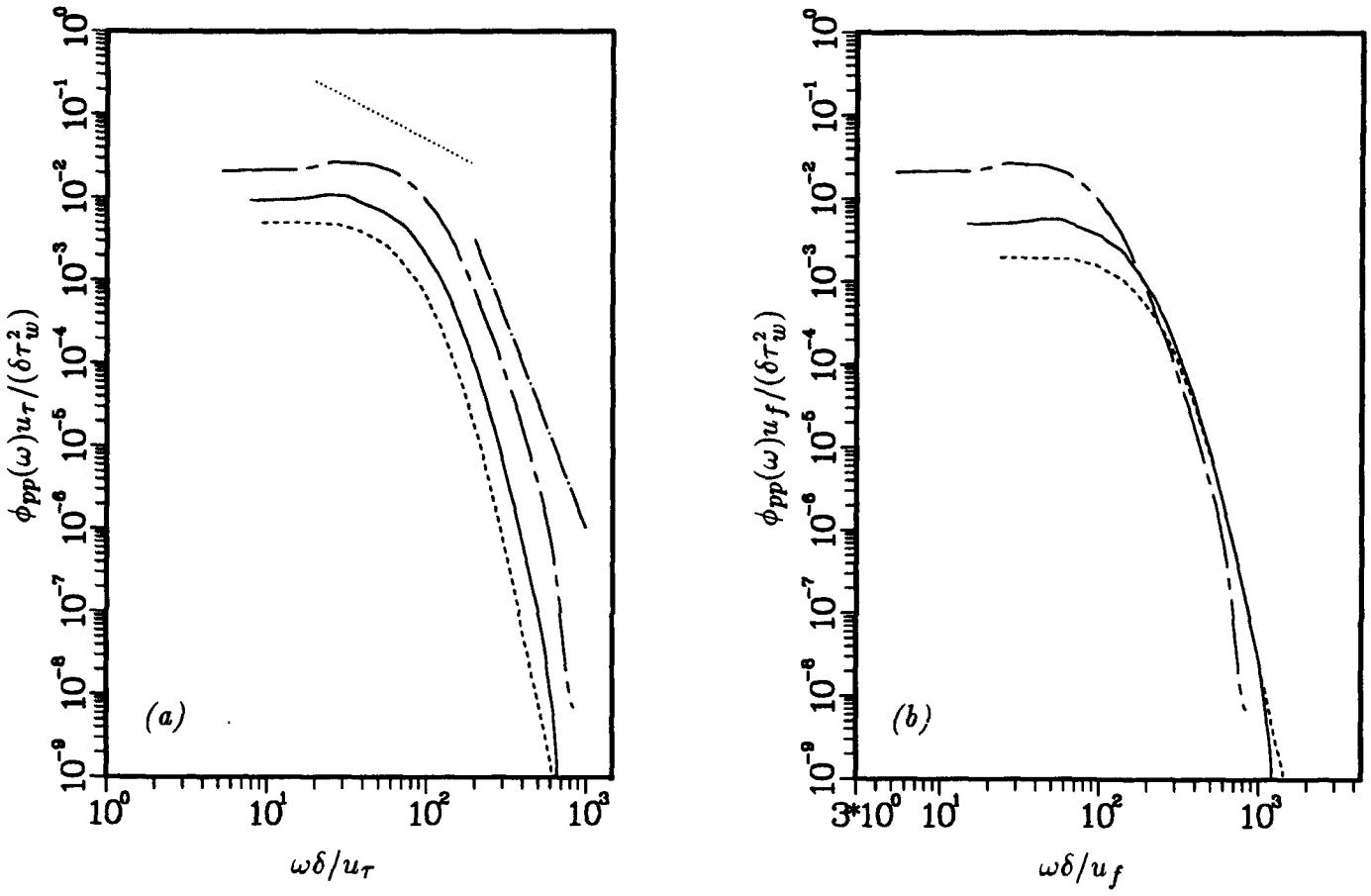

FIGURE 4.17 Temporal spectra of the wall pressure fluctuations normalized by τ_w^2: (*a*) δ/u_τ time scale; (*b*) δ/u_f time scale. —·— plane channel (Choi & Moin [1990]) ($\delta/a = 0$, $u_f = u_\tau$); cylinders with —— $\delta/a = 5$ and ---- $\delta/a = 11$; ····· -1 slope; —·— -5 slope.

4.7 2-D Spectra and Correlations

The frequency/axial (streamwise) wave-number power spectra, $\Phi_{pp}(k_z,\omega)$, for the two transversely curved flows are shown in Figure 4.18. As has been the case throughout this study the intensity decreases as the curvature increases for all frequencies and axial length scales. In both cases the narrow aspect ratios of the iso-contours denote well defined convection velocities.

The space-time correlation of the wall pressure fluctuations is given by the Fourier transform of the frequency / streamwise wave-number spectrum,

$$R_{pp}(r_z,r_t) = \sum_{k_z}\sum_{\omega} \Phi_{pp}(k_z,\omega)e^{-i\omega r_t}e^{-ik_z r_z}, \qquad (4.7.1)$$

and is shown in Figure 4.19 for the two transversely curved flows. When measured in viscous units, the axial length scales of the auto-correlation contours are virtually unaffected by curvature, however, the temporal extent increases with curvature. Again, clearly defined convection velocities are evident from the oblong shape of the contours.

4.8 Convection Velocity and Taylor's Hypothesis

The idea that structures in the flow are convected at a velocity close to the free stream velocity is an attractive one which has received substantial experimental support in planar boundary layer flows. Experimentally, it is typically easier to measure temporal spectra, from which streamwise spectra are obtained by invoking the concept of a convection velocity and Taylor's hypothesis.

Several definitions for the convection velocity have been proposed in the literature. The most common are obtained from the frequency streamwise wave-number spectra, $\Phi_{pp}(k_z,\omega)$, or from its Fourier transform, $R_{pp}(r_z,r_t)$.

For example, the convection velocity as a function of the axial (streamwise) separation (r_z) for a given time delay (r_{t_c}), is defined as the ratio r_z/r_{t_c} for which $R_{pp}(r_z,r_{t_c})$ is a maximum,

$$U_c(r_z) = \frac{r_z}{r_{t_c}}, \qquad \left.\frac{\partial R_{pp}}{\partial r_z}(r_z,r_t)\right|_{r_t=r_{t_c}} = 0. \qquad (4.8.1\ a)$$

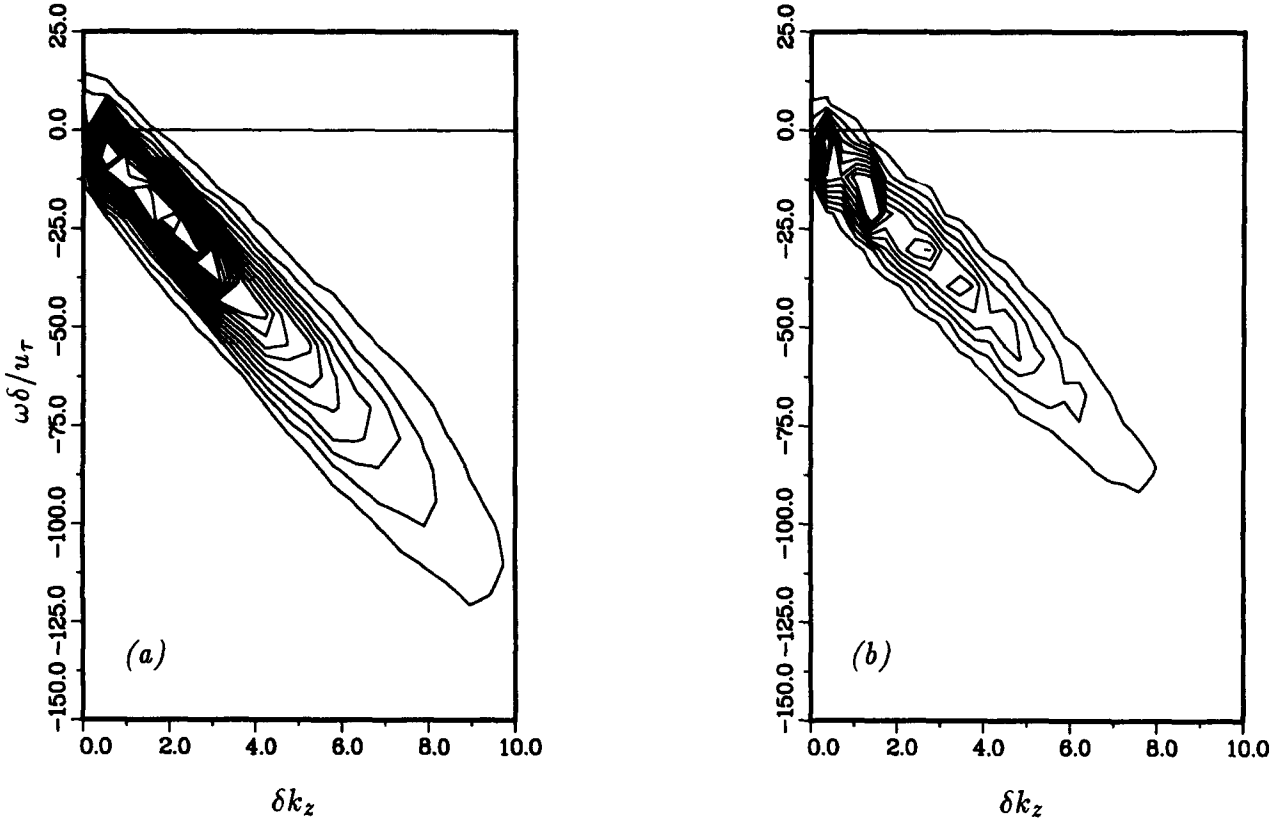

FIGURE 4.18 Contour plot of the axial (streamwise) wave-number-frequency spectra of the wall pressure fluctuations normalized by u_τ and δ: (*a*) $\delta/a = 5$ and the contour levels are from 0.00035 to 0.0070; (*b*) $\delta/a = 11$ and the contour levels are from 0.00035 to 0.0035. The contour increments are 0.00035.

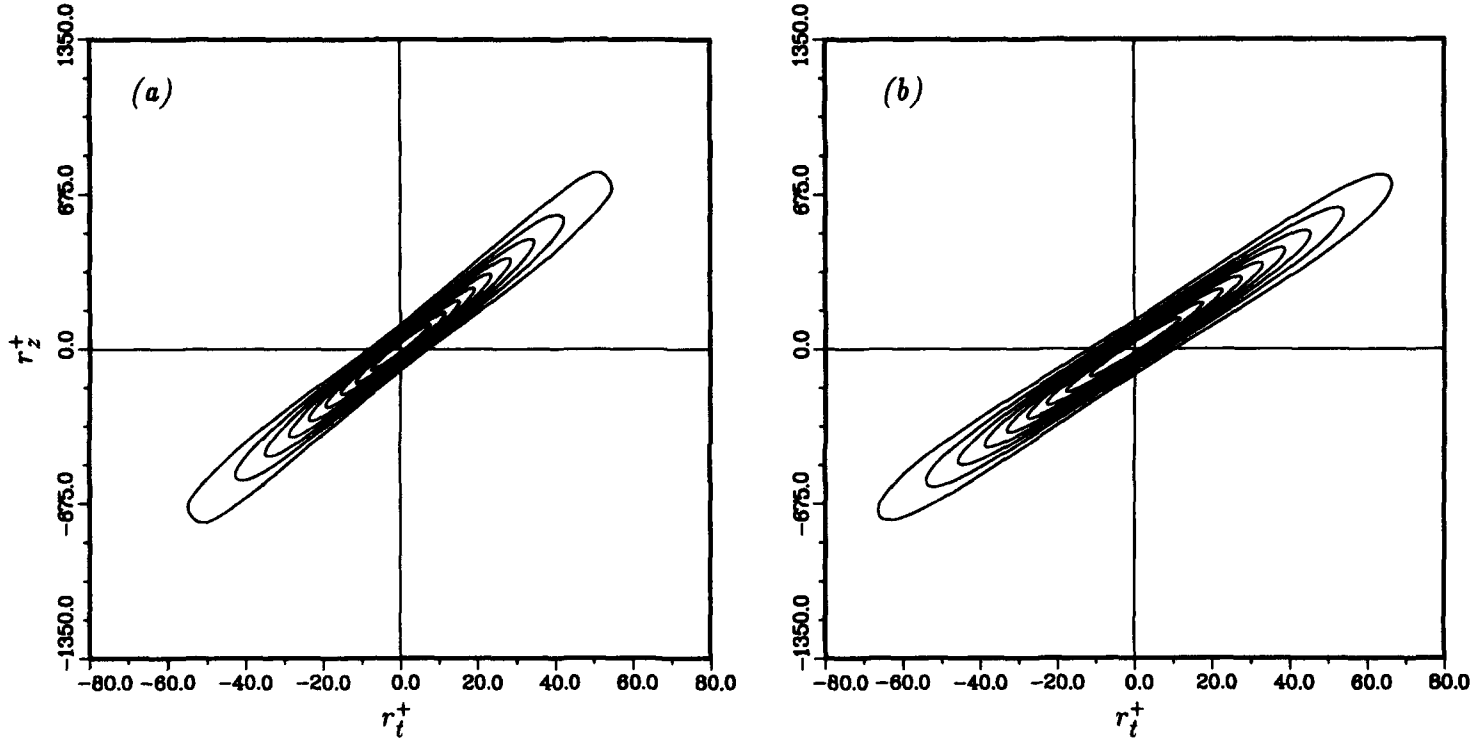

FIGURE 4.19 Contour plot of two-point correlations of the wall pressure fluctuations as a function of the axial (streamwise) spatial (r_z^+) and temporal (r_t^+) separations: (*a*) $\delta/a = 5$; (*b*) $\delta/a = 11$. The contours are from 0.1 to 0.9 with increments of 0.1.

Likewise, the convection velocity can be defined as a function of the temporal separation (r_t) according to

$$U_c(r_t) = \frac{r_{z_c}}{r_t}, \qquad \left.\frac{\partial R_{pp}}{\partial r_t}(r_z, r_t)\right|_{r_z = r_{z_c}} = 0. \qquad (4.8.1\ b)$$

The convection velocities of the wall pressure fluctuations computed from Equations 4.8.1 are shown in Figure 4.20. The convection velocities are lower than in the plane channel. As the axial separation increases, the convection velocity increases to about $0.7U_\infty$ for $\delta/a = 5$ and to about $0.65U_\infty$ for $\delta/a = 11$. Note, however, that as a function of the temporal separation the convection velocity is practically constant in both flows ($U_c \simeq 0.6U_\infty$).

The convection velocity can also be defined as a function of the streamwise wave-number (Wills ([1970]),

$$U_c(k_z) = -\frac{\omega_c}{k_z}, \qquad \left.\frac{\partial \Phi_{pp}}{\partial \omega}(k_z, \omega)\right|_{\omega = \omega_c} = 0, \qquad (4.8.2\ a)$$

and as a function of the frequency,

$$U_c(\omega) = -\frac{\omega}{k_{z_c}}, \qquad \left.\frac{\partial \Phi_{pp}}{\partial k_z}(k_z, \omega)\right|_{k_z = k_{z_c}} = 0. \qquad (4.8.2\ b)$$

When expressed as a function of the axial wave-number (Figure 4.21) the convection velocity is about $0.6U_\infty$ for large wave-numbers in all three flows. Likewise, as a function of frequency the convection velocity (Figure 4.22) is about $0.65U_\infty$ in the curved flows, which is lower than the value of about $0.8U_\infty$ for the plane channel (Choi & Moin [1990]).

In the cylinder flows, the various convection velocities show little variation among themselves. In the following a constant value of the convection velocity, $0.65U_\infty$, is used to scale the temporal spectrum ($\phi_{pp}(\omega)$) into the axial spectrum ($E_{pp}(k_z)$) according to Taylor's hypothesis:

$$E_{pp_c}(k_{zc}) = \frac{\phi_{pp}(\omega)}{U_c}, \qquad k_{zc} = \frac{\omega}{U_c}. \qquad (4.8.3)$$

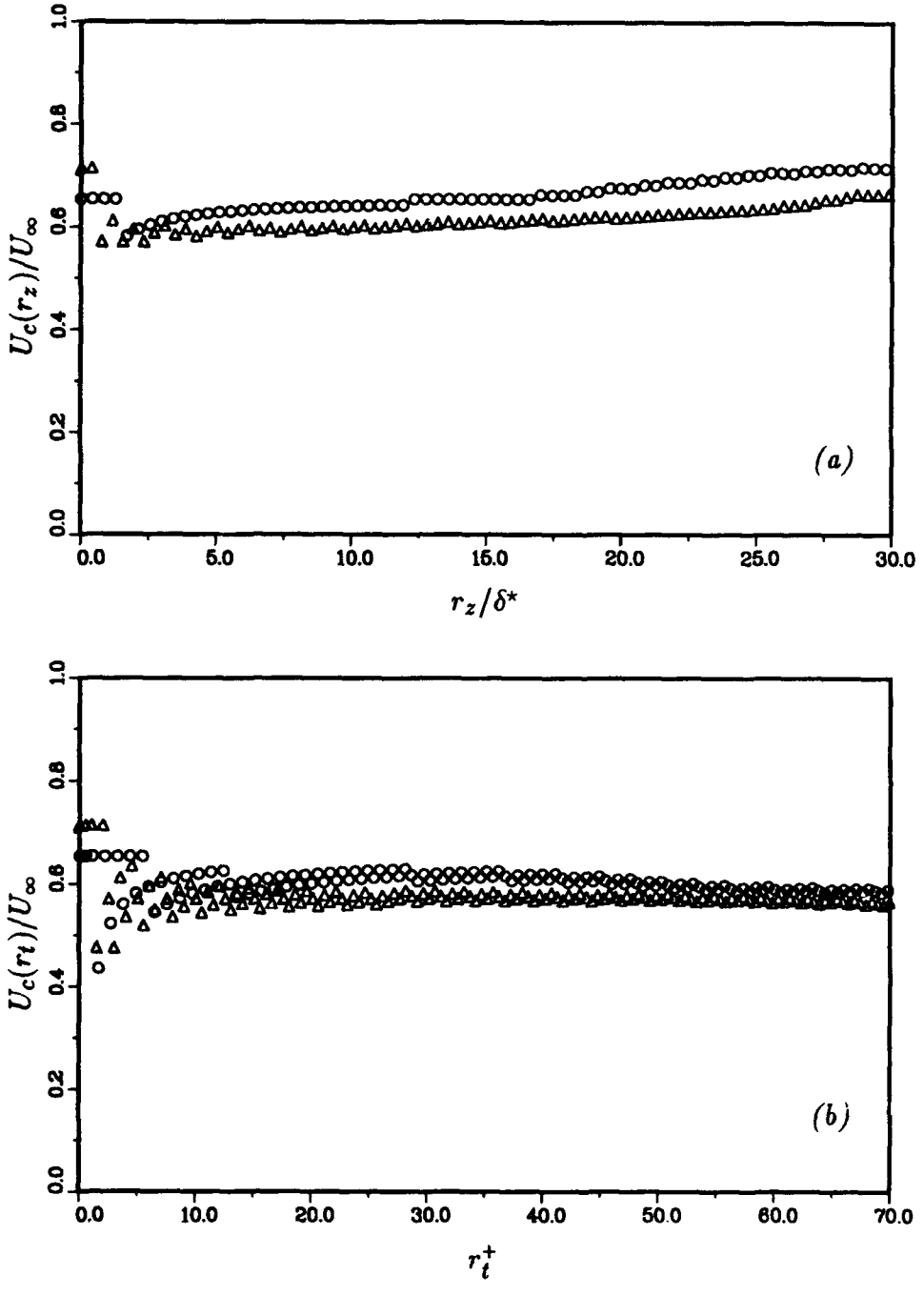

FIGURE 4.20 Convection velocity normalized by U_∞ as a function of the (a) axial (streamwise) separation (r_z/δ^*) and of the (b) temporal separation (r_t^+); cylinders: o, for $\delta/a = 5$ and Δ , for $\delta/a = 11$.

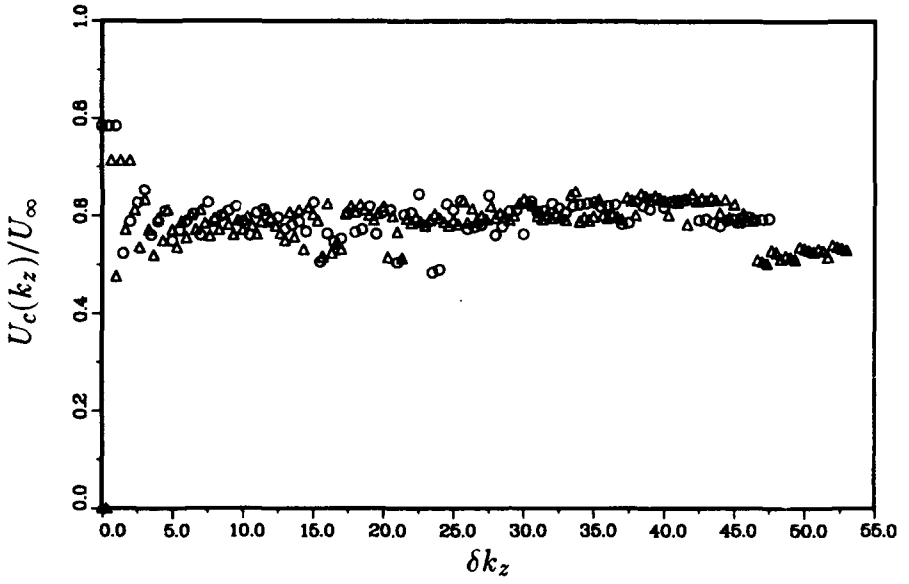

FIGURE 4.21 Convection velocity normalized by U_∞ as a function of the streamwise wave number: cylinders: o, for $\delta/a = 5$ and Δ , for $\delta/a = 11$.

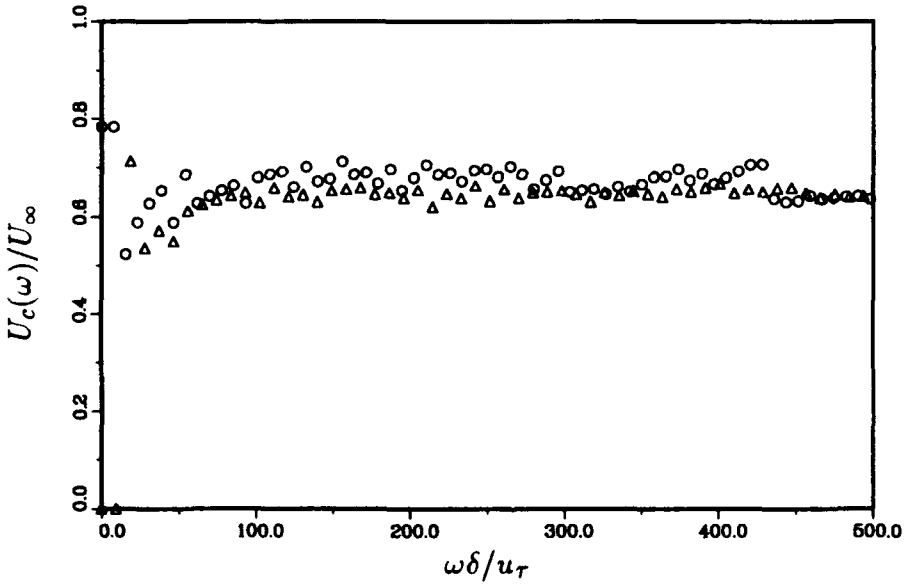

FIGURE 4.22 Convection velocity normalized by U_∞ as a function of frequency: cylinders: o, for $\delta/a = 5$ and Δ , for $\delta/a = 11$.

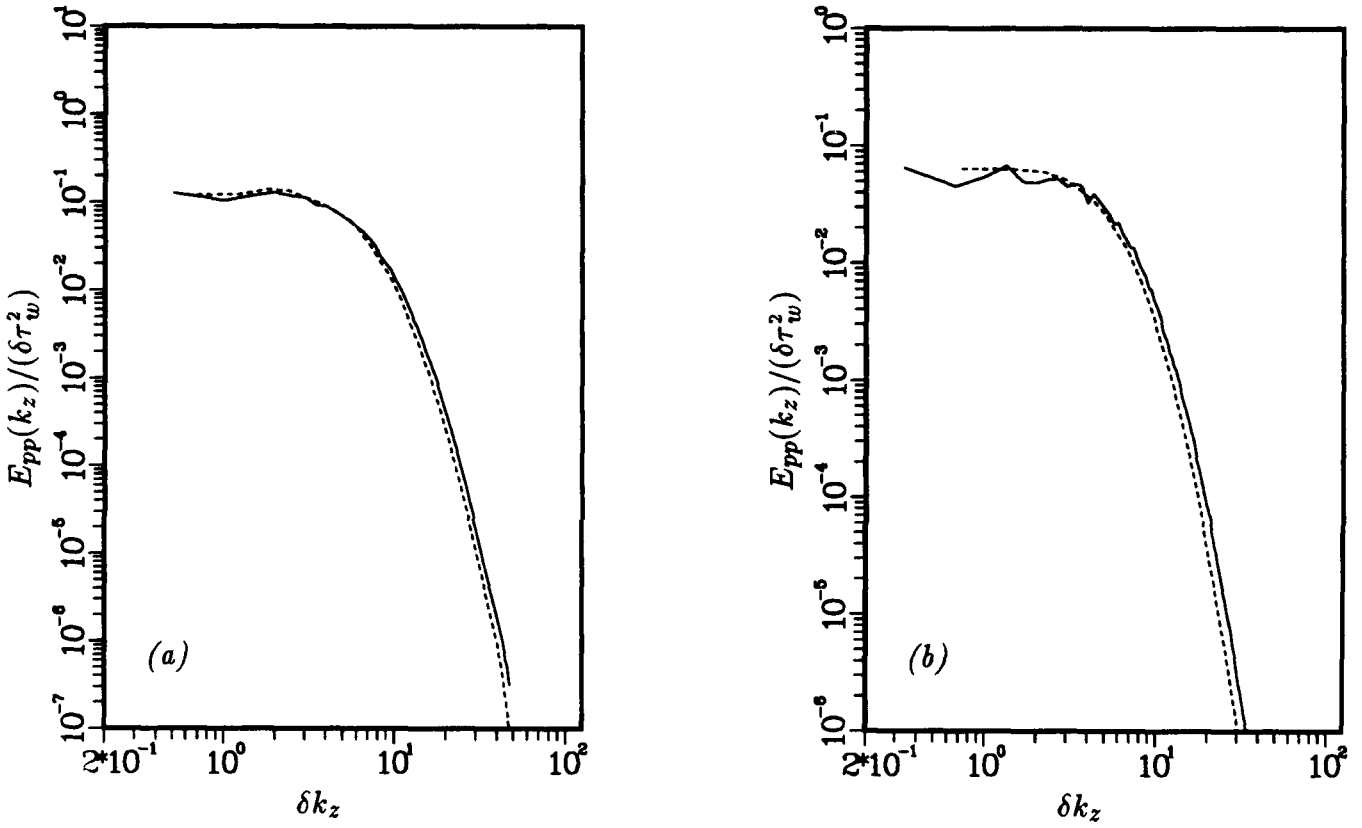

FIGURE 4.23 Conversion of the temporal spectrum to the axial (streamwise) wave-number spectrum using Taylor's hypothesis for (*a*) $\delta/a = 5$, and for (*b*) $\delta/a = 11$: —— $E_{pp}(k_z)$; ---- from $\phi_{pp}(\omega)$ using Taylor's hypothesis ($U_c \simeq 0.65U_\infty$).

Comparison of $\phi_{pp}(\omega)$ with $E_{pp_c}(k_{zc})$ (Figure 4.23) shows that Taylor's hypothesis is a better assumption for low frequencies, as was also observed in the planar case (Choi & Moin [1990]).

The decomposition of the two-dimensional spectra $\Phi_{pp}(k_z,\omega)$ and $\Phi_{pp}(k_\theta,\omega)$ into their streamwise and spanwise similarity functions $F_z(k_zU_c/\omega)$ and $F_\theta(k_\theta U_c/\omega)$, are given by

$$\begin{aligned}\Phi_{pp}(k_z,\omega) &= \phi_{pp}(\omega)\frac{U_c(\omega)}{\omega}F_z(k_zU_c/\omega),\\ \Phi_{pp}(k_\theta,\omega) &= \phi_{pp}(\omega)\frac{U_c(\omega)}{\omega}F_\theta(k_\theta U_c/\omega),\end{aligned} \tag{4.8.4}$$

respectively (Corcos [1964]). Unlike the plane channel where a self similar behavior in the spanwise direction was observed, no self similar behavior is apparent in either $F_z(k_zU_c/\omega)$ or $F_\theta(k_\theta U_c/\omega)$, as shown in Figures 4.24 and 4.25.

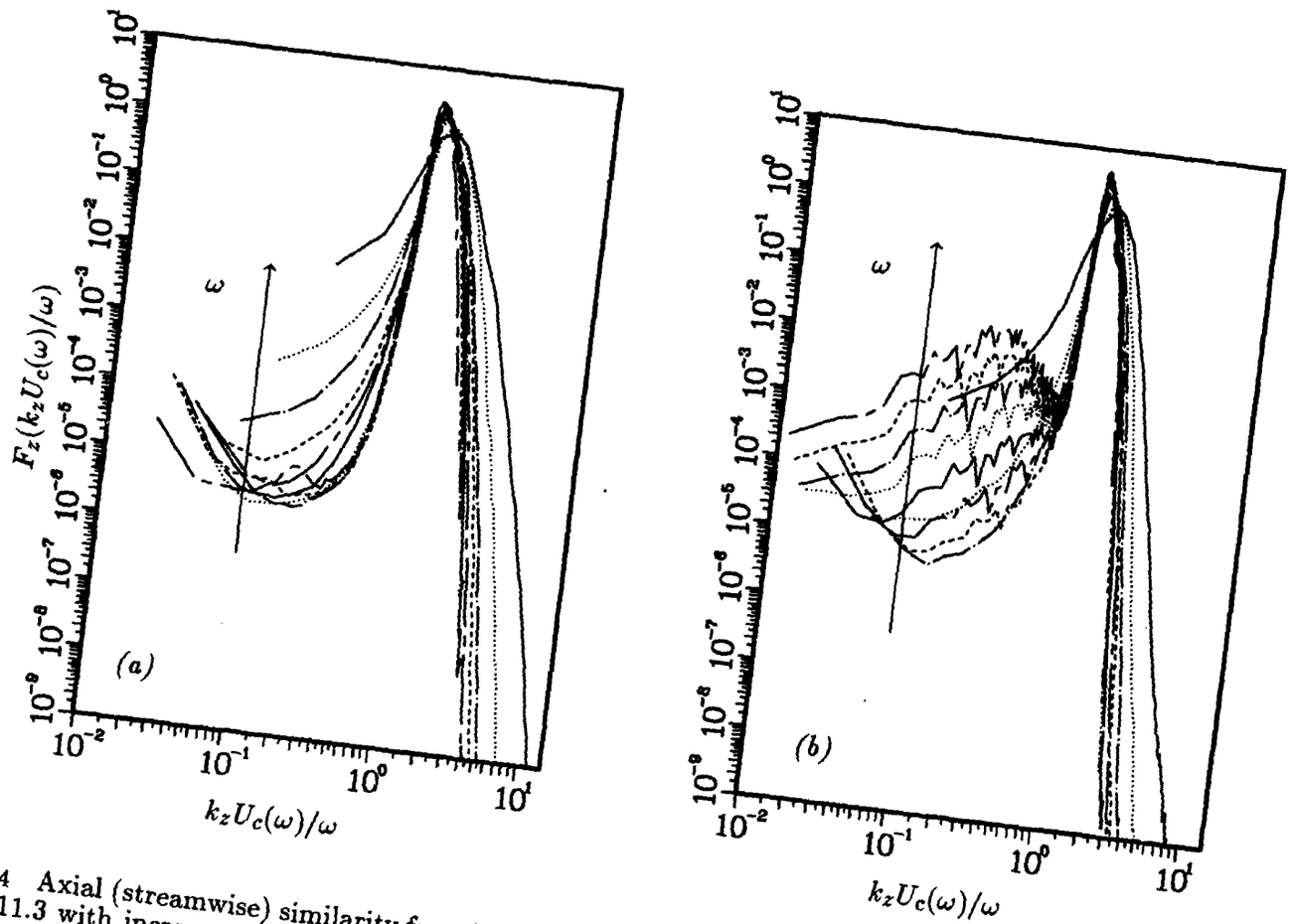

FIGURE 4.24 Axial (streamwise) similarity function $F_z(k_zU_c(\omega)/\omega)$. The frequency range of $\omega\delta/u_\tau$ is: (*a*) from 31.13 to 311.3 with increments of 31.13 for $\delta/a = 5$ and (*b*) from 38.08 to 380.8 with increments of 38.08 for $\delta/a = 11$.

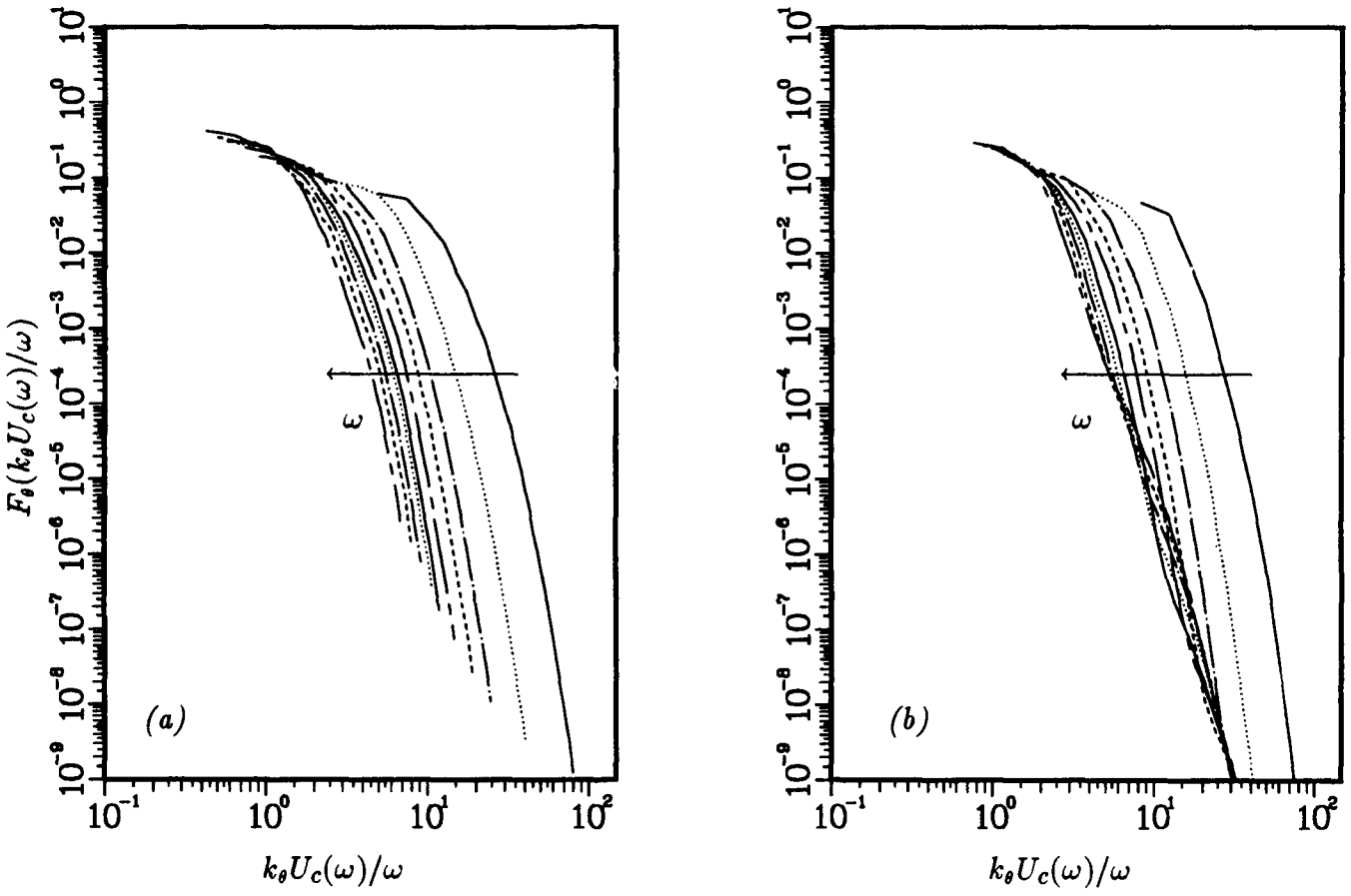

FIGURE 4.25 Azimuthal (spanwise) similarity function $F_\theta(k_\theta U_c(\omega)/\omega)$. The frequency range of $\omega\delta/u_\tau$ is: (a) from 31.13 to 311.3 with increments of 31.13 for $\delta/a = 5$ and (b) from 38.08 to 380.8 with increments of 38.08 for $\delta/a = 11$.

CHAPTER 5

Summary and Conclusions

The main objective of this study was to investigate the space-time characteristics of turbulent lfows over long towed cylinders. The main conclusions are recapitulated in this chapter.

For a sufficiently large ratio of the cylinder radius to the boundary layer thickness (δ/a) curvature affects the outer part of the layer. If the inner flow is to be influenced by the curvature then the ratio of the cylinder radius to the viscous length scale $a/(\nu/u_\tau)$ must also be small. Two simulations of transversely curved turbulent flows were successfully performed. The curvature parameters were $\delta/a = 5$ ($a^+ \approx 43$) and $\delta/a = 11$ ($a^+ \approx 21$).

In agreement with experimental measurements, as the curvature increases, the skin friction coefficient (C_f) increases and the slope of the mean velocity profile in the logarithmic region decreases. When a^+ is sufficiently small, the viscous region of the velocity profile deviates slightly from the planar law of the wall.

Measurements of the turbulence intensities and the Reynolds shear stress (when scaled with wall variables) show a decrease with increasing curvature in the outer part of the flow. These outer flow characteristics are reproduced by the present computations. In addition, and unlike their experimental counterparts, close to the wall, the computed turbulence intensities and the Reynolds shear stress decrease with increasing curvature. The reason for the difference is attributed to the large values of a^+ in most experiments, where only the outer layer is affected by the curvature. The reduction of the turbulence intensities with curvature is not the same among different components and, as the curvature increases, more of the turbulent kinetic energy is in the streamwise velocity fluctuations. This is a result of the lower intercomponent energy transfer due to the lower pressure strain correlations in the Reynolds stress budget equations of the transversely curved flows.

A new local velocity scale, which is a function of both the curvature parameter δ/a and the distance to the wall y/δ has been obtained from the mean streamwise

momentum equation. When normalized with this new velocity scale some turbulence statistics of the plane channel and the transversely curved flows collapse in the outer part of the flow ($y^+ > 30$). Near the wall the new velocity scale is unable to account for all the differences observed.

As the curvature increases, the correlation between the streamwise and wall normal velocity increases near the wall. In the higher curvature case ($\delta/a = 11$) the correlation coefficient decreases in the outer layer indicating a tendency towards stabilization. However, both flows computed are fully turbulent and statistically steady.

All vorticity intensities decrease with increasing curvature throughout the layer, with the exception of the normal vorticity intensity, which is not affected near the wall ($y^+ < 7$). The axial (streamwise) intensity suggests that, as the curvature increases, the near-wall streamwise vortices are weaker but have a radius similar to that of the plane channel. Their position away from the wall is also not affected by the curvature. As the curvature increases, the vorticity near the wall tends to be increasingly oriented in the direction normal to the wall.

Another effect of the transverse curvature is the longer streamwise length scale of the low-speed streaks. The mean spanwise spacing of the low-speed streaks is slightly less 100 wall units in both transversely curved flows at $y^+ \approx 12$. Thus, as the circumference of the cylinder decreases (as the curvature increases), there are fewer low-speed streaks around the cylinder.

Near-wall internal shear layers are common in the two transversely curved flows computed. As the shear layers lift off from the surface of the cylinder they have large spanwise length scales relative to the cylinder radius.

The linear and nonlinear sources of pressure fluctuations are strongly reduced as the curvature increases. The sources associated with streamwise vortices are still the strongest, however, as the curvature increases, a new source of pressure fluctuations associated with the strong normal vorticity fluctuations becomes increasingly important.

As the curvature increases, the axial (streamwise) wall pressure spectrum decreases for all scales, whereas the azimuthal (spanwise) wall pressure spectrum decreases only for small wave-numbers (large scales). A curvature dependent outer

length scale, which increases with curvature, is proposed from geometrical arguments. This length scale collapses the streamwise spectra of the wall pressure fluctuations of the two transversely curved flows studied with that of the plane channel in the high wave number range.

Even though the wall pressure fluctuations become increasingly better correlated around the cylinder, the azimuthal correlation length, when measured in wall units, decreases as the curvature increases. On the other hand, the axial (streamwise) correlation length increases with curvature. Unlike in the planar case, the wall pressure iso-correlation contours are elongated in the streamwise direction, for both large and small separations. Since the streamwise elongation of turbulence structures with curvature is most pronounced near the wall, it is conjectured that the near wall fluctuations are more important in determining the length scales of the wall pressure fluctuations. Fractional contributions of the flow (from inner and outer layers) to the wall pressure intensity show a minimal effect of curvature relative to the plane channel.

Like the axial (streamwise) one-dimensional spectra, the temporal spectra of the wall pressure fluctuations of the transversely curved flows also decreases as the curvature increases. A new curvature dependent time scale which increases with increasing curvature was propsed. When scaled with the mean wall shear and this time scale the temporal spectra of the wall pressure fluctuations of the two transversely curved flows studied and that of the plane channel collapse in the high frequency range.

The two-dimensional spectra and space time correlations of the wall pressure fluctuations give a lower convection velocity ($U_c \approx 0.6U_\infty$) than in the plane channel. With this convection velocity Taylor's hypothesis holds in the two transversely curved flows studied.

APPENDIX A

Reynolds Stress Budgets

In this appendix the transport equations for the Reynolds stresses and turbulent kinetic energy are presented. They are derived from the Navier-Stokes equations in general tensor notation (see for example Moser & Moin [1984])

$$\frac{\partial V^i}{\partial t} + V^k V^i_{,k} = -g^{ik} P_{,k} + \frac{1}{Re_\tau} g^{kl} V^i_{,kl}, \qquad i = 1,2,3, \tag{A.1}$$

where the superscripts denote contravariant tensors and the subscripts following a comma denote covariant derivatives. The contravariant tensor g^{ij} is the metric tensor, which in cylindrical coordinates is

$$g^{ij} = \begin{pmatrix} 1 & 0 & 0 \\ 0 & 1/x_1^2 & 0 \\ 0 & 0 & 1 \end{pmatrix}, \tag{A.2}$$

and the coordinates (x_1, x_2, x_3) correspond to (r, θ, z), respectively.

The evolution equation for the mean velocity is given by

$$\frac{\partial \overline{V}^i}{\partial t} + \overline{V}^k \overline{V}^i_{,k} + \overline{v^k v^i_{,k}} = -g^{ik} \overline{P}_{,k} + \frac{1}{Re_\tau} g^{kl} \overline{V}^i_{,kl}, \tag{A.3}$$

and the velocity fluctuations equations,

$$\frac{\partial v^i}{\partial t} + \overline{V}^k v^i_{,k} + v^k \overline{V}^i_{,k} = -g^{ik} p_{,k} + \frac{1}{Re_\tau} g^{kl} v^i_{,kl} - (v^i v^k - \overline{v^i v^k})_{,k}, \tag{A.4}$$

are obtained by subtracting Equation $A.3$ from Equation $A.1$.

From Equation $A.4$, evolution equations for the Reynolds stresses are:

$$
\begin{aligned}
&\frac{\partial \overline{v^i v^j}}{\partial t} + \overline{V}^k (\overline{v^i v^j})_{,k} = && \text{total rate of change,} \\
&-\left(\overline{v^j v^k} \overline{V}^i_{,k} + \overline{v^i v^k} \overline{V}^j_{,k}\right) && \text{production rate,} \\
&-\left[g^{ik} \overline{v^j p_{,k}} + g^{jk} \overline{v^i p_{,k}}\right] && \text{velocity pressure-gradient term,} \\
&-(\overline{v^i v^j v^k})_{,k} && \text{turbulent transport rate,} \\
&+\frac{1}{Re_\tau} g^{kl} (\overline{v^i v^j})_{,kl} && \text{viscous diffusion rate,} \\
&-\frac{2}{Re_\tau} g^{kl} \left(\overline{v^j_{,l} v^i_{,k}}\right) && \text{viscous dissipation rate.}
\end{aligned}
\qquad (A.5)
$$

The transport equation for the normal stress, $\overline{v_r^2}$,

$$
\begin{aligned}
&\frac{\partial \overline{v_r^2}}{\partial t} = -2\overline{v_r \frac{\partial p}{\partial r}} \\
&-\left\{\frac{1}{r}\frac{\partial}{\partial r}\left[r(\overline{v_r v_r v_r})\right] - \frac{2}{r}\overline{v_r v_\theta v_\theta}\right\} \\
&+\frac{1}{Re_\tau}\left[\frac{1}{r}\frac{\partial}{\partial r}\left(r\frac{\partial \overline{v_r^2}}{\partial r}\right) + \frac{2(\overline{v_\theta^2} - \overline{v_r^2})}{r^2}\right] \\
&-\frac{2}{Re_\tau}\left[\overline{\left(\frac{\partial v_r}{\partial r}\right)^2} + \frac{1}{r^2}\overline{\left(\frac{\partial v_r}{\partial \theta} - v_\theta\right)^2} + \overline{\left(\frac{\partial v_r}{\partial z}\right)^2}\right],
\end{aligned}
\qquad (A.6)
$$

is obtained from Equation $A.5$ by setting $i = j = 1$, evaluating the contravariant derivatives and taking advantage of the homogeneity in the θ and z directions

The transport equation for the azimuthal stress, $\overline{v_\theta^2}$,

$$\begin{aligned}
\frac{\partial \overline{v_\theta^2}}{\partial t} &= -2\overline{\frac{v_\theta}{r}\frac{\partial p}{\partial \theta}} \\
&- \left\{ \frac{1}{r}\frac{\partial}{\partial r}\left[r(\overline{v_\theta v_\theta v_r}) \right] + \frac{2}{r}\overline{v_r v_\theta v_\theta} \right\} \\
&+ \frac{1}{Re_\tau}\left[\frac{1}{r}\frac{\partial}{\partial r}\left(r\frac{\partial \overline{v_\theta^2}}{\partial r} \right) + \frac{2(\overline{v_r^2} - \overline{v_\theta^2})}{r^2} \right] \\
&- \frac{2}{Re_\tau}\left[\overline{\left(\frac{\partial v_\theta}{\partial r}\right)^2} + \frac{1}{r^2}\overline{\left(\frac{\partial v_\theta}{\partial \theta} + v_r\right)^2} + \overline{\left(\frac{\partial v_\theta}{\partial z}\right)^2} \right],
\end{aligned} \tag{A.7}$$

is similarly obtained from Equation $A.5$ by setting $i = j = 2$.

The transport equation for the axial stress, $\overline{v_z^2}$,

$$\begin{aligned}
\frac{\partial \overline{v_z^2}}{\partial t} &= -2\overline{v_z\frac{\partial p}{\partial z}} \\
&- 2\overline{v_z v_r}\frac{d\overline{V}_z}{dr} \\
&- \left\{ \frac{1}{r}\frac{\partial}{\partial r}\left[r(\overline{v_z v_z v_r}) \right] \right\} \\
&+ \frac{1}{Re_\tau}\left[\frac{1}{r}\frac{\partial}{\partial r}\left(r\frac{\partial \overline{v_z^2}}{\partial r} \right) \right] \\
&- \frac{2}{Re_\tau}\left[\overline{\left(\frac{\partial v_z}{\partial r}\right)^2} + \frac{1}{r^2}\overline{\left(\frac{\partial v_z}{\partial \theta}\right)^2} + \overline{\left(\frac{\partial v_z}{\partial z}\right)^2} \right],
\end{aligned} \tag{A.8}$$

is similarly obtained from Equation $A.5$ by setting $i = j = 3$. The budgets of $\overline{v_z^2}$, $\overline{v_r^2}$ and $\overline{v_\theta^2}$ for $\delta/a = 5$ and $\delta/a = 11$ are shown in Figures A.1, A.2 and A.3, respectively. The various terms of the budget equations are qualitatively like their planar counterparts (Mansour *et al.* [1988]) but have their magnitude decreased as the curvature increases.

The transport equation for the Reynolds shear stress, $\overline{v_z v_r}$,

$$\begin{aligned}
\frac{\partial \overline{v_z v_r}}{\partial t} &= -\overline{v_r^2}\frac{d\overline{V}_z}{dr} \\
&- \left[\overline{v_r \frac{\partial p}{\partial z}} + \overline{v_z \frac{\partial p}{\partial r}}\right] \\
&- \left\{\frac{1}{r}\frac{\partial}{\partial r}\left[r(\overline{v_r v_z v_r})\right] - \frac{1}{r}\overline{v_z v_\theta v_\theta}\right\} \\
&+ \frac{1}{Re_\tau}\left[\frac{1}{r}\frac{\partial}{\partial r}\left(r\frac{\partial \overline{v_z v_r}}{\partial r}\right) - \frac{\overline{v_r v_z}}{r^2}\right] \\
&- \frac{2}{Re_\tau}\left[\overline{\frac{\partial v_r}{\partial r}\frac{\partial v_z}{\partial r}} + \overline{\frac{1}{r^2}\frac{\partial v_z}{\partial \theta}\left(\frac{\partial v_r}{\partial \theta} - v_\theta\right)} + \overline{\frac{\partial v_r}{\partial z}\frac{\partial v_z}{\partial z}}\right],
\end{aligned} \tag{A.9}$$

is similarly obtained from Equation A.5 by setting $i = 1$ and $j = 3$. The budget of $\overline{v_z v_r}$ for $\delta/a = 5$ and $\delta/a = 11$ is shown in Figure A.4. As in the case of the normal stresses, the budget of the Reynolds stress $\overline{v_z v_r}$ is also similar to its planar counterpart (Mansour *et al.* [1988]) but the magnitude of the terms decreases as the curvature increases.

The transport equation for the turbulent kinetic energy, $q^2 = (1/2)(\overline{v_r^2} + \overline{v_\theta^2} + \overline{v_z^2})$,

$$
\begin{aligned}
\frac{\partial q^2}{\partial t} &= -\overline{v_z v_r}\frac{d\overline{V}_z}{dr} \\
&- \left[\overline{v_r\frac{\partial p}{\partial r}} + \overline{\frac{v_\theta}{r}\frac{\partial p}{\partial \theta}} + \overline{v_z\frac{\partial p}{\partial z}}\right] \\
&- \left\{\frac{1}{r}\frac{\partial}{\partial r}\left[r(\overline{q^2 v_r})\right]\right\} \\
&+ \frac{1}{Re_\tau}\left[\frac{1}{r}\frac{\partial}{\partial r}\left(r\frac{\partial q^2}{\partial r}\right)\right] \\
&- \frac{1}{Re_\tau}\left[\overline{\left(\frac{\partial v_r}{\partial r}\right)^2} + \overline{\left(\frac{\partial v_\theta}{\partial r}\right)^2} + \overline{\left(\frac{\partial v_z}{\partial r}\right)^2}\right] \\
&- \frac{1}{Re_\tau}\frac{1}{r^2}\left[\overline{\left(\frac{\partial v_r}{\partial \theta} - v_\theta\right)^2} + \overline{\left(\frac{\partial v_\theta}{\partial \theta} + v_r\right)^2} + \overline{\left(\frac{\partial v_z}{\partial \theta}\right)^2}\right] \\
&- \frac{1}{Re_\tau}\left[\overline{\left(\frac{\partial v_r}{\partial z}\right)^2} + \overline{\left(\frac{\partial v_\theta}{\partial z}\right)^2} + \overline{\left(\frac{\partial v_z}{\partial z}\right)^2}\right],
\end{aligned}
\qquad (A.10)
$$

is obtained from the trace Equation $A.5$.

The budget of turbulent kinetic energy for $\delta/a = 5$ and $\delta/a = 11$ is shown in Figure A.4. The five terms in the right hand side of the transport equation for the turbulent kinetic energy (Equation A.10) of the two transversely curved flows are compared to their planar counterparts (Mansour *et al.* [1988]) in Figures A.6 through A.10. The magnitudes of all terms decreases as the curvature increases.

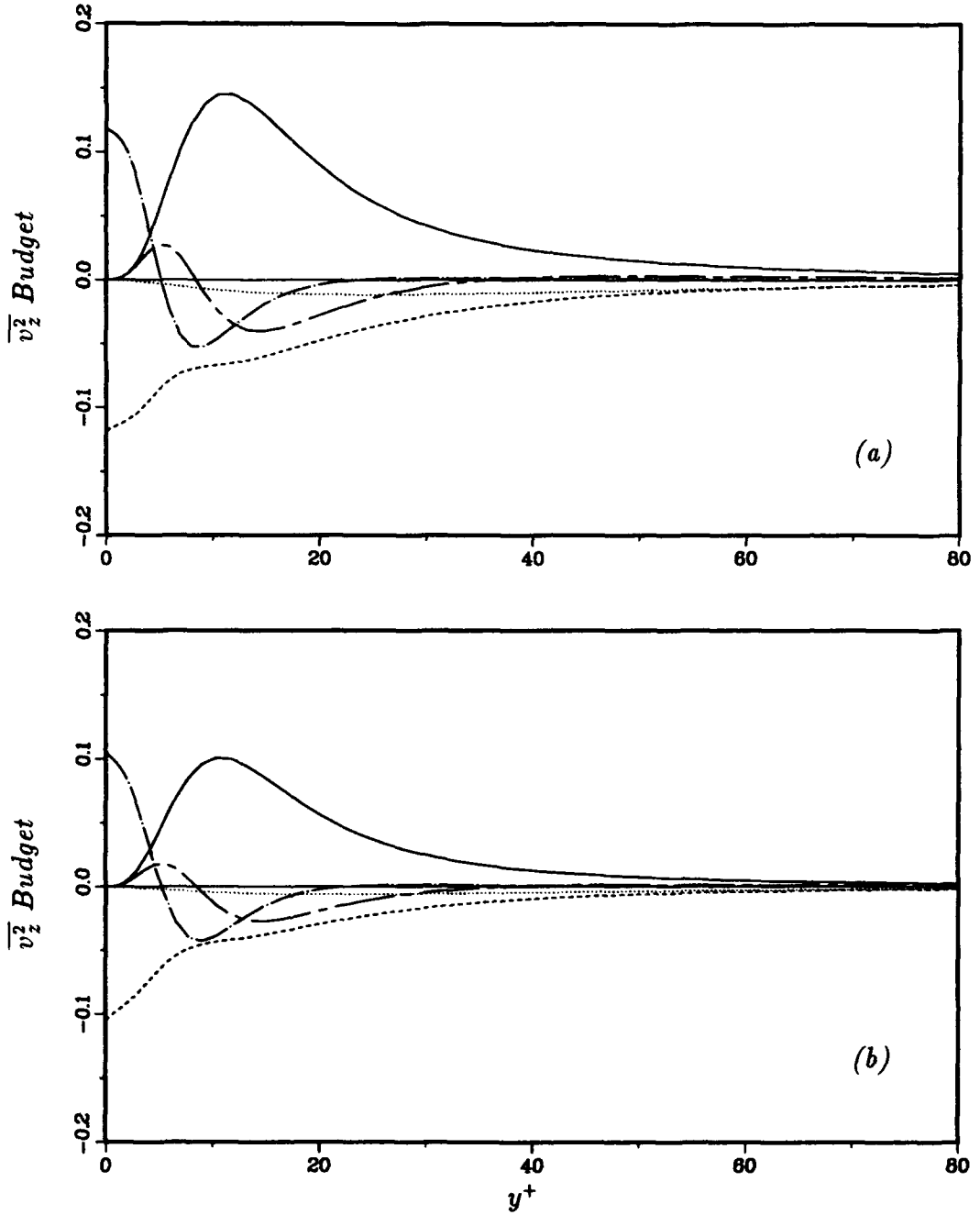

FIGURE A.1 Transport equation balance of the axial turbulence intensity normalized by ν and u_τ for (*a*) $\delta/a = 5$ and (*b*) $\delta/a = 11$: —— production, ---- dissipation rate, ····· velocity-pressure gradient (pressure diffusion), –·– turbulent transport, —·— viscous diffusion.

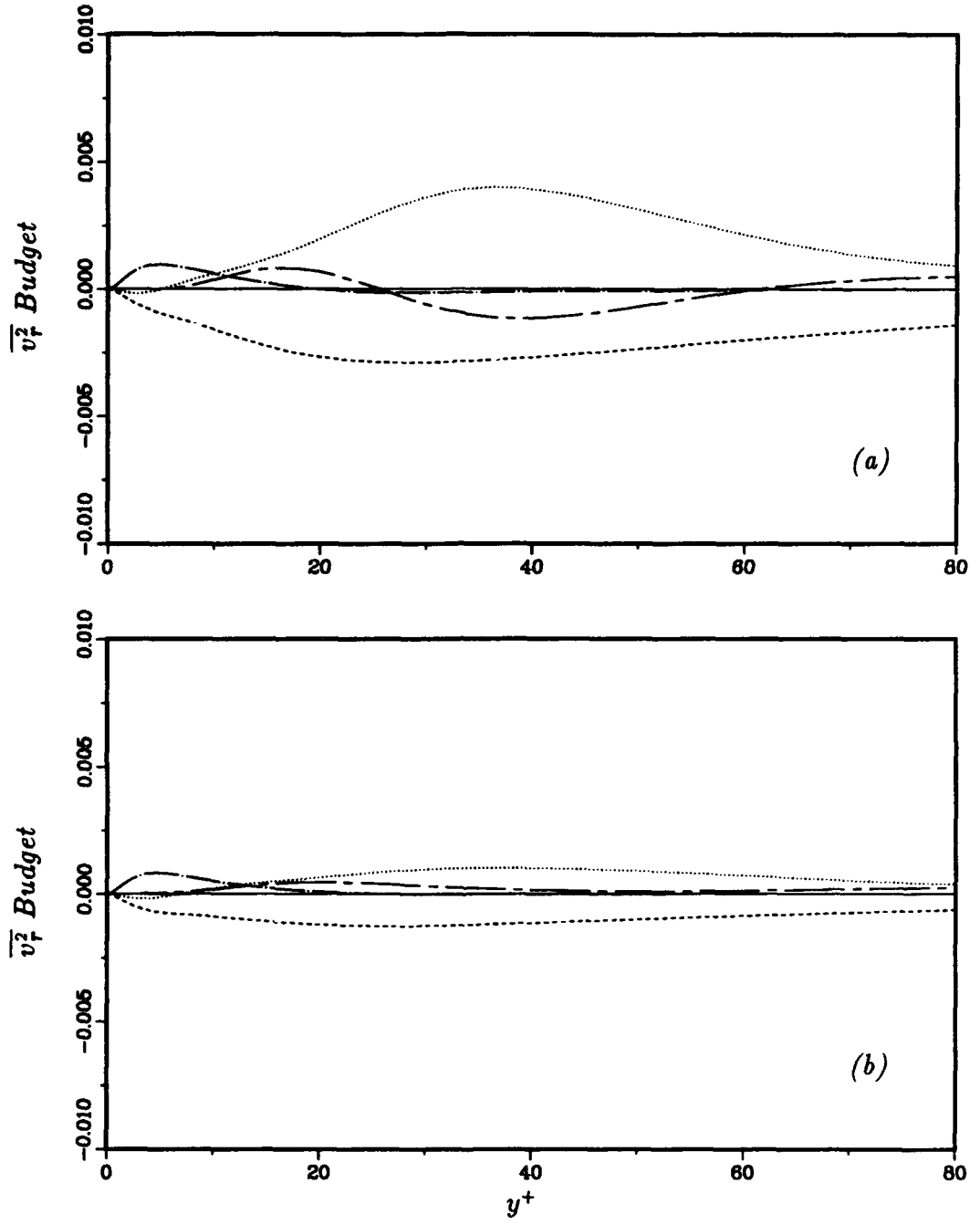

FIGURE A.2 Transport equation balance of the normal turbulence intensity normalized by ν and u_τ for (*a*) $\delta/a = 5$ and (*b*) $\delta/a = 11$: —— production, ---- dissipation rate, ····· velocity-pressure gradient (pressure diffusion), –·– turbulent transport, —·— viscous diffusion.

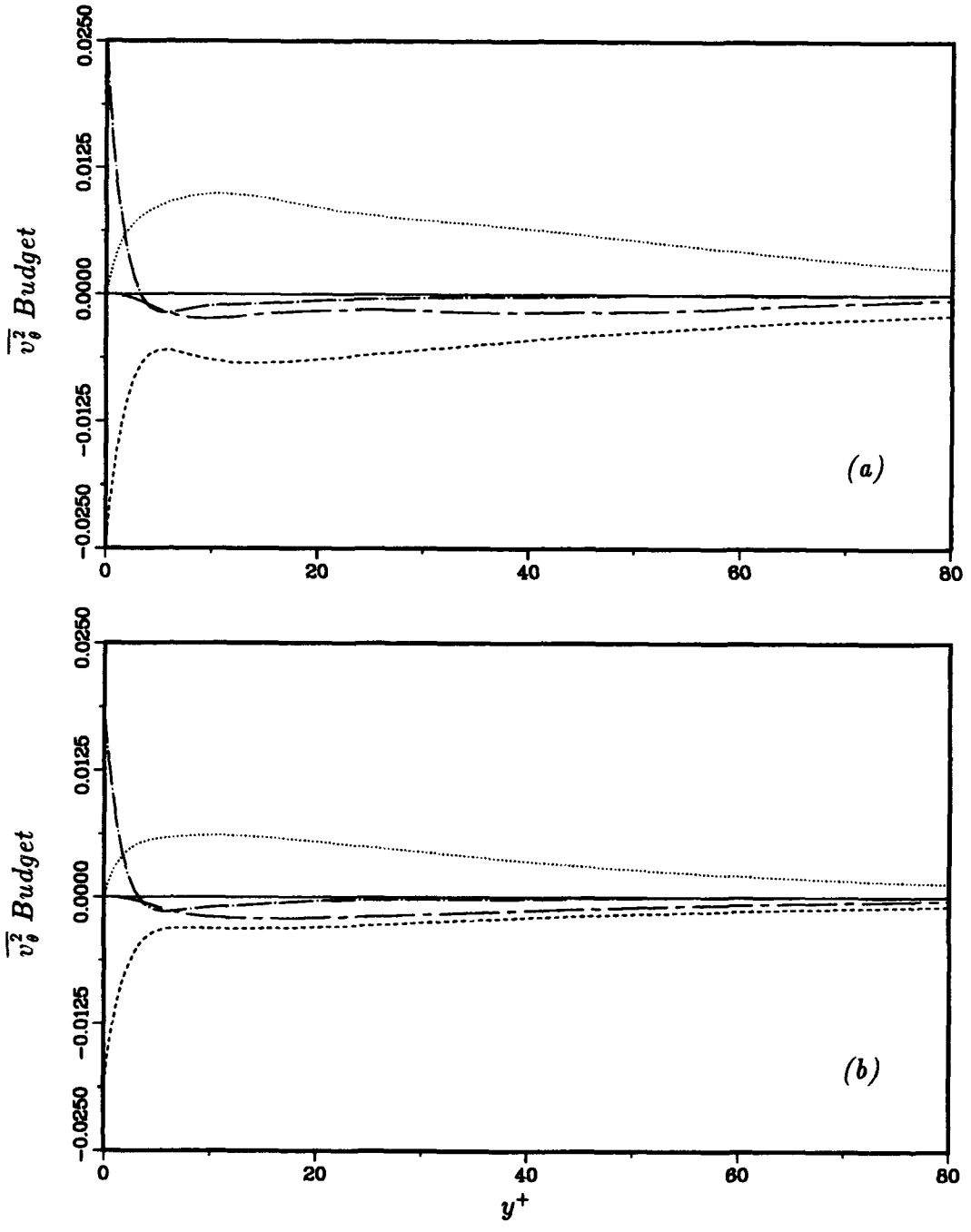

FIGURE A.3 Transport equation balance of the azimuthal turbulence intensity normalized by ν and u_τ for (*a*) $\delta/a = 5$ and (*b*) $\delta/a = 11$: —— production, ---- dissipation rate, ····· velocity-pressure gradient (pressure diffusion), —·— turbulent transport, —··— viscous diffusion.

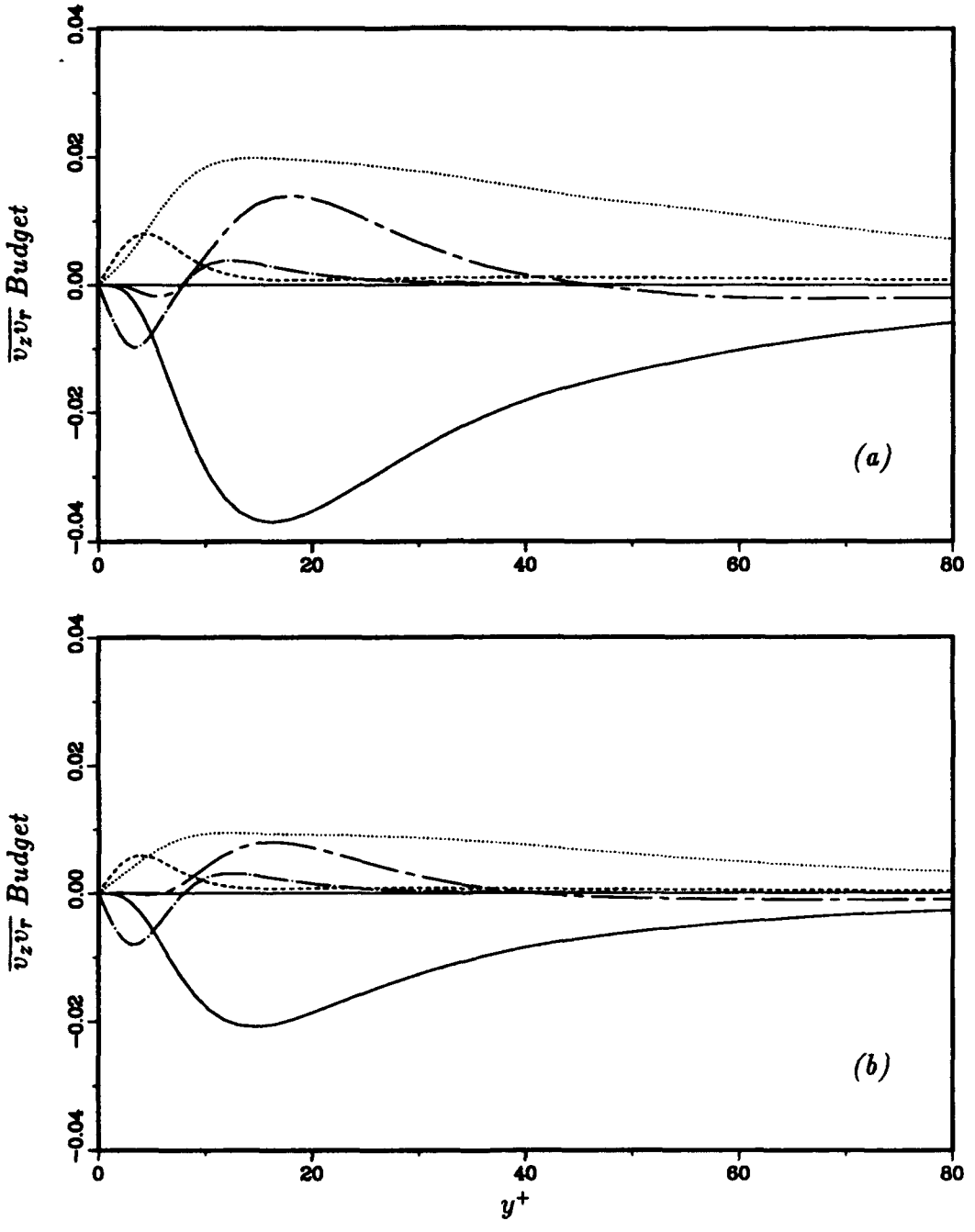

FIGURE A.4 Transport equation balance of the Reynolds shear stress normalized by ν and u_τ for (*a*) $\delta/a = 5$ and (*b*) $\delta/a = 11$: —— production, ---- dissipation rate, ····· velocity-pressure gradient (pressure diffusion), —·— turbulent transport, —·— viscous diffusion.

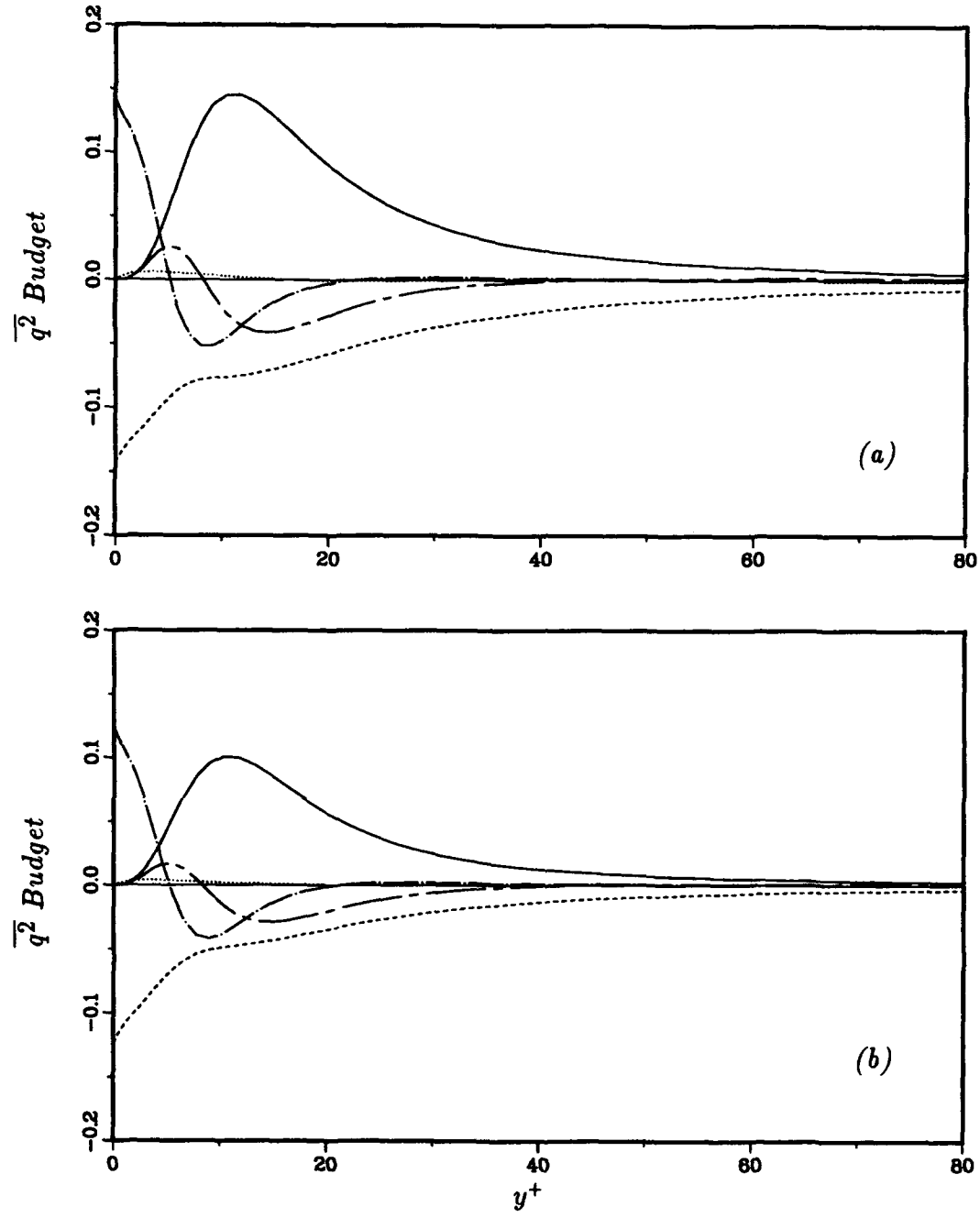

FIGURE A.5 Transport equation balance of the turbulent kinetic energy normalized by ν and u_τ for (*a*) $\delta/a = 5$ and (*b*) $\delta/a = 11$: —— production, ---- dissipation rate, ····· velocity-pressure gradient (pressure diffusion), —·— turbulent transport, —·— viscous diffusion.

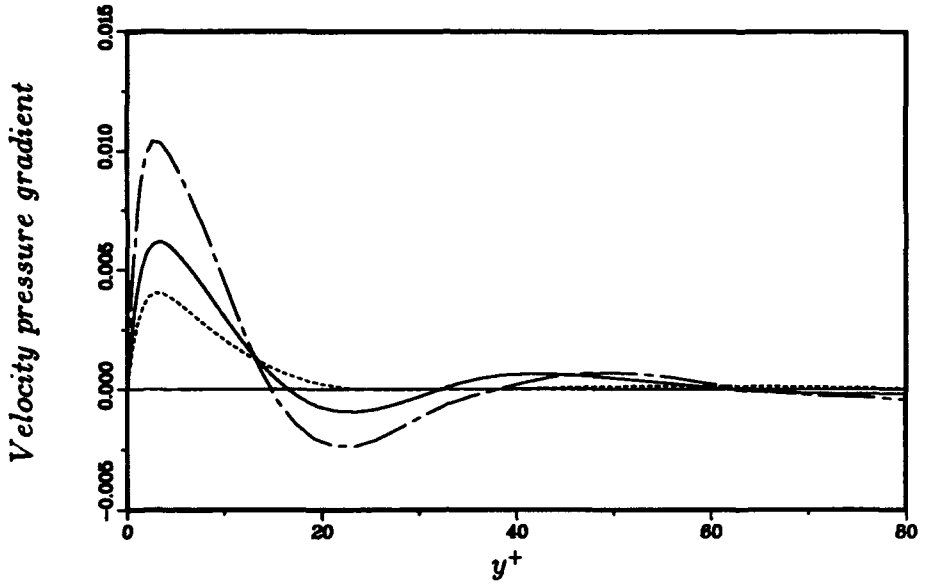

FIGURE A.6 Velocity pressure gradient term of the turbulent kinetic energy equation normalized by ν and u_τ: ——— plane channel (Mansour *et al.* [1988]); cylinders with —— $\delta/a = 5$ and ---- $\delta/a = 11$.

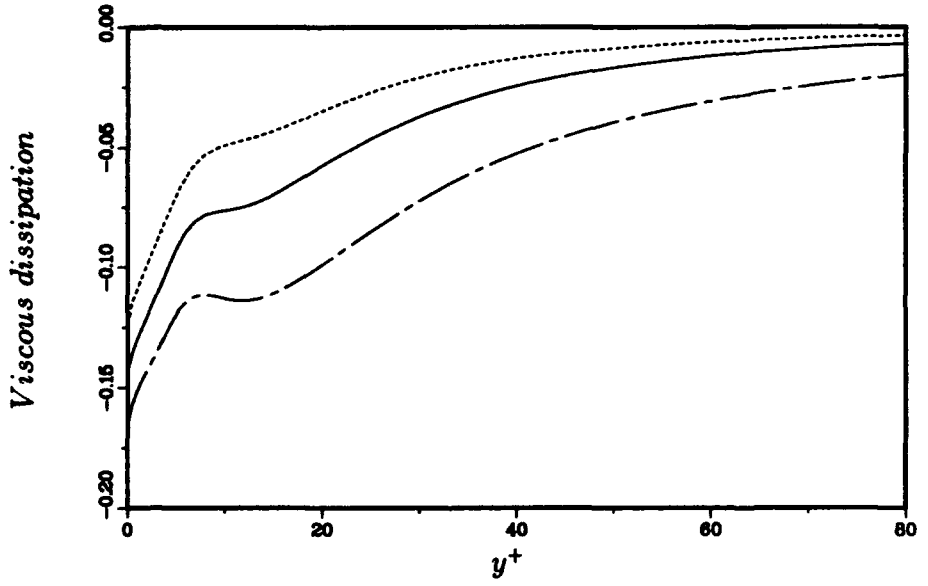

FIGURE A.7 Dissipation of turbulent kinetic energy normalized by ν and u_τ: ——— plane channel (Mansour *et al.* [1988]); cylinders with —— $\delta/a = 5$ and ---- $\delta/a = 11$.

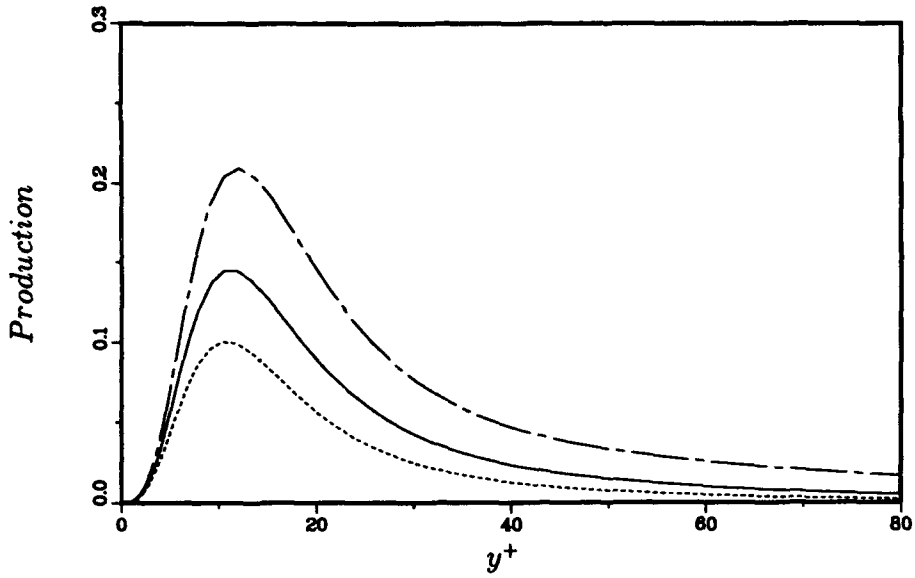

FIGURE A.8 Production of turbulent kinetic energy normalized by ν and u_τ: ——— plane channel (Mansour *et al.* [1988]); cylinders with —— $\delta/a = 5$ and ---- $\delta/a = 11$.

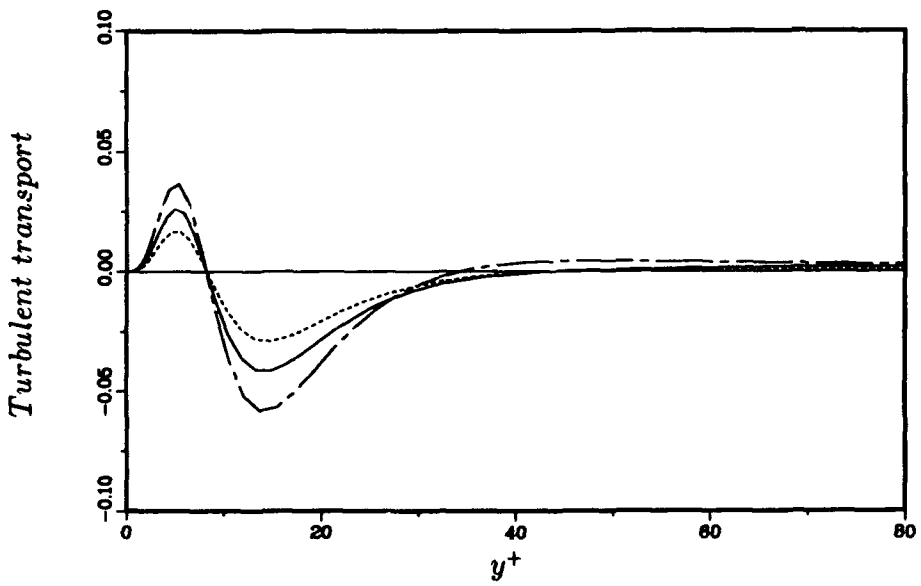

FIGURE A.9 Turbulent transport of turbulent kinetic energy normalized by ν and u_τ: ——— plane channel (Mansour *et al.* [1988]); cylinders with —— $\delta/a = 5$ and ---- $\delta/a = 11$.

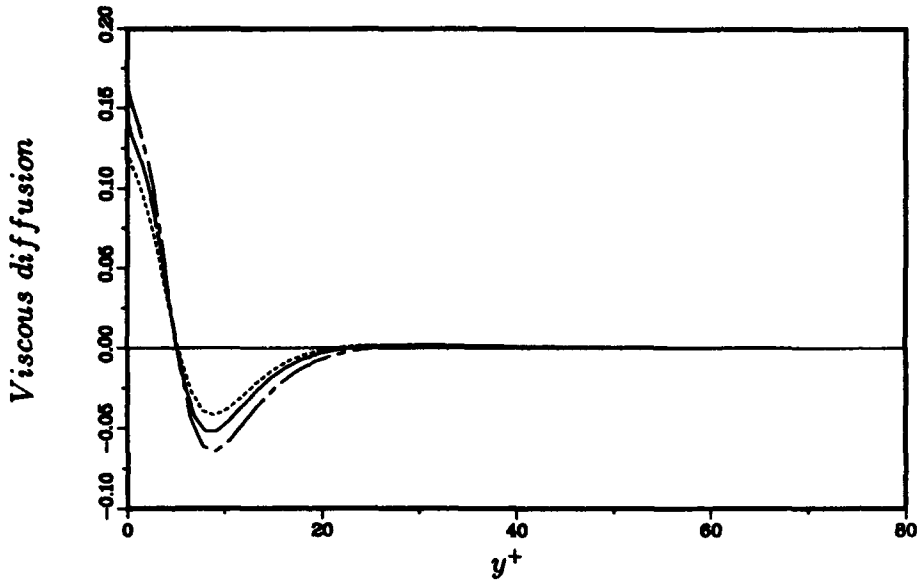

FIGURE A.10 Viscous diffusion in turbulent kinetic energy equation normalized by ν and u_τ: —·— plane channel (Mansour *et al.* [1988]); cylinders with —— $\delta/a = 5$ and ---- $\delta/a = 11$.

APPENDIX B

The Green's Function for Pressure

In cylindrical coordinates the Poisson equation for the pressure is given by Equation 4.1.1. For each wave-number pair (m, k_z) the Fourier transform of Equation 4.1.1 is given by

$$\frac{d^2\hat{p}}{dr^2} + \frac{1}{r}\frac{d\hat{p}}{dr} - \left(\frac{m^2}{r^2} + k_z^2\right)\hat{p} = \hat{f}(r),$$

$$\left.\frac{d\hat{p}}{dr}\right|_{r=a} = \left.\frac{1}{Re_\tau}\frac{d^2\hat{v}_r}{dr^2}\right|_{r=a}, \qquad \left.\frac{d\hat{p}}{dr}\right|_{r=a+1} = \left[-2im\frac{1}{Re_\tau}\frac{\hat{v}_\theta}{r^2} + \frac{\widehat{v_\theta^2}}{r}\right]_{r=a+1}, \tag{B.1}$$

where $\hat{f}(r)$ is the Fourier transform of the pressure source terms. In the Strum-Liouville form the Equation $B.1$ is

$$\mathcal{L}(\hat{p}) = r\hat{f}(r), \tag{B.2}$$

where the operator $\mathcal{L}$ is given by

$$\mathcal{L} = \frac{d}{dr}\left(r\frac{d}{dr}\right) - r\left(\frac{m^2}{r^2} + k_z^2\right). \tag{B.3}$$

The Green's function, $\hat{\mathcal{G}}$, of the operator $\mathcal{L}$ with homogeneous derivative boundary boundary conditions is the solution of

$$\mathcal{L}(\hat{\mathcal{G}}) = \delta(r - r_o),$$

$$\left.\frac{d\hat{\mathcal{G}}}{dr}\right|_{r=a} = 0, \qquad \left.\frac{d\hat{\mathcal{G}}}{dr}\right|_{r=a+1} = 0, \tag{B.4}$$

where $\delta(r - r_o)$ is the Dirac delta 'function' and r_o denotes the radial position of the source. At $r = r_o$, $\hat{\mathcal{G}}$ is continuous

$$\hat{\mathcal{G}}(r, r_o)\Big|_{r=r_o^+} = \hat{\mathcal{G}}(r, r_o)\Big|_{r=r_o^-}, \tag{B.5}$$

and satisfies the jump condition

$$\frac{d}{dr}\hat{\mathcal{G}}(r, r_o)\Big|_{r=r_o^+} - \frac{d}{dr}\hat{\mathcal{G}}(r, r_o)\Big|_{r=r_o^-} = \frac{1}{r_o}. \tag{B.6}$$

For this system, Green's identity is given by

$$\int_a^{a+1} \left[\hat{p}\mathcal{L}(\hat{\mathcal{G}}) - \hat{\mathcal{G}}\mathcal{L}(\hat{p})\right] dr = \left[r\left(\hat{p}\frac{d\hat{\mathcal{G}}}{dr} - \hat{\mathcal{G}}\frac{d\hat{p}}{dr}\right)\right]_a^{a+1}, \tag{B.7}$$

which, upon integration, gives the general form of the Fourier coefficient for the pressure fluctuations,

$$\begin{aligned}\hat{p}(r) = &\int_a^{a+1} \hat{\mathcal{G}}(r, r_o)\hat{f}(r_o) r_o dr_o + \\ &a\hat{\mathcal{G}}(r, a)\frac{d\hat{p}}{dr}\Big|_{r=a} - (a+1)\hat{\mathcal{G}}(r, a+1)\frac{d\hat{p}}{dr}\Big|_{r=a+1}.\end{aligned} \tag{B.8}$$

The Fourier coefficient of the wall pressure fluctuations is obtained by evaluating this expression at $r = a$,

$$\begin{aligned}\hat{p}_w = &\int_a^{a+1} \hat{\mathcal{G}}(a, r_o)\hat{f}(r_o) r_o dr_o + \\ &a\hat{\mathcal{G}}(a, a)\frac{d\hat{p}}{dr}\Big|_{r=a} - (a+1)\hat{\mathcal{G}}(a, a+1)\frac{d\hat{p}}{dr}\Big|_{r=a+1}.\end{aligned} \tag{B.9}$$

The contributions to the wall pressure from a volume around the cylinder bounded by $a \leq r_o \leq r_s$ are given by

$$\hat{p}_{r_s^-} = \int_a^{r_s} \hat{\mathcal{G}}(a, r_o)\hat{f}(r_o) r_o dr_o + \\ a\hat{\mathcal{G}}(a,a)\frac{d\hat{p}}{dr}\bigg|_{r=a} - r_s\hat{\mathcal{G}}(a,r_s)\frac{d\hat{p}}{dr}\bigg|_{r=r_s}. \tag{B.10}$$

Likewise, the contributions of the outer part of the volume ($r_s \leq r_o \leq a+1$) are obtained by subtracting Equation $B.10$ from Equation $B.9$

$$\hat{p}_{r_s^+} = \int_{r_s}^{a+1} \hat{\mathcal{G}}(a, r_o)\hat{f}(r_o) r_o dr_o + \\ r_s\hat{\mathcal{G}}(a,r_s)\frac{d\hat{p}}{dr}\bigg|_{r=r_s} - (a+1)\hat{\mathcal{G}}(a,a+1)\frac{d\hat{p}}{dr}\bigg|_{r=a+1}. \tag{B.11}$$

APPENDIX C

Flow Databases

Velocity and pressure fields for the two transversely curved flow calculations ($\delta/a = 5$ and 11) were saved every 200 time steps. The time step was 2.52×10^{-4} δ/u_τ time units for the $\delta/a = 5$ case and 2.06×10^{-4} δ/u_τ time units for the $\delta/a = 5$ case. The wall pressure and wall shear stresses were saved every 10 time steps in both calculations.

The data was archived in Fourier space in the axial and azimuthal directions and in physical space in the radial direction and in time. The spatial characteristics of the data are described in Table 2.2, and the temporal characteristics are summarized in Table 4.1.

C.1 Velocity and Pressure Data

The first record of each restart file is a header containing: (NR, NZ, NTH, MTH, MR, REY, $MEANPG$, DT, LTH, LZ, RA, $TIME$, $TSTEP$), which are the number of planes in the radial direction minus 1 (NR), the number of Fourier modes in the axial direction (NZ), the number of Fourier modes in the azimuthal direction (NTH), the drawer size in the azimuthal direction (MTH), the drawer size in the radial direction (MR), the Reynolds number based on the unity velocity in which the data is reported (in these units the friction velocity is 1.2615 for the $\delta/a = 5$ case and 1.3947 in the $\delta/a = 11$ case) and $\delta/2$ (REY) (in both cases this Reynolds number is 85), the time step in these units (DT), the length of the computational domain in the azimuthal direction (LTH), the length of the computational domain in the axial direction (LZ), both in units of $\delta/2$, the ratio of the outer to inner radius of the computational domain (RA), the time ($TOLD$) and the time step ($TSTEP$) (in these units the time step was 4×10^{-4} for $\delta/a = 5$ and 3×10^{-4} for $\delta/a = 11$). Next there are $(NR/MR+1) \times (NTH/MTH)$ $VDATA[RGR, THGR]$ records containing the complex Fourier coefficients of the

velocity field in the order (V_θ, V_r, V_z) followed by $(NR/MR+1)\times(NTH/MTH)$ $PDATA[RGR, THGR]$ records containing the complex Fourier coefficients of the pressure field. The indices RGR and $THGR$ identify the drawers of the database.

Each $VDATA$ and $PDATA$ drawer is a complex array dimensioned as $DATAV$ $[NZ/2, MTH, 3, MR]$ and as $DATAP[NZ/2, MTH, MR]$, respectively. The first index indicates the axial (streamwise) wave number $I_1 = 1, ..., NZ/2$. The second index indicates the azimuthal (spanwise) wave number $I_2 = 1, ..., MTH$, and the wave number associated with each I_2 is given by

$$\begin{aligned} &(THGR-1)\star MTH + I_2, \qquad I_2 \le MTH/2, \\ -&[(THGR-1)\star MTH + I_2 - MTH/2], \qquad I_2 > MTH/2. \end{aligned}$$

The third index in $DATAV$ indicates the velocity component according to $I_3 = (1 \rightarrow V_\theta, 2 \rightarrow V_r, 3 \rightarrow V_z)$.

The velocity field is given in physical space in the radial direction according to the radial coordinate mapping described by Equation 2.1.6. The last index indicates the radial plane $RPLANE = I_4 + (RGR-1)\times MR$, $I_4 = 1, ..., MR$, and $\xi = -\cos(\pi(RPLANE-1)/NR)$.

The restart files described above are in the mass storage system `Columbia.arc.nasa.gov` at the NASA Ames Research Center in the directory `/csf/rf/rft/neves/run06/rst` for the $\delta/a = 5$ calculation and in the directory `/csf/rf/rft/neves/run12/rst` for the $\delta/a = 11$ calculation. The file names are `wire.R.[edititon number]`.

C.2 Wall Data

There are 32 files with the wall data for the $\delta/a = 5$ calculation and 26 files for the $\delta/a = 11$ calculation. Each file contains 160 time samples of the wall pressure (p_w) and wall shear stresses $(\partial V_\theta/\partial r|_w)$ and $(\partial V_z/\partial r|_w)$. The first record of each file contains (NTI, NZ, NTH, MTH, MTI, REY, LTH, LZ, RA), which are the number of time samples (NTI), the number of Fourier modes in the axial direction (NZ), the number of Fourier modes in the azimuthal direction (NTH), the drawer size in the azimuthal direction (MTH), the drawer size in the temporal

direction (MTI), the Reynolds number based on the unity velocity in which the data is reported (in these units the friction velocity is 1.2615 for the $\delta/a = 5$ case and 1.3947 in the $\delta/a = 11$ case), and $\delta/2$ (REY), the length of the computational domain in the azimuthal direction (LTH), the length of the computational domain in the axial direction (LZ), both based on $\delta/2$ and the ratio of the outer to inner radius of the computational domain (RA).

Next there are $(NTI/MTI) \times (NTH/MTH)$ $PDATA[TIGR, THGR]$ records containing the complex Fourier coefficients of the wall pressure (p_w), $(NTI/MTI) \times (NTH/MTH)$ $WDATA[TIGR, THGR]$ records containing the complex Fourier coefficients of the azimuthal wall shear stress ($\partial V_\theta/\partial r|_w$) and $(NTI/MTI) \times (NTH/MTH)$ $UDATA[TIGR, THGR]$ records containing the complex Fourier coefficients of the axial wall shear stress ($\partial V_z/\partial r|_w$). The indices $TIGR$ and $THGR$ identify the drawers of the database. Each $PDATA$ drawer is a complex array dimensioned as $DATAP[NZ/2, MTH, MTI]$. The first index indicates the axial (streamwise) wave number $I_1 = 1, ..., NZ/2$. The second index indicates the azimuthal (spanwise) wave number $I_2 = 1, ..., MTH$ as described in the previous section. The third index indicates the time sample within the file $TPLANE = I_3 + TIGR \times MTI$, $I_3 = 1, ..., MTI$. The time sequence through the files is identified through the file edition number. The structure of $UDATA$ and $WDATA$ is the same as that of $PDATA$.

The wall data files described above are in the mass storage system `Columbia.arc.nasa.gov` at the NASA Ames Research Center in the directory `/csf/rf/rft/neves/run06` for the $\delta/a = 5$ calculation and in the directory `/csf/rf/rft/neves/run12` for the $\delta/a = 11$ calculation. The file names are `waldat.R.[edititon number]`.

References

AFZAL, N. & R. NARASIMHA 1976 Axisymmetric turbulent boundary layer along a circular cylinder at constant pressure. *J. Fluid Mech.* **74**, 113-128.

BATCHELOR, G. K. 1967 *An Introduction to Fluid Dynamics*, Cambridge University Press, Cambridge.

BLAKE, W. K. 1986 *Mechanics of Flow-Induced Sound and Vibration*, Academic Press, London.

CORCOS, G. M. 1964 The structure of the turbulent pressure field in boundary-layer flows. *J. Fluid Mech.* **18**, 353-378.

CHOI, H. & P. MOIN 1990 On the space-time characteristics of the wall pressure fluctuations. *Phys. Fluids* **A 2**, 1450-1460.

COLES, D. 1965 Transition in circular Couette flow. *J. Fluid Mech.* **162**, 385.

DEISSLER, R. G. 1969 Direction of maximum turbulent vorticity in a shear flow. *Phys. Fluids* **12**, 426.

DIPRIMA, R. C. & P. M. EAGLES 1977 Amplification rates and torques for Taylor-vortex flows between rotating cylinders. *Phys. Fluids* **20**, 171.

DONNELLY, R. J. & N. J. SIMON 1960 An empirical torque relation for supercritical flow between rotating cylinders. *J. Fluid Mech.* **7**, 401.

ECKELMANN, H. 1989 *Near-Wall Turbulence*, edited by S. J. Kline and N. H. Afgan, Hemisphere Press, New York.

EMMERLING, R., MEIER, G. E. A. & DINKELACKER, A. 1974 *AGARD Conference proceedings no. 131 on Noise Mechanisms.* **24**, 1-12

GLAUERT, M. B. & M. J. LIGHTHILL 1955 The axisymmetric boundary layer on a long thin cylinder. *Proc. Roy. Soc. A* **230**, 188.

GOTTLIEB, D. & S. A. ORSZAG 1967 Numerical analysis of spectral methods: Theory and applications. *CBMS-NSF Regional Conference Series in Applied Mathematics*, SIAM **26**, Philadelphia.

HANDLER, R. A., R. J. HANSEN, L. SAKELL, S. A. ORSZAG & E. BULLISTER 1984 Calculation of the wall-pressure field in a turbulent flow. *Phys. Fluids* **27**, 579-582.

HARRIS, F. J. 1978 On the use of windows for harmonic analysis with the discrete Fourier transform. *Proceedings of the IEEE,* **66**, No. 1, 51.

JIMENEZ, J. & P. MOIN 1991 The minimal flow unit in near-wall turbulence. *J. Fluid Mech.* **225**, 213-240.

KIM, J. 1989 On the structure of the pressure fluctuations in simulated turbulent channel flow. *J. Fluid Mech.* **205**, 421-451.

KIM, J., & P. MOIN 1986 The structure of the vorticity field in turbulent channel flow. Part2. Study of ensemble-averaged fields. *J. Fluid Mech.* **162**, 339-363.

KIM, J., P. MOIN & R. D. MOSER 1987 Turbulence statistics in fully developed channel flow at low Reynolds number. *J. Fluid Mech.* **177**, 133-166.

KING, G. P., Y. LI, W. LEE, H. L. SWINNEY & P. S. MARCUS 1984 Wave speeds in wavy Taylor-vortex flow. *J. Fluid Mech.* **141**, 365-390.

KLEISER, L., & U. SCHUMANN 1981 Treatment of incompressibility and boundary conditions in 3-D numerical spectral simulations of plane channel flows. *Proc. 3rd GAMM Conf. Numerical Methods in Fluid Mechanics*, ed. by E.H. Hirschel (Vieweg, Braunschweig), 165-173.

LANCZOS, C. 1956 *Applied Analisys*, Prentice-Hall, Inc., Englewood Cliffs, New Jersey.

LEE, M. J., J. KIM & P. MOIN 1990 Structure of turbulence at high shear rate. *J. Fluid Mech.* **216**, 561-583.

LUEPTOW, M. R., P. LEEHEY & T. STELLINGER 1985 The Structure of turbulent boundary layer on a cylinder in axial flow. *Phys. Fluids* **28**, 3495-3505.

LUEPTOW, M. R. & J. H. HARITONIDIS 1987 The Structure of turbulent boundary layer on a cylinder in axial flow. *Phys. Fluids* **30**, 2993-3005.

LUEPTOW, M. R. 1988 Turbulent boundary layer on a cylinder in axial flow. *NUSC T.R.* 8389, Naval Underwater Systems Center, New London, CT 06320.

LUEPTOW, M. R. 1989 Private communication.

LUXTON, R. E., M. K. BULL & S. RAJAGOPALAN 1984 The thick turbulent boundary layer on a long fine cylinder in axial flow. *Aero. J.* **88**, 186.

MANSOUR, N. N., J. KIM, & P. MOIN 1987 Reynolds-Stress and Dissipation- rate Budgets in a Turbulent Channel Flow. *J. Fluid Mech.* **194**, 15-44.

MOIN, P. & J. KIM 1985 The structure of the vorticity field in turbulent channel flow. Part1. Analysis of instantaneous fields and statistical correlations. *J. Fluid Mech.* **155**, 441-464.

MOSER, R. D. & P. MOIN 1984 Direct numerical simulation of curved turbulent channel flow. *Report No. TF-20*, Department of Mechanical Engineering, Stanford University, Stanford CA 94305.

MOSER, R. D., P. MOIN & A. LEONARD 1983 A spectral numerical method for the Navier-Stokes equations with applications to Taylor-Couette flow. *J. Comp. Phys.* **52**, 524.

PANTON, J. L. & J. H. LINEBARGER 1974 Wall pressure spectra calculations for equilibrium boundary layers. *J. Fluid Mech.* **65**, 261-287.

RAO, G. N. V. 1967 Law of the wall in a thick axsisymmetric turbulent boundary layer. *J. Appl. Mech. Trans. A.S.M.E.* **34**, 237.

RAO, G. N. V. & N. R. KESHAVAN 1972 Axisymmetric turbulent boundary layer in zero pressure gradient flows. *J. Appl. Mech. Trans. A.S.M.E.* **94**, 125.

REID, R. O. & B. W. WILSON 1963 Boundary flow along a circular cylinder. *J. Hydraulics Div., Proc. A.S.C.E.* **89**, 21.

RICHMOND, R. L. 1957 Experimental investigation of thick axially symmetric boundary layers on cylinders at subsonic and hypersonic speeds. *Ph.D. Thesis, California Institute Technology*

ROGERS, M. M. & P. MOIN 1987 The structure of the vorticity field in homogeneous turbulent flows. *J. Fluid Mech.* **176**, 33-66.

SEBAN, R. A. & R. BOND 1951 Skin friction and heat transfer characteristics of a laminar boundary layer on a cylinder in axial incompressible flow. *J. of Aero. Sci.* **18**, 671-675.

WILLMARTH, W. W. & C. E. WOOLDRIDGE 1962 Measurements of the fluctuating pressure at the wall beneath a thick turbulent boundary layer. *J. Fluid Mech.* **14**, 187-210.

WILLMARTH, W. W. & C. S. YANG 1970 Wall pressure fluctuations beneath turbulent boundary layer on a flat plate and a cylinder. *J. Fluid Mech.* **41**, 47-80.

WILLMARTH, W. W. 1975 Pressure fluctuations beneath turbulent boundary layers. *Ann. Rev. Fluid Mech.* **7**, 13.

WILLMARTH, W. W., R. E. WINKEL, L. K. SHARMA & T. J. BOGAR 1976 Axially symmetric turbulent boundary layers on cylinders: Mean velocity profiles and wall pressure fluctuations. *J. Fluid Mech.* **76**, 35-64.

WILLS, J. A. B. 1964 On convection velocities in turbulent shear flows. *J. Fluid Mech.* **20**, 417-432.

WILLS, J. A. B. 1970 Measurements of the wave-number/phase-velocity spectrum of wall-pressure beneath a turbulent boundary layer. *J. Fluid Mech.* **45**, 65-90.

WRAY, A. A. 1988 Vectoral Manual. *Internal Report*, NASA Ames Research Center, Moffett Field, California.